Mathematical modelling of membrane separation processes

Viacheslav Perfilov

THÈSE POUR OBTENIR LE GRADE DE DOCTEUR DE L'UNIVERSITÉ DE MONTPELLIER

En Génie des Procédés

École doctorale GAIA

Institut Européen des Membranes UMR 5635

En partenariat international avec : University of Chemistry and Technology, Prague, République Tchèque
KU Leuven, Belgique

Modèles Mathématiques des Procédés de Séparation Membranaire

Présentée par Viacheslav Perfilov
Le 3 Décembre 2018

Sous la direction de Prof. Vlastimil Fila
Dr. Jose Sanchez Marcano
Prof. Ivo Vankelecom

Devant le jury composé de

Mr. Denis Roizard, Directeur de Recherche CNRS, LRGP, Université de Lorraine	Rapporteur
Mr. Vladimir Jiřičný, Docteur, Czech Academy of Sciences	Rapporteur
Karel Bouzek, Professeur, University of Chemistry and Technology, Prague	Président du jury
Petr Zámostný, Professeur Associé, University of Chemistry and Technology, Prague	Examinateur
Denis Bouyer, Professeur, Université de Montpellier	Examinateur
Bart van der Bruggen, Professeur, KU Leuven	Examinateur
Jose Sanchez Marcano, Directeur de Recherche, CNRS, IEM, Université de Montpellier	Co-directeur de thèse
Ivo Vankelecom, Professor, KU Leuven	Co-directeur de thèse

UNIVERSITY OF CHEMISTRY AND TECHNOLOGY PRAGUE

UNIVERSITÉ DE MONTPELLIER

KU LEUVEN

THESIS

Prepared in the framework of
Erasmus Mundus Doctorate in Membrane Engineering (EUDIME)
to obtain multiple Doctor degree
Issued by:

1: University of Chemistry and Technology, Prague, Czech Republic
2: Université de Montpellier, France
3 : KU Leuven, Belgium

Speciality: Chemistry and chemical technology[1]
Process Engineering[2]
Bioscience Engineering[3]

MATHEMATICAL MODELLING OF MEMBRANE SEPARATION PROCESSES

Presented by
Viacheslav PERFILOV

Publicly defended on 3 December, 2018 in front of the esteemed jury comprising of

Dr. Denis Roizard, Directeur de Recherche CNRS, LRGP, Université de Lorraine	**Reviewer**
Dr. Vladimir Jiřičný, Czech Academy of Sciences	**Reviewer**
Dr. Karel Bouzek, Professor, University of Chemistry and Technology, Prague	**Chair of the Examination Committee**
Dr. Petr Zámostný, Associate Professor, University of Chemistry and Technology, Prague	**Assessor**
Dr. Denis Bouyer, Professor, Université de Montpellier	**Assessor**
Dr. Bart van der Bruggen, Professor, KU Leuven	**Assessor**
Dr. Jose Sanchez Marcano, Directeur de Recherche CNRS, IEM, Université de Montpellier	**Supervisor/assessor**
Ivo Vankelecom, Professor, KU Leuven	**Supervisor/assessor**

ACKNOWLEDGEMENTS

I am very grateful for the financial support from The Education, Audiovisual and Culture Executive Agency – EACEA/European Commission within the "Erasmus Mundus Doctorate in Membrane Engineering – EUDIME" (ERASMUS MUNDUS Programme 2009–2013, FPA n. 2011-0014, SGA n. 2013-1480), from the Operational Program Prague – Competitiveness (CZ.2.16/3.1.00/24501), and from the "National Program of Sustainability" (NPU I LO1613, MSMT-43760/2015).

I would like to express my sincere appreciation and gratitude to Prof. Vlastimil Fíla, Dr. José Sanchez Marcano and Prof. Ivo Vankelecom for supervising my research and invaluable assistance in solving all organizational issues and cooperation between universities. I am also thankful to all my colleagues and co-workers from the University of Chemistry and Technology, Prague, University of Montpellier and KU Leuven for the tremendous help and support in my work and in overcoming the difficulties.

Last but not least, I would like to thank my family and close friends for the greatest support, inspiration and assistance throughout not only the entire PhD research and but also my life.

Viacheslav Perfilov

Contents

Introduction 1
Introduction 9
1 Overview of the processes 17
1.1 Membrane distillation 17
1.1.1 Process overview and configurations 17
1.1.2 Properties of membranes in MD 19
1.1.3 Geometric configurations of MD modules 24
1.1.4 Spacers in the feed and permeate channels 27
1.1.5 MD applications 27
1.1.6 Mass transfer in MD 28
1.1.7 Heat transfer in MD 30
1.1.8 Literature review of mathematical models of DCMD 30
1.1.9 Literature review of mathematical models of SGMD 64
1.2 Anaerobic membrane bioreactors 88
1.2.1 Introduction to anaerobic membrane bioreactors 88
1.2.2 AnMBR configurations 88
1.2.3 Membrane materials 90
1.2.4 Membrane module configurations 90
1.2.5 Membrane fouling 92
1.2.6 AnMBR process operating conditions 93
1.2.7 AnMBR applications 93
1.2.8 Existing AnMBR models 94
2 Theoretical description 109
2.1 The general predictive models for direct contact and sweeping gas membrane distillation 109
2.1.1 Applied geometrical configurations and coordinates 109
2.1.2 Defined assumptions 112
2.1.3 Feed and permeate sides 113
2.1.4 Membrane domain 126
2.2 Hydrodynamic model for anaerobic membrane bioreactor 131
2.2.1 Considered assumptions 132
2.2.2 Momentum balance 132

2.2.3 Simulation of the MMV system 133
2.2.4 The influent mass balance 134
2.2.5 Boundary conditions 136
3 Experimental procedures and literature results for model validation 138
3.1 Direct contact membrane distillation 138
3.2 Sweeping gas membrane distillation 140
3.3 Anaerobic membrane bioreactors 141
4 Organisation of the simulation process 143
5 Results and discussion 145
5.1 Direct contact membrane distillation 145
5.1.1 Mesh study 145
5.1.2 Validation study 147
5.1.3 Parametric study 148
5.2 Sweeping gas membrane distillation 155
5.2.1 Mesh study 155
5.2.2 Validation study 156
5.2.3 Parametric study 157
5.3 Anaerobic membrane bioreactors equipped with the MMV system 163
5.3.1 Mesh study 163
5.3.2 Validation study 164
5.3.3 Parametric study 165
6 Conclusions et perspectives 169
6 Conclusions and perspectives 172
References 174
Abbreviations 183
Nomenclature 185
List of figures 189
List of tables 196
APPENDIX 198

Introduction

La modélisation mathématique des procédés chimiques et physiques joue un rôle essentiel dans toutes les sphères de la science et de l'ingénierie. De nos jours, l'étude de tout phénomène devrait commencer par la conception et formulation d'un modèle mathématique (MM) approprié car les modèles aident à la description, la compréhension, l'analyse et l'optimisation des procédés. L'utilisation de mathématiques et le développement des MMs au cours du siècle dernier, a permis des changements fondamentaux dans presque tous les types d'activités humaines, des technologies et des procédés existants et futurs.

La modélisation mathématique est un processus de développement de représentations de procédés et de processus (chimiques, physiques, sociales, psychologiques, etc.) sous forme de équations mathématiques. En génie des procédés, les MMS décrivent un large éventail de procédés: transfert de chaleur, de masse et de quantité de mouvement, transition de phase, réactions chimiques, adsorption, désorption, etc. [1,2]. La plus part des scientifiques et des ingénieurs en génie des procédés ont recours à la modélisation mathématique des procédés chimiques et physiques. Pour ce faire, ils développent ou utilisent des logiciels de simulation afin de résoudre les tâches suivantes [1]:

- Conception et simulation;
- Contrôle;
- optimisation;
- prédiction et planification d'expériences;
- diagnostics et dépannage;
- détermination des paramètres ne pouvant être mesurés directement;
- études scientifiques et de faisabilité.

Habituellement, le développement d'un MM est un processus dont la procédure de l'implémentation prend plusieurs étapes et cycles jusqu'à son application (Figure 1) [1-3]. La première étape est la détermination correcte du problème. Ceci a un effet fondamental sur le résultat final de l'ensemble de la procédure de modélisation. Dans cette partie, les objectifs de l'étude et la précision choisie sont déterminés. Une fois le problème formulé, le futur modèle est conceptualisé en utilisant les données recueillies, l'expérience et l'examen de la littérature. Sur la base du modèle conceptuel créé, le modèle mathématique est ensuite développé.

Tous les paramètres d'entrée, ainsi que les variables, les limitations et les hypothèses doivent être soigneusement énoncés à l'étape suivante. Le modèle mathématique correctement assemblé est ensuite testé dans le logiciel de simulation choisit pour résoudre la tâche choisie et vérifier la validité du modèle. Après vérification, le modèle peut être utilisé dans l'analyse de sensibilité et l'application. Les étapes ci-dessus de la modélisation mathématique sont nécessaires pour le développement de tous les modèles mathématiques et peuvent être complétées par des étapes spécifiques qui dépendent du problème.

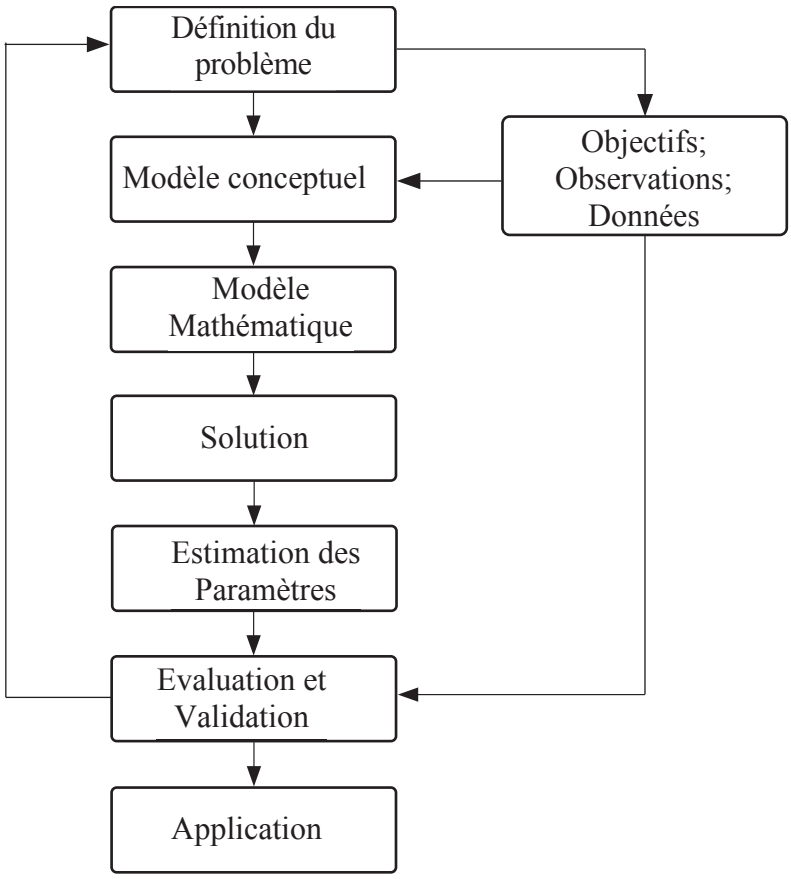

Figure 1: Algorithme du développement d'un modèle [1].

Pour comprendre la différence entre les différents MMs, leurs avantages, inconvénients et caractéristiques, ils doivent être classifiés. Les MMs peuvent être classés selon différentes caractéristiques. L'appartenance du modèle à un groupe particulier peut fournir des informations sur la structure du modèle, son comportement et les résultats obtenus. A ce jour, il existe une liste établie de critères de classification des MMs par types de variables, ses relations et l'utilisation ou non de données empiriques [1, 2]:

- linéaires versus non-linéaires;
- statiques versus dynamiques;
- paramètres localisés versus paramètres distribués;

- discrets versus continus;
- déterministes versus probabilistes
- d'interpolation versus d'extrapolation;
- mécanistiques versus empiriques;
- couplées versus non-couplées.

En programmation mathématique, le MM est linéaire si les variables dépendantes présentent une linéarité dans les équations utilisées. La présence d'au moins une variable non-linéaire dans les équations rend le MM non linéaire. Les MMs linéaires peuvent être résolus en appliquant des méthodes analytiques cependant les MMs non-linéaires sont relativement complexes et la plupart du temps ne peuvent être résolus qu'avec des méthodes numériques [1].

La comptabilisation des variables dépendant du temps dans le processus de modélisation est un autre facteur important dans la classification des MMs. Les MMs dynamiques, appliqués lorsque le système modélisé n'est pas à l'équilibre, sont plus complexes que les MMs statiques. Ainsi, la procédure de résolution pour les MMs dynamiques exige généralement plus de temps de calcul. Toutefois, une grande majorité des MMs en génie des procédés sont développés pour décrire des systèmes à l'équilibre ou en état stationnaire [1].

Si les paramètres considérés dans un MM sont regroupés ou localisés, les variations spatiales de ces paramètres peuvent être exclues. Dans ce cas, le système considéré en MM est homogène. A contrario, les MMs aux paramètres distribués prennent en compte toutes les variations des paramètres dans le compartiment considéré. La résolution des MMs aux paramètres groupés est plus facile et moins gourmande en ressources que les MMs aux paramètres distribués. Par conséquent, si elle est possible l'utilisation des MMs aux paramètres localisés ou groupés est en général préférable.

L'utilisation de variables continues dans les MMs permet d'estimer toutes les valeurs de ces variables dans des compartiments définis tandis que, dans les MMs discrets, seules des valeurs distinctes peuvent être prises dans les mêmes compartiments. Habituellement, les MMs discrets sont représentés par des équations algébriques (AE), tandis que les MMs continus sont représentés par des équations différentielles (DE). La procédure de résolution des AEs est plus facile à utiliser et plus rapide que celle des DEs. Cependant, les erreurs de calcul dans les MMs discrets sont généralement plus élevées que dans les MMs continus. En outre, ces MMs ne considèrent pas l'effet de la distribution des variables et nécessitent des données empiriques supplémentaires pour la procédure de résolution.

Les modèles qui donnent les mêmes résultats pour un ensemble des données d'entrée sont appelés déterministes. Dans ces modèles, tous les composants calculés sont surs. En revanche, les MMs probabilistes tiennent compte des effets de l'incertitude. Dans ces cas, la relation entre les données d'entrée et les valeurs de sortie n'est pas définie avec précision. Par conséquent, les résultats obtenus par les MMs probabilistes pour un ensemble de données d'entrée pourront être différents chaque fois que le calcul est réalisé.

Les méthodes d'interpolation et d'extrapolation ne sont utilisées que sur des modèles basés sur des données expérimentales. Les MMs utilisés pour l'interpolation permettent de calculer les valeurs entre les paramètres déterminés expérimentalement alors que, pour l'extrapolation, les MMs calculent les valeurs au-delà de l'ensemble des paramètres déterminés.

Si les MMs sont basés sur des données expérimentales ils sont appelés empiriques. Dans le cas contraire, les MMs qui ne nécessitent pas de données expérimentales et qui sont basés seulement sur la description des phénomènes physiques et/ou chimiques d'un processus étudié sont appelés mécanistiques. Si lors de la conception d'un procédé il est nécessaire de décrire complètement les processus physiques et chimiques, les modèles mécanistiques sont les plus adaptés. A contrario, les modèles empiriques conviennent dans le contrôle de procédés où la compréhension profonde des mécanismes n'est pas nécessaire. Il est important de mentionner qu'il existe également des modèles semi-empiriques souvent appliqués à des fins d'ingénierie.

Le degré d'interdépendance entre les variables dans un modèle est appelé couplage. Les variables interagissent entre elles dans les MMs couplés tandis que l'absence de telles interactions caractérise les MMs non couplés. Le degré d'interaction entre les variables est déterminé par la direction de la variation des variables. Un couplage faible est caractérisé par une interaction à sens unique tandis qu'un couplage fort est caractérisé par une interaction bidirectionnelle.

Outre la classification des MMs par types de variables, ses relations et l'utilisation de données expérimentales, une autre classification des MMs est basée la complexité des équations mathématiques. La figure 2 illustre la direction de l'augmentation de la complexité mathématique avec les types d'équations mathématiques utilisées dans le MMs: AE, équations différentielles ordinaires (ODE), équations différentielles partielles (PDE) et jusqu'aux équations aux différences. Par ailleurs, l'exactitude de la représentation des procédés augmente généralement avec la complexité des MMs [1].

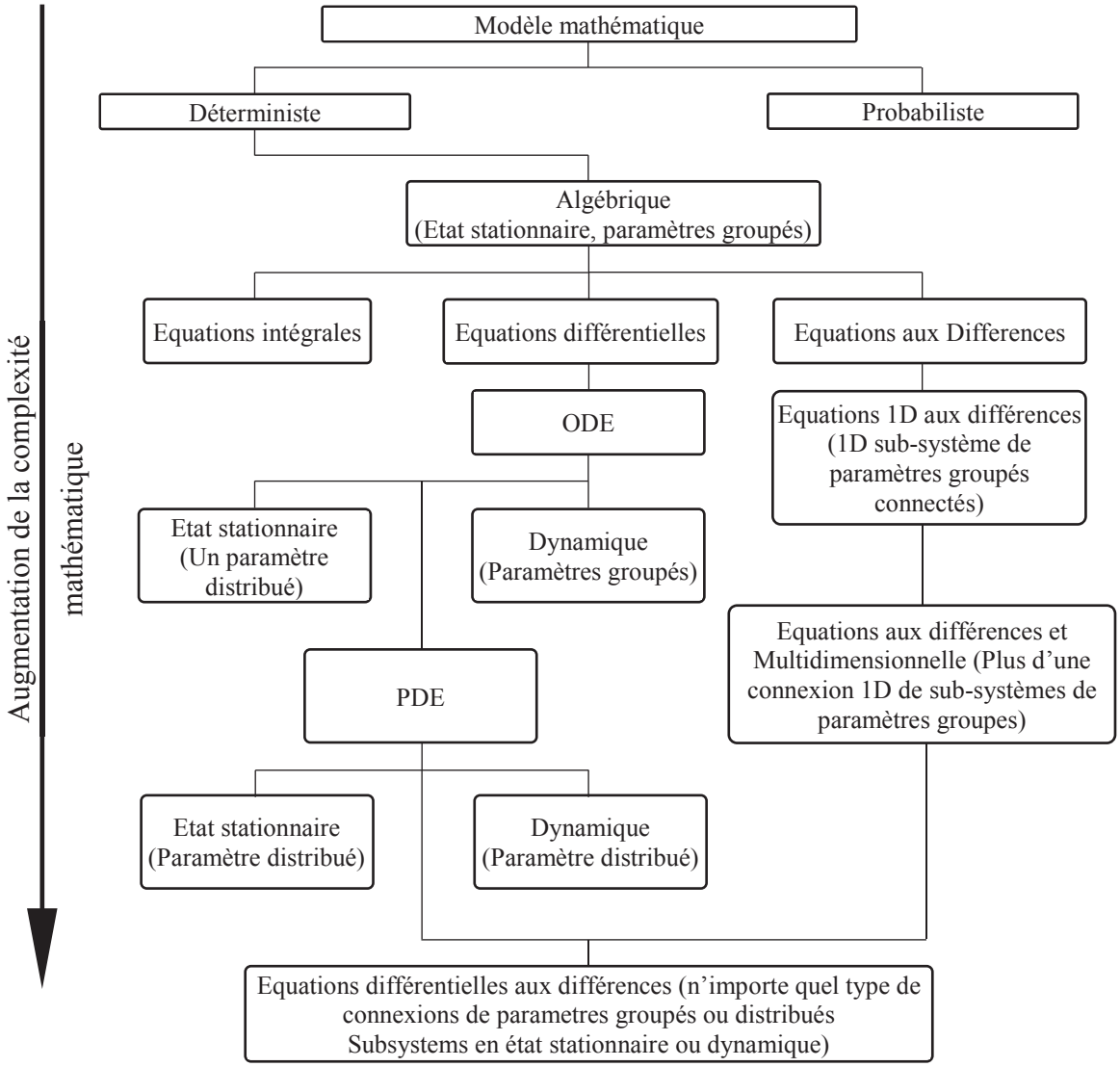

Figure 2: Classification des MMs basée sur la complexité mathématique [1].

Les équations utilisées dans les MMs peuvent être résolues par deux types de méthodes: analytiques et numériques. Comme on peut le voir dans le tableau 1, la plupart des équations nécessitent des résolutions numériques dues à l'impossibilité de trouver une solution analytique. En génie des procédés, la plupart des procédés simulés sont complexes et généralement résolus numériquement.

Enfin, les MMs peuvent être classés par l'échelle physique des problèmes formulés. Plusieurs niveaux de description physico-chimique des MMs sont possibles: moléculaire, microscopique, mésoscopique et macroscopique. Parmi les niveaux mentionnés, la description moléculaire est la plus détaillée et fournit une connaissance fondamentale d'un procédé. Le niveau moléculaire est utilisé pour étudier la mécanique quantique et statistique, la théorie cinétique et la mécanique classique. A cette échelle, les fonctions de distribution et les intégrales de collision agissent comme paramètres dans les MMs.

Tableau 1: Difficulté et possibilité de résolution des équations des modèles.

Type d'équation	Equations linéaires			Equations non linéaires		
	Une équation	Plusieurs équations	Beaucoup d'équations	Une équation	Plusieurs équations	Beaucoup d'équations
AE	Triviale	Facile	Pratiquement impossible	Très difficile	Très difficile	Impossible
ODE	Facile	Difficile	Pratiquement impossible	Très difficile	Impossible	Impossible
PDE	Difficile	Pratiquement impossible	Impossible	Pratiquement impossible	Impossible	Impossible

La modélisation au niveau microscopique est appliquée pour la modélisation des procédés continus et leur bilans de quantité de mouvement, masse et chaleur qui prennent la forme d'équations différentielles. À ce niveau de détail physique, les phénomènes de transport sont modélisés sans description détaillée des interactions entre les molécules.

La modélisation à l'échelle mésoscopique, est encore moins détaillée que la précédente. Ce degré de description est utilisé pour décrire les écoulements turbulents et les écoulements qui se déroulent dans des systèmes géométriquement complexes (p. ex. les milieux poreux). Les paramètres et variables dépendants des procédés sont pris en moyenne dans le temps ou l'espace.

La modélisation macroscopique est la moins détaillé de toutes les échelles. À ce niveau, les informations sur les détails d'un système considéré ne sont pas prises en compte et seuls les équilibres globaux avec les variables moyennes sont présentés. Les MMs macroscopiques peuvent être appliqués avec succès seulement si les informations sur les procédés internes dans le système n'affectent pas les résultats de la simulation.

La modélisation de la science des membranes et des procédés membranaires est relativement nouvelle peut être réalisée à différentes échelles et niveaux de complexité mathématique. Elle peut permettre une description physico-chimique et hydrodynamique juste pour simuler un large éventail de procédés de séparation [3, 4]. Comme on peut le voir dans le tableau 2, un grand nombre de procédés membranaires existent dans l'industrie, ils utilisent différentes forces motrices : pression, électro-, concentration ou température. Ils peuvent être appliqués comme alternatives durables et environnementales à de nombreux procédés conventionnels, y compris le dessalement, la purification, la séparation des gaz, le traitement de l'eau, concentration des solutés etc. Ces procédés sont déjà très utilisés dans l'industrie alimentaire, la biotechnologie, les industries pharmaceutiques, le génie biomédical et bien d'autres [6].

Tableau 2: Classification des procédés membranaires selon leur force motrice.

Pression	Electrique	Autres et Combinées: pression/concentration/ température/ réaction etc.
Osmose inverse (RO) Nanofiltration (NF) Ultrafiltration (UF) Microfiltration (MF)	Electrolyse Membranaire Electrodialyse Piles à combustible Electrophorèse	Distillation membranaire (MD) Séparation de gaz Pervaporation Dialyse Bioréacteur membranaire (MBR) Cristallisation membranaire (MC)

Cette thèse est consacrée au développement de modèles prédictifs généraux pour les procédés de distillation membranaire de contact direct (DCMD) et avec balayage de gazeux (SGMD). Un dernier modèle hydrodynamique pour un bioréacteur membranaire anaérobie (AnMBR) couplé avec un système de vibration membranaire induite (MMV) [8,9] a aussi été développé.

La thèse est divisée en 6 chapitres. Le chapitre 1 décrit les procédés mentionnés, leurs classifications et caractéristiques, les propriétés des membranes ; il met en évidence les configurations et les applications possibles des modules membranaires. En outre, dans ce chapitre, l'examen approfondi de la littérature révèle les avantages et les inconvénients des modèles existants pour les procédés décrits. Sur la base de l'examen de la littérature, on met en évidence la justification de l'élaboration des modèles prédictifs généraux pour le DCMD et le SGMD ainsi que le modèle hydrodynamique pour le AnMBR.

Le chapitre 2 décrit les modèles proposés pour la DCMD, la SGMD et le AnMBR. Dans ce chapitre, les hypothèses appliquées ainsi que les configurations géométriques possibles sont décrites pour les modèles étudiés. Pour la DCMD et la SGMD, on décrit les transferts de quantité de mouvement, les bilans massiques et thermiques et les conditions limites correspondantes (BCS) dans chaque domaine. Pour le AnMBRs, l'hydrodynamique est définie par le transfert de quantité de mouvement. En outre, le calcul du transfert de masse des composants clefs est donné sur la base du couplage du modèle du AnMBR proposé avec un modèle biologique existant.

Dans le chapitre 3, des données expérimentales et bibliographiques utilisées dans des simulations pour des études de validation et paramétriques sont fournies. En particulier, les paramètres d'entrée et les caractéristiques géométriques des modules membranaires pour la DCMD, la SGMD et le AnMBRs pour les modèles sont décrits.

Le chapitre 4 est consacré à la description de la stratégie et des méthodes utilisées pour la modélisation. Dans ce chapitre, la mise en œuvre des modèles développés dans le logiciel

COMSOL Multiphysics ™ est mise en évidence. En particulier, l'application des équations dans le logiciel est décrite et des échantillons de maillage pour les procédés simulés sont donnés.

Dans le chapitre 5, sont donnés les résultats de validation et les simulations obtenues avec les modèles proposés. Pour les modèles prédictifs généraux de la DCMD et de la SGMD, les résultats des études de validation et paramétriques, y compris les températures et les débits des flux d'alimentation et de perméation, la salinité du flux d'alimentation et l'épaisseur et la longueur de la membrane sont présentés et discutés. Pour le modèle du AnMBR, l'influence du dispositif MMV sur l'hydrodynamique du réservoir AnMBR est étudiée. En particulier, l'influence de la fréquence des vibrations membranaires sur la vélocité et les concentrations des composants des boues est démontrée et analysée.

Enfin, le chapitre 6 résume les résultats des modèles proposés. Dans ce chapitre, on décrit la description des modèles proposés, leurs caractéristiques, leurs avantages et leurs inconvénients par rapport à ceux qui existent déjà. Sur la base des caractéristiques et des performances des modèles proposés, les conclusions et les perspectives sont finalement identifiées.

Introduction

Mathematical modelling of chemical and physical processes plays an essential role in all spheres of science and engineering. Nowadays, the study of any phenomenon starts from the formulation and further improvement of an appropriate mathematical model (MM) since it helps to describe, understand, analyse and optimize the studied process. The use of mathematics and MMs over the last century not only in a stunning manner changed almost all existing types of human activities, technologies and production but also allowed new types to appear.

Mathematical modelling is a process of developing representations of real processes and situations (chemical, physical, social, psychological etc.) in form of mathematical equations. In chemistry and chemical technology, MMs describe a wide range of processes: heat, mass and momentum transfer, phase transition, chemical reactions, adsorption, desorption, etc. [1, 2]. The absolute majority of chemical scientists and engineers use various application programs for mathematical modelling of chemical and physical processes. The modern simulation software can help solving the following engineering tasks [1]:

- process simulation and design;
- process control;
- optimization;
- prediction and planning of experiments;
- diagnostics and troubleshooting;
- determination of parameters that could not be measured directly;
- scientific and feasibility studies.

Usually, development of MM is a time consuming multistep process (Fig. 3). Beginning from the formulation of the problem, the procedure of the MM implementation takes many stages and cycles until the application of MM [1-3]. The proper determination of the problem has a very strong effect on the final result of the whole modelling procedure. In this part, the objectives of the study with a selected accuracy are determined. Once, the problem is formulated, the concept of the future model should be stated by using the gathered data, experience and literature review. On the base of the created conceptual model, the mathematical model is developed. All the input parameters as well as variables, limitations and assumptions should be carefully stated at this stage. The properly assembled mathematical

model is then tested in the simulation software which tries to solve the defined task and verifies the model. After verification, the model can be used in the sensitivity analysis and application. The above stages of the mathematical modelling are necessary for development of all the mathematical models and can be supplemented with special steps which are dependent on the problem.

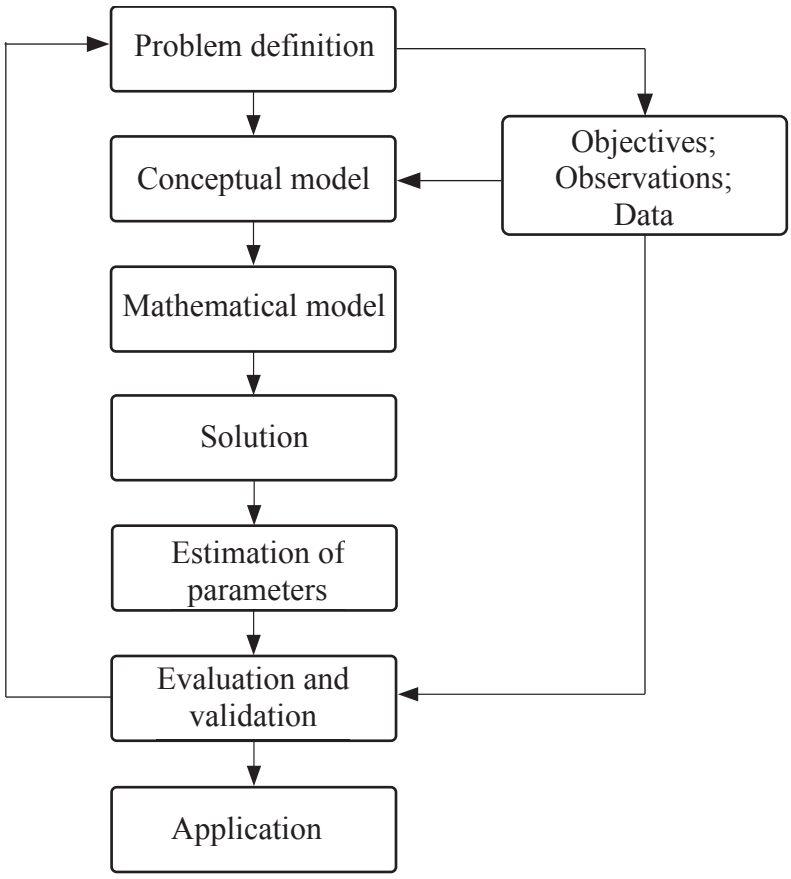

Figure 3: Algorithm of model development [1].

For understanding the difference between various MMs, their advantages and drawbacks and features, the classification of MMs should be noted. MMs can be classified according to different characteristics. Belonging of the model to a particular group can provide information about the structure of the model, its behaviour and produced results. To date, exists an established list of criteria of MM classification by types of variables, its relationships and the use of empirical data [1, 2]:

- linear versus nonlinear;
- static versus dynamic;
- lumped parameter versus distributed parameter;
- discrete versus continuous;
- deterministic versus probabilistic;

- interpolation versus extrapolation;
- mechanistic versus empirical;
- coupled versus non-coupled.

In mathematical programming, MM is linear if the dependent variables exhibit linearity in equations used in MM. The presence of at least one nonlinear variable in the equations makes MM nonlinear. The linear MMs can be solved by applying analytical methods however the nonlinear MMs can be solved with numerical methods due to complexity of such models.

Accounting of time-dependent variables in the modelling process is another important factor in classification of MMs. Dynamic MMs are more complicated than static MMs and applied when the modelled system is not at steady state. Thus, the solving procedure for the dynamic MMs usually requires more time to solve the problem. However, for chemical engineering purposes, most of the modelled processes are in steady state and can exclude the influence of time [1].

Application of lumped parameters in MMs excludes spatial variations of these parameters. In this case, the system considered in MM is homogeneous in a defined compartment. In contrast to lumped-parameter MMs, distributed-parameter MMs take into account all the variations of parameters throughout the considered compartment. Solving lumped-parameter MMs is easier and less resource-intensive process than distributed-parameter MMs. Therefore, the use of lumped-parameter MMs is preferable if it is possible [1].

The use of continuous variables in MMs allows to estimate any values of these variables within defined compartments while, in discrete MMs, only distinct values can be taken within the same compartments. Usually discrete MMs are represented by algebraic equations (AE) while continuous MMs are represented by differential equations (DE). The solving procedure for AEs is easier in use and faster than for DEs. Thus, chemists and chemical engineers prefer to use discrete MMs. However, a computational error in discrete MMs is usually higher than in continuous MMs. Also, these MMs do not consider the effect of distribution of variables and require extra empirical data for solving procedure [1].

Models which produce the same results for a given set of input data are called deterministic. In these models, all the parameters are defined and certain. In contrast, probabilistic MMs take into account effects of uncertainty. In this case, the relationship between the input and output data is not defined precisely and these MMs possess some

inherent randomness. Therefore, the results produced by probabilistic MMs for a given set of input data will be different each time [1].

Interpolation and extrapolation methods are used only on models which are based on experimental data. MMs used for interpolation calculate values between the experimentally determined data while, for extrapolation, MMs calculate values beyond the set of determined parameters.

MMs which use experimental data as a basis and describe the behaviour of occurring processes without the definition of the nature of these processes are called empirical. In the opposite case, mechanistic MMs do not require excessive experimental data and are based on physics and chemistry to describe the behaviour of a studied process. The mechanistic MMs are preferred in process design to fully describe the physics and chemistry of the process while empirical models are suitable in process control where the deep understanding of the process is not necessary. It is worth mentioning that semi-empirical models also exist are often applied for engineering purposes.

The degree of interdependence between variables in the model is called coupling. The variables are interacting between each other in coupled MMs while the absence of such interactions characterizes non-coupled MMs. The degree of interactions between the variables is determined by direction. Weak coupling is characterized by one-way interaction while strong coupling is characterized by two-way interaction.

Apart from the classification of MMs by types of variables, its relations and the use of experimental data, another classification of MMs determines the complexity of mathematical equations. Fig. 4 illustrates the direction of increase in mathematical complexity with types of mathematical equations used in MMs. On Fig. 4, the level of mathematical complexity increases from AEs to ordinary differential equations (ODE), then to partial differential equations (PDE) and has its maximum with difference-differential equations. Also, the accuracy of the representation of described physical and chemical processes increases with the complexity of MMs [1].

Equations used in MMs can be solved by two types of methods: analytical and numerical. As can be seen from Table 3, most of equations require numerical solutions due to impossibility of finding an analytical solution. In chemistry and chemical engineering, most of the simulated processes are complex and usually solved numerically.

Last but not least, MMs can be classified by a degree of physical detailing of formulated problems. Several levels of physicochemical description of MMs are presented: molecular, microscopic, mesoscopic and macroscopic. Among the mentioned levels, the molecular description is the most detailed and provide a fundamental knowledge of a modelled process. Molecular level is used to study quantum and statistical mechanics, kinetic theory and classical mechanics. For this level, distribution functions and collision integrals act as parameters in MMs [1].

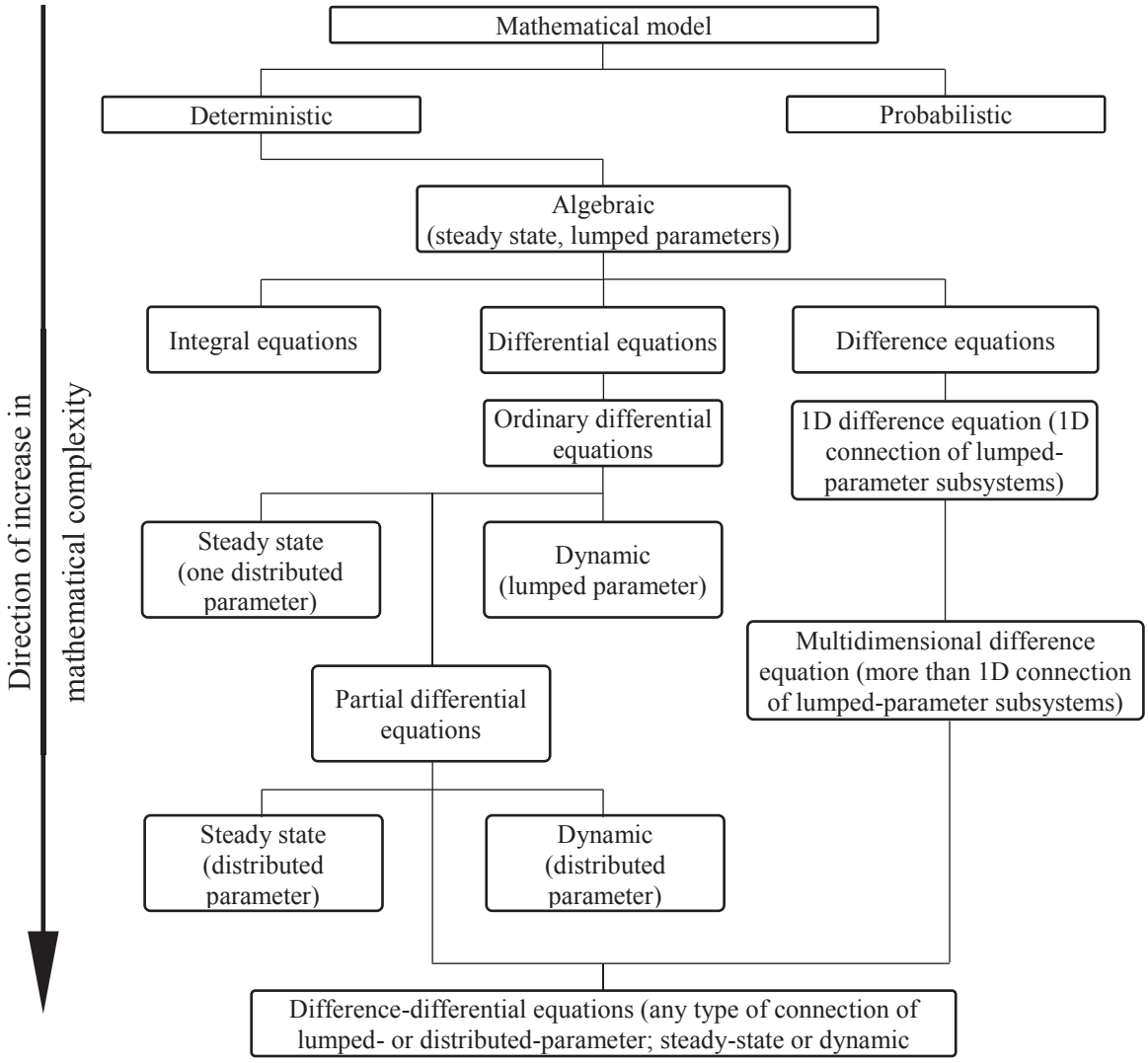

Figure 4: Classification of MMs based on mathematical complexity [1].

The next and less detailed than molecular is a microscopic level which is used for modelling of continuum processes and their momentum, mass and energy balances. At this level of physical detailing, transport phenomena are modelled without detailed description of interactions between molecules while the momentum, mass and energy balances take form of differential equations.

Table 3: Possibility of analytical solution of various equations used in MMs [1].

Type of equation	Linear equations			Non-linear equations		
	One equation	Several equations	Many equations	One equation	Several equations	Many equations
Algebraic	Trivial	Easy	Essentially impossible	Very difficult	Very difficult	Impossible
Ordinary differential	Easy	Difficult	Essentially impossible	Very difficult	Impossible	Impossible
Partial differential	Difficult	Essentially impossible	Impossible	Essentially impossible	Impossible	Impossible

Mesoscopic level, less detailed after microscopic, is based on less detailed information about the interactions which occur inside simulated processes. This degree of description is used to describe the turbulent flow and flows taking place in geometrically complex systems (e.g. porous media). Dependent parameters and variables of the processes are taken as averaged in time or space.

The least detailed level of physicochemical description of MMs is the macroscopic. At this level, information about details within a considered system is not taken into account and only overall balances with average variables are presented. Macroscopic MMs can be successfully applied only if the information about the processes that occur at the microscopic and mesoscopic levels does not affect the simulation results.

Membrane science, a relatively new complex study of artificial membranes and related processes and applications, actively uses MMs of different levels of mathematical complexity and physicochemical description to simulate a wide range of separation processes [3, 4]. As can be seen in Table 4, a lot of various membrane processes (pressure-, electro-, concentration- or temperature driven) exist in industry. They can be applied as sustainable and environmental alternatives to many conventional processes, including desalination, purification, gas separation, water treatment, resource concentration, food technology, biotechnology, pharmaceutical industries, biomedical engineering and many others [6].

Table 4: Classification of membrane processes by driving force.

Pressure-driven processes	Electro-driven processes	Processes with combined driving force and concentration-/temperature-driven processes
Reverse osmosis (RO) Nanofiltration (NF) Ultrafiltration (UF) Microfiltration (MF)	Membrane electrolysis Electrodialysis Fuel Cells Elcetrophoretically-enhanced processes	Membrane distillation (MD) Gas separation Pervaporation Dialysis Membrane bioreactor (MBR) Membrane crystallization (MC)

This thesis is devoted to the development of general predictive models of direct contact MD (DCMD) and sweeping gas MD (SGMD) and hydrodynamic model for anaerobic MBRs (AnMBRs) coupled with the induced membrane vibration system (MMV) [8, 9]. The thesis is divided into 6 chapters. The chapter 1 describes the mentioned processes and their classifications and characteristics, indicates the properties of membranes and highlights possible membrane module configurations and applications. Also, in this chapter, the comparative literature review reveals advantages and drawbacks of existing models for the described processes. On the base of the literature review, the justification for the development of the general predictive models for DCMD and SGMD and hydrodynamic model for AnMBRs is highlighted.

The chapter 2 describes the proposed models for DCMD, SGMD and AnMBRs. In this chapter, the applied assumptions of the models as well as possible geometric configurations are given. For DCMD and SGMD, the momentum, mass and heat balances and corresponding boundary conditions (BCs) in each domain are described. For AnMBRs, the hydrodynamics is defined by the momentum transfer. Also, the calculation of the mass transfer of the influent components is given on the base of cooperation of the proposed AnMBR model with the existing biological model.

In the chapter 3, experimental and literature data used in simulations for validation and parametric studies are given. In particular, the input parameters and geometric characteristics of the membrane modules for DCMD, SGMD and AnMBRs for the models are described.

The chapter 4 is devoted to development of the process simulation. In this chapter, the implementation of the developed models in of COMSOL Multiphysics™ is highlighted. In particular, the application of the equations in the software is described and meshing samples for the simulated processes are given.

In the chapter 5, the mesh, validation and parametric studies for the proposed models are given. For the general predictive models for DCMD and SGMD, the results of the validation and parametric studies including the temperatures and flow rates of the feed and permeate flows, the feed salinity and the membrane thickness and length are shown and discussed. For the proposed AnMBR model, the influence of MMV on the hydrodynamics of the AnMBR tank is presented. In particular, the influence of the membrane vibration frequency on the influent velocity and concentrations of sludge components is demonstrated and analysed.

Lastly, the chapter 6 summarizes the results and outcomes of the proposed models. In this chapter, the description of the proposed models, their features and advantages and drawbacks in comparison with the existing ones is given. On the base of the characteristics and performance of the proposed models, the conclusions and perspectives are identified.

1 Overview of the processes

1.1 Membrane distillation

1.1.1 Process overview and configurations

Membrane distillation (MD) is a relatively less-explored membrane process based on the application of macroporous or mesoporous hydrophobic membranes that allow the passage of volatile components only. The process has several advantages including the ability to concentrate the solutions to their saturation level, production of high-quality water from saline solutions and the ability to exploit low-grade heat for the operation. First mentioned in the 1960s [10-12], the process was standardized 20 years later [13]. Recently, there has been a massive increase in the number of articles focused on the improvement and application of MD. Nowadays, MD is considered to be a potentially interesting tool for desalination [15-22], wastewater treatment [23-28], concentration of acids [29,30], treatment of agro-food [31-34] and biological solutions [35-37]. For these applications, MD can be used as a standalone process or in combination with pressure driven membrane operations such as reverse osmosis [15].

The driving force of MD is the partial pressure difference between the feed-membrane interface and permeate-membrane interface. At the feed side of MD, the partial pressure is defined by the temperature and concentration of the liquid feed which is charged with one side of the membrane. The feed liquid should not penetrate the membrane pores in the course of the process. Thus, in the case of aqueous solutions, the membrane surface which is in direct contact to the feed must be hydrophobic and the pressure of the liquid should not exceed the liquid entry pressure (LEP) of the membrane [38].

At the permeate side of MD, the partial pressure can be controlled in various ways to establish the driving force. First of them is the use of another liquid which is charged with the permeate side of the membrane (Fig. 1.1(a)). This permeate liquid should be colder than the feed liquid to obtain a gradient of partial pressure decreasing from the feed-membrane interface to the permeate-membrane interface. Both of the liquids are usually operated in counter current to maintain the highest mean temperature difference and, thus, the driving force of the process. Both horizontal and vertical positions of MD unit are possible. The described MD configuration is the most common and known as direct contact membrane distillation (DCMD) [38].

Another option to establish the transmembrane gradient of the partial pressure is to apply vacuum in the permeate side of the MD module (Fig. 1.1(b)). Created by a vacuum pump, the pressure at the permeate side will be lower than the saturation pressure of volatile components at the feed-membrane interface. Thus, molecules of the volatile components evaporate at the feed side of the membrane and transfer through the membrane pores to the permeate channel condensing outside of the MD module. Due to application of vacuum, this configuration is named vacuum membrane distillation (VMD) [38].

The third option is to provide a stagnant air gap in the permeate channel between the membrane and one surface of a condensation plate while the other surface of the condensation plate should be cooled by a cold circulating flow (Fig. 1.1(c)). In this case, the volatile molecules evaporate at the feed-membrane interface, transfer through the membrane and the air gap and condensate at the cooling plate. The condensate then leaves the MD module under the influence of gravity. The mentioned MD configuration is called air gap membrane distillation (AGMD) [38].

In the fourth option, an inert gas (usually air) with a small or negligible concentration of the volatile components is sweeping through the permeate channel of the MD module (Fig. 1.1(d)). Determined by the concentration of volatile molecules, the partial pressure of these components at the permeate-membrane interface is less than the saturation pressure at the feed-membrane interface. Therefore, the volatile molecules evaporate at the feed-membrane interface through the membrane pores, transfer through the membrane and sweep through the permeate condensing outside of the MD module. This configuration is named sweeping gas membrane distillation (SGMD) [38].

In addition to the partial pressure gradient as the driving force of the process, according to the terminology of MD accepted at the “Workshop on Membrane Distillation” in Rome on May 5, 1986, the following requirements should be fulfilled [13]:

- the membrane should be porous;
- the liquids involved in MD should not wet the membrane;
- the vapour should not condense inside the pores of the membrane;
- only transfer of vapour through the membrane pores is allowed;
- the species involved in the MD process are in vapour-liquid equilibrium (VLE);
- the membrane in MD is in direct contact with at least one of the process liquids.

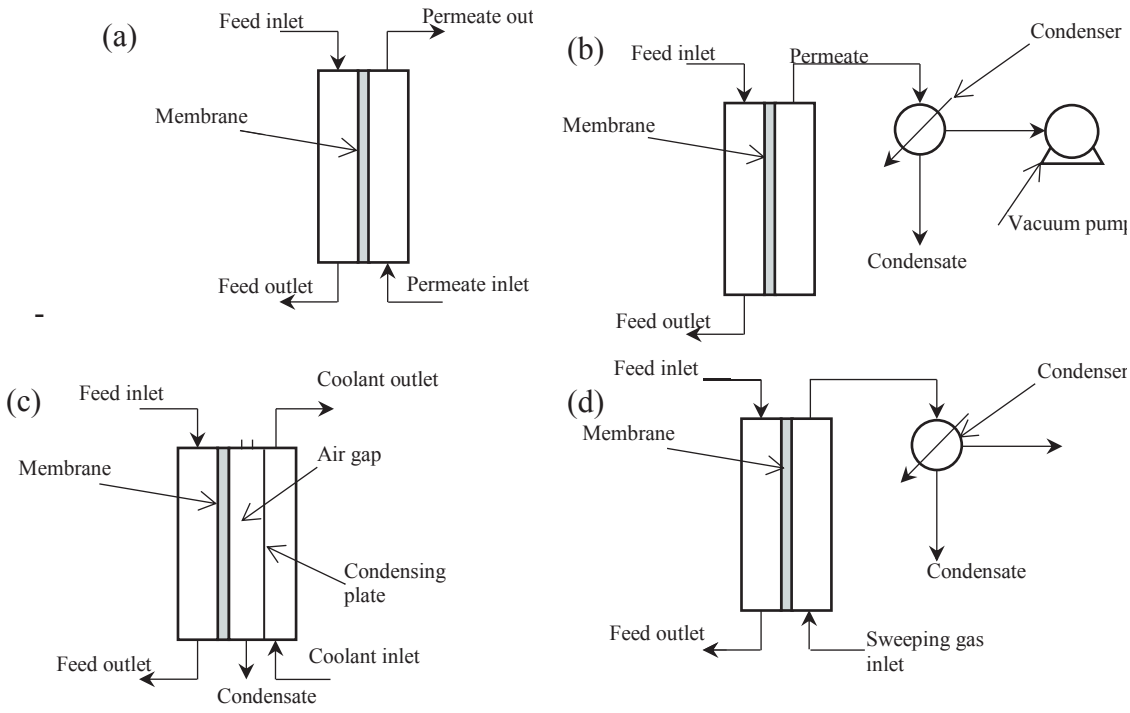

Figure 1.1: Configurations of MD: (a) DCMD, (b) VMD, (c) AGMD and (d) SGMD [38].

1.1.2 Properties of membranes in MD

Membranes which are applied in MD of aqueous solutions should have two major properties: porosity and hydrophobicity. The membrane pores provide space for volatile molecules from the feed-membrane interface to the permeate-membrane interface. The diameter of the pores of the membranes in MD ranges from 10 nm to 1 μm. The hydrophobicity of the membrane can be provided by a single layer hydrophobic membrane or composite membrane consisting of a hydrophilic/hydrophobic porous support and active hydrophobic layer from one or both sides of the support [38]. It is worth mentioning that condensation effects must not take place inside the membrane pores to prevent membrane from wetting outside and decrease in the performance.

At the present time, a huge number of porous hydrophobic materials are used to prepare membranes for MD at laboratory and industrial levels. Table 1.1 indicates main commercial membranes applied in MD. Commercial materials, such as PTFE, PE, PP or PVDF and their combination, are the most popular in the synthesis and production of membranes for MD. This choice is explained by the properties, including high porosity, large pore size, low thermal conductivity and relatively low prices. Ceramic membranes with modified surface have also been applied to this process, however, they are relatively expensive Besides the already mentioned properties, the membranes in MD should demonstrate good thermal and chemical

stability for a long-time operation in harsh conditions, high LEP and narrow pore size distribution to prevent the pores from wetting and high permeability to maintain high transmembrane vapour flux. The hydrophobic or hydrophilic supports in the composite membranes must demonstrate similar properties to ensure long-term use and reduce heat transfer through the membrane [15, 38, 51].

Table 1.1: Commercial membranes used in MD processes [15, 38].

Membrane type	Manufacturer	Material	Thickness (μm)	Porosity (%)	Mean pore size (μm)	Liquid entry pressure (kPa)
Flat sheet membranes						
TF200	Gelman	PTFE/PP	178	80	0.2	282
TF450			178	80	0.45	138
TF1000			178	80	1.00	48
PV22	Millipore	PVDF	126±7	62±2	0.22	229
PV45			116±9	66±2	0.45	110
HVHP			140	75	0.45	105
GVHP			110	75	0.22	204
FHLP		PTFE/PE	175	85	0.5	124
FALP			150	85	1.0	48.3
MD080CO2N	Enka Microdyn	PP	650	70	0.2	-
3MA	3M Corporation		91	66	0.29	
3MB			81	76	0.4	
3MC			76	79	0.51	
3MD			86	80	0.58	
3ME			79	85	0.73	
Hollow fibre membranes						
Accurel® S6/2	AkzoNobel	PP	450	70	0.2	140
MD020TP2N	Enka Microdyn		1550	70	0.2	-
Accurel® BFMF 06-30-33	Enka A.G.		200	70	0.2	
Celgard X-20	Hoechst Celanese Co.		20	30	0.03	

1.1.2.1 Thermal and chemical stability

To prevent thermal degradation at operating conditions with temperature up to 100 °C in process of time, the membranes should have a melting point higher than the operating temperatures. The commercial polymeric and ceramic materials which are used in MD processes show an excellent thermal stability and have the melting point higher than 100 °C. Chemical resistance of the membranes is necessary in MD because feed solutions can contain various active, aggressive and corrosive compounds even if the concentrations of these compounds in the brine is small to prevent pore wetting. Again, polymeric materials demonstrate its stability and satisfactory resistance to fats and almost all organic solvents under operation temperatures [15, 38, 51].

Table 1.2: Melting points of the commercial materials [15, 38].

	PP	PTFE	PVDF	PE	Hyflon
Melting point (°C)	160-165	250-255	160-180	115-135	300-400

1.1.2.2 Thermal conductivity

The heat transfer through the membrane in DCMD is considered as the heat loss because it decreases the driving force of the process, the partial pressure gradient, and reduces the transmembrane vapour flux. To reduce the heat transfer through the membrane during the process operation, membrane should have low thermal conductivity. Polymer membranes have the lowest thermal conductivities among the materials possible to apply for the membrane production. Table 1.3 shows the thermal conductivities of the commercial materials used for preparation of the DCMD membranes. In the process design, the effective thermal conductivity is taken into account. The effective thermal conductivity is a combination of the thermal conductivity of the membrane material and the thermal conductivity of the gas mixture within the membrane pores [15, 38].

Table 1.3: Thermal conductivities of the commercial materials [15, 38].

	PP	PTFE	PVDF	PE	Hyflon	Stainless steel	Ceramic
Thermal conductivity (W/m K)	0.1-0.22	0.25	0.12	0.33-0.51	0.15-0.25	16	11.7

1.1.2.3 Liquid entry pressure

LEP is the minimal hydrostatic pressure applied onto the feed or permeate liquid to overcome the hydrophobic forces of the membrane and penetrate into the membrane pores. LEP plays significant role in the selection of membranes. To ensure stable operation of the DCMD module, the hydrostatic pressures of the feed and permeate liquids should be less than LEP which depends on the pore structure, membrane hydrophobicity and pore size. Franken *et al.* [39] proposed the following equation to determine LEP:

$$P_{LEP} = \frac{B\gamma_L cos\theta}{d_p}$$

where P_{LEP} is the liquid entry pressure, B is the dimensionless geometric parameter characterizing the pore structure, γ_L is the liquid surface tension, θ is the liquid/solid contact angle and d_p is the maximum pore diameter of the membrane.

Moreover, LEP can be determined experimentally. The LEP measurement is much more precise and lower than calculated because it takes into account the pore size distribution and not a mean pore size [40]. It is worth noticing that the presence of the organic compounds and high temperatures may reduce LEP. Therefore, the control of LEP is necessary for each temperature and composition of the brine used in the MD process [39].

1.1.2.4 Pore size and porosity

The size of the pores is closely related to LEP and membrane permeability and should be chosen in such a way as to ensure maximum performance of the DCMD module while preventing pore wetting. Commercial polymers used in MD usually have the pore diameters in range from 0.1 to 1 μm (Table 1.1). The MD modules do not have a uniform pore diameter. The pores of various diameters are distributed at the membrane surface and inside the membrane. For evaluation of the membrane performance, the mean pore diameter (MPD).

Porosity of the membrane is another significant characteristic. As the transmembrane flux increases with porosity, materials with high porosity are preferred. Moreover, high porosity of materials shows the large void fraction filled with air what decreases the thermal conductivity of the membrane and improves the MD performance. Already mentioned commercial polymers demonstrate good values of porosity with narrow pore size distribution. The porosity can be analysed by mercury porosimetry for macroporous membranes or gas permeation tests for macro- and mesoporous membranes [41-43].

1.1.2.5 Membrane thickness

The thickness of the membrane is an important membrane property which affects the MD performance. The influence of the thickness on the process is complex. The thin membranes have short distances between the feed and permeate channels. In this case, the temperature and partial pressure gradients are maximal but the diffusion path as well as the heat resistance of the membrane are minimal. The thick membranes possess the opposite qualities by having lower temperature and partial pressure gradients and higher heat

resistances. Therefore, thin membranes provide high transmembrane fluxes and heat losses while thick membranes provide low transmembrane fluxes and heat losses. The optimal membrane length for each specific case can be found experimentally or from simulations [15, 38].

1.1.2.6 Tortuosity

Tortuosity is the deviation of the pore structure from the cylindrical shape. The tortuosity of the membrane is the specific membrane property which could not be optimized or measured directly. In terms of geometry, the tortuosity, τ_M, is the ratio of the average length of the membrane pore to the membrane thickness:

$$\tau_M = \frac{\langle L_{pore} \rangle}{\delta_M} \tag{1}$$

where $\langle L_{pore} \rangle$ is the average length of the membrane pores, δ_M is the membrane thickness.

The tortuosity is inversely proportional to the permeability of the membrane and high values of the tortuosity decrease the transmembrane flux by increase in the diffusion path. In MD, the tortuosity values usually vary in range between 1.1 and 3.9. Usually, the tortuosity is an adjusted parameter, however several correlations between the porosity and tortuosity were proposed. One of them requires the membrane thickness, effective membrane porosity and membrane porosity determined from the wet/dry method [38]:

$$\tau_M = \frac{\varepsilon_M}{\delta_M \varepsilon_M^{eff}} \tag{2}$$

where ε_M is the membrane porosity, ε_M^{eff} is the effective membrane porosity.

Another correlation between the tortuosity and porosity is the Bruggeman relation [44]

$$\tau_M = \begin{cases} {\varepsilon_M}^{-\frac{1}{2}} \, (spherical\ pores) \\ {\varepsilon_M}^{-1} \, (cylindrical\ pores) \end{cases} \tag{3}$$

Mackie and Meares [45] also proposed the following successfully applied correlation:

$$\tau_M = \frac{2 - \varepsilon_M}{\varepsilon_M} \tag{4}$$

Apart from the mentioned correlations, many other suggestions to predict the membrane tortuosity exist in literature [46-50]. These correlations give a mean value of the membrane tortuosity with assumption that the pore diameters do not change from one side to the other side of the membrane. Also, these relations are valid when the pore phase is connected. However, the tortuosity factor is very difficult to predict for each membrane material and the suggested correlations do not always suit experimental data.

1.1.3 Geometric configurations of MD modules

A large number of different geometric configurations of membrane modules have been introduced for application in MD. However, all the MD modules use only two types of the membrane geometry: flat sheet and hollow fibre. For scientific and research purposes, flat sheet membranes are more attractive due to their ease of manufacture and use, while in industry hollow fibre membranes are more desirable because of their large contact area. However, the contact area is not the only indicator of efficiency for industrial scale membrane modules. The correct choice of the module consists of economic and technical parameters which are interconnected between each other. Among these parameters, a regulation of temperature polarization (TP), concentration polarization (CP) and membrane fouling arising during the operation of the modules play an important role.

The most simple module configuration applied in MD is a plate and frame (Fig. 1.2(a)). In this configuration, two membranes, alone or with porous support plates, and spacers are stacked between two end plates and equipped with sealing rings. To provide a larger surface, the stack of the membranes can be increased. Depending on the number of the membranes in the stack, the packing density of the module can reach 400 m^2/m^3 [51]. The laboratory scale plate and frame modules have a more simplified form and consist of the one membrane placed between the feed and permeate channels. This simplified configuration is called flat sheet (Fig. 1.2(b)). Several laboratory modifications of the flat sheet module have been developed for MD. First of them is a thin channel module presented on Fig. 1.2(c) [52]. In this module, the feed flow has an additional side heating by heating water while the permeate flow has an additional side cooling by cooling water. Another laboratory module, a Lewis cell (Fig. 1.2(d)), consists of two chambers and the flat membrane fixed between the chambers [53-56]. The hot feed and cold permeate liquids are stirred inside the chambers by magnetic stirrers to reduce the TP and CP effects. Among the plate and frame modules, a tangential-flow module is the most popular

and simple. The tangential-flow module is not equipped with the stirrers or side heating and cooling system. In this configuration, the feed flow is heated up and the permeate flow is cooled down externally by heat exchangers. The advantages of the plate and frame modules are possibility of easy membrane replacement and quick cleaning and avoidance of the use of glue for the membrane connection. Still, the need of the sealings and the low packing density make the plate and frame configuration undesirable for industrial application of MD.

The flat membranes applied in the plate and frame modules can be arranged in spiral-wound modules [57-60]. The membranes, combined with the porous support, are rolled together with the feed spacer around a perforated permeate pipe. In this module, the feed flows axially through the feed channel while the permeate flows radially toward the permeate pipe. The packing density of the spiral-wound modules is better than of the plate and frame modules and can reach the value of 1000 m^2/m^3.

In contrast to the flat sheet, plate and frame and spiral-wound modules, shell and tube modules use the tubular, capillary and hollow fibre membranes (Fig. 1.2(e)). The tubular membranes which need the porous support have the diameters up to 25 mm and packing density of around 300 m^2/m^3. Due to the low packing density, the tubular membrane modules are not desirable in industry except in the cases when the process liquids have high viscosity and could clog and foul the capillary and hollow fibre membranes. The capillary modules with the diameters of the membranes up to 5 mm have the packing density in the order 600–1200 m^2/m^3. The hollow fibre modules, in which the diameter of the membranes ranges from 50 to 100 μm, have the packing density of about 3000 m^2/m^3. With the largest contact area among the all membrane modules and low operating costs, the hollow fibre modules are preferred for application in industrial scale. However, the hollow fibre membranes have a very high fouling tendency, are difficult to clean and could not be replaced in the module [51].

In addition to the high packing density, low operation costs and ease of cleaning, the membrane module in MD should have the following attributes:

- the possibility to obtain high feed and permeate flow rates to reduce TP and CP. The high flow rates ensure good mixing of the process liquids not only in bulk phases but partially in boundary layers what provide a smooth distribution of the temperatures and concentrations of the species;

- prevention of high pressure drop along the membrane length in the feed and permeate channels. High pressure drop can create high transmembrane hydrostatic pressure what leads to wetting of the pores of the membrane;
- prevention from heat losses. High heat losses reduce the temperature of the feed flow and, therefore, the driving force of the process. According to Fane *et al.* [61], around 20-50% of the total heat transferred in MD are the heat losses by conduction;
- resistance to erosion. The modern membrane modules usually consist of plastic materials which proved its durability and stability.

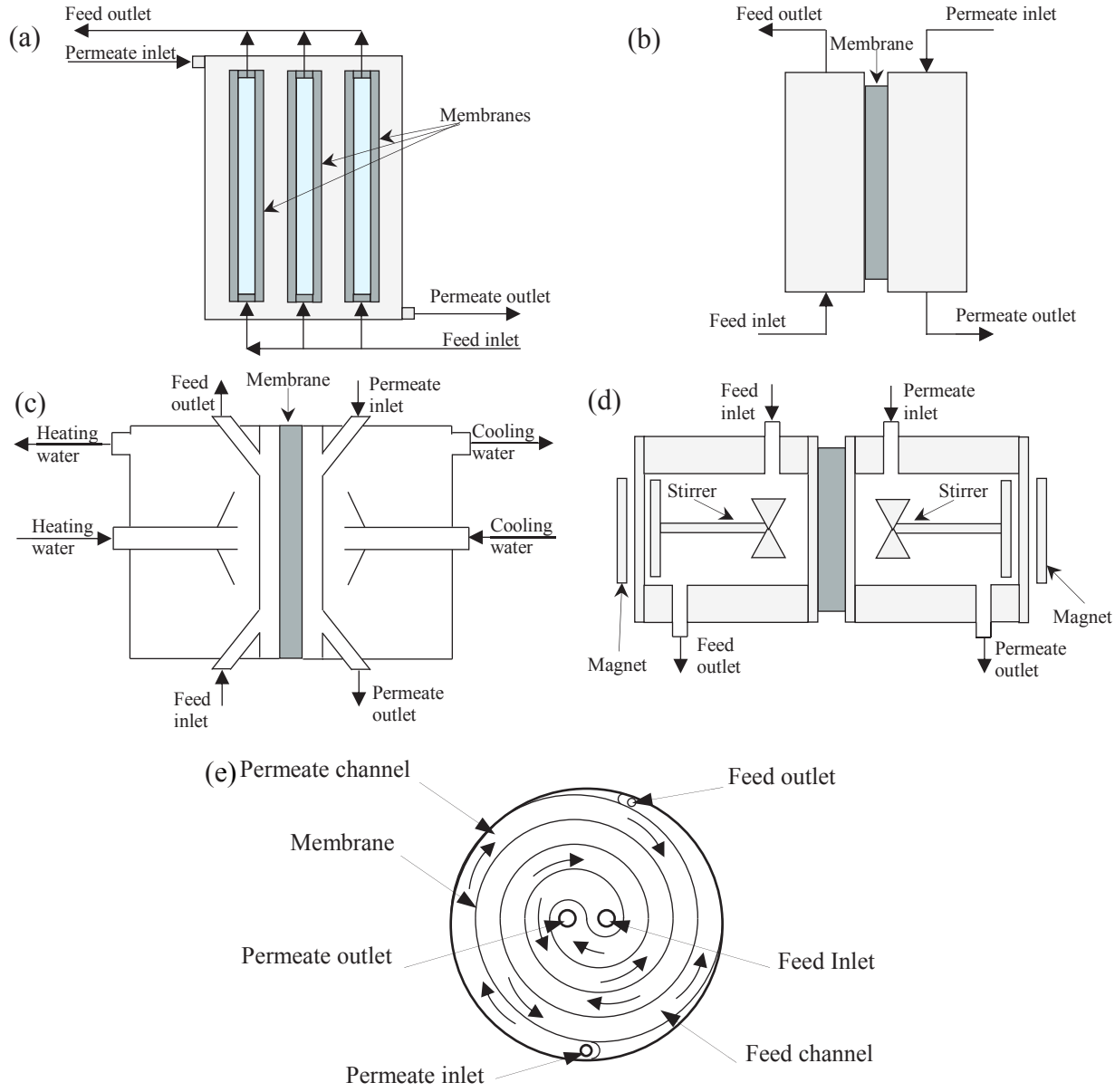

Figure 1.2: Configurations of MD modules: (a) plate and frame module; (b) flat sheet module; (c) thin channel module [52]; (d) Lewis cell [53-56]; (e) spiral-wound module (cross-section) [60].

1.1.4 Spacers in the feed and permeate channels

Spacers can be applied by filling the feed and permeate channels of membrane modules to change the parameters of the flow, enhance the mixing and create turbulence in the channel. These actions are intended to decrease TP and CP. In some cases, the presence of the spacer is necessary to keep the membrane at its position and prevent deflection of the membrane. At the same time, the use of the spacers in both the feed and permeate channels enhances the heat transfer between them, creates additional resistance to the mass transfer and decreases the effective membrane area by covering the membrane pores. Therefore, the proper design of the spacers is necessary to avoid decrease in the MD performance. Fig. 1.3 indicates schematically a typical spacer used in MD. The spacer usually consists of upper and lower filaments connected to each other. The main spacer characteristics, that determine mixing properties of a flowing liquid, are the flow attack angle, angle between filaments and distance between filaments [62].

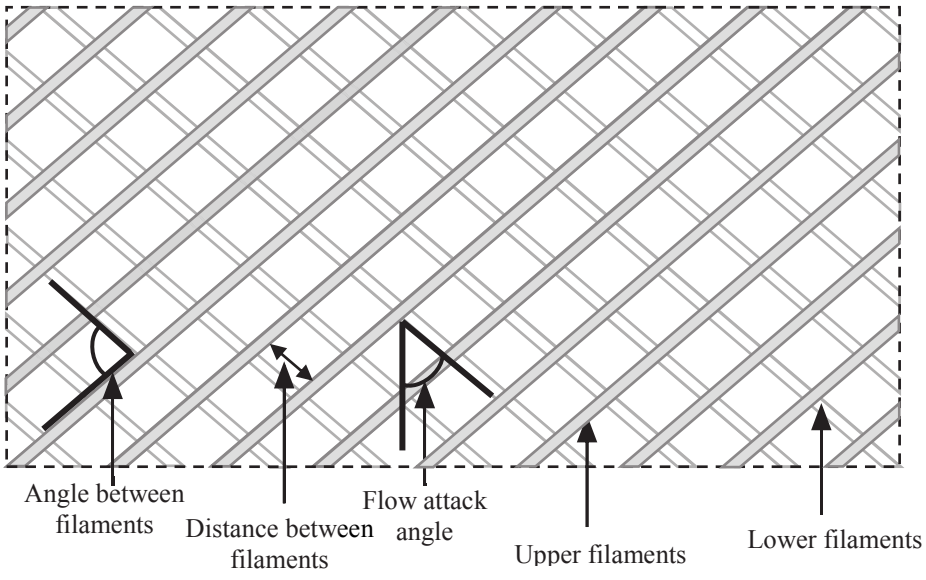

Figure 1.3: Schematic representation of spacers [62].

1.1.5 MD applications

Despite the fact that the industrial application of MD processes is not well established yet, MD is considered to have a great potential and its use can be a part of sustainable development. Because MD is aimed at separation of volatile components from non-volatile, the main area of the MD application is the separation of various volatile species from solutes.

The first of such processes is desalination of seawater, brines and brackish waters to produce high purity water [15-22]. Many publications have been devoted to the study of the application of various MD configurations with different types of membranes in desalination. The first lab scale MD units had water vapour fluxes (lower than 1 kg/(m^2 h) [63]). However, these water vapour fluxes were much lower than ones obtained by reverse osmosis (RO). Nevertheless, modern MD units with commercial membranes of high porosity and small thickness are very efficient with the water vapour fluxes higher than 50 kg/(m^2 h) [64]. It is worth mentioning that in desalination MD can be coupled to membrane crystallization (MC) and RO processes for recovering of solid substances in concentrated feed streams [65].

MD has also been applied in food industry for concentration purposes. Table 1.4 gives a list of MD works on concentration of fruit juices. As can be seen, the MD processes have been successfully tested in the concentration of orange juice, apple juice, sugarcane juice, etc. Besides juices, the AGMD process was also applied for concentration of milk, sugar and gelatine solutions. Application of MD in this area has the following advantages: improved product quality, low energy consumption and ease of use. The major disadvantage of such processes is the fouling of the membrane pores and a small number of studies aimed at eliminating this drawback which interferes with the implementation of MD in industrial scale.

The MD processes have also been tested for the removal of volatile organic compounds (VOCs) from dilute aqueous solutions [69-72], like the removal of aromatic compounds [73] or formic acid [74]. Moreover, the concentration of thermally sensitive solutions [75-78] or the ammonia removal from water and wastewater [79] have also been reported.

Table 1.4: Studies of MD applications in the food industry.

Study	MD configuration	Reference
Orange juice concentration	DCMD, AGMD	[31, 66]
Apple juice concentration	DCMD	[32, 34]
Sugarcane juice concentration	DCMD	[33]
Gelatine solution concentration	AGMD	[66]
Milk concentration	AGMD	[66]
Black currant juice concentration	VMD	[67, 68]

1.1.6 Mass transfer in MD

Each MD unit consists of the following compartments: feed channel, membrane and permeate channel. As stated in the section 1.1, the feed flow is represented by a liquid while

both the liquid and gas can be maintained as the permeate flow depending on the MD configuration. The mass transport in all of the mentioned compartments is carried out by a combination of the advection (or convection) and diffusion and, in some cases, phase changes between the compartments [84-86]. The advection dominates in the feed flow for all the MD configurations and permeate flow for the DCMD configuration while the concentration of moving molecules is much bigger in a liquid than in a gas.

In contrast to liquids, in gases which serve as permeate flows in SGMD, VMD and AGMD and transmembrane flows, the diffusion can have the same order as the convection and plays an important role. Three modes of the diffusion transport are possible: Knudsen diffusion (free-molecule transport), ordinary diffusion (continuum diffusion) and surface diffusion [84, 85].

Knudsen diffusion occurs when, during their path, molecules have much more probable collisions with membrane pores than with each other molecule in the membrane pores. For the membrane compartment, Knudsen diffusion characterizes the diffusive flux if the mean free path of molecules is bigger than the diameter of the pores and the density of the gas is low [84, 85].

Ordinary, or molecular, diffusion occurs between each two molecules of different species. The molecules collide with each other and move in opposite directions. For the membrane compartment, ordinary diffusion characterizes the mass flux if the mean free path is comparable to the pore diameter and the density of the gas is high (frequent collisions between molecules) [84, 85].

Surface diffusion is a moving of adsorbed molecules at surfaces of channels and membrane pores. This mode of mass transport is the most difficult to describe, because many factors should be taken into account: surface concentration gradients, adsorption equilibrium for each species, geometry of channel and porous medium and surface structure, etc. Surface diffusion depends strongly on the operating conditions and interactions between the surface and vapour molecules. However, if we consider the operating conditions of MD as well as materials hydrophobicity, surface diffusion does not make a significant contribution to the total mass transfer [85].

In MD, up to 2 phase changes can appear. The first of them, the separation process in MD, occurs at the feed-membrane interface, where volatile molecules evaporate through the membrane pores leaving non-volatile components in the feed flow. The second phase change,

a condensation of the volatile molecules which were evaporated at the feed-membrane interface, occurs at the permeate-membrane interface in DCMD and at the condensing plate in the permeate channel in AGMD. During the condensation and evaporation phenomena, VLE is achieved [15, 38].

1.1.7 Heat transfer in MD

In MD, heat transfer from the hotter feed side to the colder permeate side through the membrane occurs via convection (only gas phase) and conduction (gas phase and solid membrane part) [15, 38, 51]. In the feed and permeate channels of the MD unit, the heat transfer is maintained between the bulk phase and membrane surface via convection and conduction in the feed fluid and via conduction in the solid spacer if it is present in the channel. The heat transfer between the feed compartment and membrane is performed via evaporation of the volatile molecules and conduction while the heat transfer between the membrane and permeate compartment is dependent on the MD configuration. In DCMD, the heat transfers from the membrane to the feed channel by condensation of the volatile molecules into permeate liquid and conduction. In AGMD, VMD and SGMD, heat transfer is represented by convection of the transmembrane vapour flux and conduction. It is also important to note that, in AGMD, condensation takes place at condensation plate in the permeate channel and heat transfers from the permeate bulk to the cooling channel via the condensation plate [15, 38, 51].

1.1.8 Literature review of mathematical models of DCMD

The initial studies dedicated to the modelling of DCMD were published in the 1980s [52, 66, 80, 81]. Since that time, many works have been published. In this section, the description and comparative analysis of existing models for the DCMD process are presented. In the analysis, the models are compared by the following parameters: the type of variables; use of empirical data; type of equations used to describe the process; possibility of the segmentation of the module compartments; described balances; type of the process operation and type of the module geometry. The advantages and disadvantages of the existing models are highlighted.

1.1.8.1 Schofield's model

Schofield and colleagues were the first who proposed the complete mathematical model for DCMD in 1987 [52] and then complemented it in 1990 [82, 83]. This model uses the system of semi-empirical algebraic equations to describe the mass and heat transfer. Air which is trapped inside the membrane pores is considered as stationary film and the steady state operation of the process is assumed.

The following types of the transmembrane mass transfer were taken into account: the Knudsen diffusion, ordinary diffusion and viscous flow. To combine these modes of mass transfer, Schofield *et al.* carried out experiments and derived the following semi-empirical equation to describe the transmembrane vapour flux [82, 83]:

$$J = \left(\frac{1}{a_{Sch} \left(P_M / P_{ref} \right)^{b_{Sch}}} + \frac{P_a}{d} \right)^{-1} \Delta P \tag{5}$$

where a_{Sch} is the membrane permeation constant, P_M is the average pressure within the membrane pores, P_{ref} is the reference pressure, P_a is the average pressure of air within the membrane, b_{Sch} is the exponent which defines the influence of Knudsen diffusion and viscous flow on the vapour flux, d is the membrane molecular diffusion coefficient.

The membrane permeation constant which represents the proportion between the vapour flux and pressure drop at the reference pressure is defined as follows [82, 83]:

$$a_{Sch} = \frac{\varepsilon_M M \bar{v}_M}{\tau_M \delta_M R_g T_M} \left(\frac{2 r_M}{3} + \frac{\pi r_M^2 P_{ref}}{32 L} \right) \tag{6}$$

where M is the molecular weight of the gas, $\bar{v}_M$ is the mean molecular velocity, δ_M is the membrane thickness, ε_M is the membrane porosity, τ_M is the membrane tortuosity, R_g is the universal gas constant, T_M is the average temperature of the membrane, r_M is the membrane pore radius, P_{ref} is the reference pressure (average applied pressure), L is the mean free path.

The mean molecular velocity [82, 83] is:

$$\bar{v}_M = \left(\frac{8 R_g T_M}{\pi M} \right)^{0.5} \tag{7}$$

The parameter b_{Sch} which indicates the contribution of the viscous flow to permeability is calculated by the following equation [82, 83]:

$$b_{Sch} = \left(\frac{\pi r_M P_{ref}}{32L}\right) / \left(\frac{2}{3} + \frac{\pi r_M P_{ref}}{32L}\right) \tag{8}$$

The molecular diffusion coefficient which takes into account the diffusion coefficient and membrane geometry is obtained from the following equation [82, 83]:

$$d_{Sch} = \frac{\varepsilon_M D_{WA} P_M M}{\tau_M \delta_M R_g T_M} \tag{9}$$

where D_{WA} is the water vapour-air ordinary diffusion coefficient.

The heat balance of DCMD is required for calculation of the interfacial temperatures which are needed for calculation of interfacial mean vapour pressures from equations of state. To describe the heat transfer within the membrane module, the following equations are used [82, 83]:

$$Q_{MV} = J\Delta H_V = h_V \Delta T_M \tag{10}$$

$$Q_{MC} = \left(k_M^{eff}/\delta_M\right)\Delta T_M = h_c \Delta T_M \tag{11}$$

$$Q_M = Q_{MV} + Q_{MC} \tag{12}$$

$$Q_M = h_F \Delta T_F = h_P \Delta T_P \tag{13}$$

$$k_M^{eff} = \varepsilon_M k_g + (1 - \varepsilon_M) k_M \tag{14}$$

where Q_M is the transmembrane heat flux, ΔH_V is the latent heat of vaporization, h_V is the heat transfer coefficient of the vapor, T_M is the membrane temperature Q_{MC} is the transmembrane conductive heat flux, k_M^{eff} is the effective thermal conductivity of the membrane, h_c is the conductive heat transfer coefficient, Q_{MV} is the transmembrane heat transfer of the vapour, h_F is the feed heat transfer coefficient, T_F is the feed temperature, h_P is the permeate heat transfer, T_P is the permeate temperature, k_g is the thermal conductivity of the vapor, k_M is the thermal conductivity of the membrane.

After combining Eqs. (10)-(14), the vapour flux is written in the following form:

$$J = \frac{h_V}{\Delta H_V}\frac{h}{h_V + h_C + h}(T_F - T_P) \tag{15}$$

$$h = \left(\frac{1}{h_F} + \frac{1}{h_P}\right)^{-1} \tag{16}$$

$$h_V = \Delta H_V \frac{dP_M}{dT_M}\left(\frac{1}{a\left(P_M/P_{ref}\right)^b} + \frac{P_a}{d}\right)^{-1} \tag{17}$$

$$h_C = k_M^{eff}/\delta_M \tag{18}$$

where h is the film heat transfer coefficient.

In the Schofield's model, the transmembrane vapour flux is affected by the viscous flow, Knudson diffusion and ordinary diffusion. By applying an electrical analogy (Fig. 1.4) to demonstrate the combination of the mentioned modes of transport, it can be seen that the Knudsen diffusion and viscous flow are combined like resistors in parallel with additives voltage drops. Then, the total Knudsen-viscous flow and the ordinary diffusion flow are combined like resistors in series with additive currents. This combination is an alternative to one applied in the dusty gas model (DGM) where the ordinary diffusion and Knudsen diffusion are combined like resistors in series and then the resulted flux and viscous flux are combined like resistors in parallel [84, 85].

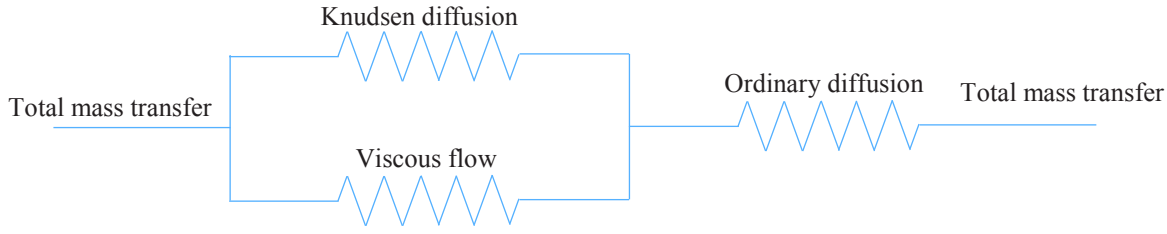

Figure 1.4: Electrical analogy circuit as a combination of different modes of the mass transfer in the Schofield's model.

The Schofield's model which is applied for the steady-state operation operates the discrete and lumped parameters (Fig. 1.5). This model is semi-empirical due to the use of the empirical correlations or experimental data. In the calculations, heat transfer coefficients, which determine the influence of the geometry of the membrane and DCMD module, type of the fluid flows and their composition, are taken from empirical correlations. The simple structure of the

model and the basic mathematical complexity allow its easy and fast application in simulation of DCMD. However, an oversimplification, dependence of the model on the empirical correlations and the use of discrete parameters make the Schofield's model unsuitable for process design. But it can be used for process control and optimization for specific cases and for basic study of DCMD.

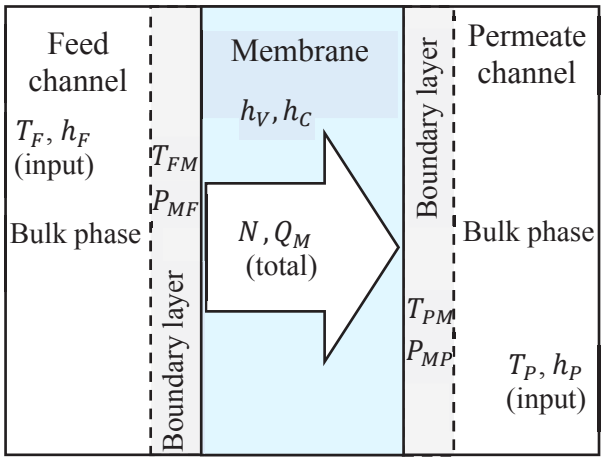

Figure 1.5: Schematic representation of calculated variables in the Schofield's model.

1.1.8.2 Tomaszewska's model

Several years after the publication of the Schofield's model, Tomaszewska and colleagues presented a 1D mathematical model for DCMD [88]. The main distinguishing feature of this model from the Schofield's model is the ability of estimation of the temperatures and concentrations of the feed and permeate flows along the DCMD unit. In this model, the transmembrane vapour flux is described as follows [88]:

$$J = \frac{\varepsilon_M M D_{VA} P_M}{\tau_M \delta_M R_g T_M} ln\left(\frac{P_M - p_{VP}}{P_M - p_{VF}}\right) \tag{19}$$

where D_{VA} is the total diffusion coefficient, p_{VF} and p_{VP} are the partial pressures of the vapour at the feed-membrane interface and permeate-membrane interface, respectively.

The total diffusion coefficient is a result of combination of the Knudsen diffusion coefficient and ordinary diffusion coefficient:

$$D_{VA} = \left(\frac{1}{D_K} + \frac{1}{D_{WA}}\right)^{-1} \tag{20}$$

where D_K is the Knudsen diffusion coefficient, D_{WA} is the water vapor-air diffusion coefficient.

The partial pressure of the water vapour at the feed-membrane interface and at the permeate-membrane interface is calculated by the Antoine equation:

$$p_{Vz} = a_{Ant} - \frac{b_{Ant}}{c_{Ant} + T_{zM}} \tag{21}$$

where a_{Ant}, b_{Ant} and c_{Ant} are the coefficients of the Antoine equation, subscript z is the indication of the side (feed or permeate), T_{zM} is the temperature of the boundary layer.

The temperatures of the boundary layers are evaluated by the following equations [29]:

$$T_{FM} = \frac{\frac{k_M^{eff}}{\delta_M}\left(T_P + \frac{h_F}{h_P}T_F\right) + h_F T_F - JH_V}{\frac{k_M^{eff}}{\delta_M} + h_F\left(1 + \frac{k_M^{eff}}{h_P \delta_M}\right)} \tag{22}$$

$$T_{PM} = \frac{\frac{k_M^{eff}}{\delta_M}\left(T_F + \frac{h_P}{h_F}T_P\right) + h_P T_P + JH_V}{\frac{k_M^{eff}}{\delta_M} + h_P\left(1 + \frac{k_M^{eff}}{h_F \delta_M}\right)} \tag{23}$$

For the feed and permeate sides, the mass balance for water vapour, total mass balance and heat balance are calculated as follows [88]:

$$\dot{m}_z x_{Vz} = (\dot{m}_z + d\dot{m}_z)(x_{Vz} + dx_{Vz}) + JdA_M \tag{24}$$

$$\dot{m}_z = (\dot{m}_z + d\dot{m}_z) + JdA_M \tag{25}$$

$$\dot{m}_z H_z(x_{Vz}, T_z) = (\dot{m}_z + d\dot{m}_z)[H_z(x_{Vz}, T_z) + dH_z(x_{Vz} + dx_{Vz}, T_z + dT_z)] + dQ + JH_V(y_V, T_M)dA_M \tag{26}$$

$$T_M = \frac{T_{FM} + T_{PM}}{2} \tag{27}$$

$$dQ = \frac{k_M^{eff}}{\delta_M}(T_{FM} - T_{PM})dA_M \tag{28}$$

$$dA_M = a_M dL_M \tag{29}$$

where $\dot{m}_z$ is the mass flux of the feed or permeate liquid, x_{Vz} is the mass fraction of water in the liquid, A_M is the surface area of the membrane, H_z is the enthalpy of the liquid, H_V is the enthalpy of the vapor, Q is the total heat, y_V is the mass fraction of water in the gas phase, T_M is the average temperature of the membrane, a_M is the membrane width, L_M is the membrane length.

From the obtained balances, Tomaszewska *et al.* derived 1D ODEs which describe changes of the temperature and concentration in the feed and permeate channels [88]:

$$dx_{Vz} = \frac{JdA_M(x_{Vz} - 1)}{\dot{m}_z} \tag{30}$$

$$dT_z = -\frac{dQ + JdA_M(H_V - c_{Hz}T_z)}{\dot{m}_z c_{Hz}} \tag{31}$$

where c_{Hz} is the specific heat of the feed or permeate fluid.

Eqs. (30) and (31) can be solved by applying the following boundary conditions (BCs) [88]:

$$T_F = T_{Fin}, T_P = T_{Pout}\ at\ l_M = 0 \tag{32}$$

$$T_F = T_{Fout}, T_P = T_{Pin}\ at\ l_M = L_M \tag{33}$$

where T_{Fin} and T_{Pin} are the inlet temperatures of the feed and permeate flows, respectively, T_{Fout} and T_{Pout} are the outlet temperatures of the feed and permeate flows, respectively, L_M is the length of the membrane.

The Tomaszewska's model is applied for the steady-state DCMD operation. The 1D ODEs used for the heat and mass balances in the feed and permeate channels give distributions of the temperature and concentration along the DCMD module (Fig. 1.6). However, the temperature of the membrane and concentration of the water vapour are described by overall integral equations with lumped discrete parameters. The model can be used for estimation of TP but requires empirical data, such as the heat transfer coefficients and the temperatures of the feed and permeate flows at outlets. The model has an average mathematical complexity with equations which can be solved numerically. The application of the model is possible for process design and optimization in limited cases where the heat transfer within the DCMD module is well-studied.

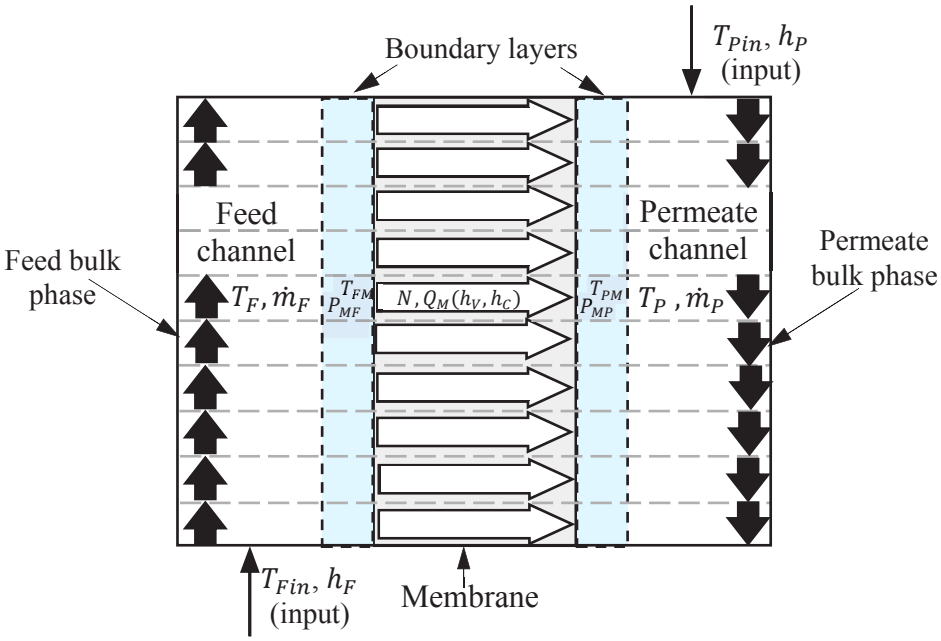

Figure 1.6: Schematic representation of calculated variables in the Tomaszewska's model.

1.1.8.3 Lawson-Lloyd model

Approximately at the same time when the Tomaszewska's model was introduced, Lawson and Lloyd proposed another DCMD model which is based on the DGM [90, 91]. The main feature of the DGM is the representation of the solid porous medium as an additional component of the gas mixture. This component consists of giant dust particles which have a huge molar weight and remain motionless under the influence of the virtual external force. Fig. 1.7 illustrates the electrical analogy circuit for the mass transfer modes determined in the DGM. As can be seen, the Knudsen diffusion and ordinary diffusion are combined like resisters in series with additives voltage drops. Then, the resulted diffusive flow and the viscous flow are combined like resisters in parallel with additive currents [90, 91].

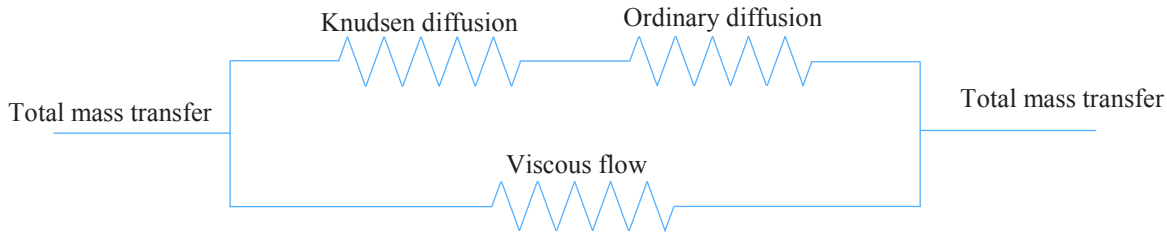

Figure 1.7: Electrical analogy circuit as a combination of different modes of the mass transfer in the DGM.

In their model, Lawson and Lloyd assumed that the viscous flux in porous media can be neglected. Therefore, the diffusive vapour flux of the component i is described by the following equation [90, 91]:

$$\frac{N_{Di}}{D_{Ki}^{eff}} + \sum_{j \neq i} \frac{p_j N_{Di} - p_i N_{Dj}}{P_M D_{ij}^{eff}} = -\frac{\nabla p_i}{R T_M} \tag{34}$$

where p_i and p_j are the partial pressures of the components i and j, respectively, N_{Di} and N_{Dj} are the diffusive fluxes of the components i and j, respectively, D_{ij}^{eff} is the effective ordinary diffusion coefficient of the components i and j, D_{Ki}^{eff} is the effective Knudsen diffusion coefficient of the component i, P_M is the pressure of the gas mixture.

For the calculation of the transmembrane flux, Lawson and Lloyd integrated Eq. (34) and obtained the overall value. For the binary gas mixture of air and water, they described the transmembrane water vapour flux , N_{Vavg}, by the following integral equation [90, 91]:

$$N_{Vavg} = \frac{P_M D_{WA}^{eff}}{\delta_M R_g T_{Mavg}} ln\left(\frac{p_{A1} D_{Ki}^{eff} + D_{WA}^{eff}}{p_{A2} D_{Ki}^{eff} + D_{WA}^{eff}}\right) \tag{35}$$

where T_{Mavg} is the average temperature of the gas mixture in the membrane pores, p_{A1} and p_{A2} are the partial pressures of air on the permeate and feed sides, respectively.

Heat transfer within the DCMD unit in the Lawson-Lloyd model is described by the following equation [90, 91]:

$$Q = \left[\frac{1}{h_F} + \frac{1}{h_M^{eff} + \frac{N \Delta H_V}{\Delta T_M}} + \frac{1}{h_P}\right]^{-1} \Delta T \tag{36}$$

Where, Q is the transmembrane heat flow, h_F and h_P are the boundary layer heat transfer coefficients for the feed and permeate sides, respectively, h_M^{eff} is the effective heat transfer coefficient of the membrane, ΔT_M and ΔT are the transmembrane and bulk temperature differences, ΔH_V is the molar heat of vaporization.

To solve Eq. (36), the required values of h_F, h_M^{eff} and h_P are estimated by using experimental data or calculated from empirical correlations applied for the selected type of flow (laminar, turbulent or transient).

The Lawson-Lloyd model properly determines the type of the transport modes affecting the transmembrane vapour flux in steady-state operation of DCMD by using the DGM. Fig. 1.8 represents the DCMD process simulation by the Lawson-Lloyd model similar to the Schofield's model (Section 1.1.8.1). The Lawson-Lloyd's model is static and uses overall integral and algebraic equations with the lumped and discrete parameters. The drawback of the model is the presence of the heat transfer coefficients in the equations which require empirical correlations or experimental data. The Lawson-Lloyd model cannot determine velocity, concentration and temperature profiles within the DCMD module. The model can be basically applied for process design and control for specific cases with known empirical correlations or conduction of experiments.

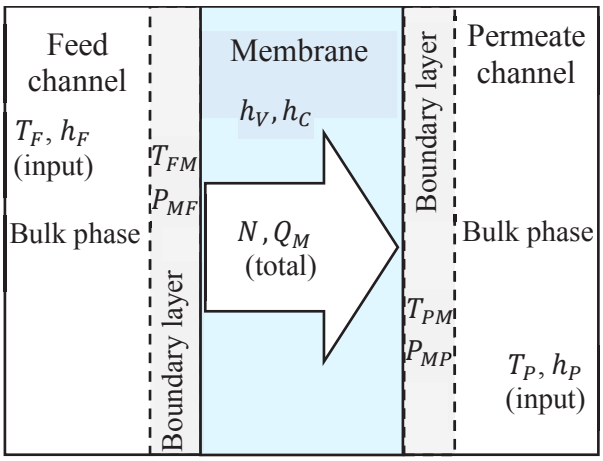

Figure 1.8: Schematic representation of calculated variables in the Lawson-Lloyd model.

1.1.8.4 Laganà's model

Using the DGM, Laganà and colleagues proposed the model which is applied for hollow fibre DCMD modules with cylindrical geometry [32]. In that model, the laminar flow of the feed and permeate liquids and the steady-state operation are determined. The mass and heat balances for the lumen (feed) side of the fibres are described as follows [32]:

$$\frac{JR}{\rho_W D_{SW}} \vec{v}_{Fr} \frac{\partial c_{WF}}{\partial r} + \frac{\langle v_{Fz} \rangle R}{D_{SW}} v_{Fz} \frac{\partial c_{WF}}{\partial z} = \frac{1}{r} \frac{\partial}{\partial r} \left(r \frac{\partial c_{WF}}{\partial r} \right) \tag{37}$$

$$\frac{JC_{PF}R}{k_F} \vec{v}_{Fr} \frac{\partial T_F}{\partial r} + \frac{\rho_F C_{PF} R \langle v_{Fz} \rangle}{k_F} \vec{v}_{Fr} \frac{\partial T_F}{\partial z} = \frac{1}{r} \frac{\partial}{\partial r} \left(r \frac{\partial T_F}{\partial r} \right) + \frac{\mu_F \langle v_{Fz} \rangle^2}{k_F \Delta T_F} \left(\frac{\partial \vec{v}_{Fz}}{\partial r} \right)^2 \tag{38}$$

where J is the transmembrane mass flux of the vapour, ρ_F is the density of water, D_{SW} is the diffusion coefficient of solute in water, $\vec{v}_{Fr}$ is the radial velocity, c_{WF} is the concentration of water in the feed flow, r is the radial coordinate, R is the inner radius of the hollow fiber, g $\langle v_{Fz} \rangle$ is the average axial velocity, $\vec{v}_{Fz}$ is the axial velocity, z is the axial coordinate, C_{PF} is the specific heat capacity of the feed liquid, k_F is the thermal conductivity of the feed liquid, ρ_F is the feed density, μ_F is the feed viscosity.

The explicit forms of axial and radial velocities for the lumen side of the membrane were taken by solving equations for the momentum balance. The pressure, axial and radial velocities are calculated from the following equations [32]:

$$P_F = \frac{8\mu_F J}{c_{WF} R^3} z^2 + \left[\left(\frac{P_{FL} - P_{F0}}{L_M} \right) - \frac{8\mu_F J L_M}{c_{WF} R^3} \right] z + P_{F0} \tag{39}$$

$$v_{Fz} = \left[\frac{4Jz}{c_{WF} R^3} + \left(\frac{P_{FL} - P_{F0}}{4\mu_F L_M} \right) - \frac{2JL_M}{c_{WF} R^3} \right] (r^2 - R^2) \tag{40}$$

$$v_{Fr} = \frac{4J}{c_{WF} R^3} \left(\frac{rR^2}{2} - \frac{r^3}{4} \right) \tag{41}$$

where P_{FL} and P_{F0} are the pressures of the feed flow at the inlet and outlet, respectively, L_F is the length of the membrane.

Eqs. (37)-(38) require the following set of BCs [32]:

$$r = 0: \quad \frac{\partial c_{WF}}{\partial r} = 0; \frac{\partial T_F}{\partial r} = 0 \tag{42}$$

$$r = R: \quad -D_{SW} \frac{\partial c_{WF}}{\partial r} + \vec{v}_{Fr} c_{WF} = 0; \quad -k_F \frac{\partial T_F}{\partial r} + h_T (T_{FM} - T_{PM}) = 0 \tag{43}$$

$$z = 0: \quad c_{WF} = c_{WF0}; \, T_F = T_{F0} \tag{44}$$

where c_{WF0} is the inlet concentration of water in the feed flow, T_{F0} is the temperature of the feed flow at the inlet.

For the shell (permeate) side of the membrane, the equations for the mass and heat balances are:

$$\frac{d\dot{m}_P}{dz} = -n_{HF}\pi D_{Pout}\vec{J} \tag{45}$$

$$\frac{dT_P}{dz} = \frac{n_{HF}\pi D_{Pout}}{\dot{m}_P}\left[\vec{J}T_P - \frac{h_T(T_{FM} - T_P)}{C_{PP}}\right] \tag{46}$$

where $\dot{m}_P$ is the mass flow rate of the permeate flow, n_{HF} is the number of hollow fibers, D_{Pout} is the diameter of the pipe connected to the permeate channel, C_{PP} is the specific heat capacity of the permeate liquid [32].

The transmembrane vapour flux is calculated by applying the DGM [32]:

$$\vec{J}_{DW} = \left(\frac{1}{D_{KW}^{eff}} + \frac{y_{Air}P_M}{D_{WA}^{eff}}\right)\left(\frac{-1}{R_g T_M}\right)\frac{dp_1}{r} \tag{47}$$

where y_{Air} is the mole fraction of air in the gas mixture, D_{KW}^{eff} is the effective Knudsen diffusion coefficient for the water vapor, D_{WA}^{eff} is the effective ordinary diffusion coefficient for the water vapour and air, p_1 is the partial pressure of the water vapour.

BCs for Eq. (47) are:

$$r = R: x_{WF}\gamma_{WF}P_W^*(T_M^F) = y_{W,R}P_M \tag{48}$$

$$r = R + \delta: x_{WF}\gamma_{WF}P_W^*(T_M^P) = y_{W,R+\delta}P_M \tag{49}$$

where x_{WF} and x_{WP} are the molar fractions of water in the feed and permeate, respectively, γ_{WF} and γ_{WP} are the activity coefficients of water in the feed and permeate, respectively, P_W^* is the saturated vapour pressure of the pure water vapour [32].

The integral form of Eq. (47) for further calculations is:

$$J_{DW} = \frac{D_{WA}^{eff}}{R_g T_{Mavg}}\frac{1}{Rln\left(1 + \frac{\delta_M}{R}\right)}ln\left(\frac{y_{W,R+\delta}D_{KW}^{eff} - \left(D_{KW}^{eff} + D_{WA}^{eff}\right)}{y_{W,R}D_{KW}^{eff} - \left(D_{KW}^{eff} + D_{WA}^{eff}\right)}\right) \tag{50}$$

where $y_{W,R}$, $y_{W,R+\delta}$ are the mole fractions of the water vapour in the gas mixture at the feed-membrane interface and permeate-membrane interface, respectively, D_{KW}^{eff} is the effective Knudsen diffusion coefficient for the water vapor.

The total transmembrane vapour flow rate for all sizes of pores is calculated from the following equation [32]:

$$F_M = \int_0^\infty J(r_M)\pi r_M^2 f(r_M) dr_M \tag{51}$$

where r_M is the pore radius.

From Eq. (51), the effective flux can be written in the following form:

$$J_{eff} = \varepsilon_M J_{avg} = \varepsilon_M K_M J(\langle r_M \rangle) = \frac{\varepsilon_M F_M}{\int_0^\infty \pi r_M^2 f(r_M) dr_M} F_M \tag{52}$$

where K_M is the coefficient accounting the shape of the distribution of pore diameters.

The value of the effective transmembrane vapour flux is measured experimentally. The coefficient K_M can be calculated from the experimental data or from empirical correlations.

In the Laganà's model, the thickness of the membrane is assumed to be dependent on the difference between the pressures of the liquids and vapour pressure. Indeed, the penetration of the liquid is considered dependent from the transmembrane pressure, which approaches the reality. The thickness if found from the following correlation [32]:

$$\delta = \delta_0 - \delta' \Delta P = \delta_0 \left(1 - \frac{\delta'}{\delta_0} \Delta P\right) \tag{53}$$

The tortuosity factor is estimated from the following equation:

$$\tau = \frac{\delta_{eff}}{\delta} = \frac{\delta_{0eff} - \delta' \Delta P}{\delta_0 - \delta' \Delta P} = \frac{\tau_0 \delta_0 - \delta' \Delta P}{\delta_0 - \delta' \Delta P} \tag{54}$$

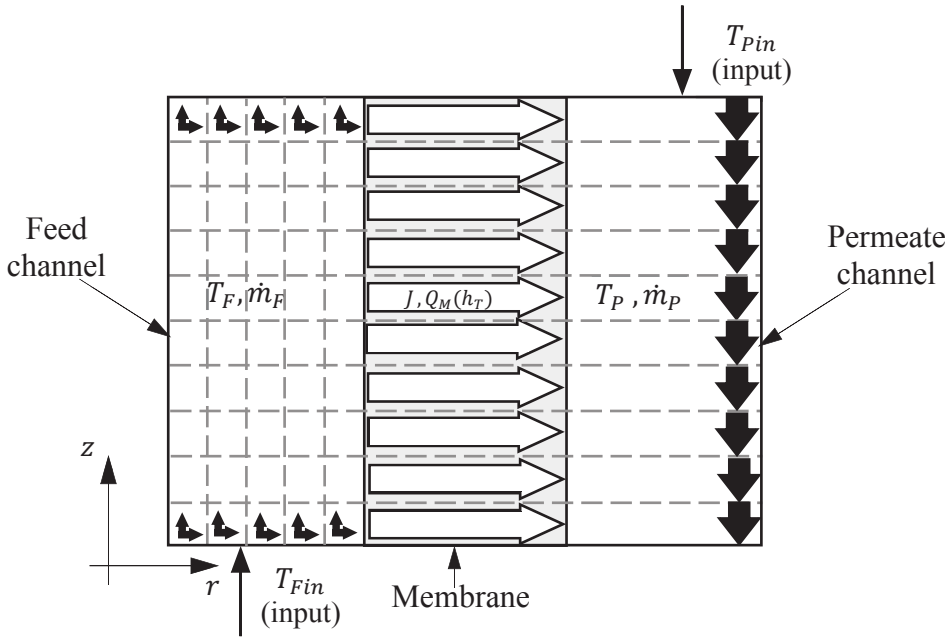

Figure 1.9. Schematic representation of calculated variables in the Lagana's model.

In comparison with the previously mentioned models, the Lagana's model was a significant step forward with more detailed description of the mass and heat balances. The mathematical structure of the model includes PDEs at the lumen side of the membrane and ODEs at the shell side of the membrane for simulation of the heat and mass transfer (Fig. 1.9). This approach allows a precise estimation of the temperature and concentration profiles in the feed (lumen) side of the hollow fibres in the DCMD module and determines these parameters at the permeate (shell) side along the DCMD module. However, the model uses integral equations to describe the mass and heat transfer through the membrane. The equations which are applied for the transmembrane heat transfer require the empirical correlations or experimental data. Thus, the Lagana's model is an empirically-dependent model with distributed continuous parameters for the steady-state operation of the DCMD module.

1.1.8.5 Yu's model

Yu and colleagues presented a computational fluid dynamics (CFD) approach in the DCMD modelling [92, 93]. They simulated the hollow fibre module containing only one membrane. In addition the heat and mass balance which were used in all the previously mentioned mathematical models of DCMD, the Yu's model also describe the momentum balance. To describe the momentum transport for the feed and permeate domains, the Yu's model uses the following equation [92]:

$$\nabla \cdot (\rho_z \vec{v}_z \vec{v}_z) = -\nabla P_z + \nabla \cdot \left(\mu_z \left((\nabla \vec{v}_z + \nabla \vec{v}_z^T) - \frac{2}{3} \nabla \cdot \vec{v}_z I \right) \right) + \rho_z \vec{g} \quad (55)$$

where z is the indicator of the compartment (feed or permeate), ρ_z is the fluid density, $\vec{v}_z$ is the fluid velocity, P_z is the fluid pressure, μ_z is the dynamic viscosity of the fluid, I is the identity matrix, $\vec{g}$ is the gravitational constant.

The momentum transport equation is complemented by the continuity equation [92]:

$$\nabla \cdot (\rho_z \vec{v}_z) = 0 \quad (56)$$

The heat transfer in the feed and permeate channels is described by the energy conservation equation [92]:

$$\nabla \cdot (\vec{v}_z \rho_z C_{Pz} T_z) = \nabla \cdot (k_z \nabla T_z) + S_h \quad (57)$$

$$S_h = \begin{cases} \frac{q_M}{\delta r} \cdot \frac{R_{M+\delta}}{R_M} \; for \; r = R_M \\ -\frac{\vec{q}_M}{\delta r} \; for \; r = R_{M+\delta} \\ 0 \; otherwise \end{cases} \quad (58)$$

where C_{Pz} is the specific heat capacity of the fluid, T_z is the fluid temperature, k_z is the thermal conductivity, S_h is the source term, $\vec{q}_M$ is the transmembrane heat flux, r is the radial coordinate, R_M is the inner radius of the hollow fibre, $R_{M+\delta}$ is the outer radius of the hollow fibre.

The following BCs for Eqs. (55)-(58) are applied [92]:

- feed and permeate entrances: $-n \cdot \vec{v}_F = v_{Fin}$, $-n \cdot \vec{u}_P = u_{Pin}$, $T_F = T_{Fin}$, $T_P = T_{Pin}$;
- feed and permeate outlets: $P_F = P_{Fout}$, $P_P = P_{Pout}$;
- membrane walls: no-slip condition, $\vec{q}_F|_{r=R_{M+\delta}} = \vec{q}_M|_{r=R_{M+\delta}}$, $\vec{q}_M|_{r=R_M} = \vec{q}_P|_{r=R_M}$, $T_F|_{r=R_{M+\delta}} = T_M|_{r=R_{M+\delta}}$, $T_M|_{r=R_M} = T_P|_{r=R_M}$.

The overall transmembrane heat transfer is described as follows [92]:

$$Q_T = Q_F = Q_P = Q_{MD} + Q_{HL} \quad (59)$$

where Q_T is the total heat flow, Q_F is the heat flow in the feed channel, Q_P is the heat flow in the permeate channel, Q_{MD} is the transmembrane latent heat flow, Q_{HL} is the conductive heat flow.

The overall heat transfer coefficient for the hollow fibre module is:

$$\frac{1}{K_{M+\delta}} = \frac{1}{h_F} + \frac{1}{h_M} + \frac{1}{h_P} \cdot \frac{R_{M+\delta}}{R_M} \tag{60}$$

where $K_{M+\delta}$ is the overall heat transfer coefficient, h_M is the membrane heat transfer coefficient.

The membrane heat transfer coefficient is calculated as follows:

$$h_M = h_{MD} + h_{HL} \cdot \frac{R_{M+\delta}}{R_M} = \frac{q_M}{(T_{FM} - T_{PM})} \tag{61}$$

where h_{MD} is the heat transfer coefficient due to evaporation and conduction, h_{HL} is the conductive heat transfer coefficient.

The heat transfer coefficient due to evaporation and conduction is calculated from the following equation [92]:

$$h_{MD} = C_M \left.\frac{dP_M}{dT}\right|_{T=T_M} \Delta H_{T_M} \tag{62}$$

where C_M is the intrinsic mass transfer coefficient, ΔH_{T_M} is the latent heat of vaporization of water.

The heat transfer coefficients of the bulk fluids are:

$$h_F = \frac{q_F}{(T_F - T_{FM})} \tag{63}$$

$$h_P = \frac{q_P}{(T_{PM} - T_P)} \tag{64}$$

The temperatures of the feed-membrane interface and permeate-membrane interface are evaluated from the following integral equation [92]:

$$T_{zM} = \frac{\int_S \rho_z u_z T_z dS}{\int_S \rho_z u_z dS} \tag{65}$$

where S is the membrane area, u_z is the fluid velocity normalized to the membrane surface.

The transmembrane heat flux, q_{MD}, is:

$$q_{MD} = J\Delta H_{T_{FM}} \tag{66}$$

where $\Delta H_{T_{FM}}$ is the latent heat of evaporation occurring at the membrane surface on the feed side.

The transmembrane vapour flux is described by the following equation:

$$J = C_M(P_{MF} - P_{MP}) \tag{67}$$

The Yu's CFD model applied for the steady-state operation is based on PDEs with distributed continuous parameters for the feed and permeate channels and on overall AEs with lumped discrete parameters for the membrane domain. This structure allows estimation of the concentration, velocity and temperature profiles in the feed and permeate domains and overall values for the heat and mass transfer through the membrane (Fig. 1.10). The heat transfer within the membrane is based on the heat transfer coefficients which are determined empirically.

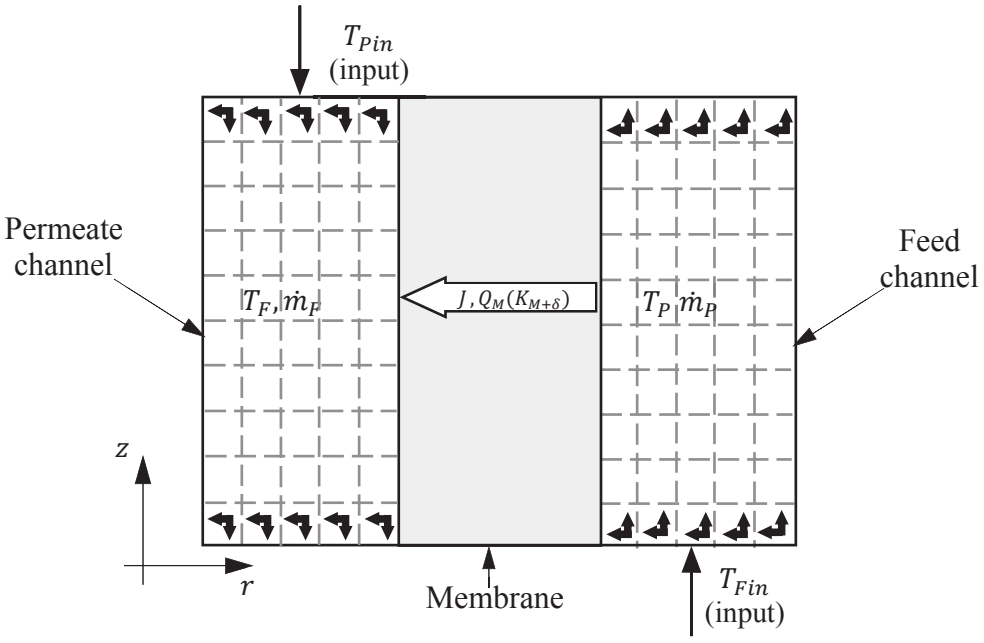

Figure 1.10: Schematic representation of calculated variables in the Yu's model.

1.1.8.6 Hayer's model

Another model based on the CFD approach was proposed by Hayer *et al.* [94]. In this model, the following assumptions are determined:

1. The DCMD process is performed under steady-state condition.
2. The feed liquid is an ideal mixture which is presented by salty water.
3. The membrane is fully hydrophobic without wetting effects.
4. No air molecules are present in the membrane pores.
5. No solute (salt) is transferred.
6. No slip condition at the membrane surface is obtained.

The momentum transfer in shell and lumen sides of the membrane is described by the Navier-Stokes equation coupled with the continuity equation [94]:

$$\rho_z(\vec{v}_z \cdot \nabla)\vec{v}_z = \nabla \cdot \left(-P_z + \mu_z(\nabla\vec{v}_z + (\nabla\vec{v}_z)^T)\right) \quad (68)$$

$$\nabla \cdot (\rho_z \vec{v}_z) = 0 \quad (69)$$

The heat transfer for the shell and lumen sides is:

$$\rho_z C_{Pz} \vec{v}_z \nabla T_z = \nabla \cdot (k_z \cdot \nabla T_z) \quad (70)$$

The mass transfer of the dissolved salt in the feed liquid is described by the following equation [94]:

$$\nabla(-D_{SW}\nabla c_S) + \vec{v}_F \cdot \nabla c_S = 0 \quad (71)$$

where c_S is the molar concentration of the salt in the feed flow.

The Darcy's law is used to describe the velocity of the vapour within the membrane pores [94].

$$\vec{u}_M = -\frac{\varepsilon_M d_M^2}{32\tau_M \mu_M}\nabla P_M \quad (72)$$

where d_M is the diameter of the membrane pores.

The transmembrane flux is described by the following equations [94]:

$$\vec{N}_M = \vec{N}_V + \vec{N}_D = \vec{u}_M c_M - D_{eff} \nabla c_M \tag{73}$$

$$\nabla\left(D_{eff} \nabla c_M\right) = 0 \tag{74}$$

$$D_{eff} = \frac{\varepsilon_M}{\tau_M}\left(\frac{1}{D_K} + \frac{1}{D_{WA}}\right)^{-1} \tag{75}$$

Hayer *et al.* applied PDEs to describe the momentum, heat and mass transfer within the feed and permeate channels and through the membrane. Therefore, the velocity and concentration profiles are determined in each point of the DCMD module (Fig. 1.11) while the temperature profiles are defined for the feed and permeate domains. The mathematical structure of the model is the most complicated among the models considered in Section 1.1.8. The model accounts the viscous flow, Knudsen diffusion and ordinary diffusion. Despite the promising opportunities, the Hayer's has significant drawbacks. In particular, the heat transfer through the membrane is not simulated, so the temperatures at the membrane surfaces remain almost the same as in the bulk phases. In particular, only water vapour is assumed to be inside the membrane pores but it is a rough approximation because air molecules definitely present there. Also, BCs which are necessary to solve PDEs are not determined making the model impossible in use. Thus, the Hayer's model could not be fully applied for the process design, control and optimization.

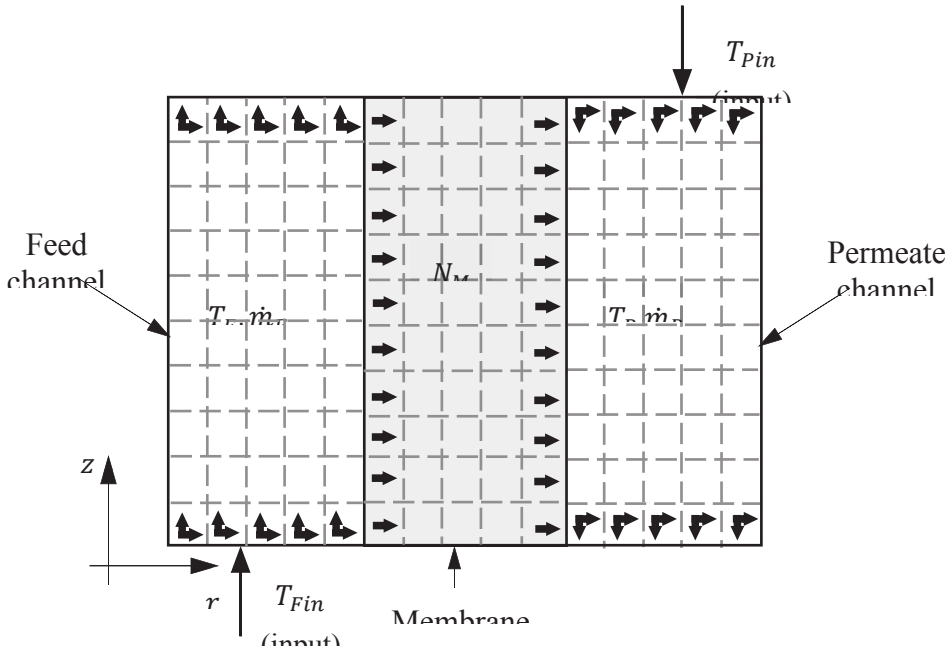

Figure 1.11: Schematic representation of calculated variables in the Hayer's model.

1.1.8.7 Gustafson's stepwise model

The model proposed by Gustafson *et al.* [95] uses a stepwise approach in which the DCMD unit is divided into numerous segments. For each segment, the mass and heat balances are determined. In co-current mode, the mass flow rates for the feed and permeate channels in each segment are calculated from the following equations [95]:

$$\dot{m}_{F,i+1} = \dot{m}_{F,i} - J_i A_{M,i} \tag{76}$$

$$\dot{m}_{P,i+1} = \dot{m}_{F,i} + J_i A_{M,i} \tag{77}$$

where $\dot{m}_{F,i}$ and $\dot{m}_{F,i+1}$ are the mass flow rates of the feed fluid for the segments i and $i+1$, respectively, $\dot{m}_{P,i}$ and $\dot{m}_{P,i+1}$ are the mass flow rates of the permeate fluid for the segments i and $i+1$, respectively, J_i is the transmembrane vapour flux for the segment i, $A_{M,i}$ is the are of the membrane surface in the segment i.

The heat balance for each step for the feed and permeate channels is described as follows [95]:

$$\dot{m}_{F,i}\left(e_{F,i} + \frac{v_{F,i}^2}{2}\right) = \dot{m}_{F,i+1}\left(e_{F,i+1} + \frac{v_{F,i+1}^2}{2}\right) + Q_i A_{M,i} \tag{78}$$

$$\dot{m}_{P,i}\left(e_{P,i} + \frac{v_{P,i}^2}{2}\right) + Q_i A_{M,i} = \dot{m}_{P,i+1}\left(e_{P,i+1} + \frac{v_{P,i+1}^2}{2}\right) \tag{79}$$

where $e_{F,i}$ and $e_{F,i+1}$ are the specific enthalpies of the feed fluid for the segments i and $i+1$, respectively, Q_i is the transmembrane heat transfer.

Additionally, the mass balance for the salt in the feed channel is expressed by the following equation [95]:

$$\frac{\dot{m}_{F,i}}{\rho_{F,i}} S_{F,i} = \frac{\dot{m}_{F,i+1}}{\rho_{F,i+1}} S_{F,i+1} \tag{80}$$

where $\rho_{F,i}$ and $\rho_{F,i+1}$ are the densities of the feed fluid for the segments i and $i+1$, respectively, $S_{F,i}$ and $S_{F,i+1}$ are the salinities of the feed fluid for the segments i and $i+1$, respectively.

The iteration calculation process uses the following BCs [95]:

$$N_T = \frac{\sum_{i=1}^{n} J_i \, A_{M,i}}{\sum_{i=1}^{n} A_{M,i}} \tag{81}$$

$$T_{F,0} = T_{Fin} \tag{82}$$

$$T_{F,n} = T_{Fout} \tag{83}$$

$$T_{P,0} = T_{Pin} \tag{84}$$

$$T_{P,n} = T_{Pout} \tag{85}$$

$$S_{F,0} = S_{Fin} \tag{86}$$

$$S_{P,0} = 0 \tag{87}$$

$$S_{P,n} = 0 \tag{88}$$

$$S_{P,i} = 0 \tag{89}$$

For counter-current operation, Eqs. (78) and (79) which describe the mass flow rate and heat balance in each segment are substituted by the following equations [95]:

$$\dot{m}_{P.i+1} = \dot{m}_{F.i} - N_i A_{M,i} \tag{90}$$

$$\dot{m}_{P.i+1}\left(e_{P,i+1} + \frac{v_{P,i+1}^2}{2}\right) + Q_i A_{M,i} = \dot{m}_{P.i}\left(e_{P,i} + \frac{v_{P,i}^2}{2}\right) \tag{91}$$

where $e_{P,i}$ and $e_{P,i+1}$ are the specific enthalpies of the permeate fluid for the segments i and $i+1$, respectively.

Additionally, BCs for Eqs. (84) and (85) are substituted by the following equations [95]:

$$T_{P,0} = T_{Fin} - T_g \tag{92}$$

$$T_{P,n} = T_{Pin} \tag{93}$$

$$\dot{m}_{P.0} = \dot{m}_{Pin} + J_g \sum_{i=1}^{n} A_{M,i} \tag{94}$$

where T_g is the initially guessed value of the temperature at the permeate outlet, J_g is the initially guessed value of the average transmembrane vapour flux.

The transmembrane mass flux in each segment is calculated from the following equation [95]:

$$J_i = C_{M,i}\left[P_V\left(T_{FM,i}, S_{FM,i}\right) - P_V\left(T_{PM,i}, S_{PM,i}\right)\right] \tag{95}$$

where $C_{M,i}$ is the membrane distillation coefficient, P_V is the water vapour pressure.

The transmembrane heat flux is described as follows [95]:

$$\begin{aligned} q_{M,i} &= q_{M,i}^V + q_{M,i}^C = J_i \Delta H_{Vi}\left(T_{FM,i}, S_{FM,i}\right) + k_M \frac{T_{FM,i} - T_{PM,i}}{\delta_M} \\ &= \left(\frac{J_i \Delta H_{Vi}\left(T_{FM,i}, S_{FM,i}\right)}{T_{FM,i} - T_{PM,i}} + \frac{k_M}{\delta_M}\right)\left(T_{FM,i} - T_{PM,i}\right) = \left(h_V + h_C\right)\left(T_{FM,i} - T_{PM,i}\right) \end{aligned} \tag{96}$$

where ΔH_{Vi} is the latent heat of vaporization.

The thermal conductivity of the membrane is described by the isostress model [95]:

$$k_M = \left(\frac{\varepsilon_M}{k_V} + \frac{1 - \varepsilon_M}{k_S}\right)^{-1} \tag{97}$$

The temperature of the feed flows at the membrane surfaces are determined by the following expressions [95]:

$$T_{FM,i} = T_{F,i} - \frac{h_F^{-1}\left(T_{F,i} - T_{P,i}\right)}{h_F^{-1} + h_P^{-1} + \left(h_V + h_C\right)^{-1}} \tag{98}$$

$$T_{PM,i} = T_{P,i} - \frac{h_P^{-1}\left(T_{F,i} - T_{P,i}\right)}{h_F^{-1} + h_P^{-1} + (h_V + h_C)^{-1}} \tag{99}$$

The heat and mass transfer coefficients for the feed and permeate channels are calculated from the following correlations [95]:

$$h_{F,P,i} = Nu_{F,P,i}\frac{h_{F,D,i}}{d_h} = \left(0.023Re_{F,P,i}^{0.8}Pr_{F,P,i}^{1/3}\right)\frac{k_{F,P,i}}{d_h} \tag{100}$$

$$K_{F,i} = Sh_{F,P,i}\frac{D_{F,i}}{d_h} = \left(0.023Re_{F,i}^{0.8}Sc_{F,i}^{1/3}\right)\frac{D_{F,i}}{d_h} \tag{101}$$

where $Nu_{F,P,i}$ and $Sh_{F,i}$ are the dimensionless Nusselt and Sherwood numbers, respectively, Re is the dimensionless Reynolds number, Sc is the dimensionless Schmidt number, d_h is the hydraulic diameter of the flow channel, $D_{F,i}$ is the diffusion coefficient of the solute through the solution, $k_{F,P,i}$ is the thermal conductivity of the feed or permeate liquid.

The hydraulic diameter of the flow channel is evaluated by using the following equation [95]:

$$d_h = \frac{2b_{eff}w_{ch}}{b_{eff} + w_{ch}} \tag{102}$$

where b_{eff} is the effective channel height, w_{ch} is the channel width.

The effective channel height is found from the following equation [95]:

$$b_{eff} = b_{ch} - \frac{V_{sp}}{A_{xs,ch}} \tag{103}$$

where b_{ch} is the channel height, V_{sp} is the volume of the spacer, $A_{xs,ch}$ is the cross-sectional area of the channel.

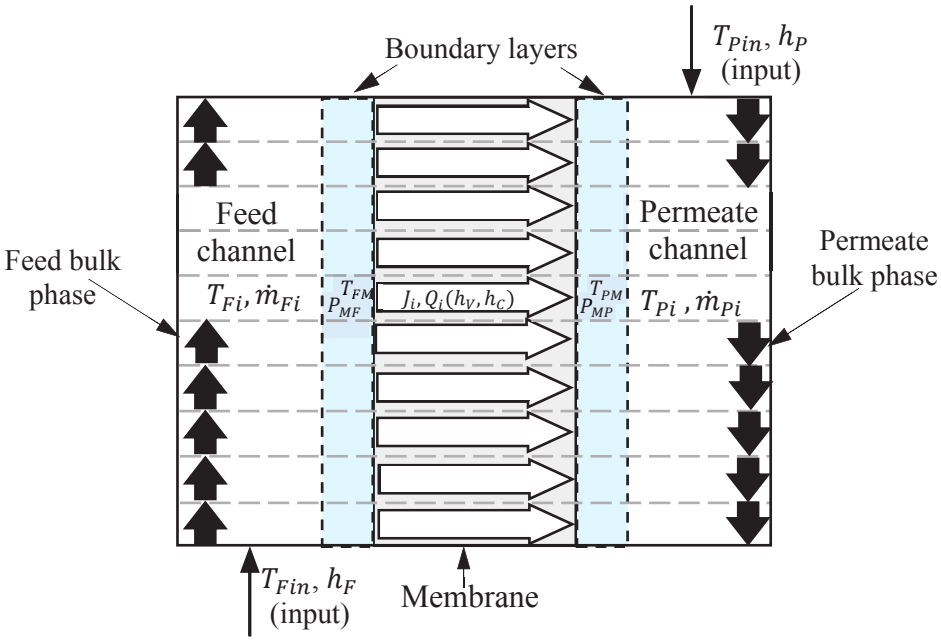

Figure 1.12: Schematic representation of calculated variables in the Gustafson's model.

Fig. 1.12 illustrates the segmentation approach of the Gustafson's model. Application of the approach in the models which use integral and overall equations with lumped discrete parameters for the mass and heat balances increases the precision of calculations and allows to estimate changes of the temperatures and concentrations along the DCMD unit. With these advantages, the Gustafson's multistep model is preferable in use than one segment models like the Lawson-Lloyd's model or Schofield's model. The multistep model is also suitable for the optimization of the length of DCMD modules. However, the model requires empirical data for determination and calculation of the heat transfer and do not describe the concentration, velocity and temperature profiles within the DCMD module. Thus, the model can be used for the process design and optimization with defined empirical correlations.

1.1.8.8 Eleiwi's dynamic model

A modelling approach based on dynamic operation of DCMD was proposed by Eleiwi *et al.* [96]. In this model, 2D advection-diffusion equations (ADE) were used to describe the heat and mass transfer within the DCMD unit. The temperatures of the feed and permeate channels of the DCMD unit are calculated from the following equation [96]:

$$\frac{\partial T_z(x,z,\tau)}{\partial \tau} + v_z \frac{\partial T_z(x,z,\tau)}{\partial z} = a_z \frac{\partial^2 T_z(x,z,\tau)}{\partial x^2} \tag{104}$$

The transmembrane flux is described as follows [96]:

$$J = C_M\left(P_{MF}(T_{FM}) - P_{MP}(T_{PM})\right) \tag{105}$$

The membrane transfer coefficient accounts only Knudsen diffusion [96]:

$$C_M = 1.064\frac{\varepsilon_M r_M}{\tau_M \delta_M}\left(\frac{M}{R_g T_{Mmean}}\right) \tag{106}$$

The heat flux through the membrane is

$$Q_M = \frac{A_M k_M}{\delta_M}(T_{FM} - T_{PM}) + A_M J \Delta H_V(T_{Mmean}) \tag{107}$$

BCs and initial conditions for Eqs. (104)-(107) are

$$\begin{cases} T_F(x,0,\tau) = T_{Fin}\ for\ x \in [0, x_{FM}] \\ T_P(x,L_M,\tau) = T_{Pin}\ for\ x \in [x_{PM}, X] \\ \left.\frac{\partial T_z(x,z,\tau)}{\partial x}\right|_{x=0} = 0, \left.\frac{\partial T_z(x,L_M,\tau)}{\partial x}\right|_{x=X} = 0 \\ \left.\frac{\partial T_F(x,z,\tau)}{\partial x}\right|_{x=MF} = \left(J\Delta H_V(T_{Mmean}) + \frac{k_M}{\delta_M}T_F(x_{MF},z,\tau) - \frac{k_M}{\delta_M}T_P(x_{MP},z,\tau)\right)\Big/k_F \\ \left.\frac{\partial T_P(x,z,\tau)}{\partial x}\right|_{x=MP} = \left(J\Delta H_V(T_{Mmean}) + \frac{k_M}{\delta_M}T_F(x_{MF},z,\tau) - \frac{k_M}{\delta_M}T_P(x_{MP},z,\tau)\right)\Big/k_P \\ \left.\frac{\partial T_z(x,z,\tau)}{\partial z}\right|_{z=L_M} = \phi, \left.\frac{\partial T_z(x,z,\tau)}{\partial z}\right|_{z=0} = \phi \end{cases} \tag{108}$$

After semi-discretization of the ADE model, Eq. (104) is transformed into the following form:

$$\frac{\partial T(x,z,\tau)}{\partial \tau} + v_z^k \frac{T_{i,j+1} - T_{i,j}}{\Delta z} = \alpha_z^k \frac{T_{i,j+1} - 2T_{i,j} + T_{i-1,j}}{\Delta x^2} \tag{109}$$

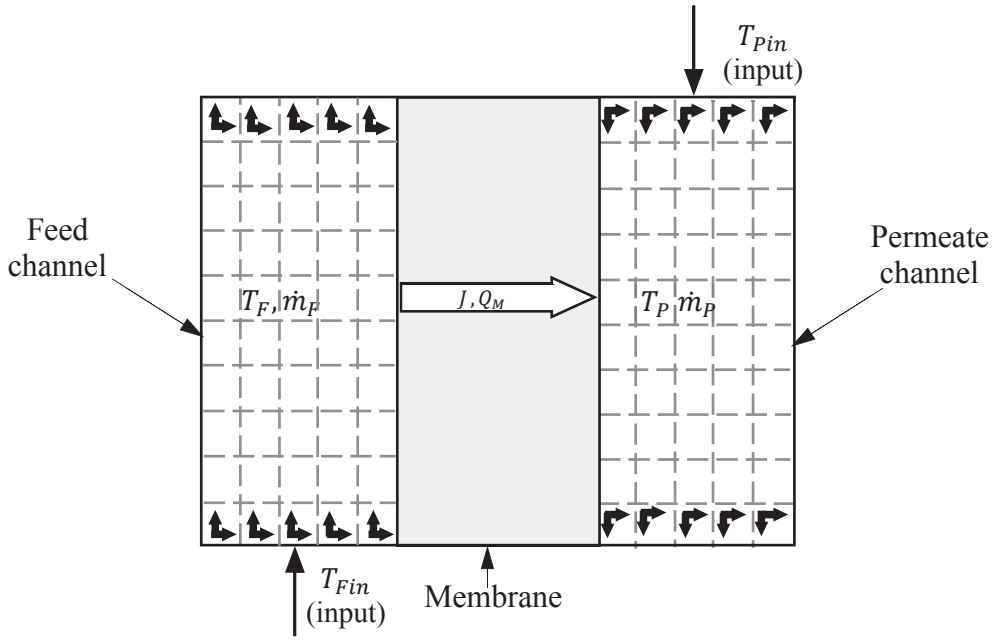

Figure 1.13: Schematic representation of calculated variables in the Eleiwi's model.

The application of the dynamic regime in the Eleiwi's model which is illustrated on Fig. 1.13 can help with estimation of the time to establish the steady state of the DCMD operation. The temperature distribution within the feed and permeate channels is fully described by using PDEs, however, for the membrane domain, the heat and mass transfer is described by the integral equations which do not allow fully estimate the temperature and concentration of the water vapour. At the same time, the momentum and mass balances within the feed and permeate channels are not described. It makes impossible to analyse the effect of the fluid velocity and concentration on the module efficiency. Therefore, the application of the Eleiwi's dynamic model in the process design, control and optimization is limited due to oversimplification and absence of description of the mass balances for the feed and permeate side.

1.1.8.9 Response surface model

The model based on the response surface (RS) methodology was proposed by Cheng *et al.* [97]. The RS model uses experimental relationships between controlled variables and response variables. In that model, the response is a function of two input variables. The RS method allows estimation of interactions between the variables. As influencing factors, the inlet temperatures of the feed and permeate flows, velocity of the feed fluid, module packing density and length-diameter ratio were taken into consideration as optimization variables. The transmembrane flux, water productivity per unit volume of module, water production per unit

energy consumption and comprehensive index are taken as the response objectives. The comprehensive index takes into account a balance between the permeate flux and thermal energy consumption. The linear flow velocity of the feed solution in hollow fibres is calculated as follows [97]:

$$v_F = \frac{4}{n_M \pi d_{HFin}^2} \tag{110}$$

The packing density, ρ_{Pack}, is:

$$\rho_{Pack} = \frac{n_M r_{HFout}^2}{r_{MM}^2} \cdot 100\% \tag{111}$$

where r_{MM} is the inner radius of the membrane module.

The ratio of the effective length of the membrane module to inner diameter of the membrane module, R_{LD}, is:

$$R_{LD} = \frac{L_M}{d_{MM}} \tag{112}$$

where L_M is the effective length of the membrane module, d_{MM} is the inner diameter of the membrane module.

The transmembrane flux, as one of the model objectives, is determined by the following equation [97]:

$$J = \frac{\dot{m}_P}{A_M \tau} \tag{113}$$

where A_M is the area of the hollow fibre surface in the lumen side, $\dot{m}_P$ is the mass flow variation on the permeate side over a given period of time, τ.

The water productivity, pr_W, which is used to evaluate the overall water production capacity of the membrane module is calculated as follows [97]:

$$pr_W = \frac{\dot{m}_P}{\pi r_{MM}^2 L_M \tau} \tag{114}$$

where r_{MM} is the inner radius of the membrane module.

The water production per kilojoule, pr_E, is

$$pr_E = \frac{\dot{m}_P}{Q_E \tau} \tag{115}$$

where Q_E is the total energy consumption.

The comprehensive index, CI, is calculated as follows [97]:

$$CI = w_j x_j + w_{prw} x_{prw} + w_{pre} x_{pre} \tag{116}$$

where w_j, w_{prw} and w_{pre} are the weight coefficients of J, pr_W and pr_E, respectively, x_j, x_{prw} and x_{pre} are the normalized objectives of J, pr_W and pr_E, respectively.

The weight coefficients are determined in the semi-empirical way by using of the expert consultation method, order relation analysis method and statistical method.

For the modelling purpose, a quadratic rotation-orthogonal composite design (QRCD) was used. With QRCD, the model equation takes the following form [97]:

$$Y = b_0 + \sum_i b_i X_i + \sum_i b_{ii} X_i^2 + \sum_{ij} b_{ij} X_{ij} \tag{117}$$

where Y is the response (objective of the model), b_i is the linear coefficient, b_{ii} is the quadratic coefficient, b_{ij} is the binary interaction coefficient, and X_i and X_{ij} are the values of the variables.

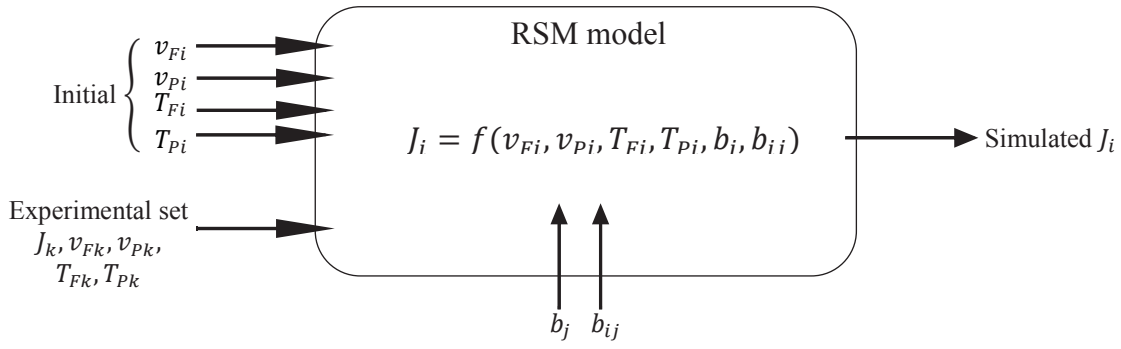

Figure 1.14: Schematic representation of the mathematical structure of the RSM model.

The RS model considers the DCMD process as the "black box" in which the dependence between input variables and output results is not determined physically however it is described mathematically on the base of the multiple experiments (Fig.1.14). Before

simulation, the model requires experimental data (e.g. inlet temperatures and velocities of the flows and corresponding transmembrane water vapour fluxes) for a learning process. Therefore, the RS model is fully empirical model which requires experimental data and can be applied only for analysis and optimization of the performance of the already prepared DCMD module in the range of experimental values.

1.1.8.10 Ali's model

Recently, Ali *et al.* [98, 99] proposed the model for design of DCMD units. The Ali's model is based on a multiple segmentation of the DCMD unit. For each segment, the heat and mass balances are defined. The transmembrane heat flux, q_M, is described by the following equation [99]:

$$q_M = K\left(T_{W,F} - T_{W,P}\right) = J_M \Delta h_V + \frac{k_M}{\delta_M}\left(T_{W,F} - T_{W,P}\right) \tag{118}$$

The transmembrane mass flux, J, is described by the following equation [98, 99]:

$$J = C_M(p_{MF} - p_{MP}) \tag{119}$$

The membrane distillation coefficient takes into account the Knudsen diffusion and ordinary diffusion [98, 99]:

$$C_M = \left[\frac{3\tau_M \delta_M}{2\varepsilon_M r_M}\left(\frac{\pi R_g T_M}{8M}\right)^{1/2} + \frac{\tau_M \delta_M p_A R_g T_M}{\varepsilon_M P_M D_{WA} M}\right]^{-1} \tag{120}$$

The temperatures at the feed-membrane interface and permeate-membrane interface are calculated as follows [99]:

$$T_{FM} = T_F - \frac{q_M}{h_F} \tag{121}$$

$$T_{PM} = T_P + \frac{q_M}{h_P} \tag{122}$$

The heat transfer coefficients are determined from the empirical correlations. The pressure drop, ΔP_z, in the feed and permeate channels is determined from the following equation [99]:

$$\Delta P_z = f \frac{L_M}{d_{HFin}} \frac{\rho_z v_{z,ave}^2}{2} \tag{123}$$

where f is the Darcy friction factor.

Energy balances for the feed and permeate channels are described by the following equations [99]:

$$\dot{m}_F C_{PF} \left(T_F^{(i-1)} - T_F^{(i)} \right) = (n_M d_{HFin} \Delta L_M) q_M \tag{124}$$

$$\dot{m}_P C_{PP} \left(T_P^{(i)} - T_P^{(i+1)} \right) = (n_M d_{HFin} \Delta L_M) q_M \tag{125}$$

For counter-current operation, the mass balance of the feed and permeate channels for each step is determined as follows:

$$\dot{m}_{zi} = \dot{m}_{zi-1} - n_M J_{i-1} A_{Mi-1} \tag{126}$$

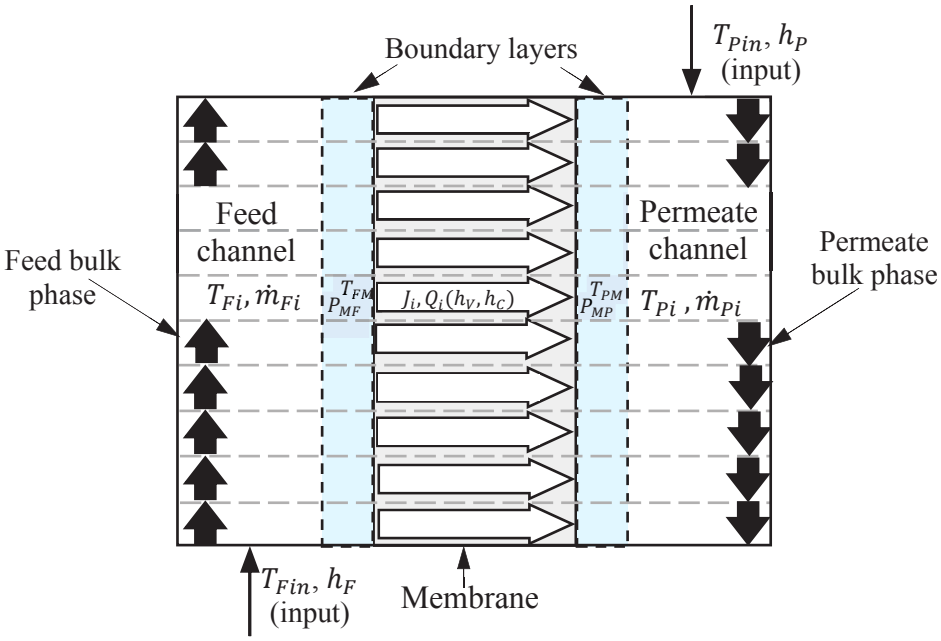

Figure 1.15. Schematic representation of calculated variables in the Ali's model.

The equations applied in the Ali's model are similar to the Gustafson's model as well as the segmentation method (Fig. 1.15). The calculations of the mass and heat balances in each segment of the DCMD module introduce the temperatures and flows distributions along the DCMD module and allow precise estimation of TP. In each segment, the calculated parameters are lumped and discrete. For the calculation of the heat balances, the empirical heat transfer

coefficients are introduced. With the knowledge of these coefficients, the Ali's model is suitable for the design and optimization of the DCMD module.

1.1.8.11 Comparison of the existing models

Various DCMD models have been described in Section 1.1.8. These models vary in many features: type of variables and parameters, the use of empirical data, type of equations which describe the heat and mass balances, availability of the momentum, mass and heat balances, possibility of simulation of hollow fibre or flat sheet DCMD modules. The comparison by the mentioned characteristics is given in Table 1.5. It is seen that the quality of the models have been improved significantly from the first to the recent studies with the increased mathematical complexity and features of the models.

The Schofield's model [52, 82, 83], as one of the pioneering models, is the most basic and simple model which is used to calculate the total values of the transmembrane vapour and heat fluxes and average values of the temperatures at the membrane surfaces because the mass and heat balances are given only for the membrane compartment. The heat balance in the Schofield's model is based on the heat transfer coefficients which can be calculated using empirical calculations or experimental data. The combination of different modes of mass transport is described by an equation derived by Schofield *et al.* [52, 82, 83].

The Lawson-Lloyd model [90, 91] is similar to the Schofield's model in terms of the description of the mass and heat transfer, the use of discrete lumped parameters and simulated data. It is worth mentioning that the combination of the mass transfer modes in the Schofield's model is different from the DGM, applied in the Lawson-Lloyd model and other DCMD mathematical models. The electrical analogy circuits for the both Schofield's model and the DGM are present in Fig. 1.4 and 1.7, respectively.

In contrast to the Lawson-Lloyd model and Schofield's model, the Tomaszewska's model [29, 88, 89] describes the mass and heat balances within the feed and permeate channels. The mass and heat transfer in the feed and permeate compartments is described by a system of 1D ODEs with distributed continuous variables which allow to obtain concentration and temperature profiles in the channels. In terms of the transmembrane mass and heat transfer, the Tomaszewska's model is similar to the Lawson-Lloyd model by using of the algebraic equations with lumped distributed parameters.

After the Tomaszewska's model, the Lagana's model [32] continues the trend in increasing the complexity of the equations for the mass and heat balances. Indeed, the Lagana's model uses 2D PDEs for simulation of the heat and mass transfer in the feed channel and ODEs for simulation of the heat and mass transfer in the permeate channel. Therefore, the 2D and 1D concentration and temperature profiles are obtained for the feed and permeate compartments, respectively. The transmembrane mass transfer in the Lagana's model is described in the same way as in Lawson-Lloyd model by integral equation derived from the DGM. Thus, only overall value of the vapour flux and temperature at the membrane surfaces are obtained.

The Eleiwi's model [96] is the only model which can be applied for dynamic operation of the DCMD module. This model describes the heat transfer in the feed and permeate channels by PDEs but do not describe the mass and momentum transfer. Instead of it, the Eleiwi's model uses empirical correlations and coefficients to describe the type of the flow and its characteristics. The transmembrane mass and heat transfer is described by AEs with distributed lumped parameters and empirical correlations for the heat transfer coefficients. Therefore, the Eleiwi's model is very limited in use and range of simulated parameters.

The Yu's model [92, 93] and the Hayer's model [94] have the maximal mathematical complexity among the models presented in Section 1.1.8. The Yu's model and Hayer's model describe the momentum, mass and heat transfer in the feed and permeate channels by systems of PDEs. Moreover, the Hayer's model also applies the system of PDEs for the membrane compartment while the Yu's model applies AEs. However, the Hayer's model is incomplete and could not be used because the boundary conditions for the equations are not described. The Yu's model can be applied in the DCMD process design but the drawbacks of the model in the part of the transmembrane fluxes are the same as the ones in the previously mentioned models: the need of the experimental data or empirical calculations and impossibility to obtain concentration and temperature profiles in the membrane domain.

The Ali's model [98, 99] and the Gustafson's model [95] apply the same approaches which were used in the Lawson-Lloyd model. In particular, the transmembrane mass and heat transfer is described by AEs with discrete lumped parameters with the use of the DGM. The mass and heat transfer within the feed and permeate channel is also described by AEs. But, for increase of the precision of calculations in comparison with the Lawson-Lloyd model, these models apply segmentation approach and divide the DCMD module into numerous interconnected segments, or steps, where the mass and heat balance is determined for each compartment in each segment.

In contrast to all the other models, the RS model [97] is an empirical model which is not based on the description of physical phenomena but is using the approximate function to describe the dependence of the results of experiments on the process parameters (operating conditions, membrane properties, etc.). The initial set of the experimental data is needed to set the parameters of this approximative function. The application of such model is limited in the range of conducted experiments. This model can be used mainly for optimization of the operating conditions of existing modules and not for process design.

All of the presented models have at least one of the following disadvantages: oversimplification, the use of empirical correlations to describe heat and mass transfer and poor prediction for the cases out of the experimental data range. To eliminate the use of empirical heat and mass transfer coefficients, increase prediction of DCMD simulations and deepen our understanding of the process design of a DCMD unit, a new general predictive model for DCMD is proposed in this work. The model is applicable for hollow fibre and flat sheet membranes with empty as well as spacer filled channels. The mathematical model, based on mass, heat and momentum balances and mass transfer equations, results in systems of ODEs, PDEs and AEs. The equations are solved using COMSOL Multiphysics™ software with use of CFD approach what improves the accuracy of the simulation. The effects of key parameters and membrane properties on the performance of a DCMD unit are also predicted and compared with the corresponding experimental data.

Table 1.5: Comparison of different models for DCMD.

Model	Type of variables	Use of empirical data	Type of equations	Possibility of segmentation	Described balances	Type of operation	Geometry	Note
Schofield's model	Lumped, discrete	Yes	Integral overall	No	Mass and heat (membrane domain)	Steady-state	Flat sheet	[52, 82, 83]
Tomaszewska's model	Lumped discrete (Membrane), Distributed continuous (Feed, Permeate)	Yes	Integral overall (membrane), 1D ODE (feed, permeate)	Yes (feed, permeate)	Mass and heat	Steady-state	Flat sheet	[88-89]
Lawson-Lloyd model	Lumped discrete	Yes	Integral overall	No	Mass and heat (membrane)	Steady-state	Flat sheet, hollow fibre	[90,91]
Laganà's model	Lumped discrete (Membrane), Distributed continuous (Feed, Permeate)	Yes	Integral overall (membrane), 2D PDE (feed, permeate)	Yes	Momentum, mass and heat	Steady-state	Hollow fibre	[32]
Yu's model	Lumped discrete (Membrane), Distributed continuous (Feed, Permeate)	Yes	Integral overall (membrane), 2D PDE (feed, permeate)	Yes	Momentum, mass and heat	Steady-state	Hollow-fibre	[92, 93]
Hayer's model	Distributed continuous	No	2D PDE	Yes	Momentum, mass and heat	Steady-state	Hollow-fibre	[94]
Gustafson's stepwise model	Lumped discrete	Yes	Integral overall	Yes	Mass and heat	Steady-state	HF, FS	[95]
Eleiwi's dynamic model	Lumped discrete (Membrane), Distributed continuous (Feed, Permeate)	Yes	Integral overall (membrane), 2D PDE (feed, permeate)	Yes	Heat	Dynamic	FS	[96]
Response surface model	Lumped discrete	Yes	AE (to describe relationship between input and output)	No	-	Steady state	FS, HF	[97]
Ali's model	Lumped discrete	Yes	Integral overall	Yes	Mass and heat	Steady-state	HF, FS	[98, 99]

1.1.9 Literature review of mathematical models of SGMD

In this section, the existing mathematical models for SGMD are described, analysed and compared. The comparison of the models is made on the base of the advantages and drawbacks of the models, their mathematical structure and complexity, the possibility of application and range of simulated data.

1.1.9.1 First Khayet's model

One of the first theoretical models for SGMD was presented by Khayet *et al.* [100, 101]. This theoretical model allows to calculate the mass and heat balance within the flat sheet module. For better understanding and comparison with other model, that model is further denoted as the first Khayet's model. The mass transfer of water in the feed channel is described by the following relationship [100, 101]:

$$d\dot{m}_W = -Jbdx \tag{127}$$

where J is the transmembrane vapour flux, b is the width of the feed channel, x is the spatial coordinate.

The mass transfer of the water vapour in the permeate channel is:

$$d\dot{m}_{WA} = -Jbdx \tag{128}$$

The total heat transfer within the SGMD module is described by the following equations [100, 101]:

$$Q = h_T(T_F - T_P) \tag{129}$$

$$Q_F = h_F(T_F - T_{FM}) \tag{130}$$

$$Q_P = h_P(T_{PM} - T_P) \tag{131}$$

$$Q_{MC} = h_{MC}(T_{FM} - T_{PM}) \tag{132}$$

$$Q_{MV} = h_{MV}(T_{FM} - T_{PM}) \tag{133}$$

$$Q_M = Q_{MC} + Q_{MV} = Q_F = Q_P \tag{134}$$

where Q is the overall heat flux, h_T is the overall heat transfer coefficient, T_F and T_P are the feed and permeate temperature, respectively, Q_F is the overall heat flux through the feed channel, h_F is the feed heat transfer coefficient, T_{FM} is the temperature at the feed-membrane interface, Q_P is the overall heat flux through the permeate channel, h_P is the permeate heat transfer coefficient, T_{PM} is the temperature at the permeate-membrane interface, Q_{MC} is the heat flux through the membrane material, h_{MC} is the membrane material heat transfer coefficient, Q_M is the overall heat flux through the membrane.

The overall heat transfer coefficient is determined as follows [100, 101]:

$$h_T = \left(\frac{1}{h_F} + \frac{1}{h_M} + \frac{1}{h_P}\right)^{-1} \tag{135}$$

For the feed channel, the enthalpy balance is described by the following equation [100, 101]:

$$\rho_F C_F \vec{v}_F \frac{\partial T_F(x,y)}{\partial x} = k_F \frac{\partial^2 T_F(x,y)}{\partial y^2} \tag{136}$$

where ρ_F is the density of the feed liquid, C_F is the specific heat of the feed liquid, $\vec{v}_F$ is the feed velocity, y is the spatial coordinate, k_F is the feed thermal conductivity.

The enthalpy balance for the sweeping gas at the permeate channel is:

$$\frac{\dot{m}_{SG}}{b}\frac{dH_{SG}}{dx} = -h_T(T_F - T_P) \tag{137}$$

where H_{SG} is the specific enthalpy of the sweeping gas.

The enthalpy of the moist sweeping gas is described by the following equation [100, 101]:

$$H_{SG} = C_{hSG}T_P + \omega\Delta H_{vap} = (C_{SG} + \omega C_W)T_P + \omega\Delta H_{vap} \tag{138}$$

where C_{hSG} is the specific heat of the humid sweeping gas, ω is the humidity ratio, ΔH_{vap} is the enthalpy of vaporization, C_{SG} is the specific heat of the dry sweeping gas, C_W is the specific heat of the water vapour.

The overall transmembrane vapour flux, J, is described as function of the partial pressure [100, 101]:

$$J = B_M \Delta P_W \tag{139}$$

where B_M is the global mass transfer coefficient, ΔP_W is the water vapour pressure difference.

The final view of the heat transfer equation for the permeate channel is:

$$\frac{dT_P}{dx} = \left(\left(h_T - h_M \left(1 - \frac{h_T}{h_{FP}} \right) \right) \frac{\Delta H_{vap,0}}{\Delta H_{vap}} - h_T \right) \frac{b}{\dot{m}_P c_{hSG}} \tag{140}$$

The set of BCs for Eq. 136 is:

$$\begin{cases} T_F(0,0) = T_F(L_M, 0) = T_{Fout} = T_{Fin} \\ T_P(L_M) = T_{Pin} \\ T_P(0) = T_{Pout} \\ Q_M = -k_F \left. \dfrac{\partial T_F}{\partial y} \right|_{y=d_F} \end{cases} \tag{141}$$

where T_{Fin} and T_{Fout} are the temperatures at the feed inlet and feed outlet, respectively, T_{Pin} and T_{Pout} are the temperatures at the permeate inlet and feed outlet, respectively.

With the use of PDEs for description of the mass and heat transfer in the feed and permeate channels, the model can provide the temperature and concentration distributions in the channels for the steady-state operation of the SGMD module (Fig. 1.16). However, the membrane media are described by AEs which can produce only lumped discrete parameters. The model also allows to estimate the bulk and boundary layer temperatures of the feed liquid and sweeping gas along the SGMD module. The mathematical complexity of the model is an average with 2D PDEs, ODEs and AEs and it requires numerical methods for solving. The model is suitable for basic process design and determination of TP and optimization of the operating parameters. The drawbacks of the model are the need of the heat transfer coefficients and the temperatures of the feed and permeate flows at outlets, capability of simulation of only

flat sheet configuration and possibility of the transfer of only one species through the membrane.

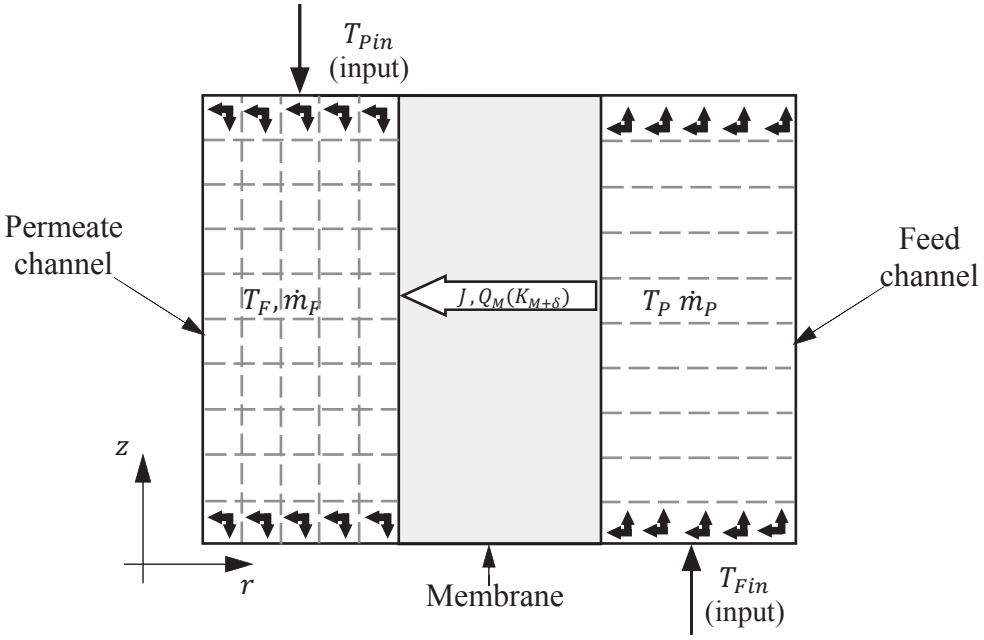

Figure 1.16: Schematic representation of calculated variables in the first Khayet's model.

1.1.9.2 Second Khayet's model

Another model which was presented by Khayet's *et al.* several years later [102] is based on AEs. That model is further denoted as the second Khayet's model. The mass transfer through the membrane, J, is described by the following equation [102]:

$$J = C_M \Delta P_V = \frac{M}{R_g T_M}\left(\frac{3\tau_M}{3\varepsilon_M r_M}\left(\frac{\pi M}{2R_g T_M}\right)^{1/2} + \frac{\tau_M P_V D_{WA}}{\varepsilon_M P_A}\right)^{-1} \frac{\Delta P_V}{\delta_M} \tag{142}$$

where M is the water molar mass, R_g is the gas constant, T_M is the membrane temperature, τ_M is the membrane tortuosity, ε_M is the membrane porosity, r_M is the membrane pore size, P_V is the total vapour pressure, P_A is the air pressure, δ_M is the membrane thickness.

The overall heat transfer is presented by the following equation [102]:

$$h_F(T_F - T_{FM}) = J\Delta H_{vap} + \frac{k_M^{eff}}{\delta_M}(T_{FM} - T_{PM}) = h_P(T_{PM} - T_P) \tag{143}$$

The concentration of the water at the feed-membrane interface is determined from the following expression [102]:

$$c_{W,FM} = c_{W,F} \exp\left(\frac{J}{\rho_F B_F}\right) \tag{144}$$

where $c_{W,F}$ is the bulk concentration, ρ_F is the feed density, B_F is the feed mass transfer coefficient.

The pressure of the water vapour at the feed-membrane interface, $P_{V,F}$, is found from the following equation [102]:

$$P_{V,F}\left(c_{W,FM}, T_{FM}\right) = a\left(c_{W,FM}, T_{FM}\right) P_V^0(T_{FM}) \tag{145}$$

where a is the feed activity, P_V^0 is the pressure of the saturated water vapour.

The pressure of the water vapour at the permeate-membrane interface, $P_{V,P}$, is calculated by the following equation [102]:

$$P_{V,P}(T_{PM}) = \frac{\omega P_P}{\omega + 0.622} \tag{146}$$

where P_P is the total pressure at the permeate side and ω is the humidity ratio which is calculated as follows:

$$\omega = \omega_{in} + \frac{J A_M}{\dot{m}_{SG}} \tag{147}$$

where ω_{in} is the humidity of the sweeping gas at the permeate inlet, A_M is the membrane area.

In fact, the second Khayet's model is a result of the simplification of the first Khayet's model with the use of AEs to describe the heat and mass transfer in the feed and permeate channels. The mathematical representation of the model is a dot with macroscopic degree of physical detailing. Therefore, it has a low mathematical complexity and its equations can be easily solved. The predicted results and calculated parameters are lumped and discrete (Fig. 1.17). The solving procedure requires the knowledge of the flow pattern in channels, presence of spacer and type of the SGMD module. However, TP could not be properly estimated along and across the SGMD module.

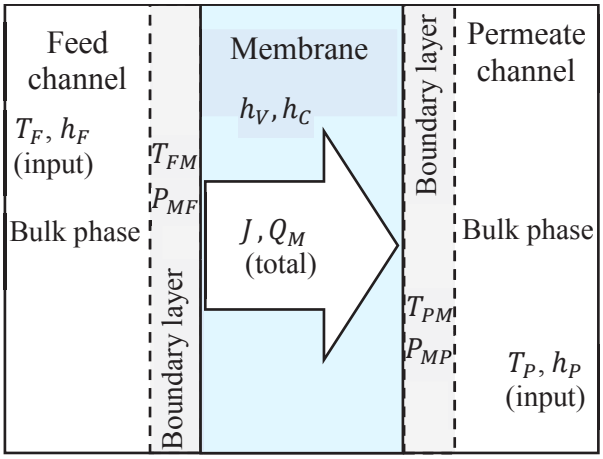

Figure 1.17: Schematic representation of calculated variables in the second Khayet's model.

1.1.9.3 Boi's model

In 2005, Boi *et al.* proposed a simplified mathematical model for SGMD [69]. This model describes multicomponent mass transfer in the gas phase. For the membrane compartment, the Maxwell-Stefan equations are used to model the multicomponent diffusion of organic compound and water vapours through a stagnant film of gas. For simplification, coupling effects between VOCs and water are neglected. Therefore, the mass transfer through the membrane, N_T, is described as follows [69]:

$$N_T = B_{Mi} c_M \ln \frac{N_i/N_T - y_{Pi}}{N_i/N_T - y_{Fi}} \tag{148}$$

where B_{Mi} is the mass transfer coefficient of the i-th component in the membrane, c_M is the total molar concentration, y_{Fi} is the molar fraction of the i-th component in the gas phase at the feed-membrane interface, y_{Pi} is the molar fraction of the i-th component in the gas phase at the permeate-membrane interface.

For the feed and permeate channels, the mass transfer is described analogously [69]:

$$N_{TF} = B_{Fi} c_F \ln \frac{N_{Fi}/N_{TF} - x_{FMi}}{N_{Fi}/N_{TF} - x_{Fi}} \tag{149}$$

$$N_{TP} = B_{Pi} c_P \ln \frac{N_{Pi}/N_{TP} - y_{Pi}}{N_{Pi}/N_{TP} - y_{PMi}} \tag{150}$$

where B_{Fi} and B_{Pi} are the mass transfer coefficients of the i-th component in the feed and permeate channels, respectively, c_F and c_P are the total feed and permeate concentrations,

respectively, x_{Fi} are x_{FMi} is the molar fractions of the i-th component in the feed liquid in the bulk and at the feed-membrane interface, respectively, y_{Pi} are y_{PMi} is the molar fractions of the i-th component in the sweeping gas in the bulk and at the permeate-membrane interface, respectively.

The heat balance is described by the following equation [69]:

$$h_F(T_F - T_{FM}) = \sum_i N_i \Delta H_{vap,i} + h_M(T_{FM} - T_P) \tag{151}$$

where h_M is the membrane heat transfer coefficient calculated as follows:

$$h_M = \frac{1}{h_{MC}} + \frac{1}{h_{MV}} \tag{152}$$

The Boi's model is based on AEs which have a low mathematical complexity, low computational burden and macroscopic degree of physical detailing. As the results of the simulation, the Boi's model produces the discrete lumped parameters for steady-state operation (Fig. 1.18). The simulation process requires the heat transfer coefficients which can be found from the empirical correlations or conducted experiments. The Boi's model can be applied for basic process design and control for specific cases with known empirical correlations or conduction of experiments.

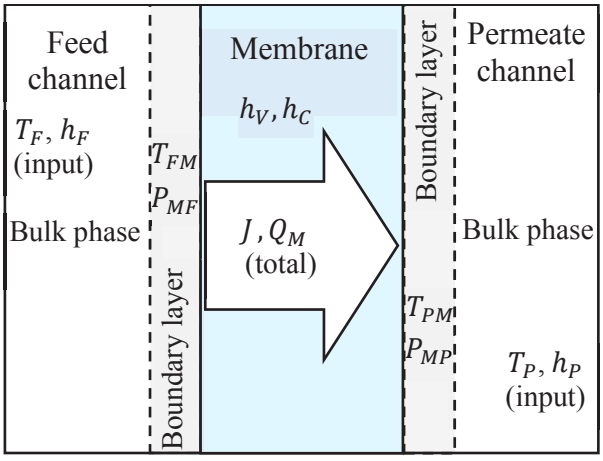

Figure 1.18: Schematic representation of calculated variables in the Boi's model.

1.1.9.4 Mourgues's model

Mourgues *et al.* in their works [76, 77] presented the heat and mass transfer model for the case of water solution based on the following assumptions:

- Steady state operation.
- Ideal gas behaviour.
- The total pressure is constant in the whole gas compartment and across the membrane.
- The properties of the membrane are perfectly homogeneous.
- No boundary layer in feed channel is present for the mass transfer due to the use of pure water as the feed liquid.
- Air solubility in the feed liquid is negligible.
- The feed-membrane interface is at thermodynamic equilibrium.

The mass balances for the feed and permeate sides are described as follows [76, 77]:

$$\frac{d\dot{m}_{FW}}{dz} = -J_W l_F \tag{153}$$

$$\frac{d\omega_{PW}}{dz} = -\frac{J_W l_F}{\dot{m}_{SG}} \tag{154}$$

$$\dot{m}_{hSG} = (1 + \omega_{PW})\dot{m}_{SG} \tag{155}$$

$$y_W = \frac{\omega_W (M_{SG}/M_W)}{1 + \omega_W (M_{SG}/M_W)} \tag{156}$$

Where J_W is the transmembrane vapour flux, z is the spatial coordinate, l_F is the width of the membrane, ω_{PW} is the humidity of the sweeping gas, $\dot{m}_{SG}$ is the mass flow rate of the dry sweeping gas, $\dot{m}_{hSG}$ is the mass flow rate of the humid sweeping gas, y_W is the molar fraction of the water vapour in the permeate, M_{SG} is the molar mass of the sweeping gas, M_W is the water molar mass.

The resistances-in-series model is used to describe the mass transfer in the SGMD module. For this model, the global mass transfer coefficient and transmembrane vapour flux are calculated from the following equations [76, 77]:

$$B_T = \left(\frac{1}{B_{FM}} + \frac{1}{B_M}\right)^{-1} \tag{157}$$

$$J_W = k_T (P_{Wsat} - p_{WP}) \tag{158}$$

where B_{FM} and B_M are the mass transfer coefficients for the boundary layer and membrane, respectively, P_{Wsat} is the saturated water vapour pressure at the feed side, p_{WP} is the partial pressure of the water vapour at the permeate side.

For the mass transfer through the membrane, the molecular diffusion has been chosen as the main mass transport mechanism. The molar transmembrane water vapour flux, N_W, is calculated from the following equation [76, 77]:

$$N_W = -c_M D_{VA}^{eff} \frac{\partial y_W}{\partial x} + y_W (J_W + J_A) \tag{159}$$

Due to low solubility of air in water, it is assumed that no air flux inside the pores is presented. Therefore, Eq. 159 is transformed into

$$N_W = -\frac{c_M D_{VA}^{eff}}{(1 - y_W)} \frac{dy_W}{dx} \tag{160}$$

where D_{VA}^{eff} is the effective ordinary diffusion coefficient.

The continuity equation is applied for the mass transfer through the membrane pores [76, 77].

$$-\frac{dN_W}{dx} = 0 \tag{161}$$

After merging with Eq. 160, the continuity equation takes the following form:

$$-\frac{d}{dx}\left(-\frac{c_M D_{VA}^{eff}}{(1 - y_W)} \frac{dy_W}{dx}\right) = 0 \tag{162}$$

The following set of BCs for Eq. is applied [76, 77]:

$$\begin{cases} x = 0 : y_W = \dfrac{P_{Wsat}}{P_M} \\ x = \delta_M : y_W = \dfrac{P_W}{P_M} \end{cases} \tag{163}$$

where P_{Wsat} is the water vapour saturation pressure.

The partial pressure of water vapour at the feed-membrane interface is the saturated vapour pressure which is calculated by the Antoine equation while the effective water vapour-air diffusion coefficient, D_{VA}^{eff}, is calculated as follows [76, 77]:

$$D_{VA}^{eff} = \frac{\varepsilon_M}{\tau_M} D_{VA} = \frac{\varepsilon_M}{\tau_M} \frac{2.634}{P_M} \left(\frac{T_M}{273.15} \right)^{3/2} \tag{164}$$

where D_{VA} is the ordinary diffusion coefficient.

The mass transfer of the water vapour in the permeate channel, J_W, is:

$$J_W = B_{PM}(P_{W_{PM}} - P_{W_P}) \tag{165}$$

The mass transfer coefficient in the boundary layer for the permeate channel is found from the calculation of the Sherwood number using an appropriate correlation [76, 77]:

$$B_{PM} = \frac{ShD_{VA}\rho_P}{P_P d_{PH}} \tag{166}$$

where ρ_P is the density of the permeate, d_{PH} is the hydraulic diameter of the permeate channel, Sh is the Sherwood number.

$$Sh = 1.62 \left(\frac{v_P d_{PH}^2}{L_M D_{VA}} \right)^{1/3} \tag{167}$$

where L_M is the length of the membrane.

The density of the air-water vapour mixture is determined from the following correlation [76, 77]:

$$\rho_P = \frac{P_M\big((1 - y_{WPM})M_A + y_{WPM}M_W\big)}{R_g T_{PM}} \tag{168}$$

The energy balance equation for the feed-membrane interface is

$$Q_F^{conv} = Q_{vap} + Q_M^{cond} \tag{169}$$

$$h_W(T_F - T_{FM}) = J_W \Delta H_{vap} + \frac{k_M^{eff}}{\delta_M}(T_{FM} - T_{PM}) \tag{170}$$

where Q_{vap} is the heat flux by vaporization, Q_M^{cond} is the heat flux by conduction.

For the permeate-membrane interface, the energy balance is described as follows [76, 77]:

$$Q_M^{conv} = Q_P^{cond} \tag{171}$$

$$\frac{\lambda_M^{eff}}{\delta_M}(T_{FM} - T_{PM}) = h_P(T_{PM} - T_P) \tag{172}$$

where λ_M^{eff} is the effective thermal conductivity of the membrane, h_P is the permeate heat transfer coefficient.

The heat transfer coefficient of the feed flow is calculated as follows [76, 77]:

$$h_F = \frac{Nu\lambda_F}{d_{FH}} \tag{173}$$

where Nu is the Nusselt number, λ_F is the thermal conductivity of the feed, d_{FH} is the hydraulic diameter of the feed channel.

For the spacer-filled feed channel, the heat transfer coefficient is

$$h_{FF} = \left(\frac{1}{h_F} + \frac{\delta_{FF}}{\lambda_F^{eff}}\right)^{-1} \tag{174}$$

where δ_{FF} is the thickness of the spacer, λ_F^{eff} is the effective thermal conductivity of the feed.

The heat transfer in the feed channel along the membrane is given by the following equation:

$$\frac{dq_F}{dz} = -\left(Q_F^{conv} + Q_F^{liq}\right)l_M \tag{175}$$

$$\begin{aligned}\frac{dT_F}{dz} = \frac{1}{\dot{m}_F C_{PF}}\Big[&-h_F(T_F - T_{FM})l_F - J_W C_{PF}\left(T_{FM} - T_{ref}\right)l_M \\ &- C_{PF}\left(T_F - T_{ref}\right)\frac{d\dot{m}_F}{dz}\Big]\end{aligned} \tag{176}$$

where q_F is the feed heat flow.

The energy balance in the permeate channel is

$$\frac{dq_P}{dz} = -\left(Q_P^{conv} + Q_P^{vap}\right) l_P \tag{177}$$

$$\frac{dT_P}{dz} = \frac{1}{\dot{m}_P C_{PP}} \Big[h_P (T_{PM} - T_P) l_P + J_W C_{PP} \left(T_{PM} - T_{ref}\right) l_P - C_{PP} \left(T_F - T_{ref}\right) \frac{d\dot{m}_P}{dz} \Big] \tag{178}$$

where q_P is the permeate heat flow.

The Mourgues' model uses 1D ODEs for the calculation of the heat and mass transfer within the SGMD model. For the feed and permeate domains, the 1D ODEs describe the heat and mass transfer for z coordinate along the SGMD module while, for the membrane domain, the 1D ODEs describe the heat and mass transfer across the membrane on x coordinate (Fig. 1.19). Therefore, the Mourgues' model is represented by a 2D plate and the mathematical complexity of the model is average. The model predicts the temperatures of the bulk and boundary layers in the feed and permeate channels and gives the distribution of the temperature and concentration in the membrane. However, the model uses the empirical correlations to describe the type of the feed or permeate flow and geometry of the membrane and membrane unit. Also, the model does not produce the full profiles of the velocities, concentrations and temperatures within the membrane module.

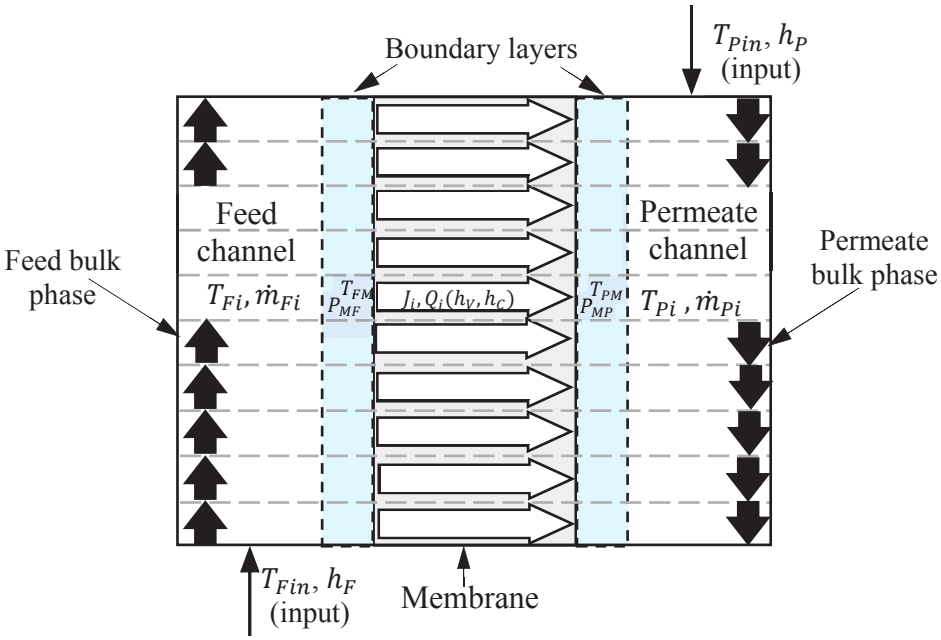

Figure 1.19: Schematic representation of calculated variables in the Mourgues' model.

1.1.9.5 Charfi's model

Charfi *et al.* in their work [103] presented the CFD model for SGMD. This CFD model considers the following assumptions:

1. Dynamic regime.
2. Laminar incompressible flow.
3. Constant physical properties of the fluids.
4. Darcy-Brinkman-Forchheimer formulation in the momentum equation for the vapour transfer inside the porous media.

The momentum, mass and heat transfer in the feed and permeate domains is described as follows [103]:

$$\nabla \vec{v}_z = 0 \tag{179}$$

$$\frac{\partial \vec{v}_z}{\partial \tau} + \vec{v}_z \nabla \vec{v}_z = -\frac{1}{\rho_{zin}} \nabla P_z + \vec{v}_z \nabla^2 \vec{v}_z + \frac{\rho_z}{\rho_{zin}} \vec{g} \tag{180}$$

$$\frac{\partial c_z}{\partial \tau} + \vec{v}_z \nabla c_z = D_z \nabla^2 c_z \tag{181}$$

$$\frac{\partial T_z}{\partial \tau} + \vec{v}_z \nabla T_z = D_{Tz} \nabla^2 T_z \tag{182}$$

where $\vec{v}_z$ is the fluid velocity, τ is the time, ρ_{zin} is the inlet fluid density, ρ_z is the fluid density, $\vec{g}$ is the gravitational constant, c_z is the concentration, D_z is the thermal diffusion coefficient, T_z is the temperature.

The following equations describe the momentum (coupled with the continuity equation), mass and heat transfer within the membrane [103]:

$$\nabla \vec{v}_M = 0 \tag{183}$$

$$\frac{1}{\varepsilon_M} \frac{\partial \vec{v}_M}{\partial \tau} + \frac{1}{\varepsilon_M^2} \vec{v}_M \nabla \vec{v}_M = -\frac{1}{\rho_M} \nabla P_M - \frac{\vec{v}_M}{\Pi} \vec{v}_M + \frac{\vec{v}_M}{\varepsilon_M} \nabla^2 \vec{v}_M - \frac{F_{SM} |\vec{v}_M| \vec{v}_M}{\Pi^{1/2}} + \frac{\rho_M}{\rho_{M0}} \vec{g} \tag{184}$$

$$\varepsilon_M \frac{\partial c_W}{\partial \tau} + \vec{v}_M \nabla c_W = D_M^{eff} \nabla^2 c_W \tag{185}$$

$$D_M^{eff} = \frac{\varepsilon_M}{\tau_M}\left(\frac{1}{D_K} + \frac{1}{D_{VA}}\right) \tag{186}$$

$$\xi_M \frac{\partial T_M}{\partial \tau} + \vec{v}_M \nabla T_M = \frac{k_M^{eff}}{\rho_M C_{PM}} \nabla^2 T_z \tag{187}$$

$$\xi_M = \varepsilon_M + (1 - \varepsilon_M)\frac{\rho_S C_{PS}}{\rho_M C_{PM}} \tag{188}$$

where $\vec{v}_M$ is the velocity of the vapour inside the membrane pores, ε_M is the membrane porosity, ρ_M is the gas density, P_M is the gas pressure, Π is the permeability, F_{SM} is the Forchheimer coefficient, ρ_{M0} is the inlet gas density, D_M^{eff} is the effective ordinary diffusion coefficient, c_W is the molar concentration of the water vapour, ξ_M is the ratio of the specific effective heat between the solid membrane and the water vapour, D_K is the Knudsen diffusion coefficient, D_{VA} is the ordinary diffusion coefficient.

Eqs. 179-186 are transformed in the following forms to use dimensionless variables. Therefore, for the feed channel, the momentum, mass and heat balances take the following form [103]:

$$\frac{\partial^2 \psi}{\partial y^2} + \frac{\partial^2 \psi}{\left(\frac{L_M}{d_F}\right)^2 \partial y^2} = \omega \tag{189}$$

$$\frac{\partial \omega}{\partial \tau} + \frac{\partial v\omega}{\partial x} + \frac{\partial\, \vec{v}\omega}{\left(\frac{L_M}{d_F}\right) \partial y} = \frac{\frac{\partial^2 \omega}{\partial x^2} + \frac{\partial^2 \omega}{\left(\frac{L_M}{d_F}\right)^2 \partial y^2}}{Re_z} - Ri_z^T \left(\frac{\partial T}{\partial x} - N_F \frac{\partial c}{\partial x}\right) \tag{190}$$

$$\frac{\partial c}{\partial \tau} + \frac{\partial \vec{v} c}{\partial x} + \frac{\partial \vec{v} c}{\frac{L_M}{d_F} \partial y} = \frac{\frac{\partial^2 c}{\partial x^2} + \frac{\partial^2 c}{\left(\frac{L_M}{d_F}\right)^2 \partial y^2}}{Re_z Sc_z} \tag{191}$$

$$\frac{\partial T_z}{\partial \tau} + \frac{\partial \vec{v} T_z}{\partial \tau} + \frac{\partial \vec{v} T}{\frac{L_M}{d_F}\partial y} = \frac{\frac{\partial^2 T}{\partial x^2} + \frac{\partial^2 T}{\left(\frac{L_M}{d_F}\right)^2 \partial y^2}}{Re_z Pr_z} \tag{192}$$

where ψ is the dimensionless stream function, ω is the vorticity, L_M is the length of the membrane module, d_F is the thickness of the feed channel.

The momentum, mass and heat balances for the permeate balance take the following form [103]:

$$\frac{\partial^2 \psi}{\partial y^2} + \frac{\partial^2 \psi}{\left(\frac{L_M}{d_P}\right)^2 \partial y^2} = \omega \tag{193}$$

$$\frac{\partial \omega}{\partial \tau} + R_v \frac{d_F}{d_P}\left(\frac{\partial v\omega}{\partial x} + \frac{\partial\, v\omega}{\left(\frac{L_M}{d_P}\right)\partial y}\right) = \frac{R_v \left(\frac{d_F}{d_P}\right)^2 \left(\frac{\partial^2 \omega}{\partial x^2} + \frac{\partial^2 \omega}{\left(\frac{L_M}{d_F}\right)^2 \partial y^2}\right)}{Re_z} - R_v \left(\frac{d_F}{d_P}\right) Ri_z^T \left(\frac{\partial T}{\partial x} - N_P \frac{\partial c}{\partial x}\right) \tag{194}$$

$$\frac{\partial c}{\partial \tau} + \left(\frac{d_F}{d_P}\right)\left(\frac{\partial \vec{v} c}{\partial x} + \frac{\partial \vec{v} c}{\frac{L_M}{d_P}\partial y}\right) = \frac{R_v \left(\frac{d_F}{d_P}\right)^2 \left(\frac{\partial^2 c}{\partial x^2} + \frac{\partial^2 c}{\left(\frac{L_M}{d_P}\right)^2 \partial y^2}\right)}{Re_z Sc_z} \tag{195}$$

$$\frac{\partial T_z}{\partial \tau} + R_v \left(\frac{d_F}{d_P}\right)\left(\frac{\partial \vec{v} T_z}{\partial \tau} + \frac{\partial \vec{v} T}{\frac{L_M}{d_P}\partial y}\right) = \frac{R_v \left(\frac{d_F}{d_P}\right)^2 \left(\frac{\partial^2 T}{\partial x^2} + \frac{\partial^2 T}{\left(\frac{L_M}{d_P}\right)^2 \partial y^2}\right)}{Re_z Pr_z} \tag{196}$$

where d_P is the thickness of the permeate channel, R_v is the aspect ratio of the velocity between the feed and permeate.

For the membrane domain, the dimensionless equations are:

$$\frac{\partial^2\psi}{\partial y^2}+\frac{\partial^2\psi}{\left(\frac{L_M}{d_P}\right)^2\partial y^2}=\omega \tag{197}$$

$$\frac{1}{\varepsilon_M}\frac{\partial\omega}{\partial\tau}+\frac{\frac{d_F}{\delta_M}}{\varepsilon_M^2}\left(\frac{\partial\vec{v}\omega}{\partial x}+\frac{\partial\vec{v}\omega}{\left(\frac{L_M}{\delta_M}\right)\partial y}\right) = -\frac{\omega\frac{d_F}{\delta_M}}{Re_F Da}+\frac{\vec{v}_{vp}\left(\frac{d_F}{\delta_M}\right)^2}{\vec{v}\varepsilon_M Re_F}\frac{R_v\left(\frac{d_F}{d_P}\right)^2}{Re_z}\left(\frac{\partial^2\omega}{\partial x^2}+\frac{\partial^2\omega}{\left(\frac{L_M}{\delta_M}\right)^2\partial y^2}\right)-\frac{\left(\frac{d_F}{\delta_M}\right)F_S}{Da^{1/2}}\left(\frac{\partial\vec{v}|\vec{v}|}{\partial x}-\frac{\partial\vec{v}|\vec{v}|}{\frac{L_M}{\delta_M}\partial y}\right) \tag{198}$$

$$\frac{\partial c}{\partial\tau}+\left(\frac{d_F}{\delta_M}\right)\left(\frac{\partial\vec{v}c}{\partial x}+\frac{\partial\vec{v}c}{\frac{L_M}{\delta_M}\partial y}\right)=\frac{D_M^{eff}}{D_F^T}\frac{\left(\frac{d_F}{\delta_M}\right)^2\left(\frac{\partial^2 c}{\partial x^2}+\frac{\partial^2 c}{\left(\frac{L_M}{\delta_M}\right)^2\partial y^2}\right)}{Re_z Sc_z} \tag{199}$$

$$\xi_M\frac{\partial T_z}{\partial\tau}+\frac{d_F}{\delta_M}\left(\frac{\partial\vec{v}T_z}{\partial\tau}+\frac{\partial\vec{v}T}{\frac{L_F}{\delta_M}\partial y}\right)=\frac{D_{vp}^T}{D_F^T}\frac{R_{k_{eff}}\left(\frac{d_F}{\delta_M}\right)^2\left(\frac{\partial^2 T}{\partial x^2}+\frac{\partial^2 T}{\left(\frac{L_M}{\delta_M}\right)^2\partial y^2}\right)}{Re_z Pr_z} \tag{200}$$

The following BCs are defined [103]:

1. Vertical feed inlet.

$$\begin{cases}\omega_F=0\\ u_F=6\left(\frac{x}{d_F}-\left(\frac{x}{d_F}\right)^2\right)\\ c_1=c_W=1-c_{salt}\\ T_1=1\\ \psi(x,j=1)=\int v_1(x_i)dx=\psi(i,j=1)\,;i=1,inm\end{cases} \tag{201}$$

where inm is the inlet side of the membrane.

2. Vertical feed outlet.

$$\begin{cases} v_F = 0 \\ \omega = 0 \\ \psi(i, j = NY) = \psi(i, j = NY - 1); i = 1, inm - 1 \end{cases} \quad (202)$$

3. Vertical permeate inlet.

$$\begin{cases} \omega_P = 0 \\ u_P = 6\left(\frac{x}{d_P} - \left(\frac{x}{d_P}\right)^2\right) \\ c_2 = 1 - c_{0,vp} \\ T_2 = 0 \\ \psi(x, j = NY) = \int v_2(x_i)dx = \psi(i, j = NY)\,; i = 1, inm \end{cases} \quad (203)$$

4. Vertical permeate outlet.

$$\begin{cases} v_P = 0 \\ \omega = 0 \\ \psi(i, j = 1) = \psi(i, j = 2); i = outm + 1, NX \end{cases} \quad (204)$$

where $outm$ is the outlet side of the membrane.

5. Feed wall, permeate wall, membrane walls.

$$\begin{cases} v = 0 \\ \omega(i,j) = \frac{12}{h_{st}}\left(\psi(i, j-1) + \psi(i,j)\right) + \frac{6}{h_{st}}\left[\left(\frac{\partial\psi(i,j-1)}{\partial n}\right) + \left(\frac{\partial\psi(i,j)}{\partial n}\right)\right] + \left(\frac{\partial^2\psi(i,j)}{\partial n^2}\right) \\ \frac{\partial T(i=1,j)}{\partial x} = \frac{\partial c(i=1,j)}{\partial x} = 0, j = 1, NY \\ \frac{\partial T(i=NX,j)}{\partial x} = \frac{\partial c(i=NX,j)}{\partial x} = 0, j = 1, NY \\ \frac{\partial T(i=1,j)}{\partial y} = \frac{\partial c(i=1,j)}{\partial y} = 0 = inm, outm \\ \frac{\partial T(i,j=NY)}{\partial y} = \frac{\partial c(i,j=NY)}{\partial y} = 0 = inm, outm \end{cases} \quad (205)$$

where h_{st} is the space step.

The CFD approach, which allows to use continuous distributed variables, reduces the dependence of the model on the empirical or experimental data and increases the level of physical description. Indeed, the velocity, concentration and temperature distributions in the SGMD module are calculated (Fig. 1.20). The mentioned qualities of the CFD model make it suitable for the process design and the module optimization. Nevertheless, the model presented

by Charfi *et al.* has some significant drawbacks: the use of the model is limited to the specific case where the feed and permeate fluids are binary mixtures; the effect of the concentration of SG on the effective diffusion coefficient is not included; the model takes into account transport of only a single component through the membrane; SG is presented as an incompressible flow; the momentum balance is determined only for the laminar flow; different compartments (feed channel, permeate channel and membrane) are combined in one domain. In addition, internal boundary conditions (BCs) responsible for the momentum, heat and mass transfer from the feed side to the membrane media and from the membrane media to the permeate side are not defined clearly. This last drawback is especially important because these BCs define the driving force of the process, evaporation rate of the volatile components into the membrane pores, concentration of the sweeping gas at the feed-membrane and permeate-membrane interfaces, heat transfer between phases and, therefore, the flow rate of the target components through the membrane and then, the performance of the process.

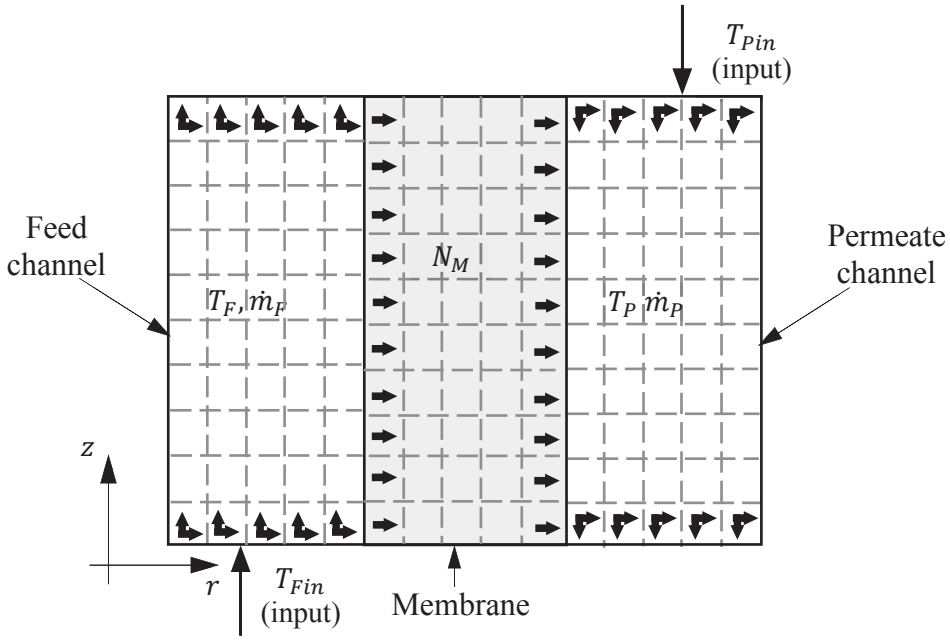

Figure 1.20: Schematic representation of calculated variables in the Charfi's model.

1.1.9.6 Response surface SGMD model

Another model offered by Khayet *et al.* [104] is based on the RS method which is already described in Section 1.1.8.9. In this model, the transmembrane vapour flux is chosen as the response objective while the permeate inlet temperature and velocity, feed inlet

temperature and velocity are taken as influencing factors. The vapour flux in the model is calculated as follows [104]:

$$J = b_0 + b_1 T_{Fin} + b_2 T_{Pin} + b_3 v_{Fin} + b_4 v_{Pin} + b_{2,2} T_{Pin}^2 + b_{1,3} T_{Fin} v_{Fin} + b_{1,4} T_{Fin} v_{Pin} + b_{2,4} T_{Pin} v_{Pin} + b_{3,4} v_{Fin} v_{Pin} \quad (206)$$

where b_0, b_1, b_2, b_3, b_4, $b_{2,2}$, $b_{1.3}$, $b_{1,4}$, $b_{2,4}$, $b_{3,4}$ are the regression coefficients, T_{Fin} is the feed inlet temperature, v_{Fin} is the feed inlet velocity, v_{Pin} is the permeate inlet velocity, T_{Pin} is the permeate inlet temperature.

In the RS model, the SGMD module is presented as the "black box" without physical determination between studied operating parameters and corresponding values of the transmembrane flux. Instead of this, dependencies between input variables and output results are described empirically based on conducted experiments (Fig. 1.21). The model studies the experimental data (e.g. inlet temperatures and velocities of the flows and corresponding transmembrane water vapour fluxes) and then gives the predictive values of the transmembrane flux for the given parameters. Therefore, the RS model is fully empirical model which can be applied only for analysis and optimization of the performance of the already existing SGMD module in the range of experimental values.

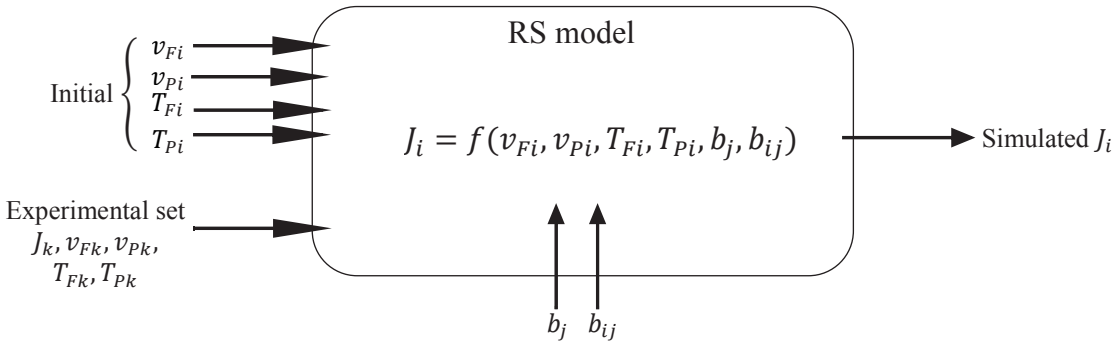

Figure 1.21: Schematic representation of the RS model.

1.1.9.7 Artificial neural network

An artificial neural network (ANN) model, which applies series of experimental results, was proposed by Khayet and Cojocaru [105]. The ANN model is an adaptive system which changes the structure under the influence of external or internal information which passes through the neural network in learning phase. ANN consists of artificial processors, or neurons, which are interconnected between each other and process input data. The neurons perform two

basic functions: a summing junction operator and transfer function. The summing junction operator summarizes weights and bias into an argument A_i. The transfer function converts the net argument into a scalar output value as it is shown on Fig. 1.22.

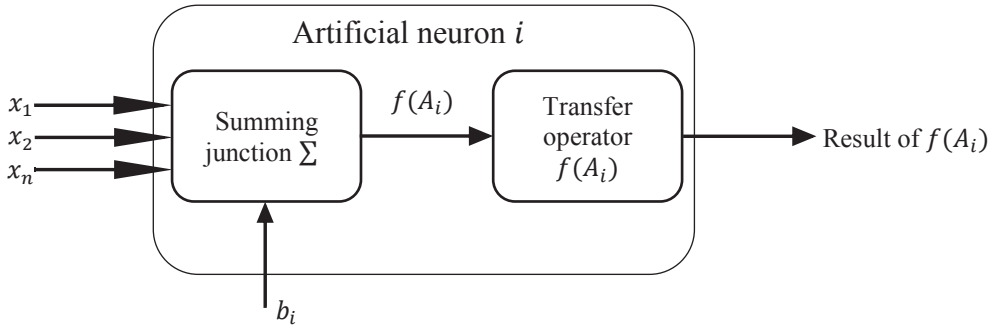

Figure 1.22: Schematic representation of the ANN model.

In the training mode of the ANN model, the weights and biases of each neuron are optimized to minimize the residual error between outputs of the model and experimental data. The back-propagation algorithm is used as the training algorithm. The mean-squared-error (MSE) is used as the optimization parameter:

$$MSE = \frac{1}{N_{exp}} \sum_{q=1}^{Nexp} \left(J_q^{exp} - J_q^{sim}\right)^2 \tag{207}$$

where N_{exp} is the number of experimental data points, J_q^{exp} is the experimental transmembrane flux, J_q^{sim} is the predicted transmembrane flux.

The weights and biases are:

$$w_{ij}^{k+1} = w_{ij}^k - \eta \frac{\partial E^k}{\partial w_{ij}^k} \tag{208}$$

$$b_i^{k+1} = w_i^k - \eta \frac{\partial E^k}{\partial b_{ij}^k} \tag{209}$$

where E is the error function (could be MSE), η is the learning rate, k is the integer index indicating the iteration in learning phase.

As in the case with the RSM model, the ANN model is fully empirical model which requires a large amount of experimental data to learn and then to predict the performance of the SGMD module. The RSM model does not study the process but analyses the dependence

between input and output variables. Therefore, the ANN model represents SGMD as a black box. Such models are suitable for already projected and working SGMD models to correct and optimize the operating conditions.

1.1.9.8 Comparison of the existing models

The comparison of the SGMD mathematical models, which are described in Section 1.1.9, is given in Table 1.6. This comparison is carried out according to the following parameters: the use of empirical correlations or experimental data, type of applied equations (PDEs, ODEs, AEs or their combination), type of variables and parameters, degree of physical detailing, type of geometric configurations of SGMD in simulations.

In contrast to the mathematical models of DCMD, first ones of which appeared in 1980s, first mathematical models of SGMD appeared later, in the end of 1990s, and the number of the publications dedicated to the modelling of the SGMD process is low. SGMD, which requires large amounts of SG, external condenser and related costs, is the least studied membrane distillation (MD) configuration [51]. According to Essalhi and Khayet [106], at the end of 2013, only 4.6% of publications related to MD were dedicated to SGMD, and, to the best of our knowledge, this trend continues until today. It is worth mentioning that most of the publications about the SGMD modelling have been published by Khayet's group [100-105]. In particular, the first Khayet's model, proposed in 2000 [100, 101], is based on systems of PDEs with distributed continuous parameters for the feed and permeate channels and system of AEs with lumped discrete parameters for the membrane media. Despite the good characterization of the feed and permeate channels, the first Khayet's model requires the empirical heat transfer coefficients for the heat balance through the membrane and temperatures of the feed and permeate fluids at the outlets.

In 2003, Khayet *et al.* proposed the second SGMD model [102]. Indeed, the second Khayet's model is the result of simplification of the first model with application of AEs for all SGMD domains. In contrast to the previous work, this model works with lumped discrete variables of the velocities, concentrations and temperatures of the fluids which are operated in the SGMD module. That simplification reduces the mathematical complexity and computational burden, but, in this case, the model is better for application for the optimization and parametric study of the existing membrane module with known empirical correlations for heat transfer coefficients.

The model proposed by Boi *et al.* in 2005 [69] has the same level of mathematical complexity as the second Khayet's using AEs to describe the mass and heat transfer within the SGMD module. However, the Boi's model describes the transmembrane mass transport with the help of the empirical correlations. Moreover, the model requires experimental data with pure water for further calculations of the mass transfer coefficients. Therefore, the Boi's model simply describes and simulates the SGMD process with the need of the experimental and empirical data. The model can be applied for optimization and prediction of the SGMD module which is already in use.

Mourgues *et al.* in their work [76] proposed another approach of the SGMD modelling. In this work, 1D ODEs are used to describe the heat and mass transfer in direction from the feed side to the permeate side (across the membrane). At the same time, for the enthalpy and mass balances in the feed and permeate side, 1D ODEs are applied in the direction from the inlet to the outlet of the corresponding compartments (along the membrane). So, the mass and heat fluxes for the feed/permeate channel and membrane media are characterized by distributed continuous variables in planes perpendicular to each other. The transmembrane mass flux is described by the molecular diffusion and viscous flow without effect of the Knudsen diffusion. As all the previous models, the Mourgues' model requires the empirical heat transfer coefficients. The model can be used for the optimization and prediction of SGMD modules.

In 2010, Charfi, Khayet and Safi proposed a SGMD model which is based on the CFD approach [103]. In the Charfi's model, the momentum, mass and heat balances for the feed flow, sweeping gas and membrane media are described by PDEs with distributed continuous parameters. The transmembrane vapour flux is characterized by DGM for the binary mixture of gases (air and water vapour). The model allows to obtain the full velocity, concentration and temperature profiles of the SGMD module. With the CFD approach, the Charfi's model can be applied not only for the optimization of the SGMD module but for process design because of the mesoscopic-microscopic level of physical detailing. However, the main problem of the model application is the absence of the boundary conditions for equations to characterize the process phenomena at the feed-membrane and permeate-membrane interfaces. Without full determination of these boundary conditions, the equations of the model could not be solved.

Apart from the description of the physical phenomena in SGMD, the RSM model [104] and the ANN model [105] offer to study the mathematical relationship between the input parameters and the output parameters such as the feed and permeate outlet temperatures and transmembrane vapour flux. These models are strongly experimental-dependent. That means

that the models require initial experimental data for the educational process, the first step, in which the relationship between the input and output parameters is made. Then, the models can be applied for prediction and optimization of the SGMD modules, which data were used in the study.

The models listed in Section 1.1.9 have the following disadvantages or their combinations: fitting the parameters and empirical correlations, oversimplification or absence of description of the physical phenomena in simulation. To eliminate these serious drawbacks, in this thesis, a new general predictive model for the SGMD process is proposed. This model (Section 2.1) is independent on experimental data and allows obtaining detailed velocity, concentration and temperature profiles extending the knowledge of the process. The model consists of the momentum, mass and heat balances which take the form of systems of the PDEs, ODE and AEs for the individual domains of the SGMD module (feed side, permeate side and membrane). For these systems of equations, all the boundary conditions, that characterize the inlets and outlets of the process unit, walls and feed-membrane and permeate-membrane interfaces, are defined. The model is suitable for both flat sheet and hollow fibre configurations and can be used for different SGMD applications. The multicomponent fluids with laminar, transient and turbulent flows are taken into account at feed and permeate compartments. Moreover, DGM is used for description of mass transfer trough the porous membrane [84, 85]. The solving procedure is done in COMSOL Multiphysics™ software which uses the principle of the finite element method. The model is validated by experimental data which are in good agreement with the predicted results. The influence of the process parameters and process conditions on the SGMD performance is inspected.

Table 1.6: Comparison of different models for SGMD.

Model	Type of variables	Use of empirical data	Type of equations	Possibility of segmentation	Described balances	Type of operation	Geometry	Ref.
First Khayet's model	Lumped discrete (Membrane), Distributed continuous (Feed, Permeate)	Yes	Integral overall (membrane), 2D PDE (feed, permeate)	Yes	Mass and heat (membrane domain)	Steady-state	Flat sheet	[100, 101]
Second Khayet's model	Lumped discrete	Yes	Integral overall	No	Mass and heat (membrane)	Steady-state	Flat sheet, hollow fibre (by using appropriate coordinates)	[102]
Boi's model	Lumped discrete	Yes	Integral overall	No	Mass and heat (membrane)	Steady-state	Flat sheet, hollow fibre (by using appropriate coordinates)	[69]
Mourgues's model	Distributed continuous	Yes	1D ODE (feed, permeate)	Yes	mass and heat	Steady-state	Flat sheet	[76, 77]
Charfi's model	Distributed continuous	No	2D PDE	Yes	Momentum, mass and heat	Dynamic	Flat sheet	[103]
Response surface model	Lumped discrete	Yes	AE (to describe relationship between input and output)	No	-	Steady State	FS, HF	[104]
Artificial neural network	Lumped discrete	Yes	AE (to describe relationship between input and output)	No	-	Steady State	FS, HF	[105]

1.2 Anaerobic membrane bioreactors

1.2.1 Introduction to anaerobic membrane bioreactors

The anaerobic membrane bioreactor (AnMBR) involves a complex process which combines membrane separation technology with anaerobic biological processes for water treatment. The biological processes in AnMBRs that occur inside the reactor tank are presented by the treatment of sludge by microorganisms. After the anaerobic digestion, the treated sludge is undergoing a solid-liquid membrane separation with production of high-quality effluent at the permeate side of the membranes, while biomass at high concentration is retained at the feed side. Indeed, the anaerobic treatment is accompanied by the production of the methane-rich biogas which can be utilized as a source of energy [107, 108].

In comparison with the conventional activated sludge process (CAS), where separation of the sludge is carried out by gravity separation coupled with sand filtration and disinfection, the MBR can produce effluent, or permeate, of the best quality and purity. The good results of filtration are obtained due to membrane resistance to solids, adsorbed compounds, bacteria and viruses. Moreover, the possibility of the process to treat mixtures of higher mixed-liquor suspended solid (MLSS) concentrations allows to reduce the number of sedimentation tanks on the plant [109]. AnMBRs have one significant drawback which is the membrane fouling. The cake formation at the surface of the membranes in AnMBR leads to membrane fouling and seriously reduces the efficiency of the process. However, the decrease of this drawback is of great interest and many studies showing a successful fouling control have been published recently [8, 9, 109, 136].

1.2.2 AnMBR configurations

Several possible configurations depending on the position of membrane modules in the AnMBR are applied in industry. The first one is submerged configuration which assumes immersion of the membrane module in the feed, or influent, flow. In this configuration, the transmembrane flux is caused by vacuum pumps or gravitational forces. The submerged AnMBRs are accomplished by fouling preventing tools like a recirculation of the biogas through the feed flow or stirrers at the bottom of the reactor tank because of the high risk of the fouling. The submerged AnMBRs can be used in two configurations: with the membrane

module immersed inside the feed tank (Fig. 1.23(a)) or immersed inside an external filtration tank (Fig. 1.23(b)) [107, 108].

In the second AnMBR configuration which is called side-stream, the membrane module of tubular form is located outside of the feed tank (Fig. 1.24). Because the activated sludge is flowing though the tubular membranes, the tube clogging and membrane fouling must be constantly checked by pumping the MLSS through the membrane module and using an anti-clogging system in the feed tank. The presence of the pump between the feed tank and membrane module and the anti-clogging system increases energy demands and decreases the attractiveness of the side-stream configuration [107, 108]. For normal operation, the side-stream AnMBRs require anti-fouling and anti-clogging devices not only for the reaction tank but for membrane module. The use of this additional equipment increases the energy demand in comparison with the submerged systems and makes the side-stream configuration less attractive. Cornel and Krause [114] estimated the energy consumption at 3 kWh/m^3 for the side-stream AnMBRs against 0.4 for the submerged AnMBRs.

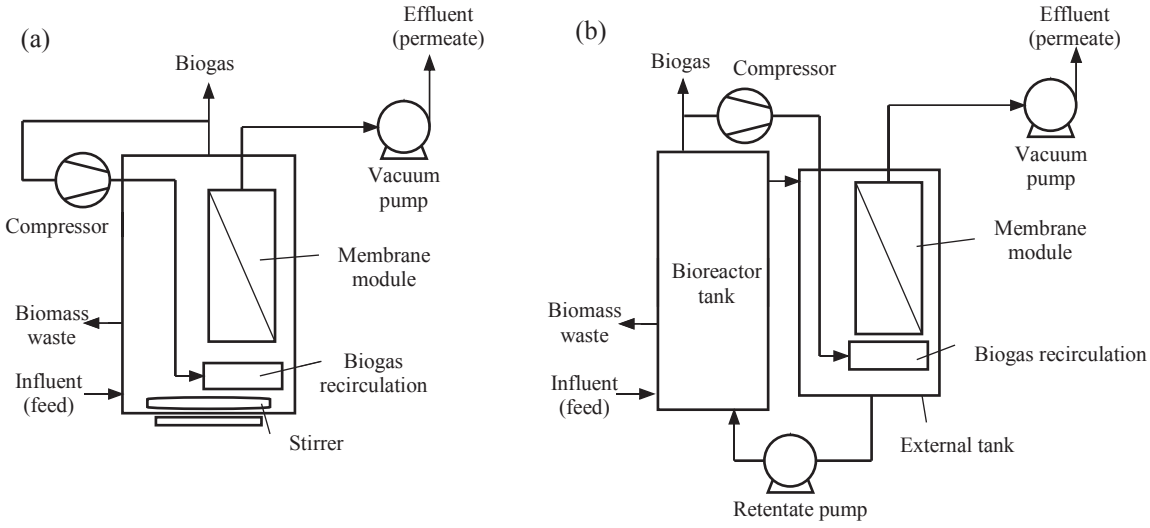

Figure 1.23: Submerged AnMBR configuration with (a) the membrane module immersed inside the feed tank and (b) the membrane module immersed inside an external filtration tank.

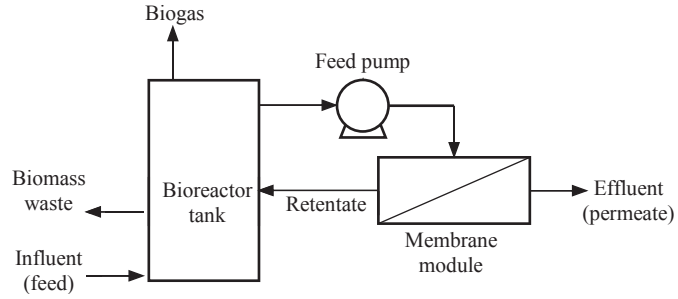

Figure 1.24: Side-stream AnMBR configuration.

1.2.3 Membrane materials

The AnMBR process requires porous membranes with excellent mechanical strength and physical and chemical resistance due to work in harsh conditions [114]. Apart from the mentioned characteristics, the membranes must possess narrow pore size distribution, high permeability and fouling resistance. Polymeric and ceramic membranes satisfy the given criteria. The ceramic membranes are too expensive for industrial production while the polymeric membranes which have a reasonable price are in use in AnMBRs in various configurations. Membranes used in the AnMBR processes usually consist of one or two layers. The one-layer membranes are self-supported and perm-selective while the two-layer membranes require these properties only for a surface layer which is in direct contact to the activated sludge and the second layer, support, must be mechanically strong. The comparison of the various membrane materials involved in the AnMBR process is given in Table 1.7.

Table 1.7. Membrane materials and membrane modules applied in AnMBRs.

Membrane material	Module configuration	Influent source	Reference
Chlorinated PE	Flat sheet	Molasses	[115]
PVDF	Tubular	Dairy manufacture	[116]
PVDF	Hollow fibre	Bamboo industry	[117]
Polyetherimide	Hollow fibre	Food industry	[118]
Polyester	Flat sheet	Municipal wastewater	[119]
PP	Hollow fibre	Acidified wastewater	[120]
Ceramic	Tubular	Volatile fatty acid mixture	[121]
Metal	Tubular	Municipal sewage	[122]

1.2.4 Membrane module configurations

Membrane configurations applied in the process should possess the following characteristics [114]:

- high membrane surface area to provide a good packing density;

- possibility to permit turbulent regime of the feed flow to increase mixing and prevent fouling;
- mechanical and chemical stability;
- ease of cleaning;
- low pressure drop, or transmembrane pressure (TMP);
- low energy consumption and operating costs;
- possibility of parsing and cleaning;
- possibility of changing the number of membranes and their replacement (modularization).

Despite the various possible membrane configurations, only three types indicated in Table 1.7 could be applied in the AnMBR process. First of them is the flat sheet configuration in which only one membrane is presented in the module or membranes of the module are not connected in stack. The flat sheet module possesses the low packing density but is easy to clean and replace. The module configuration with flat membranes organized in stack is named plate-and-frame. The interstitial distance the flat sheet and plate-and-frame configurations are determined by the channel width or the distance between the membranes in stack, respectively. The membranes of the flat sheet/plate-and-frame modules are easily cleaned by dismantling. Turbulence can be promoted by installing an additional equipment in the feed channel. In the plate-and-frame configuration, the packing density is higher than in the flat sheet, however too high value can reduce the interstitial gap and cause the clogging of the AnMBR module.

Tubular configuration (TC) can also be used in the AnMBR process. The TC module consists of numerous tubes packed inside tubular cartridge. In this configuration, the feed stream is operated at the lumen side of the membranes and the interstitial distance is defined by the diameter of the tubular membrane. The flow turbulence in the feed channels is easily promoted. Also, the TC modules have good cleaning performance and can be cleaned by back flushing. However, the small diameter of the tubular membranes leads to clogging at the feed side and small packing density increases the energy consumption of the module and decreases the performance per the area of the membrane.

The hollow fibre configuration is also possible in the AnMBR technology. In this configuration, the activated sludge is operated at the shell side of the membranes and the interstitial distance is determined by the distance between the hollow fibres in the module. The hollow fibre modules have a good cleaning performance by back flushing and high packing density, however, as in the case with the flat sheet/plate-and-frame configuration, too high

packing density increases the risk of clogging by decreasing the interstitial distance and hampers the turbulence promotion [107, 108].

1.2.5 Membrane fouling

The main drawback of application of AnMBRs in water and wastewater treatment is the membrane fouling which is characterized by reduction of the transmembrane flux or increase in TMP. Various types of foulants can block the membrane pores: colloidal, biological, organic and mineral [109, 123, 124].

There are three main groups of the factors which can be highlighted: biomass (feed) flow characteristics, membrane and membrane module characteristics and operating conditions. The feed flow characteristics include the MLSS composition, size of solid particles in the sludge, its viscosity and hydrophobicity. The membrane characteristics which affect the fouling are the size and shape of membrane pores, chemical and physical properties of the surface of the membrane as well as the geometry and size of the membrane and membrane module. Among the operating conditions, the feed flow rate, relaxation time and intervals of cleaning effect on the membrane fouling [109, 123, 124].

The membrane fouling is reversible if the membrane surface can be cleaned physically. The irreversible fouling can be removed only by chemical cleaning. Physical cleaning of the membranes in the AnMBR process can be operated by backflushing, biogas recirculation or other mechanical tools. Chemical cleaning of the membrane can be carried out by mineral acids, organic acids, caustic soda or sodium hypochlorite in situ or ex situ. The combination of physical and chemical cleaning is also possible by backflushing the membrane with a low concentrated solution of cleaning agent. Physical cleaning is preferable because it is faster than chemical cleaning, operated without chemical waste and less likely to enhance membrane degradation. However, chemical cleaning is a more effective process. Also exists biological cleaning which is used to remove microorganisms with biocides [109, 123, 124].

Apart from the cleaning procedure, the membrane fouling could be sufficiently reduced by introduction of mechanical devices into the AnMBR unit. One of such devices is the tank stirrer which creates turbulence and enhances mixing [107, 108, 109]. Another interesting approach is to use micro-channel turbulence promoters (MCTPs). MCTPs [136, 137] create turbulence directly near the membrane surface and, therefore, inhibit the cake formation. In addition to the mentioned techniques, the induced membrane vibration system (MMV) [8, 9]

could be used. MMV creates vibrations of the membranes immersed in the AnMBR tank. Therefore, the enhanced liquid mixing and the fouling prevention are achieved. All of the mentioned approaches were successfully tested in lab-scale units and strongly recommended for the use [8, 9, 109, 136].

1.2.6 AnMBR process operating conditions

The operating conditions of the AnMBR process include: hydraulic retention time, solids retention time, temperature, hydrodynamic conditions and cross-flow velocity (for the external configuration). The hydraulic retention, or residence, time (HRT) is a time which the influent remains in the AnMBR tank. HRT can be calculated as follows [109]:

$$HRT = \frac{V_{AnMBR}}{\dot{V}_F} \tag{210}$$

where V_{AnMBR} is the volume of the AnMBR tank, $\dot{V}_F$ is the flow rate of the influent.

The solids retention time (SRT) indicates the time that the solute components of the influent remain in the system. SRT affects both the membrane fouling and AnMBR performance. However, the relationship between SRT and AnMBR performance is complex and not fully studied yet. HRT can be increased for improving the removal of pollutant but for a limited value. The values of SRT are ranged from 20 to 300 days while HRT is varied from 2 h to 20 days [109].

The temperature of the process strongly influences the removal of chemical oxygen demand (COD). Most of the AnMBRs are operated at temperatures varied in range from 20 to 37 °C. Anaerobic digestion taking place inside the AnMBR can be grouped by the applied range of temperatures: psychrophilic (0-20 °C), mesophilic (20-37 °C) and thermophilic (42-75 °C) [107]. The choice of the temperature of the process is determined by the type of bacteria in the bioreactor and applied influent.

1.2.7 AnMBR applications

AnMBRs have been applied since the past decade for the industrial wastewater treatment. In particular, the treatment of dairy wastewater, ethanol stillage, salad dressing, municipal wastewater and palm oil mill effluent have been successfully operated by full-scale

AnMBRs [107]. As can be seen in Table 1.7, lab-scale and pilot-scale AnMBRs have been applied for the treatment of the wastewaters from the production of molasses, bamboo industry, municipal sewage and volatile fatty acid mixtures.

1.2.8 Existing AnMBR models

1.2.8.1 Arros-Alileche's model

The model presented in 2008 by Arros-Alileche and colleagues [125] has a simple structure and operates overall AnMBR characteristics. This model is based on mass balances for the whole AnMBR tank and allows calculation of the solute degradation rate and SRT, The solute degradation rate is defined as the function of the concentration and activity of biomass [125]:

$$\frac{dS}{d\tau} = q_s X = \frac{S_f - S}{HRT} \tag{211}$$

where S_f is the solute concentration in the feed, τ is the time, S is the solute concentration in the reactor, q_s is the specific activity of active biomass, X is the concentration of active biomass.

SRT is calculated from the mass balance [125]:

$$SRT = \frac{SV}{Q_P S_P + Q_S S} = \frac{HRT}{1 - R} \tag{212}$$

where Q_P is the permeate flow, Q_S is the sludge withdrawal, S_P is the solute concentration in the permeate, V is the reactor volume, R is the solute membrane retention.

The solute concentration in the reactor after time τ is defined from the following equation [125]:

$$S(\tau) = \left(S_0 + \frac{S_F SRT}{HRT}\right) e^{-\frac{\tau}{SolRT}} + \frac{S_F SRT}{HRT} \tag{213}$$

where S_0 is the solute concentration inside the reactor at $\tau = 0$.

The substrate mass balance according to degradation of organic compounds by biomass in the reactor is defined as follows [125]:

$$\frac{dS}{d\tau} = \frac{S_F}{HRT} - \frac{S}{HRT}(1-R) - \frac{SR}{SRT} - r_S = OLR - \frac{S}{HRT}(1-R) - \frac{SR}{SRT} - r_S \quad (214)$$

where r_S is the rate of substrate degradation, OLR is the volume organic loading rate.

The biomass mass balance is:

$$\frac{dX}{d\tau} = r_X - \frac{X}{SRT} \quad (215)$$

where r_X is the rate of biomass growth.

The Arros-Alileche's model is easy in use, however, it operates only the basic terms of AnMBRs and does not take into account the geometric parameters of the membrane, configuration of AnMBR or configuration of the membrane module. This model also does not simulate the increase in membrane fouling, growth of biomass and its activity. By calculating only SRT and mass balances, the model is suitable for initial estimation of the process and not for process design and detailed optimization.

1.2.8.2 Jeong's Response surface model

Jeong *et al.* in their paper proposed the model based on the RS methodology [126]. In this model, HRT and the substrate concentration are used as the input independent variables. As the target output response of this model, the increase in the concentration of the volatile fatty acids (VFA) is assumed. The predicted response is calculated from the predictive polynomial quadratic equation [126]:

$$Y = b_0 + \sum_i b_i X_i + \sum_i b_{ii} X_i^2 + \sum_i \sum_j b_{ij} X_{ij} \quad (216)$$

where Y is the predicted response, X_i and X_j are the independent input variables, b_0, b_i, b_{ii} and b_{ij} are the coefficients of the equation.

The RS model is simple due to low complexity of applied equations and consideration of the AnMBR unit as the "black box" (Fig. 1.25). This model needs the initial set of experiments to determine the coefficients described in Eq. (216). However, the RS model is only empirically-based and is suitable for optimization of the operating parameters of the existing AnMBR unit which is used for producing of the initial set of experiments.

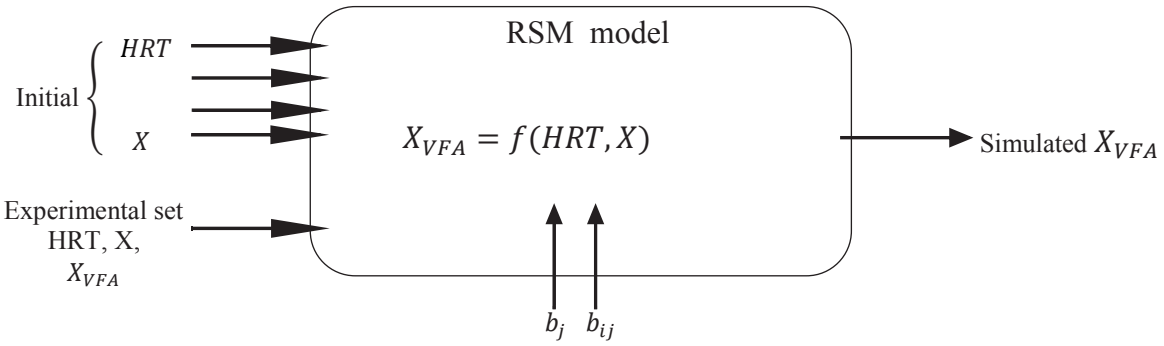

Figure 1.25: Schematic representation of the mathematical structure of the RS model.

1.2.8.3 AM2b model

The AM2b model proposed by Benyahia and colleagues describes bioreactions inside the tank of the side-stream AnMBRs [127]. In this model, the following assumptions are considered [127]:

1. The AnMBR reaction medium is considered homogeneous.
2. The substrates with molecules smaller than the membrane pore diameter go through the external membrane without retention.
3. The membrane is able of total retention of biomass and solids.
4. Decay rate of biomasses is taken into account.
5. The biomass withdrawal is considered.
6. Soluble microbial products (SMP) are grouped into a single variable of concentration with only a considered fraction leaving the reactor. The remainder is retained by the membrane.

In the AM2b model, anaerobic digestion is simulated in two steps. The first step is acidogenesis and SMP production (with reaction rate $r_1 = \mu_1 X_1$) [127]:

$$k_1 S_1 \xrightarrow{r_1} X_1 + k_2 S_2 + b_3 S + k_4 CO_2 \tag{217}$$

where k_1 is the yield of degradation of organic matter by acidogenic bacteria (AB), S_1 is the concentration of organic matter, X_1 is the concentration of AB, k_2 is the yield of production of methanogenic bacteria (MB) from organic matter, S_2 is the concentration of VFA, k_4 is the yield of production of CO_2 from organic matter, S is the concentration of SMP, b_3 is the yield of SMP production from organic matter.

The second step is the methanogenesis and SMP production with the reaction rate $r_2 = \mu_2 X_2$ [127]:

$$k_3 S_2 \xrightarrow{r_2} X_2 + b_4 S + k_5 CO_2 + k_6 CH_4 \quad (218)$$

where k_3 is the yield of degradation of VFA by MB, X_2 is the concentration of MB, k_5 is the yield of CO_2 from VFA, k_6 is the yield of CH_4 production from VFA, b_4 is the yield of SMP production from MB.

Methanogenesis is accomplished by the production of SMP from biomasses and SMP degradation. The degradation of SMP with the reaction rate $r = \mu X_1$ is described as follows [127]:

$$b_1 S \xrightarrow{r} X_1 + b_2 S_2 + k_7 CO_2 \quad (219)$$

where b_1 is the yield of SMP degradation by AB, b_2 is the yield of VFA production from SMP, k_7 is the yield of CO_2 production from SMP degradation.

The SMP production from biomass decay is determined by the following equations [127]:

$$D_0 X_1 \rightarrow D_0 S, D_0 X_2 \rightarrow D_0 S \quad (220)$$

where D_0 is the biomass decay rate.

On the base of the described reactions (Eqs. (217)-(220)), mentioned assumptions and the law of the conservation of matter, the equations of the AM2b model are described as follows [127]:

$$\frac{dS_1}{d\tau} = D(S_{1in} - S_1) - k_1 \mu_1(S_1) X_1, \quad (221)$$

$$\frac{dX_1}{d\tau} = (\mu_1(S_1) - \mu(S) - D_0 - D_1) X_1, \quad (222)$$

$$\frac{dS_2}{d\tau} = D(S_{2in} - S_2) - k_3 \mu_2(S_2) X_2 + \big(k_2 \mu_1(S_1) + b_2 \mu(S)\big) X_1, \quad (223)$$

$$\frac{dX_2}{d\tau} = (\mu_2(S_2) - D_0 - D_1) X_2, \quad (224)$$

$$\frac{dS}{d\tau} = \big(b_3 \mu_1(S_1) + D_0 - b_1 \mu(S)\big) X_1 + (b_4 \mu_2(S_2) + D_0) X_2 - MS, \quad (225)$$

$$M = (\beta D + (1 - \beta)D_1) \tag{226}$$

where D is the dilution rate, D_1 is the biomass withdrawal, μ_1, μ_2 and μ are the acidogenesis rate, methanogenesis rate and SMP degradation kinetics, respectively, M is the model constant.

The reaction rates of acidogenesis, methanogenesis and SMP degradation are assumed to be dependent on the concentrations of organic matter, VFA and SMP. Also, the quantity of the produced biomass (or products) is assumed to be always smaller than the quantity of substrate consumed [127]:

$$k_3 \geq 1 + b_4 \tag{227}$$

$$b_1 \geq 1 + b_2 \tag{228}$$

The quantity of VFA produced from organic matter is considered higher than the quantity produced from SMP [127]:

$$k_2 > b_2 \tag{229}$$

Eqs. (221)-(226) are solved for the equilibrium conditions [127]:

$$0 = D(S_{1in} - S_1) - k_1\mu_1(S_1)X_1, \tag{230}$$

$$0 = (\mu_1(S_1) - \mu(S) - D_0 - D_1)X_1, \tag{231}$$

$$0 = D(S_{2in} - S_2) - k_3\mu_2(S_2)X_2 + \big(k_2\mu_1(S_1) + b_2\mu(S)\big)X_1, \tag{232}$$

$$0 = (\mu_2(S_2) - D_0 - D_1)X_2, \tag{233}$$

$$0 = \big(b_3\mu_1(S_1) + D_0 - b_1\mu(S)\big)X_1 + (b_4\mu_2(S_2) + D_0)X_2 - MS, \tag{234}$$

The AM2b model describes only biochemical processes that occur in the bioreactor media of the AnMBR unit without considering the filtration part, fluid dynamics and geometric characteristics of the unit. Extension of the AM2b model by a model of hydrodynamics allows application in process design and control of AnMBRs.

1.2.8.4 Charfi's AnMBR model

Charfi *et al.* proposed the model [112] which is, in fact, the AM2b model extended by a fouling model with the side-stream AnMBR configuration assumed in simulations. In the Charfi's AnMBR model, the biological part of the model is the same as the AM2b model. This biological model is coupled with the separation model responsible for the simulation of membrane fouling. The two major foulant groups are considered: the total suspended solids (TSS) and SMP. In the Charfi's AnMBR model, the layer formed by totally rejected TSS and partially rejected SMP during cake formation is described as follows [112]:

$$X_{TSS} = X_1 + X_2 \tag{235}$$

where X_1 is the acidogens concentration, X_2 is the methanogens concentration.

The cake formation is assumed to occur in two steps simultaneously with the filtration. The first step is the cake baseline forming on the base of deposition of TSS. The second step is the SMP introduction in the cake pores and further decrease in the cake porosity [112]:

$$\frac{dm_C}{d\tau} = Q_{out} X_{TSS}(1 - \beta m_C) \tag{236}$$

$$\frac{d\varepsilon_C}{d\tau} = -k_\varepsilon \frac{Q_{out}}{A_M} \sigma S \frac{\varepsilon_C}{\varepsilon_C + n} \tag{237}$$

where m_C is the cake mass, Q_{out} is the permeate flowrate, β is the shear parameter. k_ε is the coefficient of the deposit porosity decrease, A_M is the membrane surface area, σ is the SMP fraction retained by the membrane, S is the SMP concentration.

The increase in cake resistance is expressed by the Kozeny-Carman equation [112]:

$$\alpha = \frac{180(1 - \varepsilon_C)}{\rho_C d^2 \varepsilon_C^3} \tag{238}$$

where α is the specific cake resistance, d is the cake particle diameter, ρ_C is the cake density.

The theoretical TMP is calculated using the resistance in series model [112]:

$$TMP = \mu(R_0 + R_C)\frac{Q_{out}}{A_M} \tag{239}$$

where μ is the permeate viscosity, R_0 is the intrinsic membrane resistance, R_C is the deposit resistance.

The deposit resistance is calculated as follows [112]:

$$R_C = \alpha m_c \tag{240}$$

where m_C is the deposit mass.

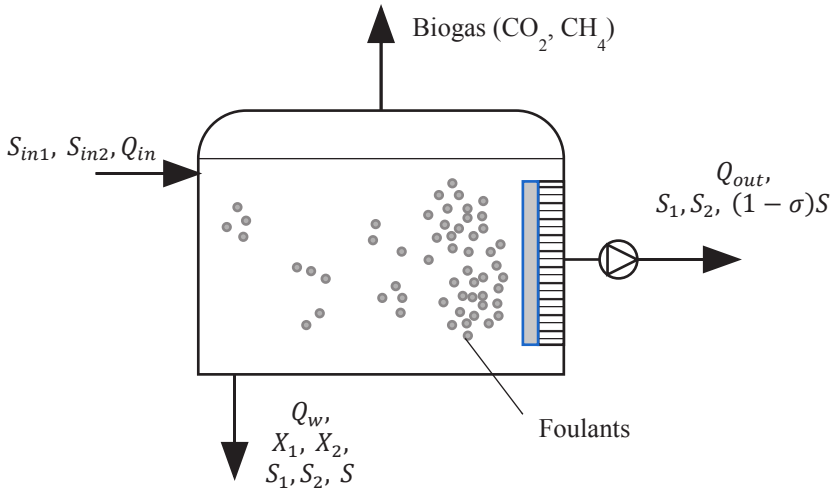

Figure 1.26: Schematic representation of the Charfi's AnMBR model.

The schematic representation of the Charfi's AnMBR model is shown in Fig. 1.26. The model is suitable for optimization of the membrane filtration and biological processes, however, it is not suitable for the process design and does not simulate the hydrodynamic processes taking place inside the AnMBR unit.

1.2.8.5 Charfi's model for particle-sparged AnMBR with fluidized polyethylene terephthalate beads

Another model proposed by Charfi *et al.* [128] simulates the work of the particle-sparged AnMBR with fluidized polyethylene terephthalate beads (AFMBR). As in case with the Charfi's AnMBR model, the AFMBR model is based on combination of the biological AM2b model and the fouling model but for the submerged configuration of AnMBR. In this case, the AM2b model is similar to the AnMBR model. The fouling model simulates also the membrane cleaning procedure with the cleaned area expressed as follows [128]:

$$\frac{dA_B}{d\tau} = A_M \delta_{PB} \frac{Q_{out}}{A_0} \sigma S = -\frac{dA_F}{d\tau} = -\gamma A_M \quad (241)$$

where A_M is the total membrane area, δ_{PB} is the pore blocking parameter, Q_{out} is the permeate flow rate, σ is the SMP fraction rejected by the membrane A_0 is the initial membrane open area, A_F is the free membrane area, γ is the pore blocking mitigation parameter.

TMP is expressed by the following equation [128]:

$$TMP = \frac{\mu_P (R_0 + R_C) Q_{out}}{A_M} \quad (242)$$

where R_0 is the intrinsic membrane resistance, μ_P is the permeate viscosity, R_C is the deposit resistance defined by Eq. (240).

The mass balance of the cake is described as follows [128]:

$$\frac{dm_C}{d\tau} = \frac{dm_{att}}{d\tau} - \frac{dm_{det}}{d\tau} \quad (243)$$

where m_C, m_{det} and m_{att} are the deposit mass, the specific cake mass detached from the membrane and the specific cake mass attached to the membrane, respectively.

The mass balance for the specific cake mass attached to the membrane can be written as follows:

$$\frac{dm_{att}}{d\tau} = \frac{Q_{out}}{A_0} (X_{VSS} + \sigma S) \quad (244)$$

where X_{VSS} is the total solids concentration, S is the SMP concentration, A_0 is the total membrane area.

The mass balance of the specific cake mass detached from the membrane is described by the following equation [128]:

$$\frac{dm_{det}}{d\tau} = \frac{dm_{att}}{d\tau} \frac{m_c}{m_{c.lim}} = \frac{dm_{att}}{d\tau} \beta m_c \quad (245)$$

Where $m_{c.lim}$ is the specific cake mass reached at steady state, β is the cake migration parameter.

The specific cake mass reached at steady state is assumed to be inversely proportional to the cake migration parameter as follows:

$$\beta = \frac{1}{m_{c,lim}} \tag{246}$$

The specific cake resistance, α (Eq. 240), is assumed to be proportional to TMP [128]:

$$\alpha = \alpha_0 TMP_c^n \tag{247}$$

where α_0 is the initial cake resistance, TMP_c is the transmembrane pressure due to the cake formation, n is the cake compressibility.

In fact, the Charfi's model for particle-sparged AnMBR with fluidized polyethylene terephthalate beads is the same model described in Section 1.2.8.4 but with modifications which take into account the presence of the beads in the bioreactor. The model can be applied in the membrane filtration optimization and analysis.

1.2.8.6 Boyle-Gotla hydrodynamic model

Boyle-Gotla *et al.* [129] in 2014 proposed a 3D hydrodynamic model for submerged AnMBRs equipped with the sparging unit. In this model, the Euler-Euler CFD approach was used in combination with the fouling model [131] proposed by Li and Wang. The model assumes the sludge mixture as a homogenous single liquid phase while sparging nitrogen is taken as the gas phase. The Bingham model combined with the Arrhenius relationship is applied to describe the sludge rheology for the total solids concentrations between 1.2 and 22.3 g/L [129]:

$$\mu_T = \mu_{22}\theta^{(T-22)} = 0.001e^{0.04c_S} \tag{248}$$

where c_S is the total solids concentration in the sludge, θ is the temperature correction coefficient, μ_{22} is the sludge viscosity at 22 °C, T is the sludge temperature.

In the Euler-Euler hydrodynamic model, the k-epsilon model [130] is applied to characterize fluid turbulence. Default values of the constants for the k-epsilon model are applied.

The Boyle-Gotla's model also includes the fouling model [131] and accounts the cake accumulation and increase in TMP. Thus, cake accumulation rate is described as follows:

$$\left(\frac{dm_{Cake}}{d\tau}\right)_{ij} = \left(\frac{24c_s J^2}{24J + K_l G_{int}}\right)_{ij} - \left(\frac{\beta(1-\alpha)G_{int}m_{Cake}^2}{\gamma V_F \theta_F + m_{Cake}}\right)_{ij} \quad (249)$$

where m_{Cake} is the cake mass, J is the transmembrane flux, K_l is the lift concentration, G_{int} is the shear intensity, β erosion rate coefficient, γ is the compression coefficient, α is the stickiness coefficient, V_F is the filtrate volume, θ_F is the filtration period in a cycle.

The resistance to flow created by the accumulated cake layer at each membrane section is:

$$R_{C,ij} = r_{c,ij} m_{Cake} \quad (250)$$

where $r_{c,ij}$ is the specific cake resistance.

The overall resistance to flow is the sum of inherent membrane resistance and cake layer resistance [129]:

$$R_{ij} = R_M + R_{C,ij} \quad (251)$$

where R_M is the primary contributor to total resistance at low flux.

Darcy's law is applied for the description of the transmembrane flux [129]:

$$J_{ij} = \frac{P}{\mu R_{ij}} \quad (252)$$

where P is the transmembrane pressure, μ is the dynamic viscosity of the sludge.

The specific cake resistance for a compressible material is:

$$r_c = r_{c0}\left(1 + \frac{P}{P_a}\right)^c \quad (253)$$

where r_{c0} is the initial specific cake resistance, P_a is the compressibility parameter, c is the compressibility coefficient.

The Boyle-Gotla model applies a complex system of equations to describe hydrodynamics of the liquid and gas flows inside the AnMBR tank. Moreover, in simulations,

this model also takes into account the formation of the cake at the membrane surface. The model is well described and could be applied for the simulations of the AnMBR units.

1.2.8.7 Trad's model

Trad *et al.* [132] proposed a hydrodynamic AnMBRs model which combines 1D and 3D modelling approaches for simulation of the side-stream AnMBR configuration with the stirred tank. In this model, the k-epsilon Navier-Stokes model (Eqs. (273)-(278)) is used to describe the turbulent flow of the incompressible fluid.

Additionally, a tracer transport equation is applied for mixing [132]:

$$\frac{\partial c_i}{\partial \tau} + \nabla(c_i \vec{v}) = \nabla \cdot (D_{Turb} \nabla c_i) + R_i \tag{254}$$

where c_i is the concentration of the component i, τ is the time, v is the velocity, D_{Turb} is the turbulent diffusion coefficient, R_i is the mass source term (equals 0 without chemical reactions or interfacial mass transfer).

The following BCs are applied:

- no-slip conditions at the walls of the tank;
- the gas-liquid interface is defined as a solid wall with allowed slip.

For modelling of the rotating flows driven by impellers, the moving frame of reference approach [135] is applied in the model. In this approach, the cut-cell technique is used to define the grid with Cartesian coordinates and the impeller's moves are not affecting the grid.

To describe the interactions of the liquid and gas phases, the volume of fluid (VOF) method combined with the algebraic slip model (ASM) are applied. The VOF method determines the location of two immiscible phases and simulates the transport of the volume fraction of the gas phase but with a single-fluid approach applied for the calculation of the velocity. In the calculations, the average material properties are determined [132]:

$$\alpha_L + \alpha_G = 1 \tag{255}$$

$$\rho_{avg} = \alpha_L \rho_L + \alpha_G \rho_G \tag{256}$$

$$\mu_{avg} = \alpha_L \mu_L + \alpha_G \mu_G \tag{257}$$

where α_L and α_G are the volume fractions of the liquid phase and gas phase, respectively, ρ_{avg} is the averaged density, ρ_L is the liquid density, ρ_G is the gas density, μ_{avg} is the averaged dynamic viscosity, μ_L and μ_G are the dynamic viscosities of the liquid and gas, respectively.

The continuity equation for the gas phase is:

$$\frac{\partial \alpha_G}{\partial \tau} + \nabla \cdot (\alpha_G \vec{v}) = 0 \tag{258}$$

The dispersive mixing of a solid phase in the stirred tank is simulated by the use of the ASM. Thus, the relative velocity between the liquid and solid phases is expressed without solving the momentum equation of the dispersed phase due to a local mechanical equilibrium between the phases [132]:

$$\rho \vec{v} = \sum \alpha_i \rho_i \vec{v}_i \tag{259}$$

where α_i, ρ_i and $\vec{v}_i$ are the volume fraction, density and velocity of the phase i.

The Trad's model accurately simulates hydrodynamics of the AnMBR unit coupled with the stirrer. With the use of VOF, the Trad's model simulates not only the flow of the liquid but the flow of the gas formed inside the AnMBR tank.

1.2.8.8 Xie's model

Xie *et al.* [136, 137] proposed a 2D CFD model for the submerged AnMBRs equipped with micro-channel turbulence promoters (MCTPs). This model is based on the Euler multiphase and the k-epsilon Navier-Stokes models. The motion of each phase is described by the corresponding momentum transfer equation coupled with the continuity equation [137]:

$$\frac{\partial (\rho_G \alpha_G \vec{v}_G)}{\partial \tau} + \nabla \cdot (\rho_G \alpha_G \vec{v}_G \cdot \vec{v}_G) = -\alpha_G \nabla P + \nabla\left(\alpha_G \mu_G (\nabla \vec{v}_G + (\nabla \vec{v}_G)^T)\right) + \rho_G \alpha_G \vec{g} - M_{I,G} \tag{260}$$

$$\frac{\partial (\rho_L \alpha_L \vec{v}_L)}{\partial \tau} + \nabla \cdot (\rho_L \alpha_L \vec{v}_L \cdot \vec{v}_L) = -\alpha_L \nabla P + \nabla\left(\alpha_L \mu_L (\nabla \vec{v}_L + (\nabla \vec{v}_L)^T)\right) + \rho_L \alpha_L \vec{g} + M_{I,L} \tag{261}$$

$$\frac{\partial(\rho_S \alpha_S \vec{v}_S)}{\partial \tau} + \nabla \cdot (\rho_S \alpha_S \vec{v}_S \cdot \vec{v}_S) = -\alpha_S \nabla P - \nabla P_S + \nabla\left(\alpha_S \mu_S (\nabla \vec{v}_S + (\nabla \vec{v}_S)^T)\right) + \rho_S \alpha_S \vec{g} - M_{I,S} \quad (262)$$

$$\frac{\partial(\rho_i \alpha_i)}{\partial \tau} + \nabla \cdot (\rho_i \alpha_i \vec{v}_i) = 0 \quad (263)$$

where ρ_i is the density of the phase i, τ is the time, $\vec{v}_i$ is the velocity of the phase i, μ_i is the dynamic viscosity of the phase μ_i, α_i is the volume fraction of the phase i, g is the universal gas constant, subscripts G, L and S indicate gas, liquid and solid phases, respectively.

The sum of volume fractions of each phase (liquid, gas and solid) is equal to 1 in all of the points of AnMBR [137]:

$$\alpha_L + \alpha_G + \alpha_S = 1 \quad (264)$$

where α_L, α_G and α_S are the volume fractions of the liquid, gas and solid phases, respectively.

With the help of the described equations, Xie *et al.* simulated the work of a submerged AnMBR with MCTPs in dynamics and steady state. The transmembrane flux and membrane fouling resistance are calculated according to Darcy's law [137]:

$$J = \frac{1}{A_M}\frac{dV}{d\tau} = \frac{\Delta P}{\mu R_T} = \frac{\Delta P}{\mu(R_M + R_B + R_C)} \quad (265)$$

where A_M is the membrane area, V is the volume of the filtrate, τ is the filtration time, R_T is the total resistance, μ is the dynamic viscosity, R_M is the intrinsic resistance of the new membrane, R_B is the pore blockage resistance, R_C is the cake layer resistance.

The Xie's model uses the same approach applied in the Trad's model (Section 1.2.8.7) in the simulation of hydrodynamics inside the AnMBR tank. However, in addition to the gas and liquid phases, the Xie's model accounts also the solid phase formed inside the tank. While the Trad's model simulates rotation of the stirrer, the Xie's model takes into account the work of MCTPs to prevent membrane fouling.

1.2.8.9 Conclusions on the literature review

The mathematical models for AnMBRs presented in the literature can be divided in the following groups: biological models, fouling models, hydrodynamic models and experimentally-based models. The RS model [126] is a typical experimentally-based model

which requires a set of experimental data for the study process in which the dependencies between input and output data are defined. Then, the model could be applied for prediction of the target output (represented by the concentration of VFA). Due to full dependence of the model on the experimental data, its application is strictly limited to performance optimization of existing AnMBRs.

The biological models simulate chemical and biochemical processes occurring in an AnMBR tank without considering filtration and hydrodynamic processes. As an example, the AM2b model describes the following chemical and biological reactions: acidogenesis, methanogenesis and the formation and degradation of SMP [127]. With the help of the biological models, it is possible to predict and control the chemical processes and concentrations of components and bacteria located inside the AnMBR tank.

Apart from the biological models, the fouling models allow simulating the formation of cakes which hinders the membrane filtration process and causes the TMP increase. The Arros-Alileche's model [125], the Charfi's models [112, 128] and the model proposed by Li and Wang [131] belong to this category. These models calculate the material balance of the solid components participating on the cake formation. After the calculation of the cake mass, the resistance to the transmembrane flow and the TMP value are estimated. It is worth mentioning that the fouling models can be applied alone [125] or in cooperation with biological models [112, 128] or with CFD models [129].

The last group of the models describes hydrodynamics of the feed flow inside AnMBRs. These models simulate flows of the fluids and solids inside the AnMBR tank, describe interfaces between the phases and predict velocity, pressure and concentration profiles. The Boyle-Gotla's model applies the Euler-Euler method combined with the k-epsilon Navier-Stokes model to describe the gas sparging through the feed flow [129]. The Trad's model [132] uses the VOF method coupled with the k-epsilon Navier-Stokes model to describe dynamics of the gas and liquid flows in the side-stream AnMBR reactor equipped with the stirrer which rotations are simulated by the ASM model [132]. The 2D Xie's model [137] makes possible the simulation of the simultaneous flows of the liquid phase, gas phase and solids in the influent with the help of the Euler multiphase model combined with the k-epsilon Navier-Stokes model.

For a more complex study of the AnMBR process, the hydrodynamic models are accompanied by the fouling models. Thus, the Boyle-Gotla's model [129] is coupled with the

model proposed by Li and Wang [131] to calculate the material balance in the cake formation and estimate TMP. To describe the mass transfer of the influent components in the Trad's model [132], the advection-diffusion equation (Eq. (254)) is applied. In the Xie's model [137], the fouling process is not simulated, however, the resistance to the transmembrane flux is estimated from the Darcy's law (Eq. (265)).

The existing CFD models for AnMBRs are applied with the fouling model and not with the biological models. In the models, the fluid flow in all points of the AnMBR domain is assumed to be turbulent due to stirrer rotations, sparging or MCTPs. The MMV system in AnMBRs has not been simulated before and only experimental studies are present [8, 9, 133, 134].

2 Theoretical description

This theoretical section describes the models developed in this work for the following processes: DCMD, SGMD and AnMBRs equipped with the MMV system. The general predictive models for DCMD and SGMD describe the momentum, mass and heat transfer in all domains of the membrane module. The models for DCMD and SGMD are presented together in Section 3.1.

The model for AnMBRs simulates hydrodynamics of the fluids inside the reactor tank coupled with the MMV system. The possibility of the coupling of the developed model with the biological AM2b model (Section 1.2.8.3) is considered. The hydrodynamic model for AnMBRs is described in Section 3.2.

2.1 The general predictive models for direct contact and sweeping gas membrane distillation

2.1.1 Applied geometrical configurations and coordinates

Three different domains of modules for DCMD and SGMD are defined: the feed channel, the permeate channel (also called SG channel in SGMD) and the membrane (Fig. 2.1). The developed general predictive models for DCMD and SGMD are designed to simulate the process with different geometries: i) the flat sheet configuration by using of Cartesian coordinates (Fig. 2.2(a)) and ii) the hollow fibre configuration by using of axisymmetric coordinates (Fig. 2.2(b)). The variables considered in the models are presented in Fig. 2.2(a).

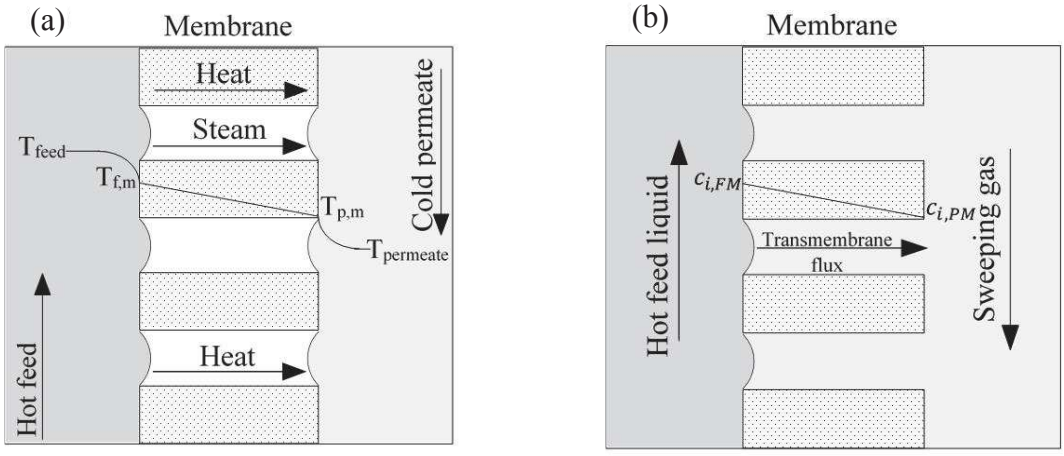

Figure 2.1: (a) Schematic representations of the (a) DCMD and (b) SGMD processes.

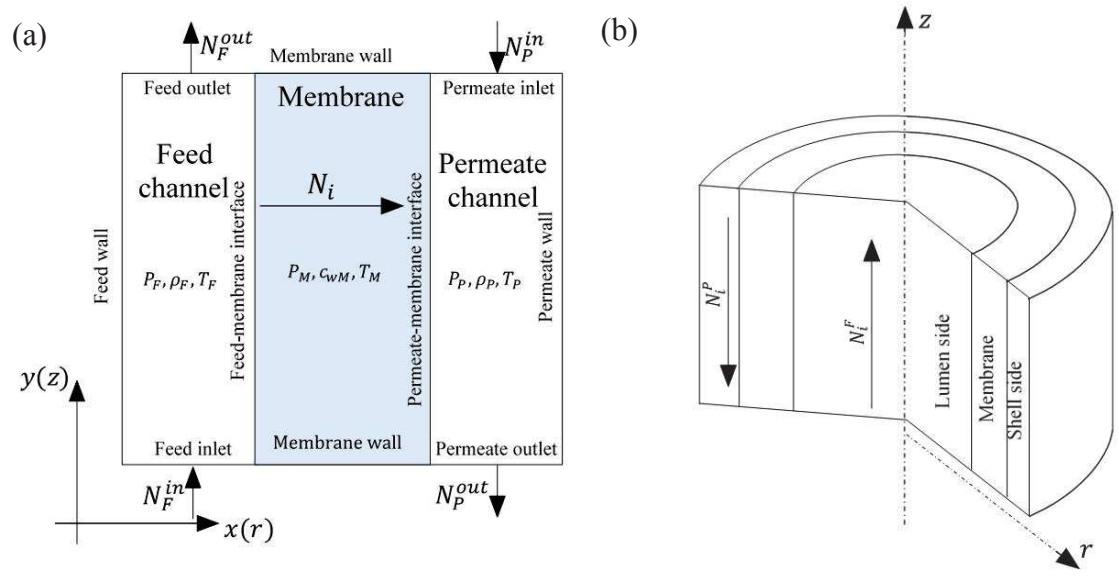

Figure 2.2: Schematic representation of the model for (a) the flat sheet configuration and (b) the hollow fibre configuration, respectively. P_F, P_P, P_M and T_F, T_P, T_M are the pressures and temperatures in the feed, permeate and membrane domain respectively; ρ_F and ρ_P are the densities of the feed and permeate flows respectively; c_{iM} is the molar concentration of the component i in the membrane pores; N_i is the molar transmembrane flux of the component i; N_F^{in}, N_P^{in} and N_F^{out}, N_P^{out} are the total fluxes of the feed liquid and permeate fluid at the inlet and outlet of feed and permeate respectively.

In the case of a module containing multiple hollow fibres, the momentum, mass and heat transfer at the lumen side of the hollow fibre has been considered similar for any single fibre in the module. However, in the shell side of the hollow fibre, these processes are complex and dependent on many parameters, such as the packing density, number of the hollow fibres in the module and distance between them. Thus, for that type of the modules, the proper simulation accounting all the mentioned parameters can be done only in 3D. This procedure is an extremely resource- and time-consuming task. To reduce the computational burden and intensify the calculation process of the mathematical model, the simulation of the whole module with numerous hollow fibres is transformed into the simulation of the part of the module with only one hollow fibre surrounded by a defined volume of shell side module (Fig. 2.3). This approach has already been successfully applied for the modelling of hollow fibres modules for liquid-liquid extraction processes [138-140]. The concept of the flow in pipe is considered in the lumen side of the membrane. To model the momentum, mass and heat transfer in the shell side of the membrane, we assume that the considered hollow fibre is equidistant from the surrounding hollow fibres as it is shown on Fig.2.3(b). In real situations (Fig. 2.3(a)) the distances between hollow fibres may vary. For the simulation purpose, we divide the cross-sectional area of the permeate channel (dash lines on Fig. 2.3(b)) in such a way that it formed annuli around the hollow fibres. For the modelled part of the module (one hollow fibre with

the annular permeate channel), the feed and permeate flow rates are calculated in proportion to values used for the multiple hollow fibre module. Therefore, the flow rates of the feed and permeate fluids are calculated by the following equation:

$$\dot{m}_z = \frac{\dot{m}_{tz}}{n_{HF}} \tag{266}$$

where $\dot{m}$ is the proportional total flow rate used in the module simulation, $\dot{m}_t$ is the total flow rate used in the real module, n_{HF} is the number of the hollow fibres in the real module, z is the identifier of the side (F for feed, P for permeate).

The proportional shell diameter of the considered annular permeate domain is calculated as follows:

$$D_{Shell} = \sqrt{(\frac{A_{Shell}}{n_{HF}} + A_{OF})\frac{4}{\pi}} \tag{267}$$

where A_{Shell} is the cross section area of the shell side channel of the DCMD module, n_{HF} is the number of the hollow fibres, A_{OF} is the cross section area taken by the one hollow fibre.

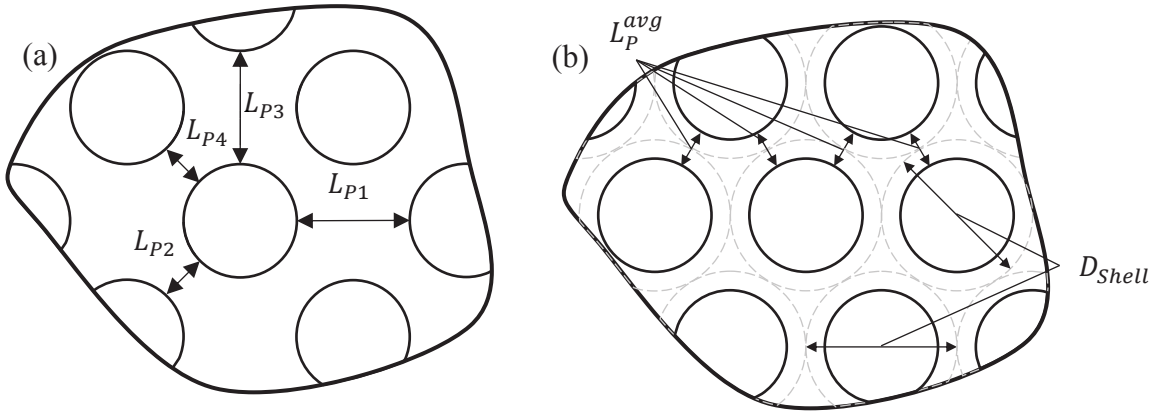

Figure 2.3: Segments of the cross-sectional area of (a) the real hollow fibre module and (b) the modelled hollow fibre module.

A similar approach can be used for flat sheet modules containing multiple frames (plate and frame modules). In this case, the model considers a half of the one feed channel, a half of the one permeate channel and a membrane between these halves (Fig. 2.4). We also assume that the number of the feed and permeate half-channels is equal to number of membranes in the plate and frame module. Therefore, the feed flow rate and the permeate flow rate in one half-channel are calculated from the following equations:

$$\dot{m}_F = \frac{\dot{m}_{TF}}{n_{FS}} \tag{268}$$

$$\dot{m}_P = \frac{\dot{m}_{TP}}{n_{FS}} \tag{269}$$

where $\dot{m}_{TF}$ is the total feed flow rate, $\dot{m}_F$ is the feed flow rate in one channel, $\dot{m}_{TP}$ is the total permeate flow rate, $\dot{m}_P$ is the permeate flow rate in one channel, n_{FS} is the number of membranes in the plate and frame module.

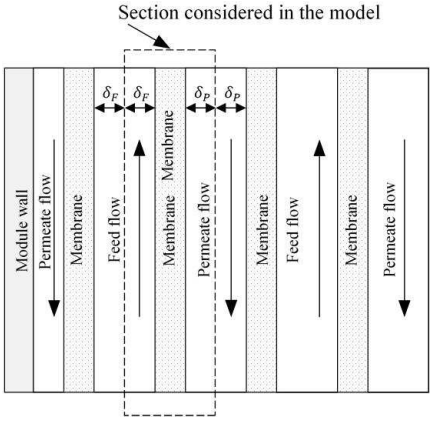

Figure 2.4: Schematic representation of the model for the flat sheet configuration containing more than one membrane.

The flow pattern in the model can be set to both co-current and counter current. For each part of the module, the momentum, mass and heat balances are described by the systems of the equations derived for the dynamic state. However, these equations could be easily simplified to the steady state conditions.

2.1.2 Defined assumptions

The mass and enthalpy balances of the developed MD models have been derived on the base of the following assumptions:

1. Ideal gas behaviour of the water vapour and air.
2. The porosity is uniformly distributed across the membrane area.
3. The diameter of pores is constant across the membrane area and equals to the mean pore diameter.
4. The solubility of air in the feed liquid is negligible.
5. The transmembrane mass transfer is described by the DGM [84, 85].
6. The liquid-gas interface is at thermodynamic equilibrium.

7. The heat losses are neglected. However, the calculation of the heat losses is possible in the model.

Additionally to the above assumptions, the following assumptions were taken into account in the DCMD model:

1. The solubility of air in the permeate liquid is negligible.
2. Air is stagnant inside the membrane pores.
3. The pressure of the gas phase is the same in any point inside the membrane pores in the steady state.

2.1.3 Feed and permeate sides

In DCMD, the feed and permeate streams flow through empty channels or spacer-filled channels. Therefore, the presented momentum, mass and heat balances of the feed and permeate channels taking into account these possible options. Subscript z in the Eqs. (270) – (297) determines the feed or permeate side.

2.1.3.1 Momentum balance

Fluids in the feed and permeate channels can flow with different velocities. The laminar and transient flow types correspond to low values of the fluid velocity and Reynolds number ($Re < 2100$). The Navier-Stokes equation is used to characterize these flow types (Eq. (270)). For higher values of the fluid velocity and Reynolds number ($Re > 2100$) the k-epsilon Reynolds-averaged Navier-Stokes model [130] can be applied (Eqs. (273)-(278)). For the full description of the momentum balance of the fluids, the Navier-Stokes equation for the laminar or the k-epsilon Reynolds-averaged Navier-Stokes model for the turbulent flow should be coupled with a continuity equation (Eqs. (279), (280)).

The Navier-Stokes equation for the description of laminar and transient flows ($Re < 2100$) in the feed or permeate channel is:

$$\rho_z \frac{\partial \vec{v}_z}{\partial \tau} = -\rho_z (\vec{v}_z \cdot \nabla)\vec{v}_z + \nabla \cdot [-P_z I + \tau_{vz}] \tag{270}$$

where ρ_z is the fluid density, τ is the time, v_z is the local mass averaged velocity, P_z is the pressure, I is the identity matrix, τ_{vz} is the viscous stress tensor.

The viscous stress tensor for Newtonian fluids is calculated as follows:

$$\tau_{vz} = 2\mu_z S_{tz} - \frac{2}{3}\mu_z(\nabla \cdot \vec{v}_z)I \tag{271}$$

where μ_z is the dynamic viscosity, S_{tz} is the strain-rate tensor determined by the following equation:

$$S_{tz} = \frac{1}{2}(\nabla\vec{v}_z + (\nabla\vec{v}_z)^T) \tag{272}$$

The k-epsilon Reynolds-averaged Navier-Stokes model [130] for the description of turbulent flow ($Re > 2100$) in the feed or permeate channel is given by the following equations:

$$\rho_z \frac{\partial \vec{v}_z}{\partial \tau} = -\rho_z(\vec{v}_z \cdot \nabla)\vec{v}_z + \nabla \cdot [-P_z I + \tau_{Tz}] \tag{273}$$

$$\tau_{Tz} = (\mu_z + \mu_{Tz})(\nabla\vec{v}_z + (\nabla\vec{v}_z)^T) - \frac{2}{3}\big((\mu_z + \mu_{Tz})(\nabla \cdot \vec{v}_z) + \rho_z k_{Tz}\big)I \tag{274}$$

$$\rho_z \frac{\partial k_{Tz}}{\partial \tau} = -\rho_z(\vec{v}_z \cdot \nabla)k_{Tz} + \nabla \cdot \left[\left(\mu_z + \frac{\mu_{Tz}}{\sigma_{kz}}\right)\nabla k_{Tz}\right] + P_{kz} - \rho_z \varepsilon_{Tz} \tag{275}$$

$$\rho_z \frac{\partial \varepsilon_{Tz}}{\partial \tau} = -\rho_z(\vec{v}_z \cdot \nabla)\varepsilon_{Tz} + \nabla \cdot \left[\left(\mu_z + \frac{\mu_{Tz}}{\sigma_{\varepsilon z}}\right)\nabla \varepsilon_{Tz}\right] + C_{\varepsilon 1z}\frac{\varepsilon_{Tz}}{k_{Tz}}P_{kz} - C_{\varepsilon 2z}\frac{\varepsilon_{Tz}^2}{k_{Tz}}\rho_z \tag{276}$$

$$P_{kz} = \mu_{Tz}\left(\nabla\vec{v}_z : (\nabla\vec{v}_z + (\nabla\vec{v}_z)^T) - \frac{2}{3}(\nabla \cdot \vec{v}_z)^2\right) - \frac{2}{3}\rho_z k_{Tz}\nabla \cdot \vec{v}_z \tag{277}$$

$$\mu_{Tz} = \rho_z C_{\mu z}\frac{k_{Tz}^2}{\varepsilon_{Tz}} \tag{278}$$

where τ_{Tz} is the turbulent viscous stress tensor, $C_{\mu z}$, $C_{\varepsilon 1z}$, $C_{\varepsilon 2z}$, σ_{kz}, $\sigma_{\varepsilon z}$ are the k-epsilon Reynolds-averaged Navier-Stokes constants, k_{Tz} is the turbulent kinetic energy, ε_{Tz} is the turbulent dissipation rate, P_{kz} is the production of k_{Tz}, μ_{Tz} is the eddy (turbulent) viscosity.

The continuity equations for the feed and permeate channels are written as follows:

$$\frac{\partial \rho_F}{\partial \tau} + \rho_F \nabla \cdot (\vec{v}_F) = 0 \tag{279}$$

$$\begin{cases} \dfrac{\partial \rho_P}{\partial \tau} + \rho_P \nabla \cdot (\vec{v}_P) = 0 \text{ (DCMD)} \\ \dfrac{\partial \rho_F}{\partial \tau} + \nabla \cdot (\rho_P \vec{v}_P) = 0 \text{ (SGMD)} \end{cases} \quad (280)$$

The DCMD and SGMD processes can be intensified by filling the feed and permeate channels by spacers to increase the fluid velocities and mixing. The enhanced mixing increases the temperature at the feed-membrane interface and decreases the concentration of the water vapour at the permeate-membrane interface. The determination of the Reynolds number in the spacer-filled channel is a complex task dependent on the spacer porosity, geometric characteristics of spacers and angles between filaments of the spacers. Li and Tung [141] determined the boundary between the laminar and turbulent flows at Reynolds number around 250 for spacers with filament diameter of 0.5 mm and angles between the crossing filaments in the range from 60 to 120°. Lou *et al.* [142] applied Reynolds numbers up to 400 for the laminar flow in the spacer-filled channels with filament diameter of 0.381 mm and angles between the crossing filaments in the range from 60 to 150°. In this thesis, we assume that the laminar flow in spacer-filled channels occurs at Re<400.

The simulation of the spacer-filled channels can be performed by using different strategies. The first and most obvious strategy is to apply the 3D CFD approach with the Navier-Stokes equation coupled with the continuity equation and to draw a model of the channel according to the geometric parameters of the spacer and the channel [141-144]. This way allows correct simulation of liquid mixing and estimation of the velocity distribution within the channel. However, the 3D simulation requires powerful hardware and enormous time resources not only to calculate but also to carefully draw the structure of the spacer and channel and determine BCs within the channel. Indeed, this strategy assumes the whole module to be simulated in 3D. Thus, the 3D CFD simulation is not reasonable in terms of the calculation time and computational resources.

Another strategy is to apply 2D CFD approach with the Navier-Stokes equation coupled with the continuity equation for the flow simulation [145-147]. In this approach, the longitudinal section of the spacer-filled channel is simulated according to geometric parameters of the channel and spacers. In this case, due to simplification, the mixing of the fluid along the width of the spacer-filled channel is not taken into account, nevertheless, the discrepancy between the model and real situation is minimal [145-147]. In comparison to the 3D approach, the 2D approach (further denoted as the strategy 1) does not fully comply with the geometry

of the modelled spacer-filled channel but less computational resource are needed to solve this problem.

The last strategy (further denoted as the strategy 2) is tentative and, to the best of our knowledge, is not tested on the spacer-filled channels. This strategy describes the fluid flow through the spacer-filled channels as the flow through the porous media with assumption that the spacer is the porous material with large pores. The aim of the strategy is to intensify the simulation process and to decrease the calculation time. However, in this approach the obtained distribution of superficial velocities is averaged in space. Thus, for the spacer-filled channel at low Re numbers (less than 10) calculated by using the hydraulic diameter for the space between filaments of the spacer, the Darcy's law [86] can be applied as the momentum balance:

$$\frac{\partial}{\partial \tau}(\varepsilon_z \rho_z) + \nabla \cdot (\rho_z \vec{v}_{Dz}) = 0 \tag{281}$$

where ε_z is the porosity of the spacer, v_{Dz} is the superficial velocity calculated by using Darcy's equation [86]:

$$\vec{v}_{Dz} = -\frac{\Pi_z}{\mu_z}(\nabla P_z - \rho_z \vec{g}) \tag{282}$$

where Π_z is the permeability of the spacer, μ_z is the dynamic viscosity of the fluid, g is the standard acceleration due to gravity.

For laminar and transient flows in the spacer-filled channel ($10<Re<400$), the Brinkman-Forchheimer equation, which is a modification of the Darcy's law, is used to describe the momentum balance [148-150]:

$$\begin{aligned}\frac{\rho_z}{\varepsilon_z}\frac{\partial}{\partial \tau}(\vec{v}_{Dz}) + \frac{\rho_z}{\varepsilon_z}(\vec{v}_{Dz} \cdot \nabla)\frac{\vec{v}_{Dz}}{\varepsilon_z} \\ = \nabla \cdot \left[-P_z I + \frac{\mu_z}{\varepsilon_z}\left((\nabla \vec{v}_{Dz} + (\nabla \vec{v}_{Dz})^T) - \frac{2}{3}(\nabla \cdot \vec{v}_{Dz})\right)\right] - \left(\frac{\mu_z}{\Pi_z} + \beta_{Fz}|\vec{v}_{Dz}|\right)\vec{v}_{Dz}\end{aligned} \tag{283}$$

where β_{Fz} is the Forchheimer correction coefficient which can be calculated as follows:

$$\beta_{Fz} = \frac{1.75}{\sqrt{150\varepsilon_z^3}}\frac{\rho_z \varepsilon_z}{\sqrt{\Pi_z}} \tag{284}$$

For turbulent flows in the spacer-filled channel, the Burke-Plummer equation is used to describe the momentum balance [86, 151]:

$$\frac{\partial}{\partial \tau}(\varepsilon_z \rho_z) + \nabla \cdot (\rho_z \vec{v}_{Dz}) = 0 \tag{285}$$

$$\nabla P_z = \frac{1.75 \rho_z \vec{v}_{Dz}^2}{D_{pz}} \frac{(1-\varepsilon_z)}{\varepsilon_z^3} \tag{286}$$

where D_{pz} is the hydraulic diameter that characterizes the distance between filaments of the spacer.

2.1.3.2 Mass balance

Mass transfer of each component in the empty channels of the feed and permeate compartments is described by the convection-diffusion equation:

$$\frac{\partial \rho_{iz}}{\partial \tau} = \sum_{j=1}^{N} \nabla \cdot \left(D_{ijz} \nabla \rho_{jz} \right) - \vec{v}_z \cdot \nabla \rho_{iz} + R_{Aiz} \tag{287}$$

where ρ_{iz} and ρ_{jz} are the mass concentrations of the components i and j respectively, D_{ijz} is the diffusion coefficient for the components i and j or thermal diffusion in the case of the transfer of the single component, R_{Aiz} is the mass transfer factor of the component i for the axisymmetric coordinates.

If we consider orthogonal coordinates, the mass transfer factor is equal to zero because the radial flow passes through an area of the same size in the each point of the domain. For the axisymmetric coordinates, the radial flow passes the area of different size at each radial point. Therefore, the mass transfer factor of the component i for the axisymmetric coordinates is calculated by the following equation:

$$R_{Aiz} = -\frac{\left(-\sum_{j=1}^{N} \left(D_{ijz} \frac{\partial \rho_{jz}}{\partial r} \right) + \vec{u}_z \cdot \rho_{iz} \right)}{r} \tag{288}$$

where r is the radial coordinate, u_z is the radial velocity.

In the previous section, the momentum balance was described taking in consideration different approaches and equations to characterize the fluid flow in the spacer-filled channel. If the flow is determined by the Navier-Stokes equation (strategy 1 in Section 2.2.1) then the mass balance could be described by Eq. (287). If the flow through the spacer is described by

the Darcy's law, Brinkman-Forchheimer equation or Burke-Plummer equation (strategy 2 in Section 2.1.3.1), then the velocity of the fluid in the Eq. (287) is substituted by the superficial velocity:

$$\frac{\partial \rho_{iz}}{\partial \tau} = \sum_{j=1}^{N} \nabla \cdot \left(D_{ijz} \nabla \rho_{jz} \right) - \vec{v}_{Dz} \cdot \nabla \rho_{iz} + R_{Aiz} \tag{289}$$

In SGMD, SG serves as solvent for other components. Assuming the ideal gas behaviour, the convection-diffusion equation for SG can be substituted by the ideal gas equation:

$$\mathrm{c}_{SG} = \frac{P_P}{R_g T_P} - \sum_{i \neq SG} c_{iP} \tag{290}$$

where c_{SG} is the molar concentration of the major component of SG in the permeate flow, c_{iP} is the concentration of the component i in the permeate flow, P_P is the permeate flow pressure, T_P is the permeate flow temperature, R_g is the universal gas constant.

The binary diffusion coefficients for liquids in multicomponent mixtures can be estimated by methods offered in the literature [86, 87]. For gases, the ordinary diffusion coefficient D_{ij} is calculated as follows [86]:

$$D_{ij} = \frac{0.0018583 \sqrt{T_M^3 \left(\frac{1}{M_i} + \frac{1}{M_j} \right)}}{P_M \sigma_{ij}^2 \Omega_{ij}} \tag{291}$$

where σ_{ij} is the average collision diameter, Ω_{ij} is the collision integral [86, 87].

2.1.3.3 Heat balance

For the feed and permeate channels without spacers, the enthalpy balance can be described by the following equation:

$$\rho_z C_{Pz} \frac{\partial T_z}{\partial \tau} = -\rho_z C_{Pz} \vec{v}_z \cdot \nabla T_z - \nabla \vec{q}_z + Q_{Az} \tag{292}$$

where C_{Pz} is the heat capacity of the fluid at constant pressure, q_z is the conductive heat flux, Q_{Az} is the heat transfer factor for the axisymmetric coordinates.

The heat transfer factor for the axisymmetric coordinates is calculated from the following equation:

$$Q_{Az} = -\frac{\rho_z C_{Pz} \vec{u}_z \cdot T_z + \vec{q}_z}{r} \tag{293}$$

The conductive heat flux q_z in Eq. (292) is described by Fourier's law:

$$\vec{q}_z = -k_z \cdot \nabla T_z \tag{294}$$

where k_z is the thermal conductivity of the fluid.

If the strategy 1 for the modelling of the spacer-filled channel is applied, the enthalpy balance of the fluid could be also described by Eq. (292). However, the enthalpy balance of the filaments of the spacers must be taken into account:

$$\delta_{Sp} \rho_{Spz} C_{PSpz} \frac{\partial T_{Spz}}{\partial \tau} = -\nabla\left(k_{Spz} \cdot \nabla T_{Spz}\right) \tag{295}$$

where C_{PSpz} is the heat capacity of the spacer, δ_{Sp} is the length of the spacer, T_{Spz} is the temperature of the spacer, ρ_{Spz} is the density of the spacer, k_{Spz} is the thermal conductivity of the spacer.

For the case, where the momentum balance is done by applying the strategy 2, the velocity of the fluid and the thermal conductivity of the fluid in Eq. (292) are substituted by the superficial velocity and the effective thermal conductivity, respectively. With the mentioned changes, the enthalpy balance can be described by the following equation:

$$\left(\varepsilon_z \rho_z C_{Pz} + (1-\varepsilon_z)\rho_{Spz} C_{PSpz}\right)\frac{\partial T_z}{\partial \tau} + \rho_z C_{Pz} \vec{v}_{Dz} \nabla T_M + \nabla\left(-k_z^{eff} \cdot \nabla T_z\right) = Q_{Az} \tag{296}$$

where ρ_{Spz} is the density of the spacer, k_z^{eff} is the effective thermal conductivity, ε_z is the porosity of the spacer.

The effective thermal conductivity is calculated as follows:

$$k_z^{eff} = \varepsilon_z k_z + (1-\varepsilon_z) k_{Spz} \tag{297}$$

where k_{Spz} is the thermal conductivity of the spacer.

2.1.3.4 Boundary conditions

The model equations (sections 3.1.3.1 – 3.1.3.3) characterizing the momentum, mass and heat transfers in the feed and permeate channels require the set of BCs. For both feed and permeate channels, the boundaries (Fig. 2.2(a)) are determined in the inlet, outlet, wall and interface between the membrane and the channel. The inlet BCs determine the input parameters of the flow (temperature, pressure and velocity profiles) while the outlet BCs define the parameters of the outlet flow (pressure and normal derivatives of concentrations and temperature). The wall BCs represent zero mass and heat fluxes for the orthogonal coordinates and symmetry for the axisymmetric coordinates. BCs for the interface between the membrane and the channel describe the momentum, mass and heat transfers between the domains, including evaporation phenomena at the feed-membrane interface. The full set of BCs for the feed and permeate domains is presented in Table 2.1.

Table 2.1: Boundary conditions for the feed and permeate domains.

Boundary	Boundary conditions	Note
Feed inlet	$\begin{cases} -\int_S \rho_F(\vec{v}_F \cdot n)\delta_F dS_F = \dot{m}_{Fin}\ (^{a,b}) \\ k_{TF} = \frac{3}{2}\left(\vec{v}_{refF} I_{TF}\right)^2\ (^b) \\ \varepsilon_{TF} = {C_{\mu F}}^{0.75} \frac{{k_{TF}}^{1.5}}{L_{TF}}\ (^b) \\ n \cdot \rho_F \vec{v}_{DF} = \frac{\dot{m}_{Fin}}{A_F}\ (^c) \\ \rho_{iF} = \rho_{iFin} \\ T_F = T_{Fin} \end{cases}$	I_{TF} is the feed turbulent intensity; k_{TF} is the feed turbulent kinetic energy; L_{TF} is the feed turbulent length scale; $\dot{m}_{Fin}$ is the feed inlet flow rate; S_F is the cross-section area of the feed channel; T_F is the feed temperature; T_{Fin} is the feed temperature at the inlet; v_F is the feed velocity; v_{DF} is the feed velocity in the spacer-filled channel; v_{refF} is the feed reference velocity scale; A_F is the cross-sectional area of the feed channel; δ_F is the feed channel thickness; ρ_F is the feed fluid density; ρ_{iF} is the mass concentration of the component i in the feed fluid; ρ_{iFin} is the mass concentration of the component i in the feed fluid at the inlet; ε_{TF} is the feed turbulent dissipation rate.
Feed outlet	$\begin{cases} [-P_F I + \tau_z] \cdot n = -P_{Fout}\ (^a) \\ [-P_F I + \tau_{Tz}] \cdot n = -P_{Fout}\ (^b) \\ \nabla k_{TF} \cdot n = 0\ (^b) \\ \nabla \varepsilon_{TF} \cdot n = 0\ (^b) \\ P_F = P_{Fout}\ (^c) \\ n \cdot \left(-D_{ijF} \nabla \rho_{iF}\right) = 0 \\ -n \cdot \vec{q}_F = 0 \end{cases}$	D_{ijF} is the ordinary diffusion coefficient for the components i and j; P_F is the feed fluid pressure; P_{Fout} is the feed fluid pressure at the outlet; q_F is the feed conductive heat flux; μ_F the dynamic viscosity of the feed fluid; μ_{TF} is the eddy (turbulent) viscosity of the feed fluid.

Feed-membrane interface	$$\begin{cases} \mathrm{n}\cdot\vec{v}_F = 0 \\ n\cdot\tau_{Tz} - (\tau_{Tz}\cdot n)n = -\rho_F \dfrac{\vec{v}_F}{k_{TV}^{-1}\ln\left(\rho_F C_{\mu F}^{0.25} k_{TF}^{0.5}\delta_w(\mu_F+\mu_{TF})^{-1}\right)+B_T}\ (^b) \\ \nabla k_{TF}\cdot n = 0\ (^b) \\ \varepsilon_{TF} = \rho_F \dfrac{C_{\mu F}^{0.75} k_{TF}^{1.5}}{k_{TV}\delta_w}\ (^b) \\ n\cdot\left(-\sum_{j\neq i}^{N}\left(D_{ijF}\nabla\rho_{iF}\right)+\vec{v}_F\rho_{iF}\right) = \left(n\cdot\vec{N}_i\right)M_i \\ -\mathrm{n}\cdot\vec{q}_F = -\sum_i H_i^{ev}\left(n\cdot\vec{N}_i\right)+k^{eff}\dfrac{\partial T_M}{\partial x}-\sum_i\left(n\cdot\vec{N}_i\right)M_i C_{Pi}\left(T_M-T_{ref}\right)\ (flat\ sheet) \\ -\mathrm{n}\cdot\vec{q}_F = -\sum_i H_i^{ev}\left(n\cdot\vec{N}_i\right)+k^{eff}\dfrac{\partial T_M}{\partial r}-\sum_i\left(n\cdot\vec{N}_i\right)M_i C_{Pi}\left(T_M-T_{ref}\right)\ (hollow\ fibre) \end{cases}$$	H_i^{ev} is the enthalpy of vaporization of the component i; N_i is the transmembrane flux of the component i; k_{eff} is the effective thermal conductivity of the membrane; M_i is the molar mass of the component i; C_{Pi} is the heat capacity at constant pressure for the component i; T_M is the temperature of the membrane; T_{ref} is the reference temperature.
Feed-spacer interface (if spacers present)	$$\begin{cases} \vec{v}_F\cdot n = 0 \\ n\cdot\tau_{Tz} - (\tau_{Tz}\cdot n)n = -\rho_F \dfrac{\vec{v}_F}{k_{TV}^{-1}\ln\left(\rho_F C_{\mu F}^{0.25} k_{TF}^{0.5}\delta_w(\mu_F+\mu_{TF})^{-1}\right)+B_T}\ (^b) \\ \nabla k_{TF}\cdot n = 0\ (^b) \\ \varepsilon_{TF} = \rho_F \dfrac{C_{\mu F}^{0.75} k_{TF}^{1.5}}{k_{TV}\delta_w}\ (^b) \\ n\cdot\left(\sum_{j\neq i}^{N}\left(D_{ijF}\nabla\rho_{iF}\right)-\vec{v}_F\rho_{iF}\right) = 0 \\ n\cdot\vec{q}_F = n\cdot\vec{q}_{SpF}\ (feed\ side) \\ T_{SpF} = T_F\ (spacer\ side) \end{cases}$$	q_{SpF} is the spacer conductive heat flux.

<table>
<tr>
<td>Feed wall</td>
<td>$$\begin{cases} \vec{v}_F \cdot n = 0 \\ n \cdot \tau_{Tz} - (\tau_{Tz} \cdot n)n = -\rho_F \dfrac{\vec{v}_F}{k_{TV}^{-1} \ln\left(\rho_F C_{\mu F}^{0.25} k_{TF}^{0.5} \delta_w (\mu_F + \mu_{TF})^{-1}\right) + B_T} \ (^{b,d}) \\ n \cdot \tau_{Tz} - (\tau_{Tz} \cdot n)n = 0 \ (^{b,e}) \\ \nabla k_{TF} \cdot n = 0 \ (^{b}) \\ \varepsilon_{TF} = \rho_F \dfrac{C_{\mu F}^{0.75} k_{TF}^{1.5}}{k_{TV} \delta_w} \ (^{b,d}) \\ \nabla \varepsilon_{TF} \cdot n = 0 \ (^{b,e}) \\ n \cdot \left(\sum_{j \neq i}^{N} \left(D_{ijF} \nabla \rho_{iF}\right) - \vec{v}_F \rho_{iF} \right) = 0 \\ -n \cdot \vec{q}_F = 0 \end{cases}$$</td>
<td></td>
</tr>
<tr>
<td>Permeate inlet</td>
<td>$$\begin{cases} -\int_S \rho_P (\vec{v}_P \cdot n) \delta_P dS_P = \dot{m}_{Pin} \ (^{a,b}) \\ k_{TP} = \dfrac{3}{2}\left(\vec{v}_{refP} I_T\right)^2 \ (^{b}) \\ \varepsilon_{TP} = {C_{\mu P}}^{0.75} \dfrac{{k_{TP}}^{1.5}}{L_{TP}} \ (^{b}) \\ n \cdot \rho_P \vec{v}_{DP} = \dfrac{\dot{m}_{Pin}}{A_P} \ (^{c}) \\ \rho_{iP} = \rho_{iPin} \\ T_P = T_{Pin} \end{cases}$$</td>
<td>k_{TP} is the turbulent kinetic energy of the permeate fluid;
$\dot{m}_{Pin}$ is the inlet flow rate of the permeate fluid;
S_P is the permeate channel cross-section area;
T_P is the permeate temperature;
T_{P0} is the permeate temperature at the inlet;
A_P is the area of the permeate channel;
v_P is the permeate fluid velocity;
δ_P is the permeate channel thickness;
ρ_P is the permeate fluid density;
ρ_{iP} is the mass concentration of the component i in the permeate fluid;
ρ_{iPin} is the mass concentration of the component i in the permeate fluid at the inlet;
ε_{TP} is the permeate turbulent dissipation rate.</td>
</tr>
</table>

Permeate outlet	$\begin{cases} [-P_P I + \tau_z] \cdot n = -P_{Pout}\ (^a) \\ [-P_P I + \tau_{Tz}] \cdot n = -P_{Pout}\ (^b) \\ \nabla k_{TP} \cdot n = 0\ (^b) \\ \nabla \varepsilon_{TP} \cdot n = 0\ (^b) \\ P_P = P_{Pout}\ (^c) \\ n \cdot \left(-D_{ijP} \nabla \rho_{iP}\right) = 0 \\ -n \cdot \vec{q}_P = 0 \end{cases}$	D_{ijP} is the diffusion coefficient for the components i and j; P_P is the permeate fluid pressure; P_{Pout} is the permeate fluid pressure at the outlet; q_p is the permeate conductive heat flux; μ_P the dynamic viscosity of the permeate flow; μ_{TP} is the permeate eddy (turbulent) viscosity.
Permeate-membrane interface	$\begin{cases} \mathrm{n} \cdot v_P = \dfrac{\sum_i \left(n \cdot \vec{N}_i\right) M_i}{\rho_P} \\ k_{TP} = \dfrac{3}{2}\left(\dfrac{\sum_i \left(n \cdot \vec{N}_i\right) M_i}{\rho_P} I_T\right)^2\ (^b) \\ \varepsilon_{TP} = {C_{\mu P}}^{0.75} \dfrac{{k_{TP}}^{1.5}}{L_{TP}}\ (^b) \\ n \cdot \left(-\sum_{j \neq i}^{N} \left(D_{ijP} \nabla \rho_{iP}\right) + \vec{v}_P \rho_{iP}\right) = \left(n \cdot \vec{N}_i\right) M_i \\ -n \cdot \vec{q}_P = \sum_i H_i^{cond} \left(n \cdot \vec{N}_i\right) + k^{eff} \dfrac{\partial T_M}{\partial x} + \sum_i \left(n \cdot \vec{N}_i\right) M_i C_{PMi} \left(T_M - T_{ref}\right)\ \ (for\ DCMD) \\ -n \cdot \vec{q}_P = k^{eff} \dfrac{\partial T_M}{\partial x} + \sum_i \left(n \cdot \vec{N}_i\right) M_i C_{PMi} \left(T_M - T_{ref}\right)\ \ (for\ SGMD) \end{cases}$	H_i^{cond} is the enthalpy of condensation of the component i.
Permeate-spacer interface (if spacers present)	$\begin{cases} \vec{v}_P \cdot n = 0 \\ n \cdot \tau_{Tz} - (\tau_{Tz} \cdot n) n = -\rho_P \dfrac{\vec{v}_P}{k_{TV}^{-1} \ln\left(\rho_P C_{\mu P}^{0.25} k_{TP}^{0.5} \delta_w (\mu_P + \mu_{TP})^{-1}\right) + B_T}\ (^b) \\ \nabla k_{TP} \cdot n = 0\ (^b) \\ \varepsilon_{TP} = \rho_P \dfrac{C_{\mu P}^{0.75} k_{TP}^{1.5}}{k_{TV} \delta_w}\ (^b) \\ n \cdot \left(\sum_{j \neq i}^{N} \left(D_{ijP} \nabla \rho_{iP}\right) - \vec{v}_P \rho_{iP}\right) = 0 \\ n \cdot \vec{q}_P = n \cdot \vec{q}_{SpP}\ (feed\ side) \\ T_{SpP} = T_P\ (spacer\ side) \end{cases}$	q_{SpP} is the spacer conductive heat flux.

Permeate wall	$\begin{cases} \vec{v}_P \cdot n = 0 \\ n \cdot \tau_{TP} - (\tau_{TP} \cdot n)n = -\rho_P \dfrac{\vec{v}_P}{k_{TV}^{-1} \ln\left(\rho_P C_{\mu P}^{0.25} k_{TP}^{0.5} \delta_w (\mu_P + \mu_{TP})^{-1}\right) + B_T} \ ({}^{b,d}) \\ n \cdot \tau_{TP} - (\tau_{TP} \cdot n)n = 0 \ ({}^{b,e}) \\ \nabla k_{TP} \cdot n = 0 \ ({}^{b}) \\ \varepsilon_{TP} = \rho_P \dfrac{C_{\mu P}^{0.75} k_{TP}^{1.5}}{k_{TV} \delta_w} \ ({}^{b,d}) \\ \nabla \varepsilon_{TP} \cdot n = 0 \ ({}^{b,e}) \\ n \cdot \left(\sum_{j \neq i}^{N} \left(D_{ijP} \nabla \rho_{iP} \right) - \vec{v}_P \rho_{iP} \right) = 0 \\ -n \cdot \vec{q}_P = 0 \end{cases}$	

Note: (a) laminar flow, empty channel; (b) turbulent flow, empty channel; (c) spacer-filled channel, (d) single membrane module, (e) hollow fibre or flat sheet module with multiple membranes.

2.1.4 Membrane domain

The membrane domain in the DCMD and SGMD processes is represented by the membrane itself and the gas located inside the pores of the membrane. The membrane can be supported by a porous hydrophobic or hydrophilic material. In these cases, the membrane domain contains an additional subdomain represented by the porous support and gas or liquid located in the pores of the support. Equations that describe the momentum, mass and heat transfer in the membrane support are identical to ones for the membrane. Therefore, the system of the equations for the membrane support is not presented.

2.1.4.1 Momentum balance

The momentum balance of the membrane media in the model for DCMD is described by Darcy's law [86].

$$\frac{\partial}{\partial \tau}(\varepsilon_M \rho_V) + \nabla \cdot (\rho_V \vec{v}_M) = 0 \tag{298}$$

where ε_M is the porosity of the membrane, ρ_V is the density of the gas mixture, v_M is the superficial velocity of the gas mixture.

In the SGMD model, the momentum balance for the membrane compartment is substituted by the ideal gas law.

$$P_M = \sum_i c_i R_g T_M \tag{299}$$

where P_M is the total vapour pressure, c_i is the molar concentration of the component i.

The superficial velocity of the gas mixture for both the DCMD and SGMD models is calculated from the Darcy's equation [86].

$$\vec{v}_M = -\frac{\Pi_M}{\mu_V} \nabla (P_M - \rho_V \vec{g}) \tag{300}$$

where Π_M is the permeability of the membrane, μ_V is the dynamic viscosity of the gas mixture, P_M is the pressure of the gas mixture.

The dynamic viscosity of gas mixture can be calculated by using the following expression derived by Wilke [152]:

$$\mu_V = \sum_i \frac{\mu_{Mi}}{1 + \frac{1}{y_i}\sum_{\substack{j \\ j \neq i}} y_j \phi_{ij}} \tag{301}$$

where y_i and y_j are the molar fractions of the components i and j, respectively, ϕ_{ij} is given by the following equation [152]:

$$\phi_{ij} = \frac{\left[1 + \left(\frac{\mu_{Mi}}{\mu_{Mj}}\right)^{0.5} \left(\frac{M_j}{M_i}\right)^{0.25}\right]^2}{\sqrt{8}\left(1 + \frac{M_i}{M_j}\right)^{0.5}} \tag{302}$$

where μ_{Mi} and μ_{Mj} are the dynamic viscosities of the components i and j, respectively.

2.1.4.2 Mass transfer

Mass transfer in the membrane media is described by the continuity equation [86].

$$\frac{\partial c_i}{\partial \tau} = -\nabla \vec{N}_i + \vec{N}_{iA} \tag{303}$$

where N_i is the molar flux of the component i, N_{iA} is the molar flux coefficient of the component i for axisymmetric coordinates.

As in case of Eq. (289), the molar flux coefficient of the component i, N_{iA}, equals zero for the orthogonal coordinates but transforms the flux in the axisymmetric coordinates.

$$\vec{N}_{iA} = \frac{-\vec{N}_{ri}}{r} \tag{304}$$

where N_{ri} is the transmembrane flux of the component i in the radial direction.

Following the applied assumptions, the mass transfer in the membrane compartment is described by DGM. Therefore, the transmembrane flux N_i is represented a combination of the viscous flux N_{Vi} and diffusive flux N_{Di}.

$$\vec{N}_i = \vec{N}_{Vi} + \vec{N}_{Di} \tag{305}$$

Viscous flux is calculated from the following equation:

$$\vec{N}_{Vi} = \vec{v}_M \cdot c_i \tag{306}$$

The diffusive flux of each component in the gas mixture is calculated according to DGM [84, 85] in the following way:

$$\sum_{j \neq i} \frac{y_j \vec{N}_{Di} - y_i \vec{N}_{Dj}}{D_{ij}^{eff}} + \frac{\vec{N}_{Di}}{D_{Ki}^{eff}} = -\frac{\nabla p_i}{RT_M} \tag{307}$$

where N_{Di} and N_{Dj} are the diffusive fluxes of the components i and j, respectively, D_{ij}^{eff} is the effective ordinary diffusion coefficient of the components i and j, D_{Ki}^{eff} is the effective Knudsen diffusion coefficient of the component i, p_i is the partial pressure of the component i.

The effective ordinary diffusion coefficient and the effective Knudsen diffusion coefficients are calculated from the following equations:

$$D_{ij}^{eff} = \frac{\varepsilon_M}{\tau_M} D_{ij} \tag{308}$$

$$D_{Ki}^{eff} = \frac{\varepsilon_M}{\tau_M} D_{Ki} \tag{309}$$

where ε_M is the porosity of the membrane, τ_M is the membrane tortuosity, D_{ij} is the ordinary diffusion coefficient of the components i and j (Eq. 291), D_{Ki} is the Knudsen diffusion coefficient of the component i.

We assume that the membrane pores are filled with air which is stagnant and present in much higher quantity than the components extracted with DCMD. Therefore, Eq. (307) can be simplified to the following form:

$$\sum_{\substack{j \neq i \\ j \neq Air}} \frac{y_j \vec{N}_{Di} - y_i \vec{N}_{Dj}}{D_{ij}^{eff}} + \frac{y_{Air} \vec{N}_{Di}}{D_{iAir}^{eff}} + \frac{\vec{N}_{Di}}{D_{Ki}^{eff}} = -\frac{\nabla p_i}{RT_M} \tag{310}$$

where D_{iAir}^{eff} is the effective ordinary diffusion coefficient of air and component i, y_{Air} is the molar fraction of the air.

In industry, DCMD is used for recovery of one volatile component from the two- or multicomponent systems. In the case of only one volatile component, the membrane pores are filled only with air and the target component and Eq. (310) can be further simplified:

$$\vec{N}_{Di} = \left(-\frac{\nabla p_i}{RT_M}\right) \Big/ \left(\frac{1}{D_{Ki}^{eff}} + \frac{y_{Air}}{D_{iAir}^{eff}}\right) \tag{311}$$

In DCMD, the mass balance for the air trapped inside the pores in steady state can be substituted by the ideal gas law:

$$c_{Air} = \frac{P_M}{RT_M} - \sum_{\substack{i \\ (i \neq Air)}} c_{iM} \tag{312}$$

where c_{iM} is the concentration of the component i in the gas mixture.

Due to low solubility of air in the feed and permeate liquids, the mass transfer of air between the gas and liquid phases can be neglected. In this case, air is assumed to be stagnant inside the membrane pores in the DCMD process. The mean concentration of the stagnant air is calculated from the following equation:

$$c_{Air}^{mean} = \frac{P_{atm}}{RT_{atm}} = \frac{\iint c_{Air} d\delta_M dL_M}{\delta_M L_M} \tag{313}$$

where P_{atm} and T_{atm} are the atmospheric pressure and atmospheric temperature, respectively, δ_M and L_M are the thickness and length of the membrane, respectively.

2.1.4.3 Heat transfer

Heat transfer within the membrane is calculated from the enthalpy balance.

$$(\varepsilon_M \rho_V C_{PV} + (1 - \varepsilon_M)\rho_M C_{PM}) \frac{\partial T_M}{\partial \tau} + \rho_V C_{PV} \vec{v}_M \nabla T_M + \nabla(-k^{eff} \cdot \nabla T_M) = Q_{AM} \tag{314}$$

where C_{PV}^V is the vapour heat capacity at constant pressure, ρ_M is the density of the membrane material, C_{PM} is the membrane material heat capacity at the constant pressure, Q_{AM} is the heat coefficient in the membrane for the axisymmetric coordinates.

The heat coefficient, which equals zero for the Cartesian coordinates, calibrates the radial heat flux for the axisymmetric coordinates:

$$Q_{AM} = -\frac{\rho_V C_{PV} \vec{u}_M T_M - k^{eff} \cdot \frac{\partial T_M}{\partial r}}{r} \tag{315}$$

where $\vec{u}_M$ is the molar averaged velocity in the radial direction.

The effective thermal conductivity of the membrane and the gas mixture is calculated as follows:

$$k_M^{eff} = \varepsilon_M k_V + (1 - \varepsilon_M) k_M \tag{316}$$

where k_V is the thermal conductivity of the gas mixture, k_M is the thermal conductivity of the material of the membrane.

The thermal conductivity of the gas mixture can be found from the following expression derived by Wilke [152]:

$$k_V = \sum_i \frac{k_{Vi}}{1 + \frac{1}{y_i} \sum_{\substack{j \\ j \neq i}} y_j \phi_{ij}} \tag{317}$$

where k_{Vi} is the thermal conductivity of the component i in the gas mixture.

2.1.4.4 Boundary conditions

The set of the boundary conditions for the membrane domain in the DCMD model and SGMD model is presented in the Table 2.2 and Table 2.3, respectively.

Table 2.2: Boundary conditions for the membrane domain in the DCMD model.

Boundary	Boundary conditions	Note
Feed-membrane interface and permeate-membrane interface	$\begin{cases} n \cdot \vec{v}_M = 0 \\ c_{iM} = \gamma_{iz} x_{iz} \dfrac{P_i^*}{RT_M} \\ T_M = T_j \\ c_{Air}^{mean} = \dfrac{P_{atm}}{RT_{atm}} \end{cases}$	x_i^j is the molar fraction of the component i in the feed or permeate flow; P_i^* is the vapor pressure of the component i (calculated from the Antoine equation [**86**]); γ_i^j is the activity coefficient of the component i in the feed or permeate flow(can be found in the literature for specific components); c_{Air}^{mean} is the mean concentration of stagnant air inside pores; P_{atm} is the atmospheric pressure; T_{atm} is the atmospheric temperature.
Membrane walls	$\begin{cases} -n \cdot \left(\rho_M \dfrac{\Pi}{\mu_V} \nabla P_M \right) = 0 \\ -n \cdot \vec{N}_i = 0 \\ -n \cdot \left(-k^{eff} \cdot \nabla T_M \right) = 0 \end{cases}$	

Table 2.3: Boundary conditions for the membrane domain in the SGMD model.

Boundary	Boundary conditions	Note
Feed-membrane interface	$\begin{cases} P_M = \sum_{i=1}^{N} c_{iM} R_g T_M \\ c_{iM} = \gamma_{iF} x_{iF} \dfrac{P_i^*}{RT_M} \ (for\ volatile\ components) \\ \vec{N}_{SG} = 0 \ (for\ sweeping\ gas\ inside\ the\ pores) \\ T_M = T_F \end{cases}$	x_{iF} is the molar fraction of the component i in the feed stream; P_i^* is the vapor pressure of the component i (calculated from the Antoine equation); γ_{iF} is the activity coefficient of the component i in the feed stream (can be found in the literature for specific components); N_{SG} is the molar flux of the sweeping gas;
Permeate-membrane interface	$\begin{cases} P_M = \sum_{i=1}^{N} c_{iM} R_g T_M \\ c_{iM} = c_{iP} \\ T_M = T_F \end{cases}$	
Membrane walls	$\begin{cases} -n \cdot \left(\rho_M \dfrac{\Pi}{\mu_V} \nabla P_M \right) = 0 \\ -n \cdot \vec{N}_i = 0 \\ -n \cdot \left(-k^{eff} \cdot \nabla T_M \right) = 0 \end{cases}$	

2.2 Hydrodynamic model for anaerobic membrane bioreactor

The proposed model allows simulating the hydrodynamics of the influent inside AnMBRs equipped with the MMV system [8, 9]. The hydrodynamic AnMBRs model could be coupled with the biological AM2b model [127] for calculation of the mass balances for influent components. To simulate the influent flow inside the AnMBR tank, the k-epsilon Reynolds-averaged Navier-Stokes model [130] is applied (Eqs. (273)-(278)). The AnMBR tank together with membrane modules form the simulation zone of the model (Fig. 2.5) in which the tank media and membrane modules are determined. While the domain for the membrane modules

is served only for the mesh displacement to simulate membrane vibrations, the velocity, pressure and concentration profiles for the influent are determined in the tank domain.

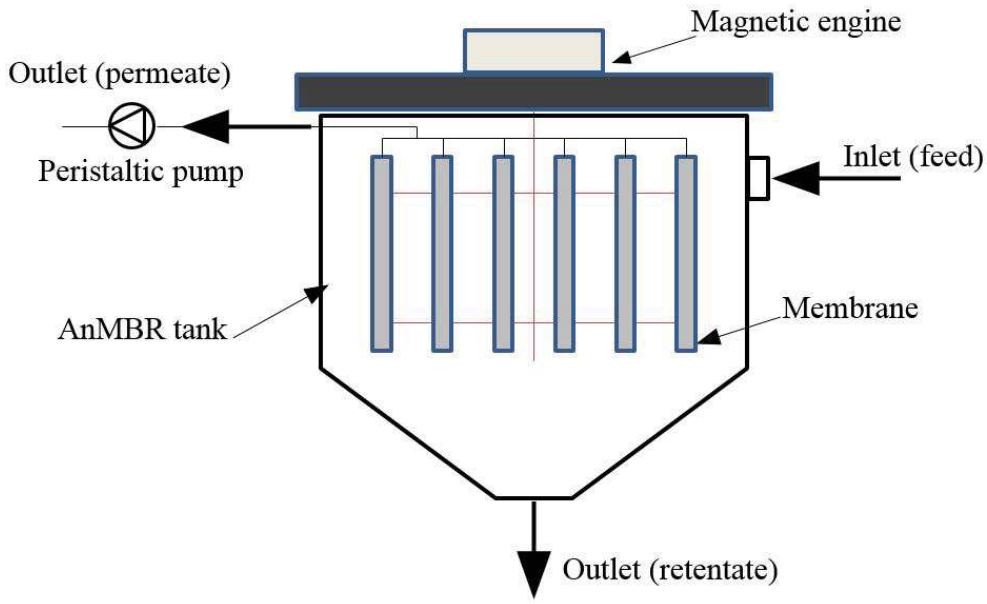

Figure 2.5: Schematic representation of the submerged AnMBR with the MMV system.

2.2.1 Considered assumptions

The following assumptions are applied in the proposed model:

1. The influent liquid is incompressible.
2. The gas phase in the influent is neglected
3. Anaerobic bacteria in the model are presented as dissolved species in the influent.
4. The suspended solids (SS) and SMP are assumed to be the only particles participating in fouling of the membrane pores.
5. Biological processes described in the AM2b model are assumed as the only chemical processes that take place inside the AnMBR tank.
6. The temperature of the influent is initially defined and is not changing seriously during the process. Thus, the heat balance of the AnMBR process is eliminated.

2.2.2 Momentum balance

The fluid dynamics inside the AnMBR tank coupled with the MMV system is mainly determined by a viscous influent flow interacting with a vibrating membrane module. Besides

the liquid phase, the influent also consists of suspended solids and gases formed during the anaerobic digestion. In the AnMBR tank coupled with the MMV system, the gases do not have a strong effect on hydrodynamics while the solids can form a cake at the membrane surface and reduce the efficiency of the process. Thus, to model the interactions between the membrane module and the influent, the Euler-Euler model with the continuous liquid phase and dispersed solid phase is applied.

$$\nabla \cdot (\phi_C \vec{v}_C + \phi_D \vec{v}_D) = 0 \tag{318}$$

$$\frac{\partial \phi_D}{\partial \tau} + \nabla \cdot (\phi_D \vec{v}_D) = 0 \tag{319}$$

$$\phi_C = 1 - \phi_D \tag{320}$$

$$\rho_C \frac{\partial}{\partial \tau}(\vec{v}_C) + \rho_C \vec{v}_C \nabla \cdot \vec{v}_C = -\nabla P + \nabla \cdot \tau_C + \frac{\nabla \cdot (\phi_C \tau_C)}{\phi_C} + \rho_C \vec{g} + \frac{F_{M,C}}{\phi_C} \tag{321}$$

$$\rho_D \frac{\partial}{\partial \tau}(\vec{v}_D) + \rho_D \vec{v}_D \nabla \cdot \vec{v}_D = -\nabla P + \nabla \cdot \tau_D + \frac{\nabla \cdot (\phi_D \tau_D)}{\phi_D} + \rho_D \vec{g} + \frac{F_{M,D}}{\phi_D} \tag{322}$$

$$\tau_C = \mu_C \left(\nabla \vec{v}_C + (\nabla \vec{v}_C)^T - \frac{2}{3}(\nabla \cdot \vec{v}_C) I \right) \tag{323}$$

$$\tau_D = \mu_D \left(\nabla \vec{v}_D + (\nabla \vec{v}_D)^T - \frac{2}{3}(\nabla \cdot \vec{v}_D) I \right) \tag{324}$$

where ϕ is the volume fraction, v is the velocity, ρ is the density, P is the influent pressure, τ_C and τ_D are the stress tensors for the liquid and solid phases, respectively, g is the gravitational constant, F is the interface momentum transfer term, μ is the dynamic viscosity, I is the identity matrix, subscripts C and D denote the liquid and solid phases, respectively.

2.2.3 Simulation of the MMV system

The MMV system controls the process of vibration of the membranes immersed in the AnMBR tank (Fig. 2.6). The membrane vibration occurs at a given frequency in the vertical plane with even membranes moving in the opposite direction to the odd ones. The amplitude of the vibration is defined before the experiments.

The vibration of the membranes is described by the following equations:

$$d_M(\tau) = A_V \sin(f_M \tau) \ \ (even\ membranes) \tag{325}$$

$$d_M(\tau) = -A_V \sin(f_M \tau) \ \ (odd\ membranes) \tag{326}$$

where d_M is the vertical displacement of the membrane in space, A_V is the amplitude of vibration, f_M is the frequency of vibration, τ is the time of vibration.

The velocity of the membrane displacement is estimated by using the following equation:

$$\vec{v}_M = \frac{dy}{d\tau} \tag{327}$$

where y is the vertical spatial coordinate.

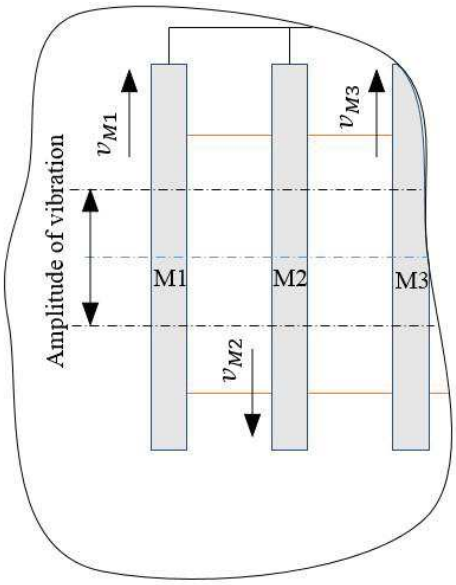

Figure 2.6: Schematic representation of the MMV system.

2.2.4 The influent mass balance

The mass balance of each component in the influent (including anaerobic bacteria) is described by advection-diffusion equation:

$$\frac{\partial \rho_i}{\partial \tau} = \sum_{j=1}^{N} \nabla \cdot \left(D_{ij} \nabla \rho_j\right) - \vec{v}_F \cdot \nabla \rho_i + R_{Ri} \tag{328}$$

where ρ_i and ρ_j are the mass concentrations of the components i and j, respectively, D_{ij} is the diffusion coefficient for the components i and j, R_{Ri} is the reaction rate of the component i.

The reaction rates of the chemical reactions occurring in the reactor are calculated according to AM2b model [127].

$$R_{OM} = -k_{OM} \mu_{AB} \rho_{AB} \tag{329}$$

$$R_{VFA} = -k_{VFA2} \mu_{MB} \rho_{MB} + (k_{VFA1} \mu_{AB} + b_{VFA} \mu_{SMP}) \rho_{AB} \tag{330}$$

$$R_{SMP} = (b_{SMP2} \mu_{AB} + D_0 - b_{SMP1} \mu_{SMP})\, \rho_{AB} + (b_{SMP3} \mu_{MB} + D_0)\, \rho_{MB} \tag{331}$$

$$R_{AB} = (\mu_{AB} + \mu_{SMP} - D_0) \rho_{AB} \tag{332}$$

$$R_{MB} = (\mu_{MB} - D_0) \rho_{MB} \tag{333}$$

$$\mu_{AB} = m_{AB1} \frac{\rho_{OM}}{\rho_{OM} + K_{OM}} \tag{334}$$

$$\mu_{MB} = m_{MB} \frac{\rho_{VFA}}{\frac{\rho_{VFA}^2}{K_{VFA2}} + \rho_{VFA} + K_{VFA1}} \tag{335}$$

$$\mu_{SMP} = m_{AB2} \frac{\rho_{SMP}}{\rho_{SMP} + K_{SMP}} \tag{336}$$

where R_{OM} is the reaction rate of organic matter degradation, R_{VFA} is the reaction rate of production/degradation of VFA, R_{SMP} is the reaction rate of SMP production/degradation, R_{AB} is the rate of AB formation/decay, R_{MB} is the rate of MB formation/decay, k_{OM} is the yield of organic matter degradation by AB, k_{VFA1} is the yield of VFA production from organic matter, k_{VFA2} is the yield of VFA degradation by MB, b_{SMP1} is the yield of SMP degradation by AB, b_{SMP2} is the yield of SMP production from organic matter, b_{SMP3} is the yield of SMP production from VFA, D_0 is the decay rate of biomasses, μ_{AB1} is the acidogenesis kinetics, μ_{MB} is the methanogenesis kinetics, μ_{SMP} is the kinetics of SMP degradation, m_{AB1} is the

maximum acidogenic biomass growth rate on organic matter, m_{AB2} is the maximum acidogenic biomass growth rate on SMP, m_{MB} is the maximum methanogenic biomass growth rate on VFA, K_{OM} is the half-saturation constant associated with organic matter, K_{VFA1} is the half-saturation constant associated with VFA, K_{VFA2} is the inhibition constant associated with VFA, ρ_{OM}, ρ_{VFA} and ρ_{SMP} are the mass concentrations of organic matter, VFA and SMP, respectively.

2.2.5 Boundary conditions

The equations in Sections 2.2.3.-2.3.4 could be solved using appropriate BCs. The initial concentrations of all the species in the influent, as well as the influent flow rate and pressure should be defined at the inlet of the AnMBR reaction tank. The velocities of the influent and membranes at feed-membrane interfaces must be determined. BCs for the outlet of the AnMBR tank characterize the outflow parameters, including the flow pressure. The full set of BCs is presented in Table 2.4.

Table 2.4: Boundary conditions for AnMBR model.

Boundary	Boundary conditions	Note
Reaction tank inlet	$\begin{cases} \vec{v}_C = \vec{v}_{C0} \\ \vec{v}_D = \vec{v}_{D0} \\ \phi_D = \phi_{D0} \\ \rho_i = \rho_{0i} \end{cases}$	v_C is the velocity of the liquid phase; v_{C0} is the velocity of the liquid phase at the inlet; ϕ_D is the volume fraction of solids in the influent; ϕ_{D0} is the volume fraction of solids in the influent at the inlet; ρ_i is the mass concentration of the component i; ρ_{0i} is the inlet mass concentration of the component i.
Reaction tank outlet	$\begin{cases} P = P_{out} \\ \tau_C n = \tau_D n = 0 \\ n \cdot (-D_{ij} \nabla \rho_i) = 0 \end{cases}$	P is the fluid pressure; P_{out} is the fluid pressure at the outlet; τ_C is the stress tensor of the liquid phase; τ_D is the stress tensor of the solid phase; D_{ijF} is the mutual diffusion coefficient for the components i and j; τ_T is the turbulent viscous stress tensor.

Feed-membrane interface	$\begin{cases} \vec{v}_{Cx} = \vec{v}_{TM} \\ \vec{v}_{Cy} = \vec{v}_M \\ \vec{v}_{Dx} = 0 \\ \vec{v}_{Dy} = \vec{v}_M \\ n \cdot \vec{J}_W = J_M \\ n \cdot \vec{J}_i = 0 \end{cases}$	v_{Cx} is the velocity of the liquid phase in the horizontal direction; v_{Cy} is the velocity of the liquid phase in the vertical direction; v_{Dx} is the velocity of the solid phase in the horizontal direction; v_{Cy} is the velocity of the solid phase in the vertical direction; v_{TM} is the transmembrane liquid velocity; v_T is the membrane velocity; J_i is the flux of the component i (except water); J_W is the water flux; J_M is the transmembrane water flux.
Feed wall	$\begin{cases} \vec{v}_C = 0 \\ \vec{v}_D = 0 \\ \phi_D \vec{v}_D \cdot n = 0 \\ n \cdot \vec{J}_i = 0 \end{cases}$	

3 Experimental procedures and literature results for model validation

3.1 Direct contact membrane distillation

For the validation of the DCMD model and further parametric study, several series of experiments had been carried out. In these experiments, two modules have been used. First of them is a commercial 45 cm long module containing 40 hollow fibres (Fig. 3.1). The second 17 cm long module was prepared in the lab from 3 hollow fibres (Fig. 3.1). The properties of the membranes used in the experiments are provided in Table 3.1.

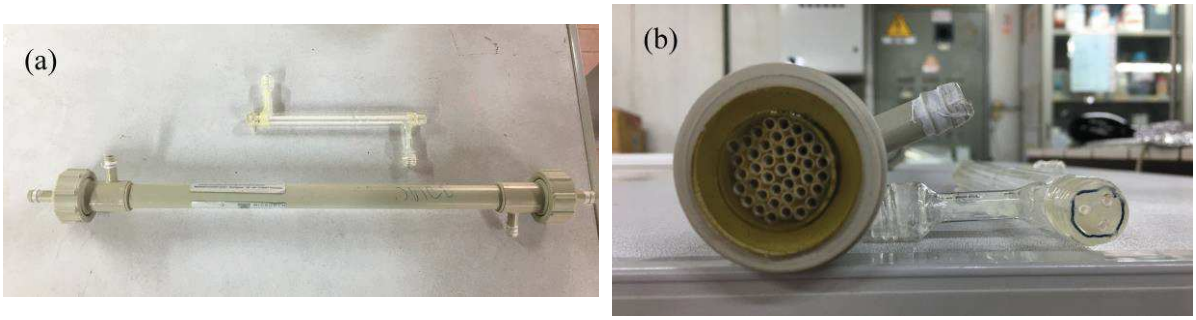

Figure 3.1: (a) The tested DCMD modules and (b) arrangement of the fibres inside the modules.

Table 3.1: Properties of the membrane used in the experiments

N	Module	Type	ID[1] (mm)	OD (mm)	Length (m)	Shell Diameter (m)	Porosity	Number of fibres	MPD[2] (μm)
1	Commercial	PP	1.8	2.7	0.45	0.021	0.73	40	0.2
2	Lab-scale	PP	1.8	2.7	0.17	0.011	0.73	3	0.2

Note: 1. ID and OD are the inner diameter and outer diameter of the hollow fibre membrane. 2. MPD is the mean pore diameter.

The first series of experiments was carried out using the commercial module and pure water as the feed and permeate. In this series, the effect of two parameters has been tested. The feed temperature, the first parameter, was varied from 35 to 55 °C while the permeate temperature remained 29 °C. The second parameter was the feed flow rate which was varied from 50 to 150 L/h. The input permeate flow rate was set constant at 50 L/h.

The second series of experiments was carried out using the commercial module and saline water as the feed. The concentration of NaCl in the feed solution was varied from 21.35 to 29.58 g/L. The entry feed and permeate temperatures remained 46±0.1 and 21±1 °C, respectively. The feed and permeate flow rates were set at 75 and 38 L/h, respectively.

The third series of experiments was carried out using the lab-scale module and saline water as the feed. In these experiments, the salinity of the feed brine increased from 248 g/L to the saturation point. The feed temperature was varied from 36 to 55 °C while the permeate temperature remained 10 °C. The feed and permeate flow rates were set at 9 and 4.2 L h^{-1}, respectively.

The scheme of the experimental setup used in DCMD test is shown in Fig. 3.2. The membrane unit was operated in a counter-current flow configuration. The feed and permeate were introduced at the lumen and shell side, respectively. The overall transmembrane vapour flux was calculated based on the measuring of permeate weight and total inner surface area of the hollow fibres.

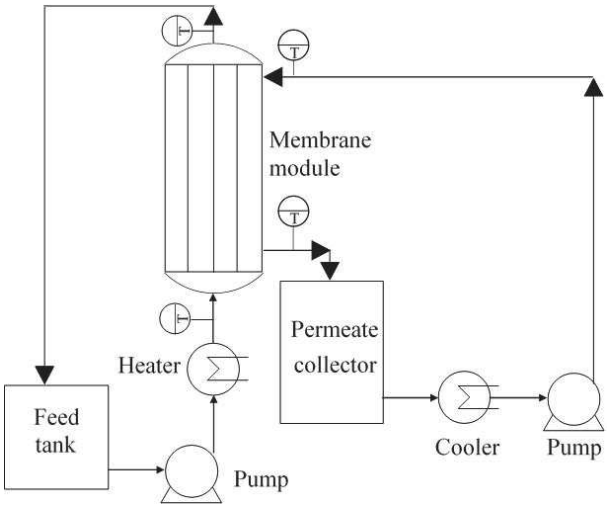

Figure 3.2: Schematic diagram of the experimental setup.

To ensure that the proposed model can be applied not only for the hollow but for the flat sheet DCMD configuration, the extra experimental data from literature (Eykens *et al.* [153]) had been used. In this study, the flat PE and PVDF membranes were used. The feed and permeate channels of the DCMD module were supported by spacers. The inlet feed and permeate temperatures were kept constant at 55.5 and 49.5 °C, respectively. The velocities of the feed and permeate flows were equal to each other and set at 0.13 m/s. The concentration of NaCl in the feed flow was varied from 0.13 to 23 wt%. Also, the additional literature data (Ali *et al.* [98]) was used in the membrane length study, in which two hollow fibre modules of different length and number of membranes were used. The feed and permeate temperatures were set at 40 and 20 °C. The inlet velocities of the feed and permeate flows were kept at 0.14 and 0.5 m/s. Full characteristics of the materials can be found in the corresponding publications [98, 153].

In a membrane thickness study, the properties of the commercial module (Table 3.1) have been used. The feed and permeate temperatures were set at 55 and 29 °C, respectively while the feed flow rate and permeate flow rate were kept at 150 and 50 L h^{-1}, respectively.

3.2 Sweeping gas membrane distillation

To validate the proposed SGMD model, experimental data from several publications with different SGMD configurations had been used (Mourgues *et al.* [76, 77], Karanikola et. al. [154, 155], and Khayet *et al.* [102]).

A first series of experiments were reported by Mourgues *et al.* [76, 77]. The experimental results were obtained with a flat sheet SGMD module without spacers in feed or permeate channels in countercurrent flow operation. Pure water was used as the feed liquid with a flow rate set 13.2 L h^{-1} while dry air under a pressure of 0.9×10^5 Pa was chosen as SG (flow rate set from 40 to 592 L h^{-1}). The temperature of the feed flow changed from 15 to 45±0.2 ^{o}C. The temperature of SG remained 20±2 ^{o}C during the experiments. The overall transmembrane vapor flux through the membrane was calculated using the measurement of the relative humidity at the inlet and outlet of the membrane module.

A second series of experiments was reported by Karanikola *et. al.* [154]. The experiments were carried out by using a flat sheet SGMD module with spacer-filled channels and the countercurrent flow operation. In that work, the feed brine at temperatures from 50 to 80 ^{o}C was recirculated through the SGMD module with the velocity of 0.11 m/s. The dry air was used as SG and its velocity was set at 9.5 m/s. The same research group [155] reported experimental results measured with the 0.127 m long hollow fibre SGMD module under countercurrent flow operation. In that study, the brine was fed in the lumen side at temperatures from 40 to 70 ^{o}C and velocities of 0.008 m/s and 0.02 m/s. Air, as SG, was blown into the shell side of the hollow fibres with the velocities from 0.13 to 0.78 m/s. The salinity of the feed brine was varied from 0 to 140 g/L.

The last series of experiments used for the model validation is based on the work reported by Khayet *et al.* [102]. In these experiments, the 0.45 m long commercial module hollow fibres was applied. The brine of different salinity was used as the feed while humid air was used as SG. The entry feed and permeate temperatures were set at 50 and 20 °C, respectively. The velocities of the feed brine and SG remained 0.8 and 11.3 m/s, respectively. The electrical conductivity of the feed brine was varied from 0 to 180 mS/cm. To estimate the

concentration of NaCl in the feed, the correlations between the salt concentration and electrical conductivity from literature [156] were used. The characteristics of the membranes and modules used in the studies are summarized in table 3.2. A more detailed description of the materials and methods for all the experimental data used for the model validation can be found in the original publications.

Table 3.2: Properties of the membrane used in the experiments.

Study	SGMD module configuration	Membrane				
		Material	Length (m)	Thickness (m)	Porosity (%)	MPD (μm)
Membrane contactor with hydrophobic metallic membranes: 1. Modeling of coupled mass and heat transfers in membrane evaporation [76]; Membrane contactor with hydrophobic metallic membranes: 2. Study of operating parameters in membrane evaporation [77]	Flat sheet	stainless steel AISI 316L	0.1646	0.00012	29	2.4
Effects of membrane structure and operational variables on membrane distillation performance [154]	Flat sheet with filler-supported channels	PVDF	0.145	0.000125	75	0.22
Sweeping gas membrane distillation: Numerical simulation of mass and heat transfer in a hollow fiber membrane module [155]	Hollow fibre	PVDF	0.127	0.00005	55	0.1
Theoretical and experimental studies on desalination using the sweeping gas membrane distillation method [102]	Hollow fibre	PVDF	0.45	0.00045	70	0.2

Note: MPD is the mean pore diameter.

3.3 Anaerobic membrane bioreactors

As the basis for simulations of AnMBRs, the experiments had been carried out by Matthias Mertens under the supervision of Dr. Ivo Vankelecom in KU Leuven, Belgium [9]. In the experiments, 6 flat sheet PVDF membranes had been used. These membranes were folded into envelopes and assembled into a module. The membrane module is immersed into an ethanol solution in the AnMBR tank for wetting purposes and then connected to the MMV system. The membrane module connected to the MMV system was vibrated in the vertical direction with the frequency set at 15 Hz. The parameters of the membrane module are indicated in Table 3.3. The properties of the simulated influent and operation parameters are shown in Table 3.4.

Table 3.3: Properties of the membrane and reactor used in the experiments.

Membrane material	Effective area (m2)	Number of membranes	Reactor height (m)	Reactor width (m)	Reactor width (m)
PVDF	0.016	6	0.2	0.15	0.19

Table 3.4: Properties of the influent and operation parameters.

Parameter	Value
Volume fraction of solids in the influent	0.003
COD in the feed (g/L)	3
Food to microorganism ratio (g COD / g MLSS day)	0.15
Organic loading rate (g COD/ L day)	2.1
HRT (days)	1.43
SRT (days)	20
Transmembrane flux (L/m^2 h)	7

4 Organisation of the simulation process

The developed mathematical models for DCMD and SGMD had been applied for the simulations using COMSOL Multiphysics™ software. The appropriate coordinate system had been applied according to the used module configuration. The Navier-Stokes equation and the k-epsilon Navier-Stokes model had been solved with the corresponding built-in interfaces of COMSOL Multiphysics™. To solve the other equations of the DCMD and SGMD models, the coefficient form PDE, general form PDE and domain ODEs interfaces had been applied. In the simulations, the calculated water vapour flux in all of the cases was evaluated as an average over the feed-membrane interface. The initial physical and chemical parameters of the feed and permeate as well as geometric characteristics of the membrane were imported from the experimental data and the referential publications [98, 102, 153-155]. Meshing of membrane modules had been done by using rectangles and triangles of various sizes. Sample fragments of the meshing of the commercial hollow fibre module and spacer-filled SGMD module are shown in Figs. 4.1 and 4.2, respectively.

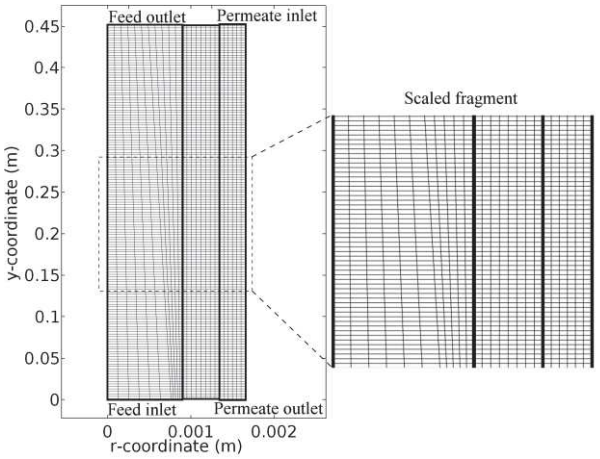

Figure 4.1: The meshing of the commercial hollow-fibre module.

The COMSOL Multiphysics™ software had also been applied for solving the proposed AnMBR model. For the simulations, the operation time of AnMBR had been set at 240 s. The geometric parameters of the membrane module and AnMBR tank were taken from experimental data. Values for the AM2b parameters were taken from the literature [7] and are summarised in Table 4.1. Meshing of membrane modules was done by using rectangles and triangles of various sizes. The meshing sample is demonstrated in Fig. 4.3.

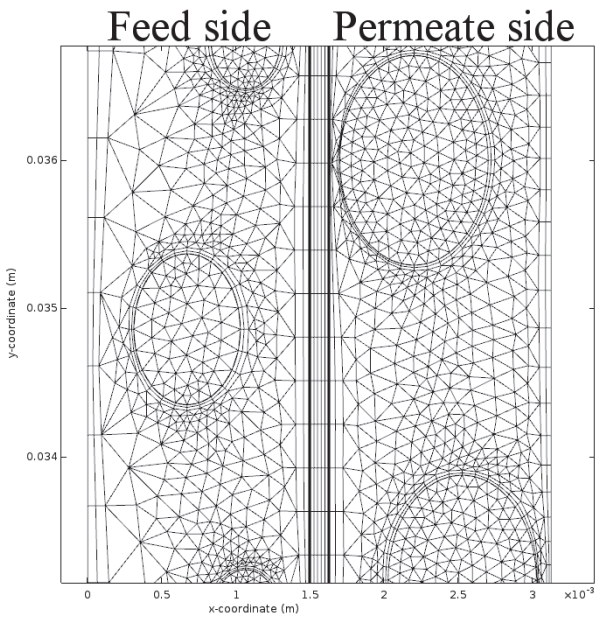

Figure 4.2: The sample fragment of the meshing of the spacer-filled SGMD module.

Table 4.1: Parameters for AM2b model [7].

Parameter	Value	Parameter	Value	Parameter	Value
k_{OM}	25	b_{SMP1}	0.6	m_{MB}	1.5
k_{VFA1}	15	b_{SMP2}	7	K_{OM}	16
k_{VFA2}	16.08	b_{SMP3}	5	K_{VFA1}	0.3
D_0	0.25	m_{AB1}	1.2	K_{VFA2}	0.9

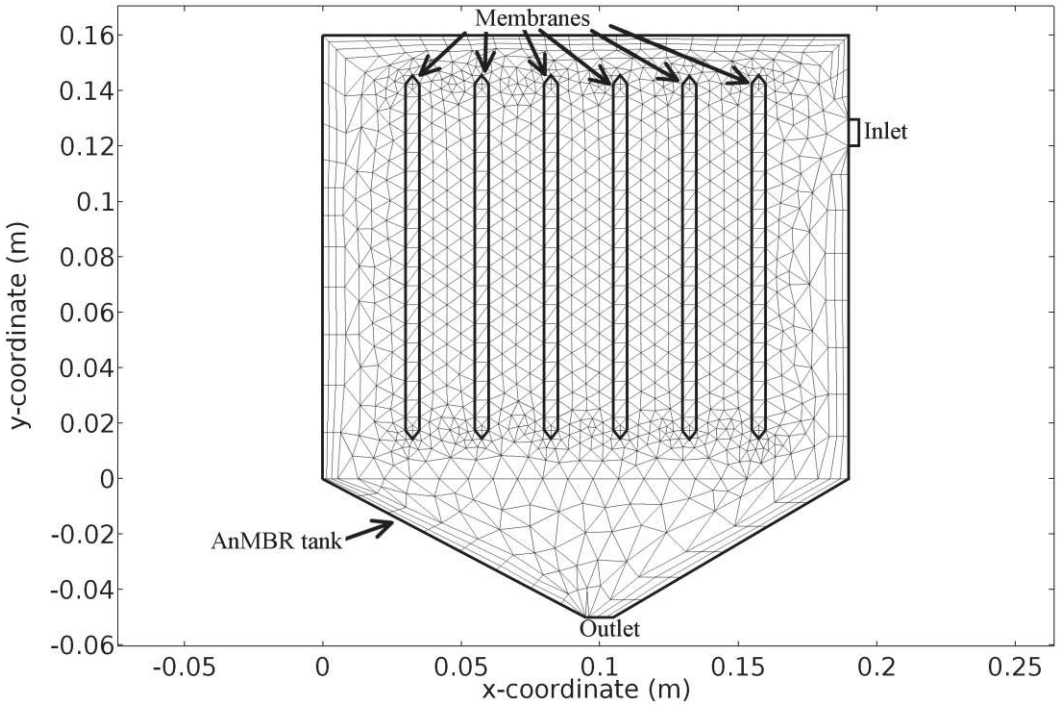

Figure 4.3: The meshing of AnMBR.

5 Results and discussion

In this section, the results of simulations of the DCMD, SGMD and AnMBR processes using the developed models (Section 2) are presented. For all of the simulated processes, the mesh, validation and parametric studies are performed. In the mesh study, the analysis of mesh elements and the choice of the optimal mesh for the validation and parametric studies are described.

5.1 Direct contact membrane distillation

5.1.1 Mesh study

The effect of the mesh on results of the simulation of the commercial hollow fibre DCMD has been analysed. In this study, 4 different meshes from the most dense (Fig. 5.1(a)) to the most coarse (Fig. 5.1(d)) have been applied in the simulations. Sizes of elements of the densest mesh vary in the range from 0.03×3 mm to 0.13×3 mm while, in the coarsest mesh, the mesh elements sizes are in between 0.03×11 mm and 0.13×11 mm. The meshes (Fig. 5.1) are analysed in terms of calculation times and relative errors of the domain mass balance, domain heat balance and transmembrane vapour and heat fluxes. To estimate the relative errors for the heat and mass balance, the difference between inlet and outlet flows has been compared to the simulated transmembrane flows.

Table 5.1 indicates the results of the mesh study for the commercial hollow fibre DCMD module. The results show that the increase in the size of the mesh elements seriously decreases the calculation time, however, the calculation error increases. Thus, for the feed domain, the increase in the mesh element size led to increase in the relative errors from 0.3 to 2.36% in the mass balance calculation and from 0.38 to 1.75% in the heat balance. For the permeate domain, the relative error has been increased from 0.12 to 1.41% in the mass balance calculation and from 0.26 to 1.23% in the heat balance calculation. At the same time, the simulated transmembrane vapour and heat fluxes remained almost the same and the calculation error is negligible. Simultaneously with the increase in the size of the mesh elements from the smallest (range from 0.03×3 mm to 0.13×3 mm) to the biggest (range from 0.03×11 mm and 0.13×11 mm), the calculation time has decreased by more than 5 times. Despite that decrease

in the calculation time, the densest mesh has been chosen as the basis for the simulations in the validation and parametric studies to increase the precision of the calculations and to reduce the computational error.

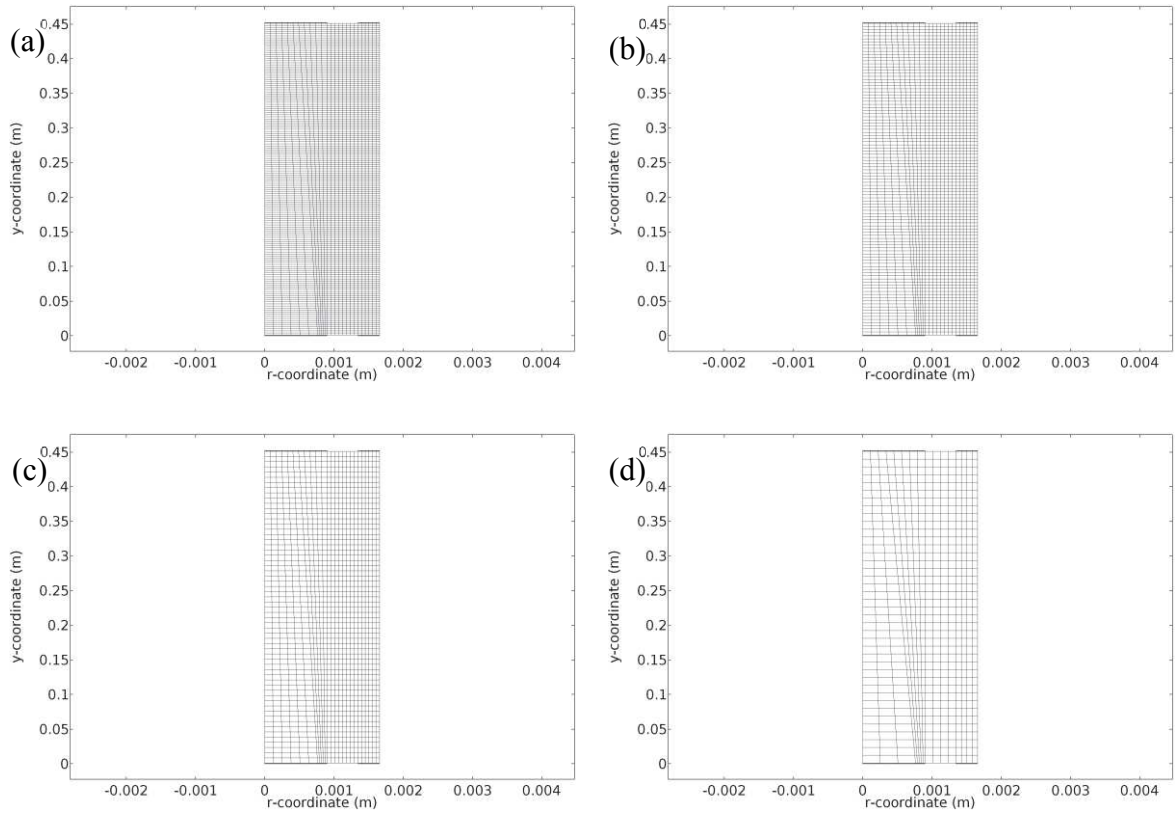

Figure 5.1: Graphical representation of the applied meshes in the mesh study for the commercial hollow fibre DCMD module.

Table 5.1: Results of the mesh study for the commercial hollow fibre DCMD module.

Mesh	Calculation time	Mass balance error - feed side (%)	Mass balance error - permeate side (%)	Transmembrane vapour flux error (%)	Heat balance error - feed side (%)	Heat balance error - permeate side (%)	Transmembrane heat flux error (%)
a	5 min 4 s	0.3	0.12	0.09	0.38	0.26	0.25
b	2 min 57 s	0.45	0.13		0.46	0.31	
c	1 min 23 s	0.83	0.35		0.72	0.63	
d	58 s	2.36	1.41		1.75	1.23	

5.1.2 Validation study

For the validation purpose, simulated data had been compared with the results of the experiments with the commercial and lab-scale hollow fibre modules. The details of the operating conditions and membrane parameters are described in Section 3.1. Figs. 5.2-5.5 show the results of the validation study and demonstrate the correlation between the experimental data (markers) and the simulated results (lines) and the corresponding goodness of fit. As can be seen in Figs. 5.2-5.5, the simulated results are in very good agreement with the experimental data and the goodness-of-fit is varied from 0.8992 to 0.9967 and from 0.8637 to 0.9986 for the simulations of the commercial hollow fibre module and the lab-scale hollow fibre module, respectively.

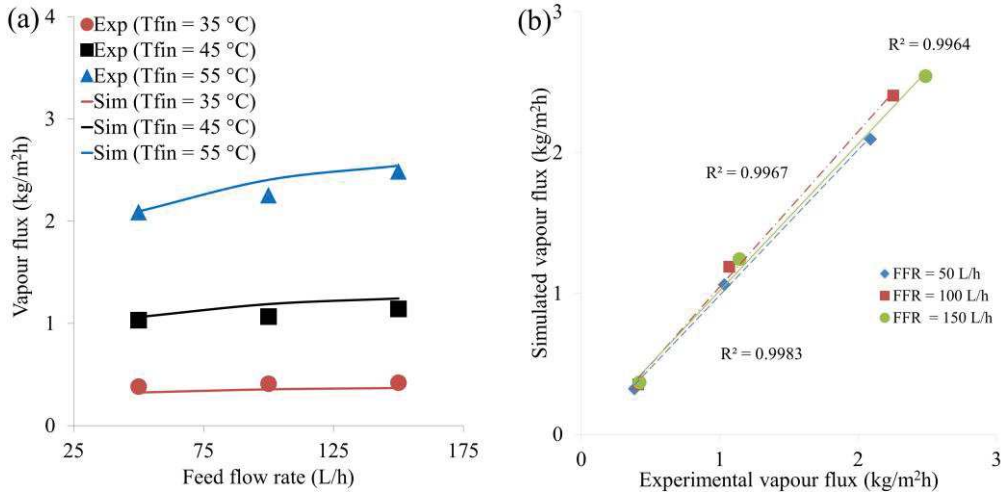

Figure 5.2: Validation of the DCMD model. (a) The effect of the feed flow rate on the performance of the commercial hollow fibre module and (b) the corresponding goodness of fit (T_F = 55 °C, T_P = 29 °C, $\dot{V}_P$ = 50 L h^{-1}).

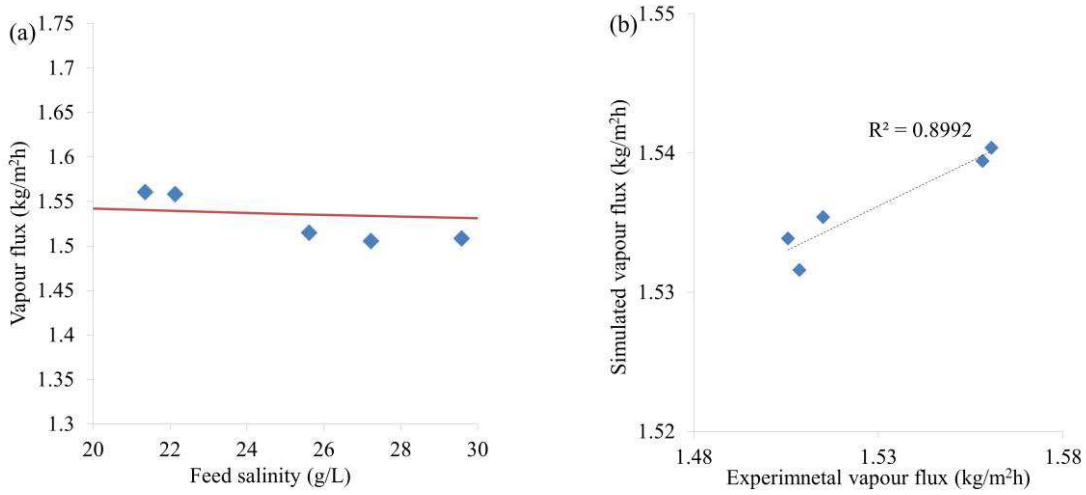

Figure 5.3: Validation of the DCMD model. (a) The effect of the feed salinity on the performance of the commercial hollow fibre module and (b) the corresponding goodness of fit (T_F= 46 °C, V_F=75 L/h, T_P= 20 °C, V_P=38 L/h).

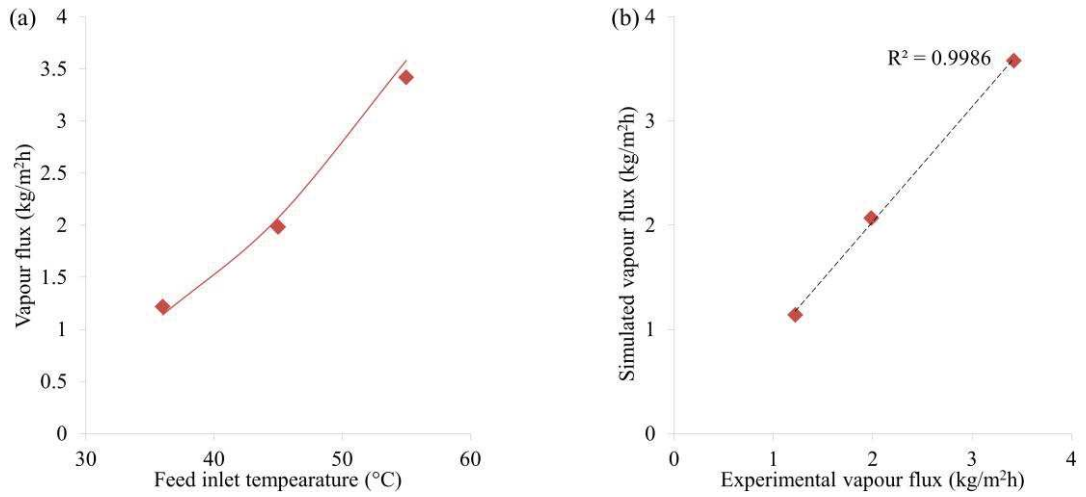

Figure 5.4: Validation of the DCMD model. (a) The effect of the feed flow rate on the performance of the lab-scale hollow fibre module and (b) the corresponding goodness of fit (T_F= 55 °C, V_F=9 L/h, T_P= 10 °C, V_P=4.2 L/h).

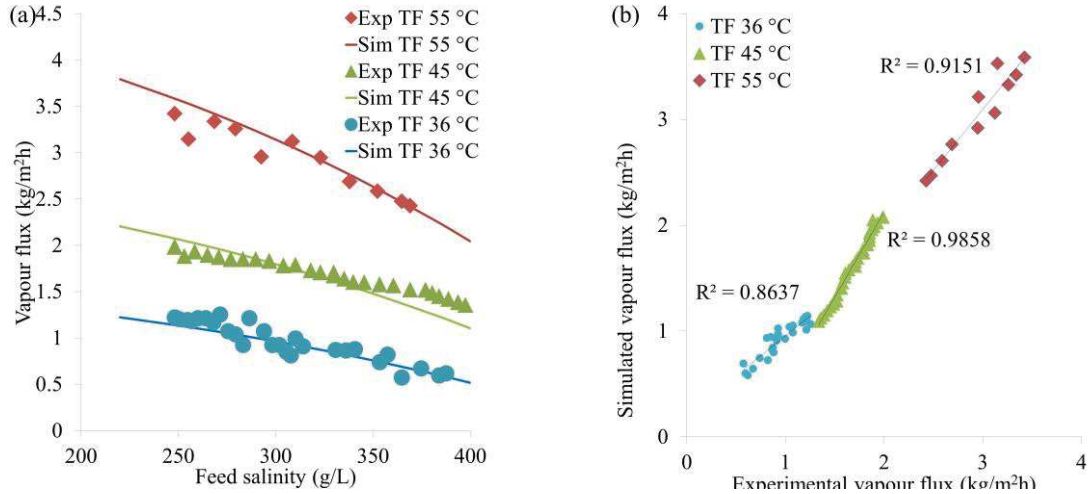

Figure 5.5: Validation of the DCMD model. (a) The effect of the feed salinity on the performance of the lab-scale hollow fibre module and (b) the corresponding goodness of fit (V_F=9 L/h, T_P= 10 °C, V_P=4.2 L/h).

5.1.3 Parametric study

In this section, the simulation results are presented for only one of the DCMD configurations (flat sheet or hollow fibre) due to similarity of the effects of operating conditions and membrane characteristics on the DCMD performance. Thus, the useless repetitions are avoided and the validation and flexibility of the model were presented.

5.1.3.1 Feed temperature and flow rate

In the simulations of the commercial hollow fibre module, the feed temperature rise from 35 to 55 °C is accompanied by the 5.9-fold increase in the vapour flux at the feed flow

rate set at 150 L/h (Fig. 5.2(a)). Also, the temperature drop at the feed-membrane interface from the feed inlet to the feed outlet increases from 1.5 °C to 6.5 °C (Fig. 5.6(a) and (b)). At the same time, the temperature of the permeate-membrane interface at the permeate outlet increases from 31 to 38.7 °C (Fig. 5.6(a) and (b)). According to the temperature increase, the changes occur in the water vapour concentration distribution in the membrane pores (Fig. 5.7(a) and (b)). The similar trends are observed in the simulations of the lab-scale hollow fibre module (Fig. 5.4(a)). In these simulations, the increase in the feed temperature from 35 to 55 °C leads to 2.8-fold increase in the vapour flux.

The increase in the feed flow rate from 50 to 150 L h^{-1} increases in the vapour flux by 13.5, 17.1 and 21.3% for cases with the feed inlet temperatures equal 35, 45 and 55 °C, respectively (Fig. 5.2(a)). Accordingly, the temperatures of the feed and permeate flows increase in the bulk phase and in the boundary layers (Fig. 5.8(a) and (b)). It is especially seen from the feed side where the temperature drop along the feed-membrane interface decreases from 10.5 to 6.5 °C (Fig. 5.8(a) and (b)). The changes in the temperature of the permeate flow are less visible due the increased velocity at the permeate-membrane interface and improved flow mixing.

The results of the DCMD simulations demonstrate an increase in the vapour flux with an increase in the feed temperature or the feed flow rate for all the studied configurations. The feed temperature rise increases the partial pressure of the water vapour at the feed-membrane interface and therefore enhances the driving force of the process. At the same time, this change also leads to increase in the permeate temperature and TP in DCMD which has the opposite effect. The final result is then given by proportion of these contributions.

The increase in the feed flow rate also increases the feed temperature at the feed-membrane interface by enhanced mixing of the feed flow and reduction of TP in the feed channel despite a slight negative effect of increasing of TP in the permeate channel.

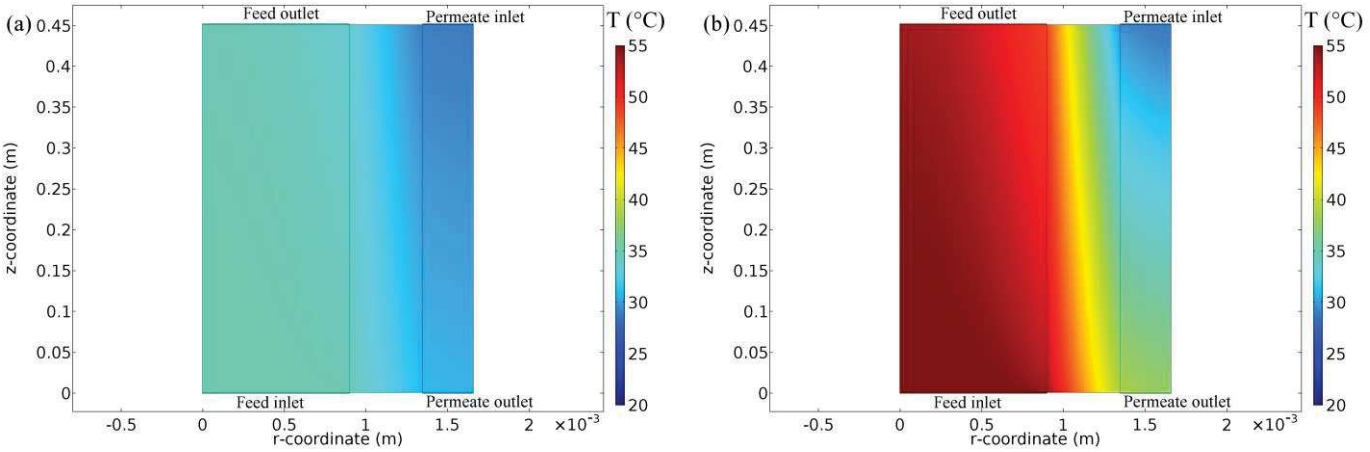

Figure 5.6: Feed temperature study. The simulated temperature distributions in the commercial hollow fibre module for the feed inlet temperature equal to (a) 35 and (b) 55 °C, respectively ($\dot{V}_F$ = 150 L h^{-1}, T_P = 29 °C, $\dot{V}_P$ = 50 L h^{-1}).

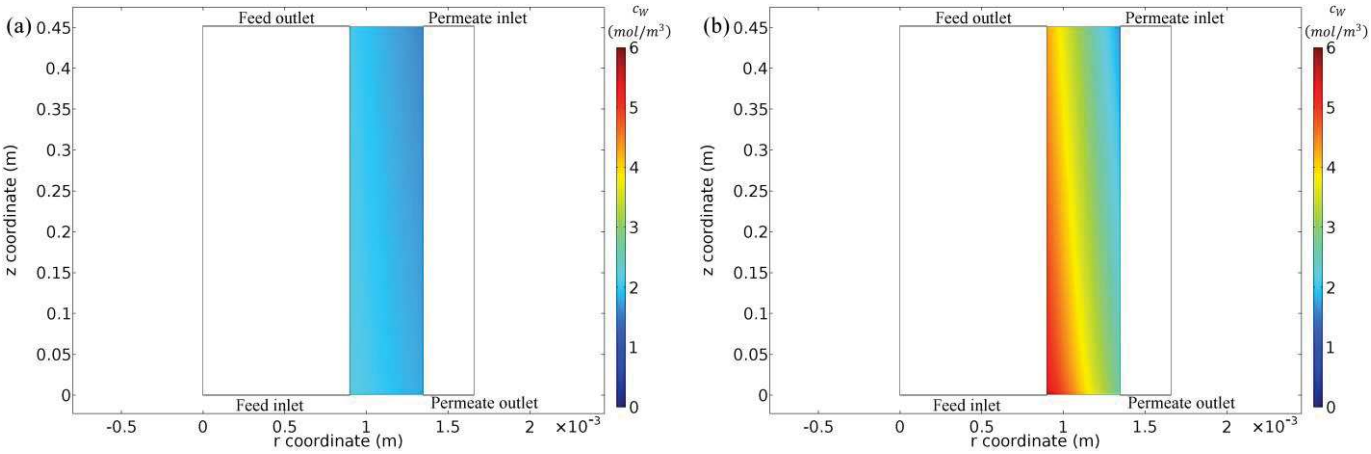

Figure 5.7: Feed temperature study. The simulated water vapour concentration distributions in the membrane pores of the commercial hollow fibre module in the simulations for the feed inlet temperature equal to (a) 35 and (b) 55 °C, respectively ($\dot{V}_F$ = 150 L h^{-1}, T_P = 29 °C, $\dot{V}_P$ = 50 L h^{-1}).

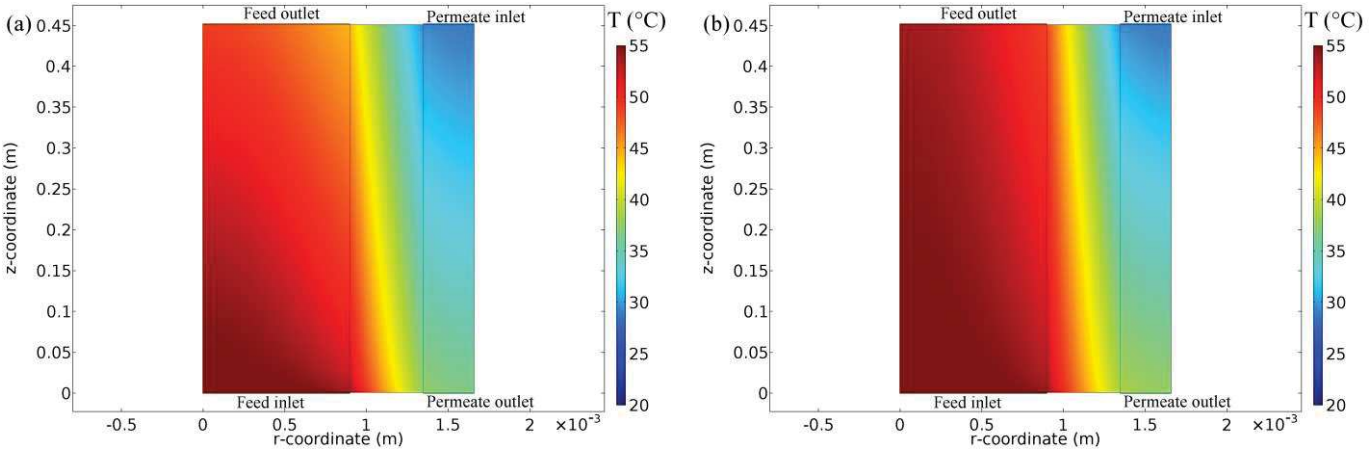

Figure 5.8: Feed temperature study. The simulated temperature distributions in the commercial hollow fibre module for the feed rate equal to (a) 50 and (b) 150 L h^{-1}, respectively (T_F = 55 °C, T_P = 29 °C, $\dot{V}_P$ = 50 L h^{-1}).

5.1.3.2 Feed salinity

In the salinity study, the salt concentration at the feed inlet was increased from zero to saturation. Fig. 5.9 indicates the dependence of the transmembrane vapour flux on the feed salinity for the PE and PVDF membranes. The experimental data (denoted by markers on Fig. 5.9) validated the simulation results (denoted by lines on Fig. 5.9). The study showed that the presence of dissolved salts in the feed solution reduces the water vapour flux in the DCMD process. The decrease in the transmembrane flux with the increase in salinity is explained by the decrease of the water activity at the feed-membrane interface and in the partial pressure of water vapour in the membrane pores. At the same time, due to insignificant changes of the heat flux through the membrane, TP across and along the DCMD unit remains constant. For the simulations of the spacer-filled flat sheet DCMD module, the increase in the feed salinity led to decrease in the vapour flux up to zero and even obtain a reverse vapour flux from the permeate side to the feed side (Fig. 5.9). The negative vapour flux can be explained by the negative value of the difference between the partial pressures of the water vapour at the feed-membrane interface and permeate-membrane interface, respectively (Fig. 5.10(a) and (b)). Although the feed stream was introduced into the module at high temperature (55.5 ^{o}C) compared to the permeate stream (49.5 ^{o}C), the presence of high quantity of salt in the feed stream suppresses the water vapour pressure below the vapour pressure of the pure permeate stream (corresponding BC for the water vapour concentration in Table 2.2) and consequently a net negative flux is observed. In other words, the process behaves as osmotic membrane distillation instead of simple (thermal) membrane distillation under these conditions.

The increase in the salt concentration decreases the concentration of the water vapour at the feed-membrane interface while at the permeate-membrane interface the concentration remains constant. At the same time, the salt concentration in the feed channel does not visibly change along and across the channel (Fig. 5.11(a) and (b)).

The similar effect of the feed salinity on the process performance for the commercial and lab-scale hollow fibre modules is observed (Figs.5.3(a) and 5.5(a)). Thus, in the simulations of the commercial hollow fibre module (Fig.5.3(a)), the increase in the feed salinity from 20 to 30 g/L is accompanied by the decrease in the vapour flux from 1.54 to 1.53 kg/(m^2 h). The more significant increase in the feed salinity from 220 to 400 g/L leads to 2.4-, 2- and 1.9-fold decreases in the vapour flux in the simulations of the lab-scale hollow fibre module with the input feed temperatures set at 36, 45 and 55 ^{o}C, respectively (Fig. 5.5(a)).

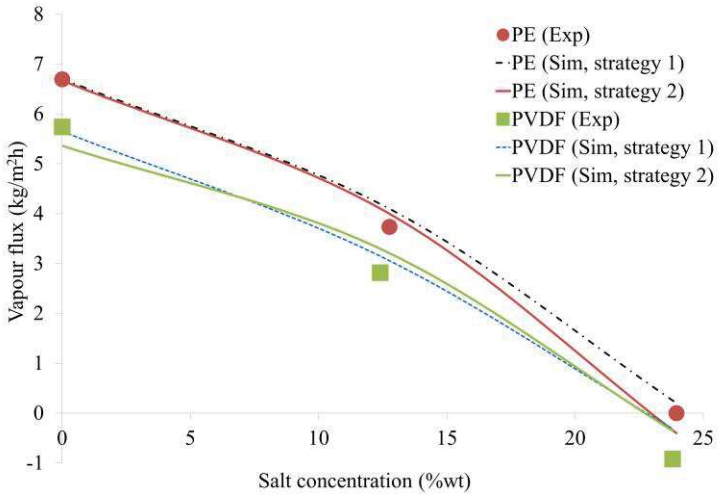

Figure 5.9: Validation of the model and effect of the feed salinity on the performance of the filler-supported flat sheet DCMD module [153].

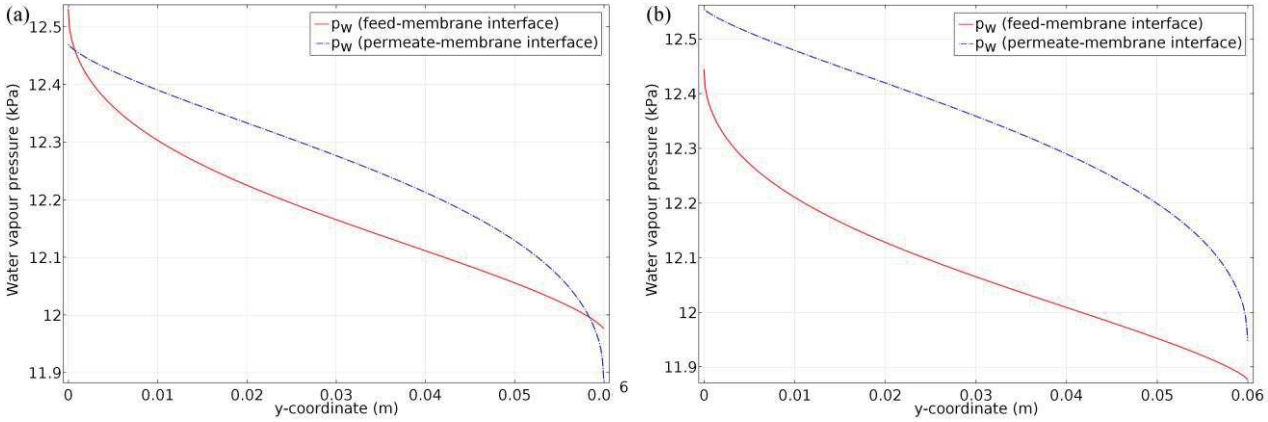

Figure 5.10: Feed salinity study. The calculated water vapour pressure at the feed-membrane and permeate-membrane interfaces in the spacer-filled flat sheet module for the (a) PE membrane and (b) PVDF membrane, respectively (simulation strategy 2, T_F = 55.5 °C, v_F = 0.13 m/s, c_{Salt}=240 g/L, T_P = 49.5 °C, v_P = 0.13 m/s).

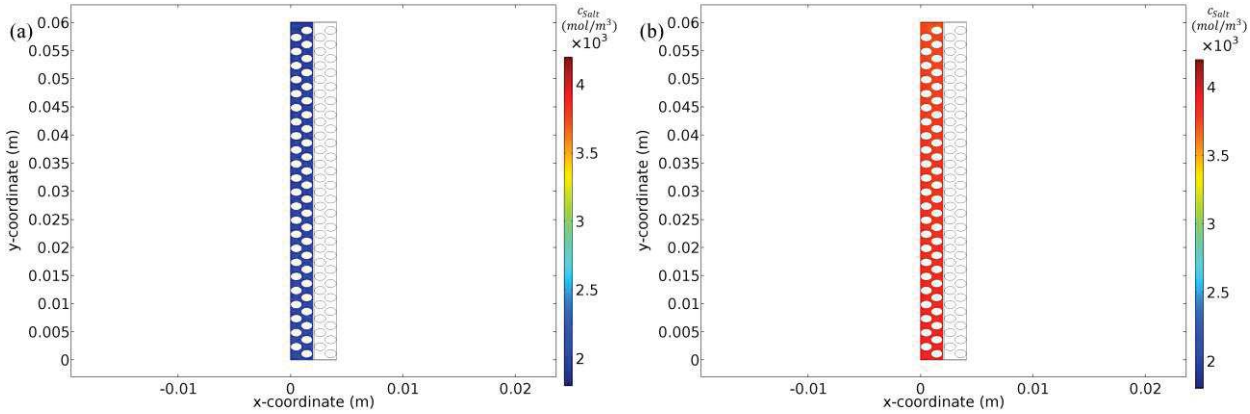

Figure 5.11: Feed salinity study. The simulated salt concentration distributions in the spacer-filled flat sheet module for the salinity equal to (a) 120 and (b) 230 g/L, respectively (simulation strategy 1, T_F = 55.5 °C, v_F = 0.13 m/s, T_P = 49.5 °C, v_P = 0.13 m/s).

5.1.3.3 Membrane length

The selection of appropriate module length is crucial from the practical implementation point of view, thus an appropriate model must be able to predict the module performance as function of its length. The effects of the module length on vapour flux and the temperature distribution profile in the membrane module are shown in Fig. 5.12(a) and (b), respectively. As evident from Fig. 5.12(a), the flux predicted by the model agrees well with the experimental results from literature data [98]. As illustrated, an increase of the membrane length from 0.2 to 0.7 m reduces the transmembrane flux by 11.7% (Fig. 5.12(a)). Fig. 5.12(b) shows the temperature profiles at the outlet of feed compartment for modules of different length. TP increases with the increasing length of membrane module. The reduction of the water vapour flux and temperature at the feed-membrane interface is due an increase in the residence time inside the module and extension of the contact area. With the increasing contact area, the total exchanged heat between the feed and permeate compartment increases. It results in the decrease in the temperature at the feed-membrane interface and increase in temperature at the permeate membrane interface. Consequently, the driving force of the process is decreasing. However, as evident from the Fig. 5.12(b) and Fig. 5.13, that temperature changes are not crucial (in the range of 3 °C).

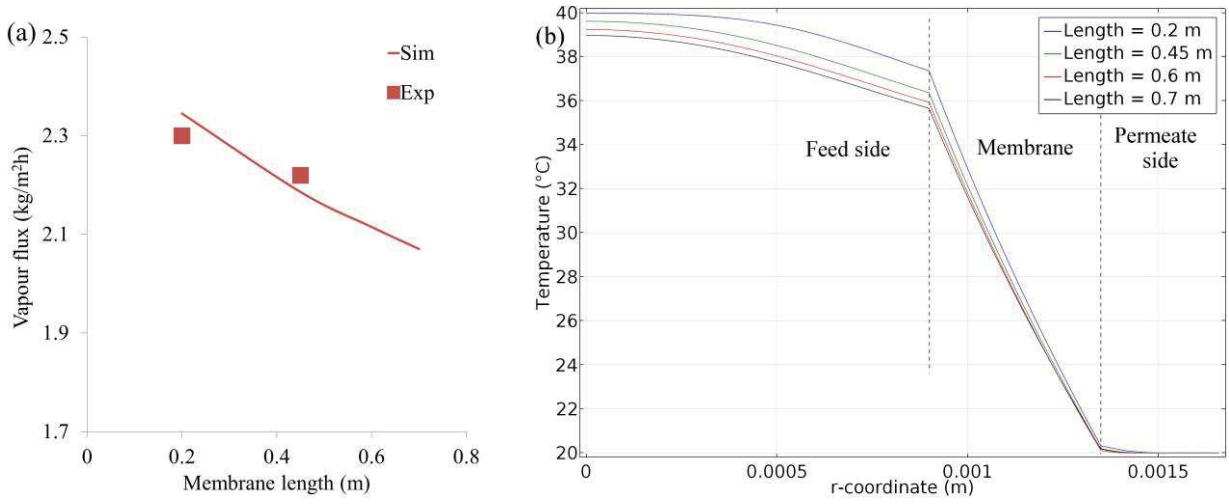

Figure 5.12: Validation of the model and effect of the membrane length on the performance of the hollow fibre DCMD module. (a) Effect of the permeate flow rate on the transmembrane flux. Experimental results from the reference [98]. (b) Temperature profiles in the DCMD module at the feed outlet for the given membrane lengths (T_F = 40 °C, v_F = 0.14 m/s, T_P = 20 °C, v_P = 0.5 m/s).

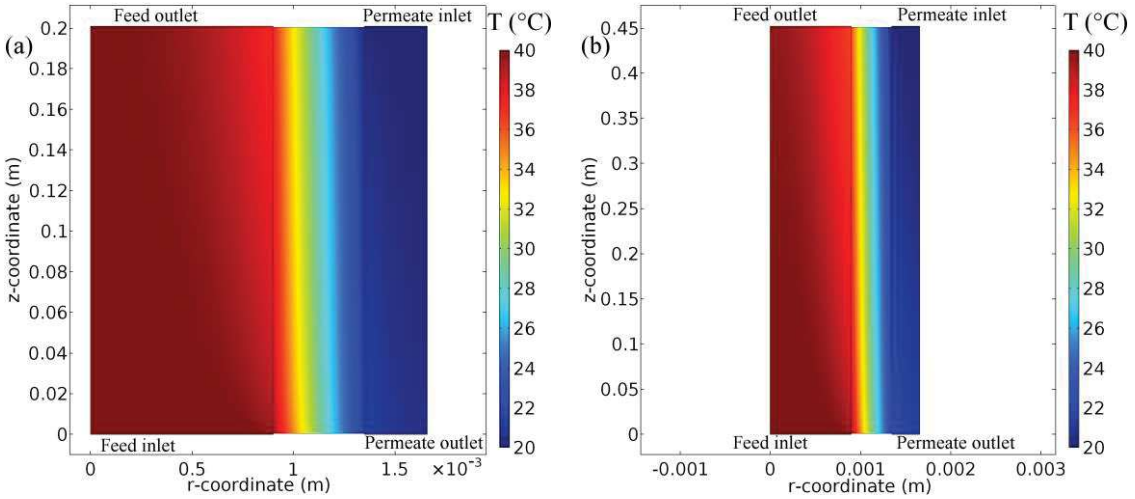

Figure 5.13: Membrane length study. The simulated temperature distributions in the hollow fibre module for the membrane length equal to (a) 0.2 and (b) 0.45 m, respectively (T_F = 40 °C, v_F = 0.14 m/s, T_P = 20 °C, v_P = 0.5 m/s).

5.1.3.4 Membrane thickness

The simulations of the effect of membrane thickness on the water vapour flux and the temperature profile within the feed channel are shown in Fig. 5.14(a) and (b). As expected from the theory (Sections 1.1.1 and 2.1.4.2), the increase in the membrane thickness reduces TP (Fig. 5.14(b)). The increased thickness of the membrane offers more resistance to the transmembrane mass transfer by decreasing a gradient of the partial water vapour pressure. Therefore, the water vapour flux decreased from 2.89 to 2.19 kg/(m^2 h) with the increase in the membrane thickness from 0.35 to 0.55 mm (Fig. 5.14(a)).

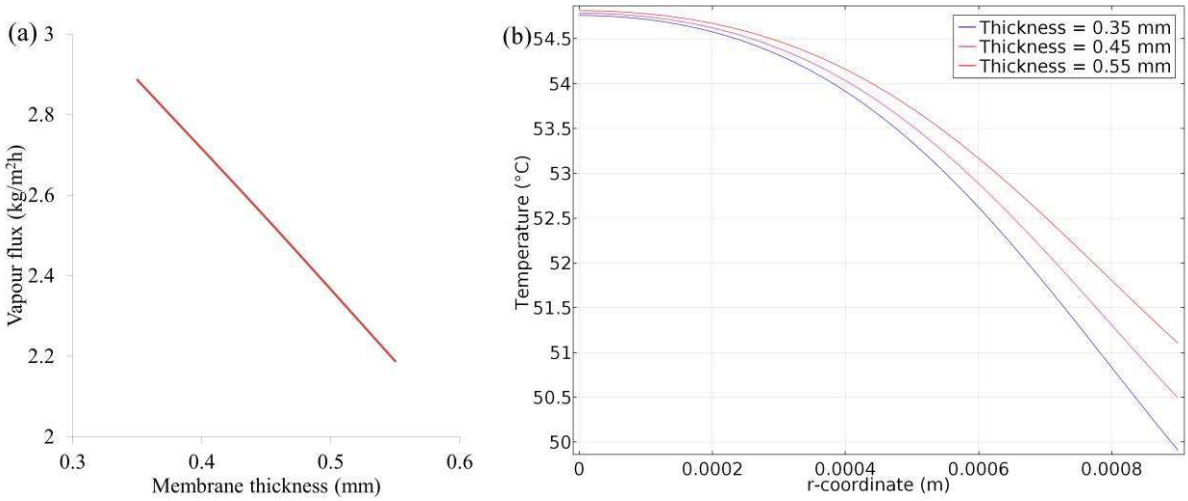

Figure 5.14: (a) Effect of the membrane thickness on the transmembrane flux and (b) temperature profile of the lumen side of the hollow fibre (feed compartment) at the reference position 0.25 m from the entrance of the feed channel.

5.2 Sweeping gas membrane distillation

5.2.1 Mesh study

Similarly to the DCMD mesh study, the study of the effect of the mesh element size on the calculation errors has been carried out for the flat sheet SGMD module. Fig. 5.15 indicates the applied meshes from the densest to the coarsest. The sizes of the mesh elements are varied in the range from 0.03×0.73 mm to 0.92×0.73 mm for the densest mesh and in the range from 0.03×0.63 mm to 2.76×0.63 mm. The relative errors of the mass balance and heat balance calculations and calculation times had been analysed.

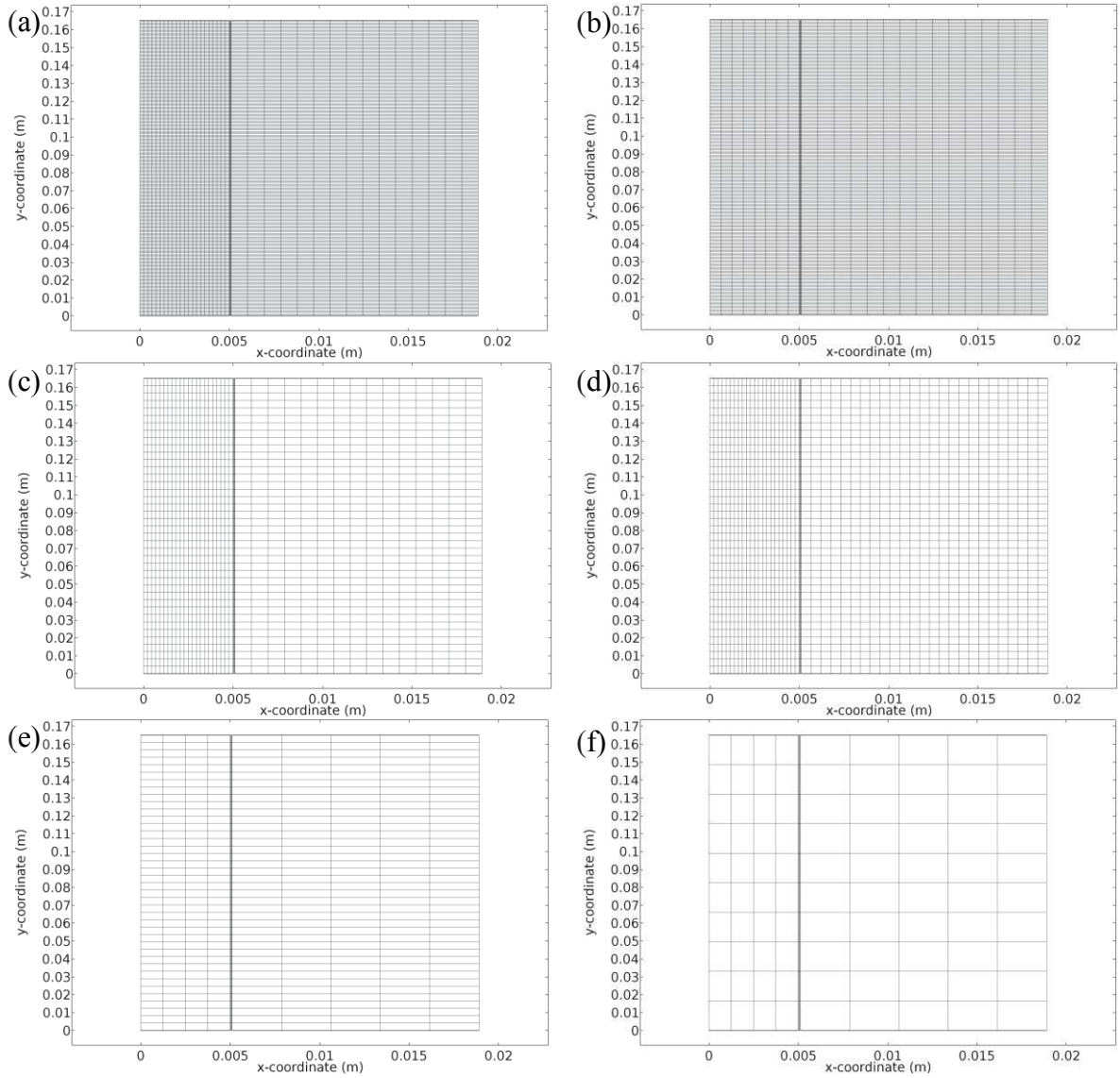

Figure 5.15: Graphical representation of the applied meshes in the mesh study for the flat sheet SGMD module.

Results of the mesh study show that the increase in the size of the mesh elements decreases the calculation time but seriously increases the calculation error (Table 5.2). For the mesh with the smallest elements (Fig. 5.15(a)), the relative error for the mass balance calculations reaches the values of 0.23 and 0.22% for the feed side and permeate side, respectively. The corresponding relative errors for the heat balance calculations do not exceed 0.6%. However, for the mesh with the coarse elements (Fig. 5.15(f)), the relative error increases up to 10% for the mass balance calculations (feed side) and up to 3% for the heat balance calculations. However, the calculation procedure for the coarse mesh is 60 times faster than for the small mesh. Table 5.2 indicates that the ideal mesh for calculations can be chosen between the options (b) and (d) with the small relative error and fast calculation process. Thus, for the validation and parametric studies (Sections 5.2.2 and 5.2.3, respectively) the option (b) with the sizes of the mesh elements in the range from 0.03×0.73 mm to 0.92×0.73 mm has been chosen as an optimal.

Table 5.2: Results of the mesh study for the flat sheet SGMD module.

Mesh	Calculation time	Mass balance error - feed side (%)	Mass balance error - permeate side (%)	Transmembrane vapour flux error (%)	Heat balance error - feed side (%)	Heat balance error - permeate side (%)	Transmembrane heat flux error (%)
a	20 min 5 s	0.23	0.22	0.47	0.54	0.46	0.35
b	5 min 23 s	0.24	0.33		0.83	0.73	
c	2 min 21 s	0.26	0.33		0.93	0.81	
d	2 min	0.35	0.44		1.49	1.03	
e	29 s	8.01	1.54		1.89	1.19	
f	19 s	9.67	3.75		2.84	1.94	

5.2.2 Validation study

The experimental data obtained by Mourgues *et al.* [76, 77] and described in Section 3.2 had been applied for the validation of the general predictive model for sweeping gas membrane distillation. Fig. 5.16(a) represents the comparison of the simulated results (lines) with the literature data (markers) and Fig. 5.16(b) demonstrates the goodness of fit of the proposed model. The results of the validation study show the good agreement between the simulated and literature data with the goodness of fit equal to 0.9944.

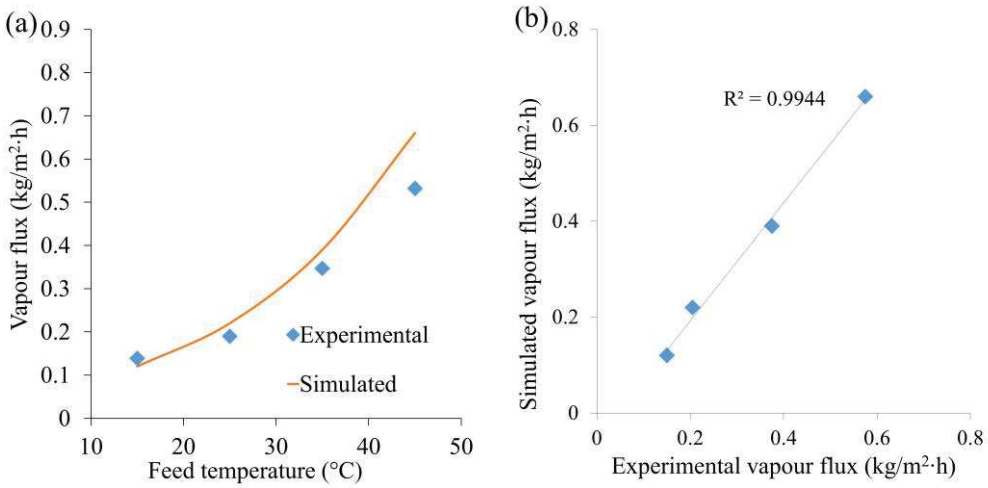

Figure 5.16: Validation of the SGMD model. (a) The effect of the feed temperature on the performance of the flat sheet SGMD module and (b) the corresponding goodness of fit (v_F=5.6×10^{-3} m/s, v_P=9.3×10^{-2} m/s, T_P= 20 °C).

5.2.3 Parametric study

5.2.3.1 Feed temperature

The simulation results with the flat sheet SGMD module without spacers are shown in Fig. 5.16 and compared with experimental data [76, 77]. It is observed that the feed inlet temperature enhancement from 15 to 45 °C is accompanied by the 5.7-fold increase of the vapour flux (Fig. 5.16(a)). As can be seen from the temperature profiles of the feed and permeate sides (Fig. 5.17), the TP effects for all the cases of feed temperatures are minor on the feed side. However, TP is not negligible on the permeate side with a maximum difference between the permeate-membrane interface temperature and the permeate wall temperature reaching 21.4 °C. It is worth mentioning that the SGMD process occurs even in the case when the feed temperature was less than the temperature of SG in the permeate side which is impossible for direct contact membrane distillation (DCMD).

The simulation results of the evolution of the vapour flux vs. the feed temperature show a simultaneous enhancement for all of the studied configurations. This behaviour was expected because the temperature enhancement results in an increase in the partial pressure (concentration) of the water vapour at the feed-membrane interface leading to the increase in the gradient of the partial pressure of the water vapour across the membrane. For all of the simulations, the predicted results are in good agreement with experimental data (Figs. 5.16(a) and 5.18) .

In contrast to the feed temperature, the change of SG temperature has a negligible positive effect on the SGMD performance. The water vapour flux remains almost constant (only 3.8% increase in the water vapour flux at the permeate temperature rise from 15 to 45 ºC is obtained) because the water vapour concentration at the permeate-membrane interface is mainly influenced by the inlet flow of SG. Moreover, the increase in the permeate temperature positively increases diffusion in gases and reduces TP. The similar effect of the feed temperature on the water vapour flux is noticed in the simulations of the spacer-filled flat sheet module (Fig. 5.18(a)) and the hollow fibre module (Fig. 5.18 (b)). For the spacer-filled flat sheet module, the increase in the feed temperature from 50 to 80 ºC is accompanied by the 3.2-fold increase in the vapour flux. For the hollow fibre module, the feed temperature rise from 40 to 75 ºC increases the vapour flux in 3.6 and 5.8 times for the simulations with the feed velocity equal to 0.008 and 0.02 m/s, respectively.

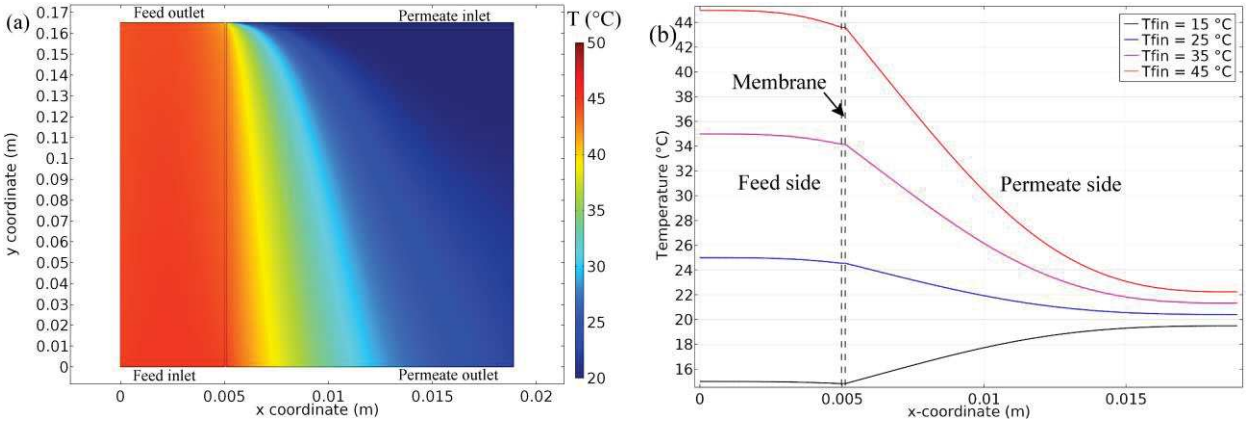

Figure 5.17: Effect of the feed inlet temperature on the temperature distribution in the flat sheet module. (a) The temperature distribution in the module at T_{Fin}= 45 °C. (b) Temperature profiles of the module at chosen reference position 0.087 m from the entrance of the feed channel (v_F=5.6×10^{-3} m/s, v_P=9.3×10^{-2} m/s, T_P= 20 °C).

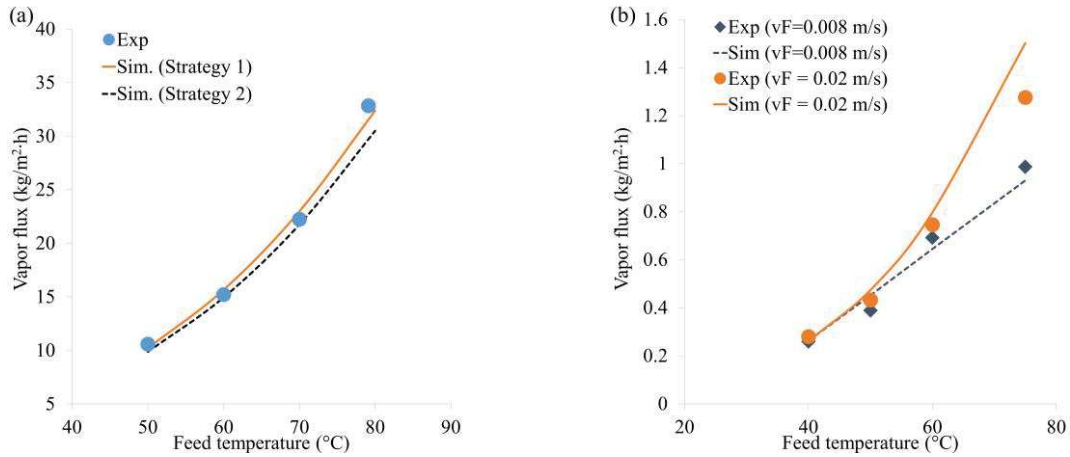

Figure 5.18: Effect of the feed temperature on the water vapour flux at (a) the spacer-filled flat sheet module (v_F=5.6×10^{-3} m/s, v_P=9.3×10^{-2} m/s) and at (b) the hollow fibre module (v_F=5.6×10^{-3} m/s, v_P=9.3×10^{-2} m/s).

5.2.3.2 Feed velocity

For the feed velocity study, the literature data for the hollow fibre SGMD module were used [155]. In this study, the increase in the feed velocity from 0.008 to 0.02 m/s is accompanied by an enhancement on the vapour flux of 1.3- and 1.6-fold for feed inlet temperatures of 60 and 71 ^{o}C, respectively (Fig. 5.19(a)). There is no perceptible TP at both feed and permeate sides of module for simulated experimental conditions. Despite the small increase in the vapour flux, the temperature profile along the module varied significantly (Figs. 5.19(b) and (c)). E.g. for the case of 71 ^{o}C of feed inlet temperature at referential position 0.06 m from the feed entrance, temperature on the feed and permeate sides increases from 43 to 66.5 ^{o}C when, the feed velocity increases from 0.008 m/s to 0.02 m/s (Fig. 5.19(d)). Further increase in the feed velocity from 0.02 to 0.03 m/s does not increase the vapour flux (Fig. 5.19(a)) because the maximum driving force of the process has been reached.

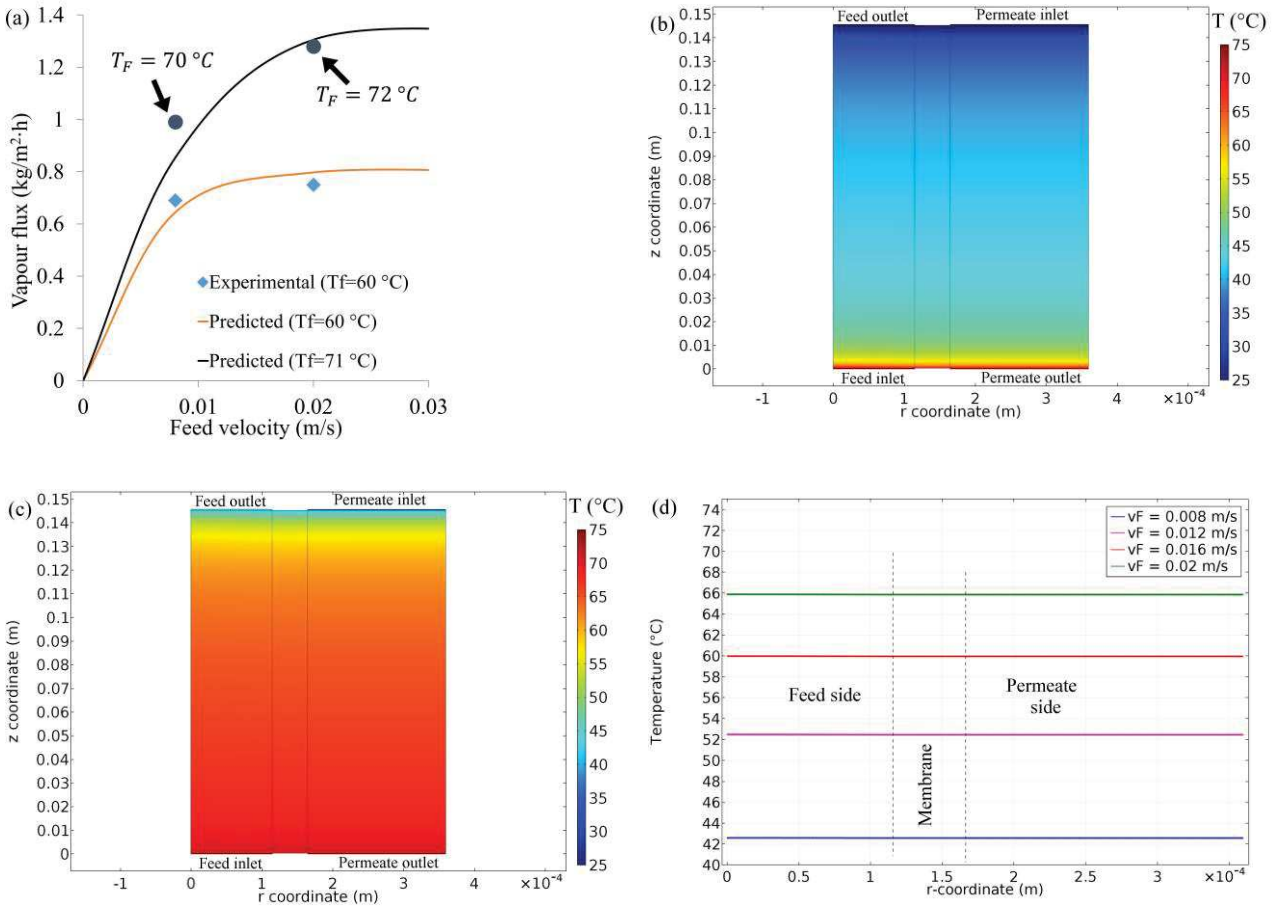

Figure 5.19: Validation of the model with the hollow fibre SGMD module and effect of the feed velocity on the module performance. (a) Water vapour flux as function of the feed velocity. (b) The temperature distribution in the module at v_F= 0.008 m/s. (c) The temperature distribution in the module at v_F= 0.02 m/s. (d) Temperature

profiles of the module at reference position 0.06 m from the entrance of the feed channel for the case of the feed inlet temperature 71 °C (v_P=0.54 m/s).

5.2.3.3 Sweeping gas velocity

Results of the simulations, together with the literature data, present a direct relationship between the water vapour flux and the SG velocity. For instance, in the case of the simulations with the spacer-filled SGMD module [154], the increase in the velocity of the sweeping air from 2 to 12 m/s (Fig. 5.20(a)) enhances the vapour flux by 86%. Also, the 2.1-fold increase in the vapour flux is reached with the increases in the SG velocity from 0.13 to 0.93 m/s (Fig. 5.21(a)). For the hollow fibre module, the 5.8-fold increase in the vapour flux is achieved at the increase in the SG velocity from 0.1 to 0.8 m/s at the feed temperature equal to 70 °C (Fig. 5.21(b)). These results can be explained by the improved mixing of the water vapour and air in the permeate side and further decrease of the vapour concentration at the permeate-membrane interface. That reduction led to increase of the water vapour concentration gradient. At the same time, the improved permeate velocity increases TP (Fig. 5.20(b)) causing the decrease in the concentration of the water vapour at the feed-membrane interface.

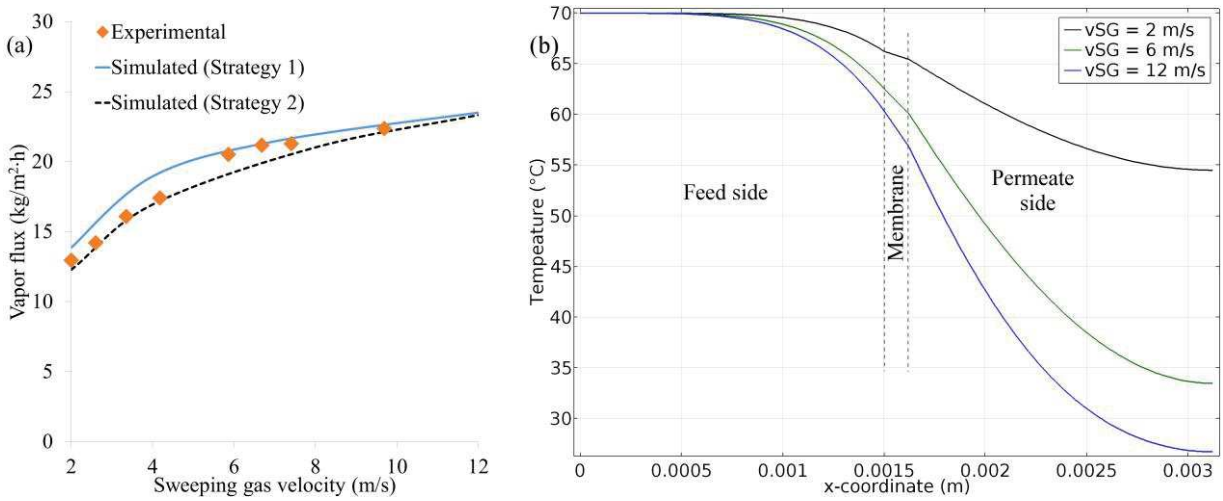

Figure 5.20: Validation of the model with the spacer-filled flat sheet SGMD module and effect of the permeate velocity on the module performance. (a) Water vapour flux as function of the permeate velocity. (b) Temperature profile of the module at reference position 0.07 m from the entrance of the feed channel (Strategy 2, T_F= 70 °C, v_F=0.11 m/s).

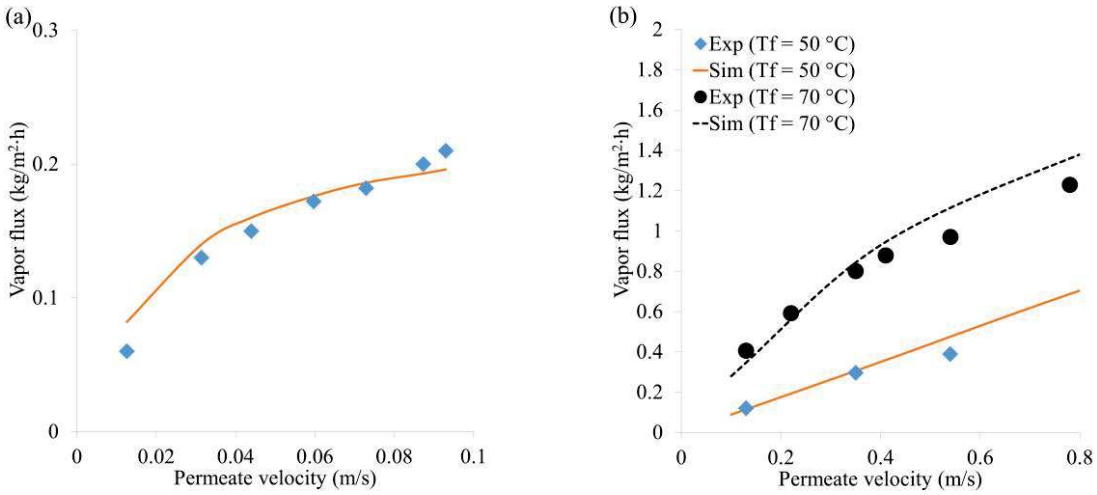

Figure 5.21: Validation of the model and effect of the SG velocity on the water vapour flux at (a) the flat sheet module (T_F= 25 °C, T_P= 20 °C, v_F=5.6×10^{-3} m/s) and at (b) the hollow fibre module (T_P= 24 °C, v_F=0.02 m/s).

5.2.3.4 Feed salinity

Results of the brine salinity study indicate a slight reduction of the water vapour flux with the increase in salt concentration. In the case of the simulation of the 0.45 m long commercial hollow fibre module [102], the vapour flux is decreased only by 9.2% with the increase in the NaCl concentration in the feed flow from 0 to 120 g/L (Fig. 5.22(a)). For the 0.127 m long hollow fibre module [155], the increase in the feed salinity is accompanied by the decrease in the vapour flux by 8.5% (Fig. 5.22(a)). These slight drops in efficiency are explained by the reduction of the driving force of the process due to the decrease of water vapour partial pressure (concentration) at the feed-membrane interface as consequence of the decrease of the water vapour saturation pressure over saline solution.

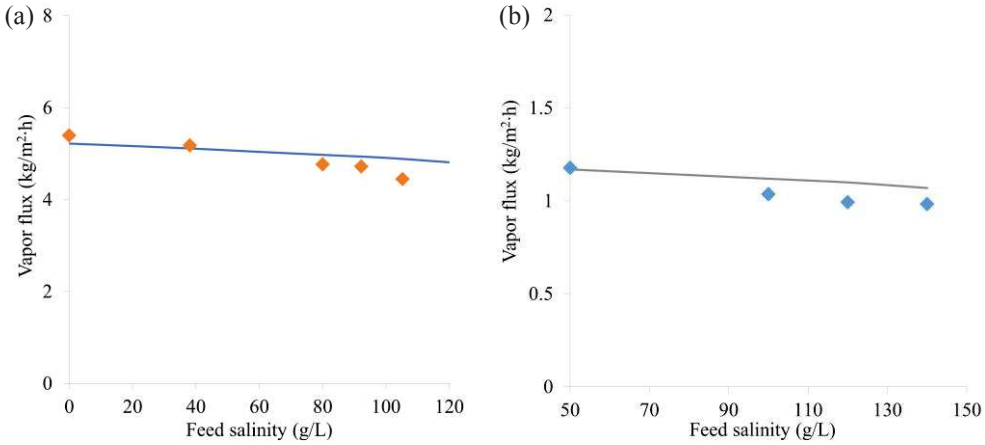

Figure 5.22: Validation of the model with the commercial hollow fibre module and effect of the feed salinity on (a) the performance of the commercial hollow fibre module containing 40 fibres (v_F= 0.8 m/s, v_P= 11.3 m/s, T_F= 50 °C, T_P= 20 °C) and on the performance of the hollow fibre module containing 10633 fibres (v_F=0.02 m/s, v_P=0.54 m/s, T_F= 70 °C, T_P= 24 °C).

5.2.3.5 Membrane length

Fig. 5.23(a) illustrates the inverse relationship between the water vapour flux and the membrane length. The increase of the membrane length increases the membrane surface which is in contact with the feed liquid from one side and with SG from opposite side of the membrane. The increased area for the transmembrane heat transfer leads not only to reduction of the temperature of the feed-membrane interface at the feed outlet but also to the increase in the water vapour concentration at the permeate-membrane interface. Both of these factors decrease the gradient of the water vapour concentration across the membrane. Indeed, the water vapour flux reduces with the increase of the membrane length.

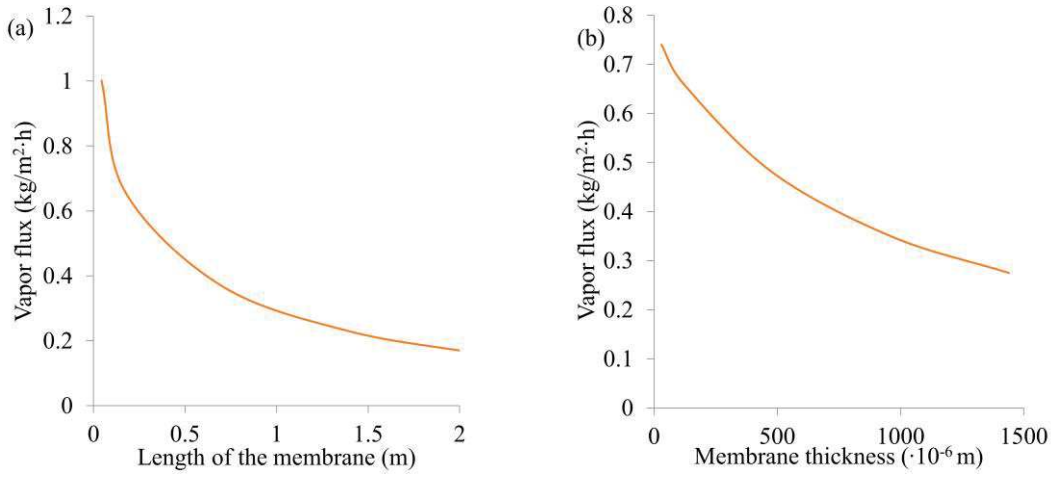

Figure 5.23: Effect of (a) the membrane length and (b) membrane thickness on the water vapour flux at the flat sheet SGMD module (v_F=5.6×10^{-3} m/s, v_P=9.3×10^{-2} m/s, P_P=0.9×10^5 Pa, T_F= 45 °C, T_P= 20 °C).

5.2.3.6 Membrane thickness

Results of the membrane thickness study show that the increase in the membrane thickness decreases the water vapour flux (Fig. 5.23(b)). It is explained by a reduction of the gradient of the water vapour concentration in the membrane pores. Despite the fact that the increase in the membrane thickness decreases the transmembrane heat transfer and increases the temperature of the feed flow at the feed-membrane interface, this positive effect is insufficient to overcome the negative effect on the process performance of the total gradient of the water vapour concentration decrease.

5.3 Anaerobic membrane bioreactors equipped with the MMV system

5.3.1 Mesh study

In the mesh study of anaerobic membrane bioreactors, three meshes with elements from fine to coarse sizes have been applied (Fig. 5.24). The calculations have been carried out for the membrane vibration set at 1 Hz with the operating time 15 s. In the study, the following parameters have been analysed: the calculation time, relative error for the total mass balance, maximum discrepancy for values of the velocity and volume fraction of solids at the liquid-membrane interface.

Results of the mesh study indicate a slight increase in the relative error for the overall mass balance and insignificant discrepancy between the calculated values of the velocity and the volume fraction of solids at the liquid-membrane interface with the increase in the size of the mesh elements (Table 5.3). However, the calculation procedure for the coarse mesh (Fig. 5.24(c)) is 5 times faster than for the fine mesh (Fig. 5.24(a)). Thus, the coarse mesh (Fig. 5.24(c)) is suitable for the calculations due to the fast calculation process and relatively small calculation error.

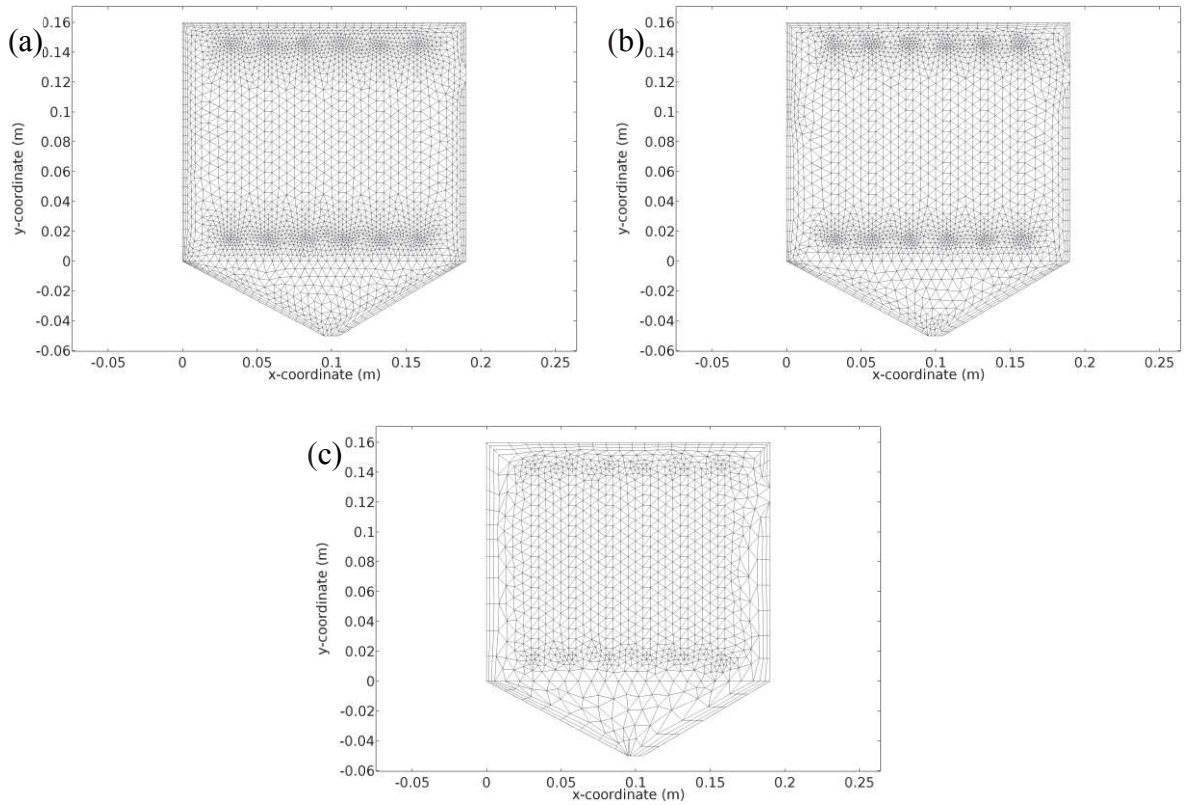

Figure 5.24: Graphical representation of the applied meshes in the mesh study for the flat sheet SGMD module.

Table 5.3: Results of the mesh study for AnMBR coupled with the MMV system.

Mesh	Calculation time	Mass balance error - feed side (%)	Discrepancy in the velocity at the feed-membrane interface (%)	Discrepancy in the volume fraction of solids at the feed-membrane interface (%)
a	51 min 3 s	0.5	0.85	0.71
b	18 min 12 s	0.73		
c	10 min 50 s	1.15		

5.3.2 Validation study

The proposed model for AnMBR coupled with the MMV system could not be validated directly due to impossibility of measurement of the simulated parameters. Thus, the proposed model had been validated indirectly via the time needed for the membrane fouling. The experimental studies show that the transmembrane flux reduces to 0 and membranes in the AnMBR tank are fully fouled after 5 minutes of the operation without the MMV system. However, with the running MMV system, the transmembrane flux remains stable during a long operation time. It indicates that the MMV system prevents the membrane module from fouling.

The simulations of AnMBR without the MMV system showed that the volume fraction of solids at the membrane surface reached the value of 0.186 after 5 minutes (Fig. 5.25(a)). Such high value indicates high risks of the cake formation and further membrane fouling. However, with the running MMV system at the frequency set at 15 Hz, the solids volume fraction at the membrane surface did not exceed the value 0.04 after 5 minutes of the operation (Fig. 5.25(b)). The obtained tendency was similar to experimental one and indirectly validated the proposed hydrodynamic model.

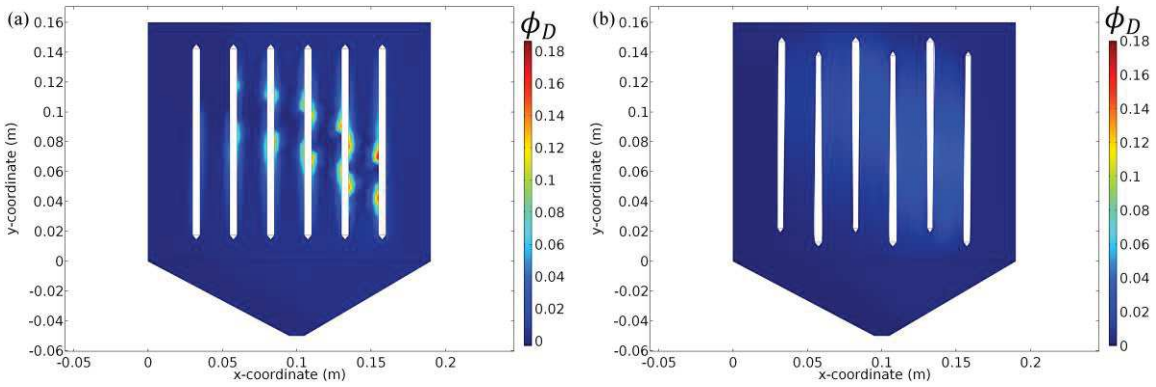

Figure 5.25: Validation of the AnMBR model. The distribution of the volume fraction of solids in the AnMBR tank at the vibration frequency set (a) 0 (without vibrations) and (b) 15 Hz (τ= 5 min).

5.3.3 Parametric study

In this section, the effects of the frequency and amplitude of membrane vibrations inside the AnMBR tank on the hydrodynamics and the distribution of the solids in the tank are highlighted. The simulated operation time of AnMBR coupled with the MMV system was set at 300 s. Due to the absence of effects of the studied parameters on kinetics of the anaerobic digestions, the distributions of the bacteria and components dissolved in the influent in the AnMBR tank are not presented.

5.3.3.1 Effect of the vibration frequency

The prediction of the sludge velocity distribution inside the AnMBR tank equipped with the MMV system is the main task of the proposed hydrodynamic model. The MMV system effects on the fluid velocity at the influent-membrane interface. Indeed, the influent velocity is constantly changing according the velocity and movement directions of the submerged membranes. In this study, the maximum absolute fluid velocity in the vertical direction was equal to 0.075 m/s at the vibration frequency set at 15 Hz. Figs. 5.26 and 5.27 show that the increase in the frequency is accompanied by the increase in the influent velocity. By increasing the velocity, the vibration frequency effects on the volume fraction of solids in the influent at the membrane surface. The calculations showed that, without the vibrations the volume fraction of solids at the feed-membrane interface reaches the value of 0.186 (Fig. 5.28(a)). Such high value indicates high risks of the cake formation and further membrane fouling. However, at the frequency set at 15 Hz, the solids volume fraction do not exceed 0.04 (Fig. 5.28(b)) and the possibility of the membrane clogging is seriously reduced. Thus, the MMV system can provide better influent mixing inside the AnMBR tank and prevents the process from the membrane fouling.

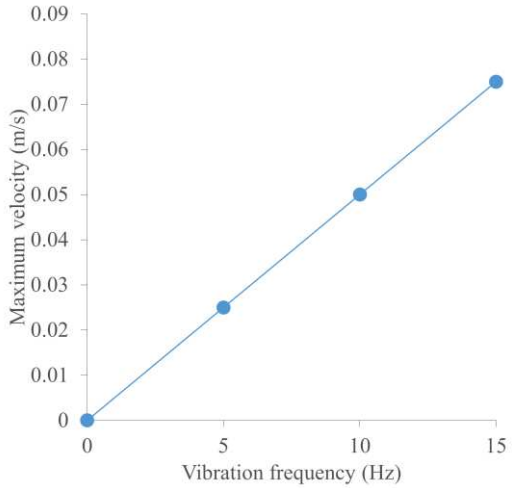

Figure 5.26: The effect of the vibration frequency on the maximum fluid velocity in the vertical direction.

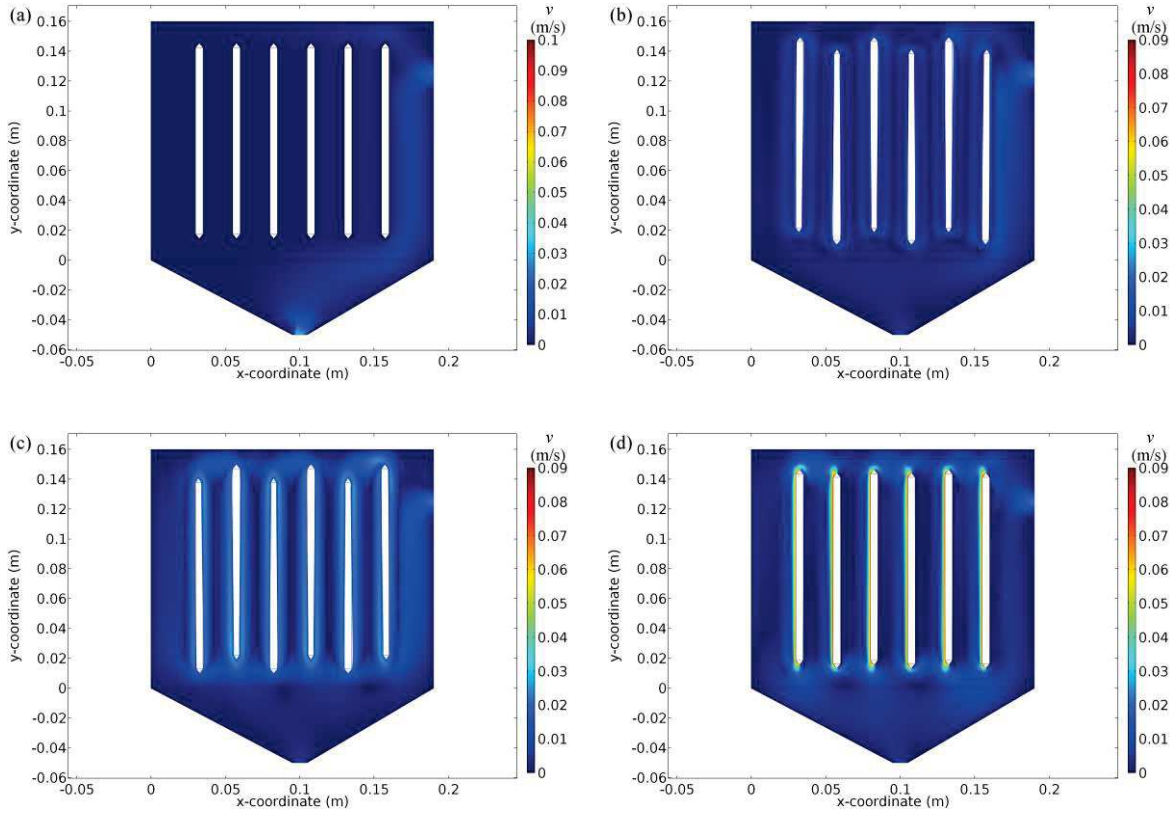

Figure 5.27: The absolute velocity distribution in the AnMBR tank at the vibration frequency set (a) 0, (b) 5, (c) 10 and (d) 15 Hz (τ=13 s, A_V =0.001 m).

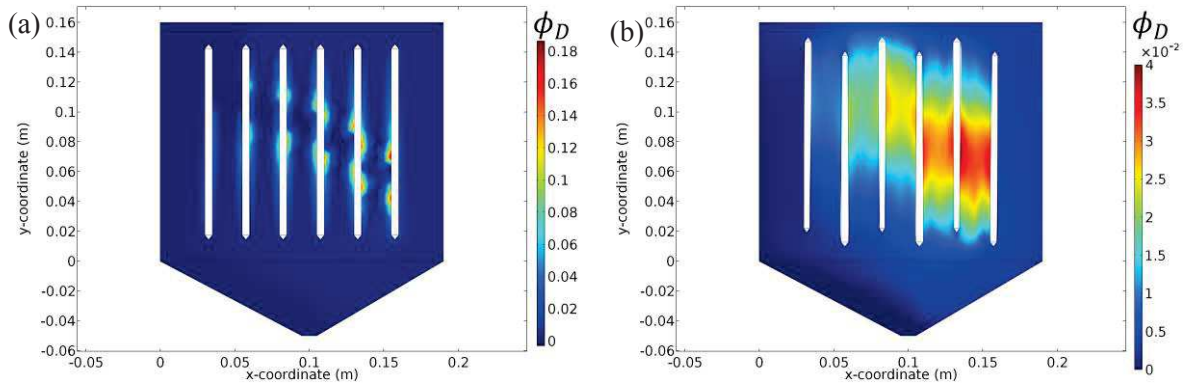

Figure 5.28: The distribution of the volume fraction of solids in the AnMBR tank at the vibration frequency set (a) 0 and (b) 15 Hz (τ=300 s, A_V=0.001 m).

5.3.3.2 Effect of the vibration amplitude

The vibration amplitude of the membranes is another MMV factor that effects on the AnMBR hydrodynamics. The study reveals the dependence of the influent velocity on the amplitude of the membrane vibrations (Fig. 5.29). With the increase in the vibration amplitude from 0.001 to 0.01, the fluid velocity at the influent-membrane interface is increased from 0.00175to 0.075 m/s. That increase also reduces the maximum volume fraction of solids at the membrane surface from 0.1 to 0.04 (Fig. 5.30) by enhancing fluid mixing. Thereby, the increase in the amplitude of the membrane vibrations leads reduces the risk of the membrane fouling.

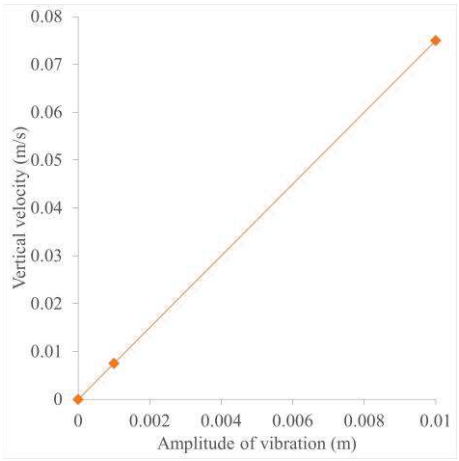

Figure 5.29: The effect of the vibration amplitude on the maximum fluid velocity in the vertical direction (f_M=15 Hz).

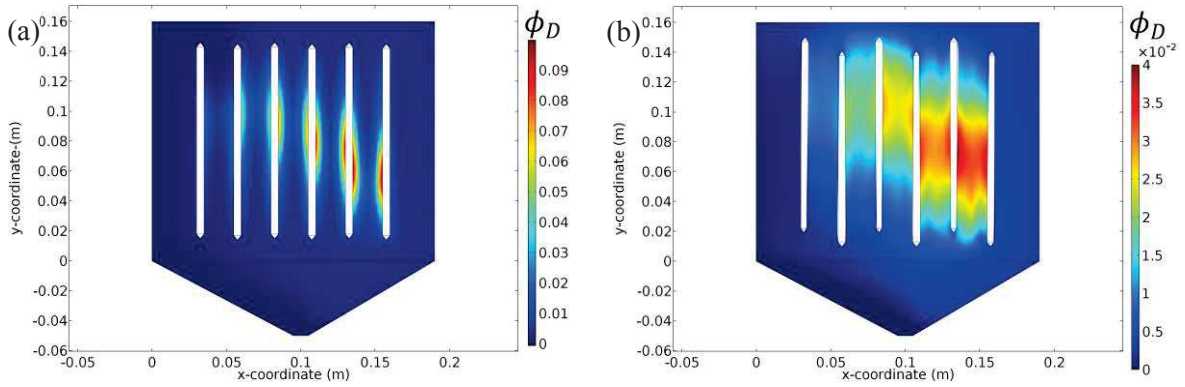

Figure 5.30: The distribution of the volume fraction of solids in the AnMBR tank at the vibration amplitude set (a) 0.001 and (b) 0.01 m (τ=300 s, f_M=15 Hz).

6 Conclusions et perspectives

Dans cette thèse, on a développé des modèles mathématiques prédictifs généraux pour les procédés de DCMD et de SGMD. Un modèle hydrodynamique pour un AnMBR couplé avec un système de vibration membranaire induite (MMV) a aussi été développé. Les modèles pour les procédés de DCMD et SGMD impliquent des systèmes de PDES, ODEs et AES pour chaque domaine des procédés. Ces modèles, qui peuvent être appliqués à la fois pour une configuration membranaire plane (avec ou sans entretoises) et de fibres creuses, éliminent la nécessité d'introduire des coefficients de transfert de chaleur et de masse spécifiques. Ainsi, cette nouvelle approche permet d'économiser les vastes efforts expérimentaux, qui sont généralement consacrés au développement et l'optimisation de ces modules dans la plupart des modèles existants. Par ailleurs, ces modèles offrent la possibilité d'optimiser et de prédire le comportement des procédés pour un grand nombre de variables (configurations membranaires, conditions de fonctionnement, caractéristiques membranaires, etc.) sans données expérimentales. Les modèles développés avec COMSOL Multiphysics ™, ont été validés avec différentes conditions expérimentales. En outre des études paramétriques complètes ont été réalisées. La comparaison entre les valeurs expérimentales et de la littérature avec les simulations permettent de dire que le modèle prédit bien les valeurs de flux de vapeur pour les deux procédés. L'étude approfondie menée a montré la souplesse des modèles et a permis d'estimer l'effet des paramètres de fonctionnement et des propriétés membranaires (la température d'alimentation et le débit, la salinité de la saumure, l'épaisseur et la longueur de la membrane) sur la performance des DCMD et SGMD. Par ailleurs la vitesse des fluides, la concentration des espèces et les distributions de température à l'intérieur les modules membranaires ont pu être simulés avec succès. En particulier, pour la DCMD, il a pu être observé que l'augmentation de la température d'alimentation de 35 à 55 ° C augmente le flux de vapeur d'eau de 5,9 fois dans le cas du module commercial à fibres creuses étudié.

En outre, il convient de mentionner que, dans certains cas très spécifiques, l'application de la DCMD pour des solutions de sels saturés peut être limitée en raison d'un effet négatif de la concentration de sel dans le débit d'alimentation, par diminution de la pression partielle de vapeur d'eau à l'interface de la membrane. Par exemple, dans le cas d'un module de DCMD à membrane plane en PE avec séparateur, l'augmentation de la concentration de sel dans le flux d'alimentation de 0 à 23% en poids a diminué le flux de vapeur d'eau de 6,7 kg m^{-2} h^{-1} à presque

zéro. Cependant, l'optimisation des conditions d'opération permet augmenter la performance de la DCMD.

Contrairement à DCMD, la température du flux de perméation a un effet mineur sur la performance de la SGMD. De plus, l'augmentation de la vitesse d'alimentation entraîne une augmentation du flux de vapeur, mais un seuil est atteint et un accroissement supplémentaire de la vitesse l'alimentation ou de perméation n'a plus d'influence sur le flux de vapeur. Comme prévu, l'augmentation de la longueur ou de l'épaisseur de la membrane diminue le flux de vapeur en raison de la diminution de la force motrice du procédé. Enfin, les simulations permettent de conclure que l'étude de longueur de membrane peut être employée pour l'optimisation de module.

Les modèles développés dans ce travail utilisent un grand nombre d'équations complexes et de conditions limites. Toutefois, ils donnent un avantage évident sur les modèles existants qui utilisent des équations intégrales et/ou des corrélations empiriques ou qui sont appliqués à des cas très spécifiques. En effet, avec les modèles développés dans ce travail il est possible de simuler différentes configurations de la DCMD et la SGMD et, en particulier, ils peuvent être appliqués aux systèmes multi-composants avec une évaluation complète des paramètres clés des procédés.

Le modèle hydrodynamique proposé pour les AnMBRs équipés du système de vibration membranaire induite MMV permet d'estimer les changements de la distribution de la vitesse à l'intérieur du réservoir du réacteur avec le temps. Le transfert de la quantité de mouvement à l'intérieur du réservoir du AnMBR et les interactions entre la phase liquide et la phase solide des influents sont décrits par le modèle d'Euler-Euler. Dans les simulations, les effets de la MMV ont été analysés. L'étude paramétrique effectuée a montré la dépendance linéaire entre la vitesse de l'influent à l'interface alimentation/membrane et la fréquence et l'amplitude des vibrations membranaires. Une augmentation de la vitesse de l'influent a diminué la fraction volumique du solide à la surface des membranes. Ce facteur met l'accent sur l'efficacité du système MMV dans le contrôle de l'encrassement membranaire. En effet, l'étude paramétrique révèle la possibilité de la prédiction et de l'analyse de la performance de l'AnMBR lorsqu'il est couplé à un système MMV.

En dépit du nombre des hypothèses et des équations impliquées, les modèles proposés ont un grand potentiel dans la simulation des modules industriels, la planification des expériences, l'optimisation et la conception des procédés. Une perspective de ce travail de thèse

est l'étude des modèles développés en 3D afin de faire une étude plus approfondie de la modélisation mathématique de ces procédés.

6 Conclusions and perspectives

In the present research, the following mathematical models for the membrane separations processes were developed: the general predictive models for DCMD and SGMD and the hydrodynamic model for AnMBRs coupled with the MMV system. The models for DCMD and SGMD involve systems of PDEs, ODEs and AEs for each domain of the membrane module (feed compartment, membrane and permeate compartment). These models which can be applied for both the flat sheet (with or without spacers) and hollow fibre configurations eliminate the need of introduction of specific heat and mass transfer coefficients. Thus, this novel approach saves the extensive experimental efforts, which are generally devoted to development and optimization of such modules in the most of existing DCMD and SGMD models, and offers the opportunity to optimize and predict the behaviour of the process over a large number of variables (membrane configurations, operating conditions, membrane properties etc.) without experimental data. With the use of the COMSOL Multiphysics™ software, the models were validated at different experimental conditions and parametric studies were carried out. The validation simulation experiments predicted values of the vapour fluxes which were in good agreement with experimental and literature data. The conducted comprehensive study showed the flexibility of the models and allowed to estimate the effect of the operating parameters and membrane properties (the feed temperature and flow rate, brine salinity, thickness and length of the membrane) not only on the performance of DCMD and SGMD but also on the velocity, concentration and temperature distributions in the membrane modules. In particular, for DCMD, the increase in the feed temperature from 35 to 55 °C increases the water vapour flux of 5.9 times for the simulated commercial hollow fibre module. It is worth mentioning that, for DCMD with salt solutions, the developed model could also predict the oversaturation at the feed-membrane interface. It may result in the salt precipitation at the membrane surface. For example, in the case of simulated filler-supported flat sheet DCMD module with the PE membrane the increase in the feed salt concentration from 0 to 23 wt% decreased the water vapour flux from 6.7 kg m^{-2} h^{-1} to almost zero.

The parametric study revealed that the temperature of the permeate flow has a minor effect on the performance of SGMD than on the performance of DCMD. Moreover, the increase in the feed velocity leads to an increase in the vapour flux, but reaching a threshold after which the vapour flux was almost independent of the feed or permeate velocity. As

expected, the increase of the length and/or thickness of the membrane decreases the vapour flux due to decrease of the driving force of the process. Last but not least, the membrane length study can be used for the module optimization.

In comparison to existing models, the proposed models use the large number of complex equations and BCs. However, the opportunity of the simulation of different DCMD and SGMD configurations and, especially, the possibility of the model application for the multicomponent systems with comprehensive evaluation of the key parameters of the process give a distinct advantage over the existing models that use algebraic equations and empirical correlations or consider specific cases.

The proposed hydrodynamic model for AnMBRs equipped with the MMV system allows estimation of changes of the velocity distribution inside the reactor tank with the time. The momentum transfer inside the AnMBR tank and the interactions between the liquid phase and solid phase of the influent are described by the Euler-Euler model. In simulations, the performance of the MMV was analysed. The conducted parametric study indicated the linear dependence of the influent velocity at the feed-membrane interface on the frequency and amplitude of the membrane vibrations. The increased influent velocity decreased the volume fraction at surfaces of the membrane module. That factor emphasises the effectiveness of the MMV system in the membrane fouling control. Indeed, the parametric study reveals the possibility of the prediction and analysis of the performance of the AnMBR complemented with the MMV system.

In spite of the number of the involved assumptions and equations, the proposed models have a great potential in simulation of industrial modules, planning of experiments, optimization and process design. All the developed models could be further studied in 3D as a prospect of the current PhD work and further study of the mathematical modelling of the membrane processes.

References

[1] A. Rasmuson, B. Andersson, L. Olsson, R. Andersson, Mathematical Modeling in Chemical Engineering, Cambridge University Press, Cambridge, 2014. doi:10.1017/CBO9781107279124.

[2] W. J. Meyer, Concepts of mathematical modeling, McGraw-Hill, New York, 1984.

[3] T. Dobre and J. Sanchez Marcano, Chemical Engineering, Modelling, Simulation and Similitude, Wiley VCH., Weinheim 2007

[4] H.K. Lonsdale, Chapter 1 Membranes and membrane processes, in: 1996: pp. 1–13. doi:10.1016/S0927-5193(96)80020-9.

[5] J.F. Richardson, J.H. Harker, J.R. Backhurst, Membrane Separation Processes, in: Chem. Eng., Elsevier, 2002: pp. 437–474. doi:10.1016/B978-0-08-049064-9.50019-9.

[6] E. Drioli, A. Brunetti, G. Di Profio, G. Barbieri, Process intensification strategies and membrane engineering, Green Chem. 14 (2012) 1561. doi:10.1039/c2gc16668b.

[7] B. Benyahia, T. Sari, B. Cherki, J. Harmand, Anaerobic membrane bioreactor modeling in the presence of Soluble Microbial Products (SMP) – the Anaerobic Model AM2b, Chem. Eng. J. 228 (2013) 1011–1022. doi:10.1016/j.cej.2013.05.073.

[8] M.R. Bilad, G. Mezohegyi, P. Declerck, I.F.J. Vankelecom, Novel magnetically induced membrane vibration (MMV) for fouling control in membrane bioreactors, Water Res. 46 (2012) 63–72. Doi:10.1016/j.watres.2011.10.026.

[9] M. Mertens, M.R. Bilad, A.Y. Gebreyohannes, L. Marbelia, I.F.J. Vankelecom, Membrane development for improved performance of a magnetically induced vibration system for anaerobic sludge filtration, Sep. Purif. Technol. 200 (2018) 120–129. Doi:10.1016/j.seppur.2018.01.068.

[10] B.R. Bodell, Silicone rubber vapor diffusion in saline water distillation, United States Patent Application Serial No. 285,032 (1963).

[11] B.R. Bodell, Distillation of saline water using silicone rubber membrane, United States Patent 3,361,645 (1968).

[12] M.E. Findley, Vaporization through Porous Membranes, Ind. Eng. Chem. Process Des. Dev. 6 (1967) 226–230. doi:10.1021/i260022a013.

[13] K. Smolders, A.C.M. Franken, Terminology for Membrane Distillation, Desalination. 72 (1989) 249–262. doi:10.1016/0011-9164(89)80010-4.

[14] I. Union, O.F. Pure, A. Chemistry, Terminology for membranes and membrane processes (IUPAC Recommendation 1996), J. Memb. Sci. 120 (1996) 149–159. doi:10.1016/0376-7388(96)82861-4.

[15] E. Drioli, A. Ali, F. Macedonio, Membrane distillation: Recent developments and perspectives, Desalination. 356 (2015) 56–84. doi:10.1016/j.desal.2014.10.028.

[16] E. Curcio, E. Drioli, Membrane Distillation and Related Operations: A Review, Sep. Purif. Rev. 34 (2005) 35–86. doi:10.1081/SPM-200054951.

[17] A. Khalifa, H. Ahmad, M. Antar, T. Laoui, M. Khayet, Experimental and theoretical investigations on water desalination using direct contact membrane distillation, Desalination. 404 (2017) 22–34. doi:10.1016/j.desal.2016.10.009.

[18] K. Ohta, I. Hayano, T. Okabe, T. Goto, S. Kimura, H. Ohya, Membrane distillation with fluoro-carbon membranes, Desalination. 81 (1991) 107–115. doi:10.1016/0011-9164(91)85049-Z.

[19] J.-M. Li, Z.-K. Xu, Z.-M. Liu, W.-F. Yuan, H. Xiang, S.-Y. Wang, Y.-Y. Xu, Microporous polypropylene and polyethylene hollow fiber membranes. Part 3. Experimental studies on membrane distillation for desalination, Desalination. 155 (2003) 153–156. doi:10.1016/S0011-9164(03)00292-3.

[20] A. Larbot, L. Gazagnes, S. Krajewski, M. Bukowska, Wojciech Kujawski, Water desalination using ceramic membrane distillation, Desalination. 168 (2004) 367–372. doi:10.1016/j.desal.2004.07.021.

[21] P. Peng, A.G. Fane, X. Li, Desalination by membrane distillation adopting a hydrophilic membrane, Desalination. 173 (2005) 45–54. doi:10.1016/j.desal.2004.06.208.

[22] S. Alobaidani, E. Curcio, F. Macedonio, G. Diprofio, H. Alhinai, E. Drioli, Potential of membrane distillation in seawater desalination: Thermal efficiency, sensitivity study and cost estimation, J. Memb. Sci. 323 (2008) 85–98. doi:10.1016/j.memsci.2008.06.006.

[23] V. Calabrò, E. Drioli, F. Matera, Membrane distillation in the textile wastewater treatment, Desalination. 83 (1991) 209–224. doi:10.1016/0011-9164(91)85096-D.

[24] M. Gryta, Concentration of saline wastewater from the production of heparin, Desalination. 129 (2000) 35–44. doi:10.1016/S0011-9164(00)00049-7.

[25] Y. Wu, Y. Kong, J. Liu, J. Zhang, J. Xu, An experimental study on membrane distillation-crystallization for treating waste water in taurine production, Desalination. 80 (1991) 235–242. doi:10.1016/0011-9164(91)85160-V.

[26] A.G. Chmielewski, G. Zakrzewska-Trznadel, N.R. Miljević, W.A. Van Hook, Membrane Distillation Employed for Separation of Water Isotopic Compounds, Sep. Sci. Technol. 30 (1995) 1653–1667. doi:10.1080/01496399508010368.

[27] T.Y. Cath, D. Adams, A.E. Childress, Membrane contactor processes for wastewater reclamation in space, J. Memb. Sci. 257 (2005) 111–119. doi:10.1016/j.memsci.2004.07.039.

[28] K.L. Hickenbottom, T.Y. Cath, Sustainable operation of membrane distillation for enhancement of mineral recovery from hypersaline solutions, J. Memb. Sci. 454 (2014) 426–435. doi:10.1016/j.memsci.2013.12.043.

[29] M. Tomaszewska, M. Gryta, A.W. Morawski, Study on the concentration of acids by membrane distillation, J. Memb. Sci. 102 (1995) 113–122. doi:10.1016/0376-7388(94)00281-3.

[30] M. Khayet, A. Velázquez, J.I. Mengual, Direct contact membrane distillation of humic acid solutions, J. Memb. Sci. 240 (2004) 123–128. doi:10.1016/j.memsci.2004.04.018.

[31] V. Calabro, B.L. Jiao, E. Drioli, Theoretical and Experimental Study on Membrane Distillation in the Concentration of Orange Juice, Ind. Eng. Chem. Res. 33 (1994) 1803–1808. doi:10.1021/ie00031a020.

[32] F. Laganà, G. Barbieri, E. Drioli, Direct contact membrane distillation: modelling and concentration experiments, J. Memb. Sci. 166 (2000) 1–11. doi:10.1016/S0376-7388(99)00234-3.

[33] S. Nene, S. Kaur, K. Sumod, B. Joshi, K.S.M.S. Raghavarao, Membrane distillation for the concentration of raw cane-sugar syrup and membrane clarified sugarcane juice, Desalination. 147 (2002) 157–160. doi:10.1016/S0011-9164(02)00604-5.

[34] O.S. Lukanin, S.M. Gunko, M.T. Bryk, R.R. Nigmatullin, The effect of content of apple juice biopolymers on the concentration by membrane distillation, J. Food Eng. 60 (2003) 275–280. doi:10.1016/S0260-8774(03)00048-7.

[35] K. Sakai, T. Koyano, T. Muroi, M. Tamura, Effects of temperature and concentration polarization on water vapour permeability for blood in membrane distillation, Chem. Eng. J. 38 (1988) 33–39. doi:10.1016/0300-9467(88)80081-9.

[36] J.M. Ortiz De Zárate, C. Rincón, J.I. Mengual, Concentration of Bovine Serum Albumin Aqueous Solutions by Membrane Distillation, Sep. Sci. Technol. 33 (1998) 283–296. doi:10.1080/01496399808544769.

[37] A. Criscuoli, E. Drioli, A. Capuano, B. Memoli, V.E. Andreucci, Human plasma ultrafiltrate purification by membrane distillation: Process optimisation and evaluation of its possible application on-line, Desalination. 147 (2002) 147–148. doi:10.1016/S0011-9164(02)00602-1.

[38] P. Cornel, S. Krause, Advanced Membrane Technology and Applications, Adv. Membr. Technol. Appl. (2008) 217–238.

[39] A.C.M. Franken, J.A.M. Nolten, M.H.V. Mulder, D. Bargeman, C.A. Smolders, Wetting criteria for the applicability of membrane distillation, J. Memb. Sci. 33 (1987) 315–328. doi:10.1016/S0376-7388(00)80288-4.

[40] F. Gabino, M.-P. Belleville, L. Preziosi-Belloy, M. Dornier, J. Sanchez, Evaluation of the cleaning of a new hydrophobic membrane for osmotic evaporation, Sep. Purif. Technol. 55 (2007) 191–197. doi:10.1016/j.seppur.2006.11.016.

[41] M. Mulder, Basic Principles of Membrane Technology, Springer Netherlands, Dordrecht, 1996. doi:10.1007/978-94-009-1766-8.

[42] A.J. Burggraaf, L. Cot, Fundamentals of inorganic membrane science and technology, Elsevier, 1996.

[43] A. Barkallah, J. Mörée, J. Sanchez, S.D. Bocquet, J. Rivenc, Modeling of coupled mass and heat transfer through venting membranes for automotive applications, AIChE J. 55 (2009) 294–311. doi:10.1002/aic.11689.

[44] B. Tjaden, S.J. Cooper, D.J. Brett, D. Kramer, P.R. Shearing, On the origin and application of the Bruggeman correlation for analysing transport phenomena in electrochemical systems, Curr. Opin. Chem. Eng. 12 (2016) 44–51. doi:10.1016/j.coche.2016.02.006.

[45] J.S. Mackie, P. Meares, The Diffusion of Electrolytes in a Cation-Exchange Resin Membrane. I. Theoretical, Proc. R. Soc. A Math. Phys. Eng. Sci. 232 (1955) 498–509. doi:10.1098/rspa.1955.0234.

[46] H.L. Weissberg, Effective Diffusion Coefficient in Porous Media, J. Appl. Phys. 34 (1963) 2636–2639. doi:10.1063/1.1729783.

[47] G.H. Neale, W.K. Nader, Prediction of transport processes within porous media: Diffusive flow processes within an homogeneous swarm of spherical particles, AIChE J. 19 (1973) 112–119. doi:10.1002/aic.690190116.

[48] J.W. Beeckman, Mathematical description of heterogeneous materials, Chem. Eng. Sci. 45 (1990) 2603–2610. doi:10.1016/0009-2509(90)80148-8.

[49] N. Iversen, B.B. Jørgensen, Diffusion coefficients of sulfate and methane in marine sediments: Influence of porosity, Geochim. Cosmochim. Acta. 57 (1993) 571–578. doi:10.1016/0016-7037(93)90368-7.

[50] B.P. Boudreau, The diffusive tortuosity of fine-grained unlithified sediments, Geochim. Cosmochim. Acta. 60 (1996) 3139–3142. doi:10.1016/0016-7037(96)00158-5.

[51] M.S. Khayet, T. Matsuura, Membrane Distillation: Principles and Applications, 2011. https://www.elsevier.com/books/membrane-distillation/khayet-souhaimi/978-0-444-53126-1.

[52] R.W. Schofield, a. G. Fane, C.J.D. Fell, Heat and mass transfer in membrane distillation, J. Memb. Sci. 33 (1987) 299–313. doi:10.1016/S0376-7388(00)80287-2.

[53] J.M.O. De Záarate, A. Velázquez, L. Peña, J.I. Mengual, Influence of Temperature Polarization on Separation by Membrane Distillation, Sep. Sci. Technol. 28 (1993) 1421–1436. doi:10.1080/01496399308018048.

[54] M.I. Vázquez-González, L. Martínez, Nonisothermal Water Transport through Hydrophobic Membranes in a Stirred Cell, Sep. Sci. Technol. 29 (1994) 1957–1966. doi:10.1080/01496399408002183.

[55] M. Sudoh, K. Takuwa, H. Iizuka, K. Nagamatsuya, Effects of thermal and concentration boundary layers on vapor permeation in membrane distillation of aqueous lithium bromide solution, J. Memb. Sci. 131 (1997) 1–7. doi:10.1016/S0376-7388(97)00109-9.

[56] M. Khayet, J.I. Mengual, T. Matsuura, Porous hydrophobic/hydrophilic composite membranes, J. Memb. Sci. 252 (2005) 101–113. doi:10.1016/j.memsci.2004.11.022.

[57] W.T. Hanbury, T. Hodgkiess, Membrane distillation - an assessment, Desalination. 56 (1985) 287–297. doi:10.1016/0011-9164(85)85032-3.

[58] J. Koschikowski, M. Wieghaus, M. Rommel, Solar thermal-driven desalination plants based on membrane distillation, Desalination. 156 (2003) 295–304. doi:10.1016/S0011-9164(03)00360-6.

[59] F. Banat, N. Jwaied, M. Rommel, J. Koschikowski, M. Wieghaus, Desalination by a “compact SMADES” autonomous solarpowered membrane distillation unit, Desalination. 217 (2007) 29–37. doi:10.1016/j.desal.2006.11.028.

[60] G. Zakrzewska-Trznadel, M. Harasimowicz, A.G. Chmielewski, Concentration of radioactive components in liquid low-level radioactive waste by membrane distillation, J. Memb. Sci. 163 (1999) 257–264. doi:10.1016/S0376-7388(99)00171-4.

[61] A.G. Fane, R.W. Schofield, C.J.D. Fell, The efficient use of energy in membrane distillation, Desalination. 64 (1987) 231–243. doi:10.1016/0011-9164(87)90099-3.

[62] J. Phattaranawik, R. Jiraratananon, A.. Fane, Heat transport and membrane distillation coefficients in direct contact membrane distillation, J. Memb. Sci. 212 (2003) 177–193. doi:10.1016/S0376-7388(02)00498-2.

[63] Weyl PK. Recovery of demineralized water from saline waters, United States Patent 3,340,186 (1967).

[64] L. Camacho, L. Dumée, J. Zhang, J. Li, M. Duke, J. Gomez, S. Gray, Advances in Membrane Distillation for Water Desalination and Purification Applications, Water. 5 (2013) 94–196. doi:10.3390/w5010094.

[65] C.A. Quist-Jensen, F. Macedonio, E. Drioli, Membrane crystallization for salts recovery from brine—an experimental and theoretical analysis, Desalin. Water Treat. 57 (2016) 7593–7603. doi:10.1080/19443994.2015.1030110.

[66] S. Kimura, S.-I. Nakao, S.-I. Shimatani, Transport phenomena in membrane distillation, J. Memb. Sci. 33 (1987) 285–298. doi:10.1016/S0376-7388(00)80286-0. //22

[67] R. Bagger-Jørgensen, A.S. Meyer, M. Pinelo, C. Varming, G. Jonsson, Recovery of volatile fruit juice aroma compounds by membrane technology: Sweeping gas versus vacuum membrane distillation, Innov. Food Sci. Emerg. Technol. 12 (2011) 388–397. doi:10.1016/j.ifset.2011.02.005.

[68] V. Soni, J. Abildskov, G. Jonsson, R. Gani, Modeling and analysis of vacuum membrane distillation for the recovery of volatile aroma compounds from black currant juice, J. Memb. Sci. 320 (2008) 442–455. doi:10.1016/j.memsci.2008.04.025.

[69] C. Boi, S. Bandini, G.C. Sarti, Pollutants removal from wastewaters through membrane distillation, Desalination. 183 (2005) 383–394. doi:10.1016/j.desal.2005.03.041.

[70] C.H. Lee, W.H. Hong, Effect of operating variables on the flux and selectivity in sweep gas membrane distillation for dilute aqueous isopropanol, J. Memb. Sci. 188 (2001) 79–86. doi:10.1016/S0376-7388(01)00373-8.

[71] H. Mahmud, A. Kumar, R.M. Narbaitz, T. Matsuura, Mass transport in the membrane air-stripping process using microporous polypropylene hollow fibers: effect of toluene in aqueous feed, J. Memb. Sci. 209 (2002) 207–219. doi:10.1016/S0376-7388(02)00320-4. . Tsai,

[72] R.S. Juang, S.H. Lin, M.C. Yang, Mass transfer analysis on air stripping of VOCs from water in microporous hollow fibers, J. Memb. Sci. 255 (2005) 79–87. doi:10.1016/j.memsci.2005.01.022.

[73] F. Gascons Viladomat, I. Souchon, V. Athès, M. Marin, Membrane air-stripping of aroma compounds, J. Memb. Sci. 277 (2006) 129–136. doi:10.1016/j.memsci.2005.10.023.

[74] M.C. García-Payo, C.A. Rivier, I.W. Marison, U. Von Stockar, Separation of binary mixtures by thermostatic sweeping gas membrane distillation II. Experimental results with aqueous formic acid solutions, J. Memb. Sci. 198 (2002) 197–210. doi:10.1016/S0376-7388(01)00649-4.

[75] E. Pomier, N. Hengl, M.P. Belleville, D. Paolucci-Jeanjean, J. Sanchez, G. Rios, Study of a new metallic membrane evaporator, Desalination. 199 (2006) 185–187. doi:10.1016/j.desal.2006.03.041.

[76] A. Mourgues, N. Hengl, M.P. Belleville, D. Paolucci-Jeanjean, J. Sanchez, Membrane contactor with hydrophobic metallic membranes: 1. Modeling of coupled mass and heat transfers in membrane evaporation, J. Memb. Sci. 355 (2010) 112–125. doi:10.1016/j.memsci.2010.02.040.

[77] N. Hengl, A. Mourgues, M.P. Belleville, D. Paolucci-Jeanjean, J. Sanchez, Membrane contactor with hydrophobic metallic membranes: 2. Study of operating parameters in membrane evaporation, J. Memb. Sci. 355 (2010) 126–132. doi:10.1016/j.memsci.2010.03.009.

[78] S. Shukla, N.E. Benes, I. Vankelecom, J.P. Méricq, M.P. Belleville, N. Hengl, J.S. Marcano, Sweep gas membrane distillation in a membrane contactor with metallic hollow-fibers, J. Memb. Sci. 493 (2015) 167–178. doi:10.1016/j.memsci.2015.06.040.

[79] Z. Xie, T. Duong, M. Hoang, C. Nguyen, B. Bolto, Ammonia removal by sweep gas membrane distillation, Water Res. 43 (2009) 1693–1699. doi:10.1016/j.watres.2008.12.052.

[80] C. Gostoli, G.C. Sarti, S. Matulli, Low Temperature Distillation Through Hydrophobic Membranes, Sep. Sci. Technol. 22 (1987) 855–872. doi:10.1080/01496398708068986.

[81] E. Drioli, Y. Wu, V. Calabro, Membrane distillataion in the treatment of aqueous solutions, J. Memb. Sci. 33 (1987) 277–284. doi:10.1016/S0376-7388(00)80285-9.

[82] R.W. Schofield, A.G. Fane, C.J.D. Fell, R. Macoun, Factors affecting flux in membrane distillation, Desalination. 77 (1990) 279–294. doi:10.1016/0011-9164(90)85030-E.

[83] R.W. Schofield, A.G. Fane, C.J.D. Fell, Gas and vapour transport through microporous membranes. I. Knudsen-Poiseuille transition, J. Memb. Sci. 53 (1990) 159–171. doi:10.1016/0376-7388(90)80011-A.

[84] R. Jackson, Transport in porous catalysts, 1977.

[85] E.A. Mason, A. Malinauskas, Gas Transport in Porous Media: The Dusty-gas Model, 1983.

[86] R.B. Bird, W.E. Stewart, E.N. Lightfoot, Transport Phenomena, 2002. doi:10.1051/jp4:20020462.

[87] B.E. Poling, J.M. Prausnitz, J.P. O'Connell, The Properties of Gases and Liquids, 2001. doi:10.1036/0070116822.

[88] M. Tomaszewska, M. Gryta, A.W. Morawski, A study of separation by the direct-contact membrane distillation process, Sep. Technol. 4 (1994) 244–248. doi:10.1016/0956-9618(94)80028-6.

[89] M. Gryta, M. Tomaszewska, A.W. Morawski, Membrane distillation with laminar flow, Sep. Purif. Technol. 11 (1997) 93–101. doi:10.1016/S1383-5866(97)00002-6.

[90] K.W. Lawson, D.R. Lloyd, Membrane distillation. II. Direct contact MD, J. Memb. Sci. 120 (1996) 123–133. doi:10.1016/0376-7388(96)00141-X.

[91] K.W. Lawson, D.R. Lloyd, Membrane distillation, J. Memb. Sci. 124 (1997) 1–25. doi:10.1016/S0376-7388(96)00236-0.

[92] H. Yu, X. Yang, R. Wang, A.G. Fane, Analysis of heat and mass transfer by CFD for performance enhancement in direct contact membrane distillation, J. Memb. Sci. 405–406 (2012) 38–47. doi:10.1016/j.memsci.2012.02.035.

[93] X. Yang, H. Yu, R. Wang, A.G. Fane, Optimization of microstructured hollow fiber design for membrane distillation applications using CFD modeling, J. Memb. Sci. 421–422 (2012) 258–270. doi:10.1016/j.memsci.2012.07.022.

[94] H. Hayer, O. Bakhtiari, T. Mohammadi, Simulation of momentum, heat and mass transfer in direct contact membrane distillation: A computational fluid dynamics approach, J. Ind. Eng. Chem. 21 (2015) 1379–1382. doi:10.1016/j.jiec.2014.06.009.

[95] R.D. Gustafson, J.R. Murphy, A. Achilli, A stepwise model of direct contact membrane distillation for application to large-scale systems: Experimental results and model predictions, Desalination. 378 (2016) 14–27. doi:10.1016/j.desal.2015.09.022.

[96] F. Eleiwi, N. Ghaffour, A.S. Alsaadi, L. Francis, T.M. Laleg-Kirati, Dynamic modeling and experimental validation for direct contact membrane distillation (DCMD) process, Desalination. 384 (2016) 1–11. doi:10.1016/j.desal.2016.01.004.

[97] D. Cheng, W. Gong, N. Li, Response surface modeling and optimization of direct contact membrane distillation for water desalination, Desalination. 394 (2016) 108–122. doi:10.1016/j.desal.2016.04.029.

[98] A. Ali, C.A. Quist-Jensen, F. Macedonio, E. Drioli, Optimization of module length for continuous direct contact membrane distillation process, Chem. Eng. Process. Process Intensif. 110 (2016) 188–200. doi:10.1016/j.cep.2016.10.014.

[99] A. Ali, J.-H. Tsai, K.-L. Tung, E. Drioli, F. Macedonio, Designing and optimization of continuous direct contact membrane distillation process, Desalination. 426 (2018) 97–107. doi:10.1016/j.desal.2017.10.041.

[100] M. Khayet, P. Godino, J.I. Mengual, Theory and experiments on sweeping gas membrane distillation, J. Memb. Sci. 165 (2000) 261–272. doi:10.1016/S0376-7388(99)00236-7.

[101] M. Khayet, P. Godino, J.I. Mengual, Nature of flow on sweeping gas membrane distillation, J. Memb. Sci. 170 (2000) 243–255. doi:10.1016/S0376-7388(99)00369-5.

[102] M. Khayet, M.P. Godino, J.I. Mengual, Theoretical and experimental studies on desalination using the sweeping gas membrane distillation method, Desalination. 157 (2003) 297–305. doi:10.1016/S0011-9164(03)00409-0.

[103] K. Charfi, M. Khayet, M.J. Safi, Numerical simulation and experimental studies on heat and mass transfer using sweeping gas membrane distillation, Desalination. 259 (2010) 84–96. doi:10.1016/j.desal.2010.04.028.

[104] M. Khayet, C. Cojocaru, A. Baroudi, Modeling and optimization of sweeping gas membrane distillation, Desalination. 287 (2012) 159–166. doi:10.1016/j.desal.2011.04.070.

[105] M. Khayet, C. Cojocaru, Artificial neural network model for desalination by sweeping gas membrane distillation, Desalination. 308 (2013) 102–110. doi:10.1016/j.desal.2012.06.023.

[106] M. Essalhi, M. Khayet, Membrane Distillation (MD), in: Prog. Filtr. Sep., Elsevier, 2015: pp. 61–99. doi:10.1016/B978-0-12-384746-1.00003-3.

[107] H.H.P. Fang, T. Zhang, Anaerobic Biotechnology, IMPERIAL COLLEGE PRESS, 2015. doi:10.1142/p1034.

[108] B.-Q. Liao, J.T. Kraemer, D.M. Bagley, Anaerobic Membrane Bioreactors: Applications and Research Directions, Crit. Rev. Environ. Sci. Technol. 36 (2006) 489–530. Doi:10.1080/10643380600678146.

[109] H. Lin, W. Peng, M. Zhang, J. Chen, H. Hong, Y. Zhang, A review on anaerobic membrane bioreactors: Applications, membrane fouling and future perspectives, Desalination. 314 (2013) 169–188. Doi:10.1016/j.desal.2013.01.019.

[110] C. Shin, J. Bae, Current status of the pilot-scale anaerobic membrane bioreactor treatments of domestic wastewaters: A critical review, Bioresour. Technol. 247 (2018) 1038–1046. Doi:10.1016/j.biortech.2017.09.002.

[111] A. Charfi, N. Ben Amar, J. Harmand, Analysis of fouling mechanisms in anaerobic membrane bioreactors, Water Res. 46 (2012) 2637–2650. Doi:10.1016/j.watres.2012.02.021.

[112] A. Charfi, N. Thongmak, B. Benyahia, M. Aslam, J. Harmand, N. Ben Amar, G. Lesage, P. Sridang, J. Kim, M. Heran, A modelling approach to study the fouling of an anaerobic membrane bioreactor for industrial wastewater treatment, Bioresour. Technol. 245 (2017) 207–215. Doi:10.1016/j.biortech.2017.08.003.

[113] P. Cornel, S. Krause, Membrane bioreactors in industrial wastewater treatment – European experiences, examples and trends, Water Sci. Technol. 53 (2006) 37–44. Doi:10.2166/wst.2006.074.

[114] P. Cornel, S. Krause, Membrane Bioreactors for Wastewater Treatment, in: Adv. Membr. Technol. Appl., John Wiley & Sons, Inc., Hoboken, NJ, USA, 2008: pp. 217–238. Doi:10.1002/9780470276280.ch9.

[115] J. De Vrieze, T. Hennebel, J. Van den Brande, R.M. Bilad, T.A. Bruton, I.F.J. Vankelecom, W. Verstraete, N. Boon, Anaerobic digestion of molasses by means of a vibrating and non-vibrating submerged anaerobic membrane bioreactor, Biomass and Bioenergy. 68 (2014) 95–105. Doi:10.1016/j.biombioe.2014.06.009.

[116] J.M. Wallace, S.I. Safferman, Anaerobic membrane bioreactors and the influence of space velocity and biomass concentration on methane production for liquid dairy manure, Biomass and Bioenergy. 66 (2014) 143–150. Doi:10.1016/j.biombioe.2014.02.021.

[117] W. Wang, Q. Yang, S. Zheng, D. Wu, Anaerobic membrane bioreactor (AnMBR) for bamboo industry wastewater treatment, Bioresour. Technol. 149 (2013) 292–300. Doi:10.1016/j.biortech.2013.09.068.

[118] V.T. Mota, F.S. Santos, M.C.S. Amaral, Two-stage anaerobic membrane bioreactor for the treatment of sugarcane vinasse: Assessment on biological activity and filtration performance, Bioresour. Technol. 146 (2013) 494–503. Doi:10.1016/j.biortech.2013.07.110.

[119] D. Martinez-Sosa, B. Helmreich, T. Netter, S. Paris, F. Bischof, H. Horn, Anaerobic submerged membrane bioreactor (AnSMBR) for municipal wastewater treatment under mesophilic and psychrophilic temperature conditions, Bioresour. Technol. 102 (2011) 10377–10385. doi:10.1016/j.biortech.2011.09.012.

[120] E. Jeong, H.-W. Kim, J.-Y. Nam, Y.-T. Ahn, H.-S. Shin, Effects of the hydraulic retention time on the fouling characteristics of an anaerobic membrane bioreactor for treating acidified wastewater, Desalin. Water Treat. 18 (2010) 251–256. doi:10.5004/dwt.2010.1781.

[121] D. Jeison, P. Telkamp, J.. van Lier, Thermophilic Sidestream Anaerobic Membrane Bioreactors: The Shear Rate Dilemma, Water Environ. Res. 81 (2009) 2372–2380. doi:10.2175/106143009X426040.

[122] J.-O. Kim, J.-T. Jung, Performance of membrane-coupled organic acid fermentor for the resources recovery form municipal sewage sludge, Water Sci. Technol. 55 (2007) 245. doi:10.2166/wst.2007.328.

[123] S.H. Yoon, I.J. Kang, C.H. Lee, Fouling of Inorganic Membrane and Flux Enhancement in Membrane-Coupled Anaerobic Bioreactor, Sep. Sci. Technol. 34 (1999) 709–724. doi:10.1080/01496399908951140.

[124] B.. Cho, A.. Fane, Fouling transients in nominally sub-critical flux operation of a membrane bioreactor, J. Memb. Sci. 209 (2002) 391–403. doi:10.1016/S0376-7388(02)00321-6.

[125] S. Arros-Alileche, U. Merin, G. Daufin, G. Gésan-Guiziou, The membrane role in an anaerobic membrane bioreactor for purification of dairy wastewaters: A numerical simulation, Bioresour. Technol. 99 (2008) 8237–8244. doi:10.1016/j.biortech.2008.03.015.

[126] E. Jeong, H.-W. Kim, J.-Y. Nam, H.-S. Shin, Enhancement of bioenergy production and effluent quality by integrating optimized acidification with submerged anaerobic membrane bioreactor, Bioresour. Technol. 101 (2010) S7–S12. doi:10.1016/j.biortech.2009.04.064.

[127] B. Benyahia, T. Sari, B. Cherki, J. Harmand, Anaerobic membrane bioreactor modeling in the presence of Soluble Microbial Products (SMP) – the Anaerobic Model AM2b, Chem. Eng. J. 228 (2013) 1011–1022. doi:10.1016/j.cej.2013.05.073.

[128] A. Charfi, E. Park, M. Aslam, J. Kim, Particle-sparged anaerobic membrane bioreactor with fluidized polyethylene terephthalate beads for domestic wastewater treatment: Modelling approach and fouling control, Bioresour. Technol. 258 (2018) 263–269. doi:10.1016/j.biortech.2018.02.093.

[129] A. Boyle-Gotla, P.D. Jensen, S.D. Yap, M. Pidou, Y. Wang, D.J. Batstone, Dynamic multidimensional modelling of submerged membrane bioreactor fouling, J. Memb. Sci. 467 (2014) 153–161. doi:10.1016/j.memsci.2014.05.028.

[130] H.K. Versteeg, W. Malalasekera, An Introduction to Computational Fluid Dynamics - The Finite Volume Method, 1995. doi:10.2514/1.22547.

[131] X. Li, X. Wang, Modelling of membrane fouling in a submerged membrane bioreactor, J. Memb. Sci. 278 (2006) 151–161. doi:10.1016/j.memsci.2005.10.051.

[132] Z. Trad, C. Vial, J.-P. Fontaine, C. Larroche, Modeling of hydrodynamics and mixing in a submerged membrane bioreactor, Chem. Eng. J. 282 (2015) 77–90. doi:10.1016/j.cej.2015.04.119.

[133] Bilad, M. R.; Discart, V.; Vandamme, D.; Foubert, I.; Muylaert, K.; Vankelecom, I. F. J. Harvesting Microalgal Biomass Using a Magnetically Induced Membrane Vibration (MMV) System: Filtration Performance and Energy Consumption. *Bioresour. Technol.* **2013**, *138*, 329–338.

[134] Li, Y.; Bilad, M. R.; Vankelecom, I. F. J. Application of a Magnetically Induced Membrane Vibration (MMV) System for Lignocelluloses Hydrolysate Filtration. *J. Memb. Sci.* **2014**, *452*, 165–170.

[135] CHAM, The Phoenics Encyclopedia, <http://www.cham.co.uk/ChmSupport/encindex.php>, 2014

[136] F. Xie, W. Chen, J. Wang, J. Liu, CFD and experimental studies on the hydrodynamic performance of submerged flat-sheet membrane bioreactor equipped with micro-channel turbulence promoters, Chem. Eng. Process. Process Intensif. 99 (2016) 72–79. doi:10.1016/j.cep.2015.10.012.

[137] F. Xie, H. Ge, J. Liu, W. Chen, H. Song, CFD and experimental studies the effect of micro-channel turbulence promoter installation on the hydrodynamic performance of submerged flat-sheet membrane bioreactor, Chem. Eng. Process. - Process Intensif. 127 (2018) 28–35. doi:10.1016/j.cep.2018.03.009.

[138] M. Younas, S. Druon-Bocquet, J. Sanchez, Kinetic and dynamic study of liquid-liquid extraction of copper in a HFMC: Experimentation, modeling, and simulation, AIChE J. 56 (2010) 1469–1480. doi:10.1002/aic.12076.

[139] M. Younas, S. Druon-Bocquet, J. Sanchez, Experimental and theoretical mass transfer transient analysis of copper extraction using hollow fiber membrane contactors, J. Memb. Sci. 382 (2011) 70–81. doi:10.1016/j.memsci.2011.07.040.

[140] A. Muhammad, M. Younas, S. Druon-Bocquet, J. Romero, J. Sanchez-Marcano, Numerical modelling and simulation of membrane-based extraction of copper(II) using hollow fiber contactors, Desalin. Water Treat. 63 (2017) 113–123. doi:10.5004/dwt.2017.20169.

[141] Y.-L. Li, K.-L. Tung, CFD simulation of fluid flow through spacer-filled membrane module: selecting suitable cell types for periodic boundary conditions, Desalination. 233 (2008) 351–358. doi:10.1016/j.desal.2007.09.061.

[142] Y. Lou, R. Gogar, P. Hao, G. Lipscomb, K. Amo, J. Kniep, Simulation of net spacers in membrane modules for carbon dioxide capture, Sep. Sci. Technol. 52 (2017) 168–185. doi:10.1080/01496395.2016.1220396.

[143] K.K. Lau, M.Z. Abu Bakar, A.L. Ahmad, T. Murugesan, Feed spacer mesh angle: 3D modeling, simulation and optimization based on unsteady hydrodynamic in spiral wound membrane channel, J. Memb. Sci. 343 (2009) 16–33. doi:10.1016/j.memsci.2009.07.001.

[144] A. Siddiqui, N. Farhat, S.S. Bucs, R.V. Linares, C. Picioreanu, J.C. Kruithof, M.C.M. van Loosdrecht, J. Kidwell, J.S. Vrouwenvelder, Development and characterization of 3D-printed feed spacers for spiral wound membrane systems, Water Res. 91 (2016) 55–67. doi:10.1016/j.watres.2015.12.052.

[145] J. Schwinge, D.E. Wiley, D.F. Fletcher, Simulation of the flow around spacer filaments between narrow channel walls. 1. Hydrodynamics, Ind. Eng. Chem. Res. 41 (2002) 2977–2987. doi:10.1021/ie010588y.

[146] S.L. Xu, W.Q. Mi, A Two-Dimensional CFD Simulation for Different Spacers of Spiral Wound Moudles, Adv. Mater. Res. 557–559 (2012) 2249–2252. doi:10.4028/www.scientific.net/AMR.557-559.2249.

[147] I. Janajreh, R. Hashaikeh, D. Suwwan, Numerical simulation of membrane desalination in a conjugated heat transfer configuration: Role of spacers, Proc. 2014 Int. Renew. Sustain. Energy Conf. IRSEC 2014. (2014) 941–947. doi:10.1109/IRSEC.2014.7059882.

[148] S. Whitaker, The Forchheimer equation: A theoretical development, Transp. Porous Media. 25 (1996) 27–61. doi:10.1007/BF00141261.

[149] A. Amiri, K. Vafai, Analysis of dispersion effects and non-thermal equilibrium, non-Darcian, variable porosity incompressible flow through porous media, Int. J. Heat Mass Transf. 37 (1994) 939–954. doi:10.1016/0017-9310(94)90219-4.

[150] A. Amiri, K. Vafai, Transient analysis of incompressible flow through a packed bed, Int. J. Heat Mass Transf. 41 (1998) 4259–4279. doi:10.1016/S0017-9310(98)00120-3.

[151] S.P. Burke, W.B. Plummer, Gas Flow through Packed Columns 1, Ind. Eng. Chem. 20 (1928) 1196–1200. doi:10.1021/ie50227a025.

[152] C.R. Wilke, A Viscosity Equation for Gas Mixtures, J. Chem. Phys. 18 (1950) 517–519. doi:10.1063/1.1747673.

[153] L. Eykens, I. Hitsov, K. De Sitter, C. Dotremont, L. Pinoy, I. Nopens, B. Van der Bruggen, Influence of membrane thickness and process conditions on direct contact membrane distillation at different salinities, J. Memb. Sci. 498 (2016) 353–364. doi:10.1016/j.memsci.2015.07.037.

[154] V. Karanikola, A.F. Corral, H. Jiang, A.E. Sáez, W.P. Ela, R.G. Arnold, Effects of membrane structure and operational variables on membrane distillation performance, J. Memb. Sci. 524 (2017) 87–96. doi:10.1016/j.memsci.2016.11.038.

[155] V. Karanikola, A.F. Corral, H. Jiang, A. Eduardo Sáez, W.P. Ela, R.G. Arnold, Sweeping gas membrane distillation: Numerical simulation of mass and heat transfer in a hollow fiber membrane module, J. Memb. Sci. 483 (2015) 15–24. doi:10.1016/j.memsci.2015.02.010.

[156] W.M. Haynes, Handbook of Chemistry and Physics, Ninety Third ed, CRC Press,

2016.

Abbreviations

AB	acidogenic bacteria
ADE	advection-diffusion equation
AE	algebraic equation
AFMBR	particle-sparged anaerobic membrane bioreactor with fluidized polyethylene terephthalate beads
AGMD	air gap membrane distillation
AnMBR	anaerobic membrane bioreactor
ANN	artificial neural network
ASM	algebraic slip model
BC	boundary conditions
CAS	conventional activated sludge
CFD	computational fluid dynamics
COD	chemical oxygen demand
CP	concentration polarization
DCMD	direct contact membrane distillation
DE	differential equations
DGM	dusty gas model
HRT	hydraulic retention time
LEP	liquid entry pressure
MB	methanogenic bacteria
MBR	membrane bioreactor
MC	membrane crystallization
MCTP	micro-channel turbulence promoters
MF	microfiltration
MD	membrane distillation
MLSS	mixed-liquor suspended solid
MM	mathematical model
MMV	induced membrane vibration system
MPD	mean pore diameter
NF	nanofiltration
ODE	ordinary differential equation
PDE	partial differential equation
QRCD	quadratic rotation-orthogonal composite design

RO	reverse osmosis
RS	response surface
SGMD	sweeping gas membrane distillation
SMP	soluble microbial products
SRT	solids retention time
SS	suspended solids
TC	tubular configuration
TMP	transmembrane pressure
TP	temperature polarization
TSS	total suspended solids
UF	ultrafiltration
VFA	volatile fatty acids
VLE	vapour-liquid equilibrium
VMD	vacuum membrane distillation
VOC	volatile organic compound
VOF	volume of fluid

Nomenclature

a_{Ant}	Antoine equation coefficient
a_M	membrane width (m)
A_V	amplitude of vibrations (m)
A_{Shell}	cross section area of the shell side channel of the SGMD module (m^2)
A_{OF}	cross section area taken by one hollow fibre (m^2)
a_{Sch}	membrane permeation constant ($kg/(m^2 \cdot s \cdot Pa)$)
b	yield of reaction
b_{Ant}	Antoine equation coefficient
b_{ch}	channel height (m)
b_{SMP1}	yield of soluble microbial products degradation by acidogenic bacteria
b_{SMP2}	yield of soluble microbial products production by organic matter
b_{SMP3}	yield of soluble microbial products production from volatile fatty acids
b_{Sch}	exponent which defines the influence of Knudsen diffusion and viscous flow on the vapour flux
c	molar concentration (mol/m^3)
c_{Ant}	Antoine equation coefficient
C_P	heat capacity at constant pressure (J/kg·K)
$C_{\varepsilon 1}$	k-epsilon Reynolds-averaged Navier–Stokes model constant
$C_{\varepsilon 2}$	k-epsilon Reynolds-averaged Navier–Stokes model constant
C_μ	k-epsilon Reynolds-averaged Navier–Stokes model constant
D_{ij}	ordinary diffusion coefficient of the components i and j (m^2/s)
D_0	decay rate of biomasses (1/d)
D_K	Knudsen diffusion coefficient (m^2/s)
D_p	hydraulic diameter (m)
D_{Shell}	shell diameter of the SGMD module (m)
F	external force in the momentum balance in the flow (Pa)
f_M	frequency of vibrations (Hz)
g	standard acceleration due to gravity ($9.80665\ m/s^2$)
H	Enthalpy (J/mol)
HRT	hydraulic residence time (d)
h	heat transfer coefficient (J/(mol·K))
H^{cond}	enthalpy of condensation (J/mol)

H^{ev}	enthalpy of vaporization (J/mol)
I	identity matrix
I_T	turbulent intensity
J	transmembrane vapour flux (kg/(m^2·s))
k	thermal conductivity (W/(m·K))
K_{OM}	half-saturation constant associated with organic matter (g/L)
K_{VFA1}	K_{VFA1} is the half-saturation constant associated with volatile fatty acids (g/L)
K_{VFA2}	inhibition constant associated with volatile fatty acids (g/L)
k_{OM}	yield of organic matter degradation by acidogenic bacteria
k_{VFA1}	yield of volatile fatty acids production from organic matter
k_{VFA2}	yield of volatile fatty acids degradation by methanogenic bacteria
k_T	turbulent kinetic energy (m^2/s^2)
L	mean free path (m)
L_M	membrane length (m)
L_T	turbulent length scale (m)
M	molar mass (g/mol)
$\dot{m}$	flow rate (kg/s)
N	molar flux (mol/m^2 s)
N_{iA}	molar flux coefficient for axisymmetric coordinates (mol/m^2 s)
N_D	vapor diffusive flux (mol/(m^2·s))
N_V	viscous flux (mol/(m^2·s))
n_M	number of membranes
P	pressure of the feed flow (Pa)
P^*	partial pressure (Pa)
P_k	production of k_T (Pa)
q	conductive heat flux (W/m^2)
Q	heat source (W/m^3)
Q_A	heat correction factor for axisymmetric coordinates (W/m^3)
R	mass source of the flow (kg/(m^3·s))
r_M	pore radius (m)
R_A	mass coefficient for axisymmetric coordinates (kg/m^{3}s)
R_R	reaction rate (kg/(m^3·s))
R_g	universal gas constant (8.3144598(48) J/(K·mol))
S	cross-section area (m^2)
S_t	strain-rate tensor

S_h	heat source term (W/m^4)
SRT	solute residence time (d)
T	temperature (K)
u	radial velocity (m/s)
V	molar volume, (m^3/mol)
v	velocity (m/s)
v_{Dz}	superficial velocity (m/s)
x	molar fraction in the liquid phase
y	molar fraction in the gas phase

Greek letters:

δ	thickness (m)
ε_M	porosity of the membrane
ε_T	turbulent dissipation rate (m^2/s^3)
μ	dynamic viscosity (Pa·s)
μ_T	eddy (turbulent) viscosity (Pa·s)
μ_{AB}	acidogenesis kinetics (1/d)
μ_{MB}	methanogenesis kinetics (1/d)
Π	Permeability (m^2)
ρ	density (kg/m^3)
ρ_i	mass concentration of the component i (kg/m^3)
σ_k	k-epsilon Reynolds-averaged Navier–Stokes model constant
σ_ε	k-epsilon Reynolds-averaged Navier–Stokes model constant
σ_{ij}	average collision diameter for the components i and j (Å)
τ	Time (s)
τ_M	membrane tortuosity
τ_{Tz}	turbulent viscous stress tensor
τ_v	viscous stress tensor
ϕ	volume fraction
ψ	association factor
Ω	collision integral

Subscripts/superscripts:

atm	atmosphere
eff	effective
F	feed side
HF	hollow fibre

i	component identifier
in	inlet
j	component identifier
Lum	lumen side of the hollow fibre
M	membrane
OF	one hollow fibre
out	outlet
P	permeate side
ref	reference
Sp	spacer
$Shell$	shell side of the hollow fibre
V	vapor
z	domain identifier
$*$	Axisymmetric coordinates

List of figures

FIGURE 1: ALGORITHME DU DEVELOPPEMENT D'UN MODELE [1]. 2

FIGURE 2: CLASSIFICATION DES MMS BASEE SUR LA COMPLEXITE MATHEMATIQUE [1]..... 5

FIGURE 3: ALGORITHM OF MODEL DEVELOPMENT [1]. 10

FIGURE 4: CLASSIFICATION OF MMS BASED ON MATHEMATICAL COMPLEXITY [1]..... 13

FIGURE 1.1: CONFIGURATIONS OF MD: (A) DCMD, (B) VMD, (C) AGMD AND (D) SGMD [38]. 19

FIGURE 1.2: CONFIGURATIONS OF MD MODULES: (A) PLATE AND FRAME MODULE; (B) FLAT SHEET MODULE; (C) THIN CHANNEL MODULE [52]; (D) LEWIS CELL [53-56]; (E) SPIRAL-WOUND MODULE (CROSS-SECTION) [60]..... 26

FIGURE 1.3: SCHEMATIC REPRESENTATION OF SPACERS [62]..... 27

FIGURE 1.4: ELECTRICAL ANALOGY CIRCUIT AS A COMBINATION OF DIFFERENT MODES OF THE MASS TRANSFER IN THE SCHOFIELD'S MODEL..... 33

FIGURE 1.5: SCHEMATIC REPRESENTATION OF CALCULATED VARIABLES IN THE SCHOFIELD'S MODEL..... 34

FIGURE 1.6: SCHEMATIC REPRESENTATION OF CALCULATED VARIABLES IN THE TOMASZEWSKA'S MODEL..... 37

FIGURE 1.7: ELECTRICAL ANALOGY CIRCUIT AS A COMBINATION OF DIFFERENT MODES OF THE MASS TRANSFER IN THE DGM..... 37

FIGURE 1.8: SCHEMATIC REPRESENTATION OF CALCULATED VARIABLES IN THE LAWSON-LLOYD MODEL. 39

FIGURE 1.9. SCHEMATIC REPRESENTATION OF CALCULATED VARIABLES IN THE LAGANA'S MODEL..... 43

FIGURE 1.10: SCHEMATIC REPRESENTATION OF CALCULATED VARIABLES IN THE YU'S MODEL. 46

FIGURE 1.11: SCHEMATIC REPRESENTATION OF CALCULATED VARIABLES IN THE HAYER'S MODEL. 48

FIGURE 1.12: SCHEMATIC REPRESENTATION OF CALCULATED VARIABLES IN THE GUSTAFSON'S MODEL. 53

FIGURE 1.13: SCHEMATIC REPRESENTATION OF CALCULATED VARIABLES IN THE ELEIWI'S MODEL. 55

FIGURE 1.14: SCHEMATIC REPRESENTATION OF THE MATHEMATICAL STRUCTURE OF THE RSM MODEL. 57

FIGURE 1.15. SCHEMATIC REPRESENTATION OF CALCULATED VARIABLES IN THE ALI'S MODEL. 59

FIGURE 1.16: SCHEMATIC REPRESENTATION OF CALCULATED VARIABLES IN THE FIRST KHAYET'S MODEL. 67

FIGURE 1.17: SCHEMATIC REPRESENTATION OF CALCULATED VARIABLES IN THE SECOND KHAYET'S MODEL. 69

FIGURE 1.18: SCHEMATIC REPRESENTATION OF CALCULATED VARIABLES IN THE BOI'S MODEL. 70

FIGURE 1.19: SCHEMATIC REPRESENTATION OF CALCULATED VARIABLES IN THE MOURGUES' MODEL. 75

FIGURE 1.20: SCHEMATIC REPRESENTATION OF CALCULATED VARIABLES IN THE CHARFI'S MODEL. 81

FIGURE 1.21: SCHEMATIC REPRESENTATION OF THE RS MODEL. 82

FIGURE 1.22: SCHEMATIC REPRESENTATION OF THE ANN MODEL. 83

FIGURE 1.23: SUBMERGED ANMBR CONFIGURATION WITH (A) THE MEMBRANE MODULE IMMERSED INSIDE THE FEED TANK AND (B) THE MEMBRANE MODULE IMMERSED INSIDE AN EXTERNAL FILTRATION TANK. 89

FIGURE 1.24: SIDE-STREAM ANMBR CONFIGURATION. 89

FIGURE 1.25: SCHEMATIC REPRESENTATION OF THE MATHEMATICAL STRUCTURE OF THE RS MODEL. 96

FIGURE 1.26: SCHEMATIC REPRESENTATION OF THE CHARFI'S ANMBR MODEL. 100

FIGURE 2.1: (A) SCHEMATIC REPRESENTATIONS OF THE (A) DCMD AND (B) SGMD PROCESSES. 109

FIGURE 2.2: SCHEMATIC REPRESENTATION OF THE MODEL FOR (A) THE FLAT SHEET CONFIGURATION AND (B) THE HOLLOW FIBRE CONFIGURATION, RESPECTIVELY. PF, PP, PM AND TF, TP, TM ARE THE PRESSURES AND TEMPERATURES IN THE FEED, PERMEATE AND MEMBRANE DOMAIN RESPECTIVELY; ρF AND ρP ARE THE DENSITIES OF THE FEED AND PERMEATE FLOWS RESPECTIVELY; ciM IS THE MOLAR CONCENTRATION OF THE COMPONENT i IN THE MEMBRANE PORES; Ni IS THE MOLAR TRANSMEMBRANE FLUX OF THE COMPONENT i; $NFin$, $NPin$ AND $NFout$, $NPout$ ARE THE TOTAL FLUXES OF THE FEED LIQUID AND PERMEATE FLUID AT THE INLET AND OUTLET OF FEED AND PERMEATE RESPECTIVELY. 110

FIGURE 2.3: SEGMENTS OF THE CROSS-SECTIONAL AREA OF (A) THE REAL HOLLOW FIBRE MODULE AND (B) THE MODELLED HOLLOW FIBRE MODULE. 111

FIGURE 2.4: SCHEMATIC REPRESENTATION OF THE MODEL FOR THE FLAT SHEET CONFIGURATION CONTAINING MORE THAN ONE MEMBRANE. 112

FIGURE 2.5: SCHEMATIC REPRESENTATION OF THE SUBMERGED ANMBR WITH THE MMV SYSTEM. 132

FIGURE 2.6: SCHEMATIC REPRESENTATION OF THE MMV SYSTEM. 134

FIGURE 3.1: (A) THE TESTED DCMD MODULES AND (B) ARRANGEMENT OF THE FIBRES INSIDE THE MODULES. 138

FIGURE 3.2: SCHEMATIC DIAGRAM OF THE EXPERIMENTAL SETUP. 139

FIGURE 4.1: THE MESHING OF THE COMMERCIAL HOLLOW-FIBRE MODULE. 143

FIGURE 4.2: THE SAMPLE FRAGMENT OF THE MESHING OF THE SPACER-FILLED SGMD MODULE. 144

FIGURE 4.3: THE MESHING OF ANMBR. 144

FIGURE 5.1: GRAPHICAL REPRESENTATION OF THE APPLIED MESHES IN THE MESH STUDY FOR THE COMMERCIAL HOLLOW FIBRE DCMD MODULE. 146

FIGURE 5.2: VALIDATION OF THE DCMD MODEL. (A) THE EFFECT OF THE FEED FLOW RATE ON THE PERFORMANCE OF THE COMMERCIAL HOLLOW FIBRE MODULE AND (B) THE CORRESPONDING GOODNESS OF FIT (TF = 55 °C, TP = 29 °C, VP = 50 L H^{-1}). 147

FIGURE 5.3: VALIDATION OF THE DCMD MODEL. (A) THE EFFECT OF THE FEED SALINITY ON THE PERFORMANCE OF THE COMMERCIAL HOLLOW FIBRE MODULE AND (B) THE CORRESPONDING GOODNESS OF FIT (TF= 46 °C, VF=75 L/H, TP= 20 °C, VP=38 L/H). 147

FIGURE 5.4: VALIDATION OF THE DCMD MODEL. (A) THE EFFECT OF THE FEED FLOW RATE ON THE PERFORMANCE OF THE LAB-SCALE HOLLOW FIBRE MODULE AND (B) THE CORRESPONDING GOODNESS OF FIT (TF= 55 °C, VF=9 L/H, TP= 10 °C, VP=4.2 L/H). 148

FIGURE 5.5: VALIDATION OF THE DCMD MODEL. (A) THE EFFECT OF THE FEED SALINITY ON THE PERFORMANCE OF THE LAB-SCALE HOLLOW FIBRE MODULE AND (B) THE CORRESPONDING GOODNESS OF FIT (VF=9 L/H, TP= 10 °C, VP=4.2 L/H). 148

FIGURE 5.6: FEED TEMPERATURE STUDY. THE SIMULATED TEMPERATURE DISTRIBUTIONS IN THE COMMERCIAL HOLLOW FIBRE MODULE FOR THE FEED INLET TEMPERATURE EQUAL TO (A) 35 AND (B) 55 °C, RESPECTIVELY (VF = 150 L H^{-1}, TP = 29 °C, VP = 50 L H^{-1}). 150

FIGURE 5.7: FEED TEMPERATURE STUDY. THE SIMULATED WATER VAPOUR CONCENTRATION DISTRIBUTIONS IN THE MEMBRANE PORES OF THE COMMERCIAL HOLLOW FIBRE MODULE IN THE SIMULATIONS FOR THE FEED INLET TEMPERATURE EQUAL TO (A) 35 AND (B) 55 °C, RESPECTIVELY (VF = 150 L H^{-1}, TP = 29 °C, VP = 50 L H^{-1}) 150

FIGURE 5.8: FEED TEMPERATURE STUDY. THE SIMULATED TEMPERATURE DISTRIBUTIONS IN THE COMMERCIAL HOLLOW FIBRE MODULE FOR THE FEED RATE EQUAL TO (A) 50 AND (B) 150 L H^{-1}, RESPECTIVELY (TF = 55 °C, TP = 29 °C, VP = 50 L H^{-1}). 150

FIGURE 5.9: VALIDATION OF THE MODEL AND EFFECT OF THE FEED SALINITY ON THE PERFORMANCE OF THE FILLER-SUPPORTED FLAT SHEET DCMD MODULE [153]. 152

FIGURE 5.10: FEED SALINITY STUDY. THE CALCULATED WATER VAPOUR PRESSURE AT THE FEED-MEMBRANE AND PERMEATE-MEMBRANE INTERFACES IN THE SPACER-FILLED FLAT SHEET MODULE FOR THE (A) PE MEMBRANE AND (B) PVDF MEMBRANE, RESPECTIVELY (SIMULATION STRATEGY 2, TF = 55.5 °C, vF = 0.13 M/S, $cSalt$=240 G/L, TP = 49.5 °C, vP = 0.13 M/S). 152

FIGURE 5.11: FEED SALINITY STUDY. THE SIMULATED SALT CONCENTRATION DISTRIBUTIONS IN THE SPACER-FILLED FLAT SHEET MODULE FOR THE SALINITY EQUAL TO (A) 120 AND (B) 230 G/L, RESPECTIVELY (SIMULATION STRATEGY 1, TF = 55.5 °C, vF = 0.13 M/S, TP = 49.5 °C, vP = 0.13 M/S). 152

FIGURE 5.12: VALIDATION OF THE MODEL AND EFFECT OF THE MEMBRANE LENGTH ON THE PERFORMANCE OF THE HOLLOW FIBRE DCMD MODULE. (A) EFFECT OF THE PERMEATE FLOW RATE ON THE TRANSMEMBRANE FLUX. EXPERIMENTAL RESULTS FROM THE REFERENCE [98]. (B) TEMPERATURE PROFILES IN THE DCMD MODULE AT THE FEED OUTLET FOR THE GIVEN MEMBRANE LENGTHS (TF = 40 °C, vF = 0.14 M/S, TP = 20 °C, vP = 0.5 M/S). 153

FIGURE 5.13: MEMBRANE LENGTH STUDY. THE SIMULATED TEMPERATURE DISTRIBUTIONS IN THE HOLLOW FIBRE MODULE FOR THE MEMBRANE LENGTH EQUAL TO (A) 0.2 AND (B) 0.45 M, RESPECTIVELY (TF = 40 °C, vF = 0.14 M/S, TP = 20 °C, vP = 0.5 M/S). 154

FIGURE 5.14: (A) EFFECT OF THE MEMBRANE THICKNESS ON THE TRANSMEMBRANE FLUX AND (B) TEMPERATURE PROFILE OF THE LUMEN SIDE OF THE HOLLOW FIBRE (FEED COMPARTMENT) AT THE REFERENCE POSITION 0.25 M FROM THE ENTRANCE OF THE FEED CHANNEL. 154

FIGURE 5.15: GRAPHICAL REPRESENTATION OF THE APPLIED MESHES IN THE MESH STUDY FOR THE FLAT SHEET SGMD MODULE. 155

FIGURE 5.16: VALIDATION OF THE SGMD MODEL. (A) THE EFFECT OF THE FEED TEMPERATURE ON THE PERFORMANCE OF THE FLAT SHEET SGMD MODULE AND (B) THE CORRESPONDING GOODNESS OF FIT (vF=5.6×10^{-3} M/S, vP=9.3×10^{-2} M/S, TP= 20 °C). 157

FIGURE 5.17: EFFECT OF THE FEED INLET TEMPERATURE ON THE TEMPERATURE DISTRIBUTION IN THE FLAT SHEET MODULE. (A) THE TEMPERATURE DISTRIBUTION IN THE MODULE AT $TFin$= 45 °C. (B) TEMPERATURE PROFILES OF THE MODULE AT CHOSEN REFERENCE POSITION 0.087 M FROM THE ENTRANCE OF THE FEED CHANNEL (vF=5.6×10^{-3} M/S, vP=9.3×10^{-2} M/S, TP= 20 °C). 158

FIGURE 5.18: EFFECT OF THE FEED TEMPERATURE ON THE WATER VAPOUR FLUX AT (A) THE SPACER-FILLED FLAT SHEET MODULE (vF=5.6×10^{-3} M/S, vP=9.3×10^{-2} M/S) AND AT (B) THE HOLLOW FIBRE MODULE (vF=5.6×10^{-3} M/S, vP=9.3×10^{-2} M/S). 158

FIGURE 5.19: VALIDATION OF THE MODEL WITH THE HOLLOW FIBRE SGMD MODULE AND EFFECT OF THE FEED VELOCITY ON THE MODULE PERFORMANCE. (A) WATER VAPOUR FLUX AS FUNCTION OF THE FEED VELOCITY. (B) THE TEMPERATURE DISTRIBUTION IN THE MODULE AT vF= 0.008 M/S. (C) THE TEMPERATURE DISTRIBUTION IN THE MODULE AT vF= 0.02 M/S. (D) TEMPERATURE PROFILES OF THE MODULE AT REFERENCE POSITION 0.06 M FROM THE ENTRANCE OF THE FEED CHANNEL FOR THE CASE OF THE FEED INLET TEMPERATURE 71 °C (vP=0.54 M/S)..... 159

FIGURE 5.20: VALIDATION OF THE MODEL WITH THE SPACER-FILLED FLAT SHEET SGMD MODULE AND EFFECT OF THE PERMEATE VELOCITY ON THE MODULE PERFORMANCE. (A) WATER VAPOUR FLUX AS FUNCTION OF THE PERMEATE VELOCITY. (B) TEMPERATURE PROFILE OF THE MODULE AT REFERENCE POSITION 0.07 M FROM THE ENTRANCE OF THE FEED CHANNEL (STRATEGY 2, TF= 70 °C, vF=0.11 M/S). 160

FIGURE 5.21: VALIDATION OF THE MODEL AND EFFECT OF THE SG VELOCITY ON THE WATER VAPOUR FLUX AT (A) THE FLAT SHEET MODULE (TF= 25 °C, TP= 20 °C, vF=5.6×10^{-3} M/S) AND AT (B) THE HOLLOW FIBRE MODULE (TP= 24 °C, vF=0.02 M/S)..... 161

FIGURE 5.22: VALIDATION OF THE MODEL WITH THE COMMERCIAL HOLLOW FIBRE MODULE AND EFFECT OF THE FEED SALINITY ON (A) THE PERFORMANCE OF THE COMMERCIAL HOLLOW FIBRE MODULE CONTAINING 40 FIBRES (vF= 0.8 M/S, vP= 11.3 M/S, TF= 50 °C, TP= 20 °C) AND ON THE PERFORMANCE OF THE HOLLOW FIBRE MODULE CONTAINING 10633 FIBRES (vF=0.02 M/S, vP=0.54 M/S, TF= 70 °C, TP= 24 °C). 161

FIGURE 5.23: EFFECT OF (A) THE MEMBRANE LENGTH AND (B) MEMBRANE THICKNESS ON THE WATER VAPOUR FLUX AT THE FLAT SHEET SGMD MODULE (vF=5.6×10^{-3} M/S, vP=9.3×10^{-2} M/S, PP=0.9×10^{5} PA, TF= 45 °C, TP= 20 °C). 162

FIGURE 5.24: GRAPHICAL REPRESENTATION OF THE APPLIED MESHES IN THE MESH STUDY FOR THE FLAT SHEET SGMD MODULE. 163

FIGURE 5.25: VALIDATION OF THE ANMBR MODEL. THE DISTRIBUTION OF THE VOLUME FRACTION OF SOLIDS IN THE ANMBR TANK AT THE VIBRATION FREQUENCY SET (A) 0 (WITHOUT VIBRATIONS) AND (B) 15 HZ (τ= 5 MIN). 164

FIGURE 5.26: THE EFFECT OF THE VIBRATION FREQUENCY ON THE MAXIMUM FLUID VELOCITY IN THE VERTICAL DIRECTION. 166

FIGURE 5.27: THE ABSOLUTE VELOCITY DISTRIBUTION IN THE ANMBR TANK AT THE VIBRATION FREQUENCY SET (A) 0, (B) 5, (C) 10 AND (D) 15 HZ (τ=13 S, AV =0.001 M). ... 166

FIGURE 5.28: THE DISTRIBUTION OF THE VOLUME FRACTION OF SOLIDS IN THE ANMBR TANK AT THE VIBRATION FREQUENCY SET (A) 0 AND (B) 15 HZ (τ=300 S, AV=0.001 M)..... 167

FIGURE 5.29: THE EFFECT OF THE VIBRATION AMPLITUDE ON THE MAXIMUM FLUID VELOCITY IN THE VERTICAL DIRECTION (fM=15 HZ)..... 167

FIGURE 5.30: THE DISTRIBUTION OF THE VOLUME FRACTION OF SOLIDS IN THE ANMBR TANK AT THE VIBRATION AMPLITUDE SET (A) 0.001 AND (B) 0.01 M (τ=300 S, fM=15 HZ). 168

List of tables

TABLEAU 1: DIFFICULTE ET POSSIBILITE DE RESOLUTION DES EQUATIONS DES MODELES. 6

TABLEAU 2: CLASSIFICATION DES PROCEDES MEMBRANAIRES SELON LEUR FORCE MOTRICE. 7

TABLE 3: POSSIBILITY OF ANALYTICAL SOLUTION OF VARIOUS EQUATIONS USED IN MMS [1]. 14

TABLE 4: CLASSIFICATION OF MEMBRANE PROCESSES BY DRIVING FORCE. 14

TABLE 1.1: COMMERCIAL MEMBRANES USED IN MD PROCESSES [15, 38]. 20

TABLE 1.2: MELTING POINTS OF THE COMMERCIAL MATERIALS [15, 38]. 21

TABLE 1.3: THERMAL CONDUCTIVITIES OF THE COMMERCIAL MATERIALS [15, 38]. 21

TABLE 1.4: STUDIES OF MD APPLICATIONS IN THE FOOD INDUSTRY 28

TABLE 1.5: COMPARISON OF DIFFERENT MODELS FOR DCMD. 63

TABLE 1.6: COMPARISON OF DIFFERENT MODELS FOR SGMD. 87

TABLE 1.7. MEMBRANE MATERIALS AND MEMBRANE MODULES APPLIED IN ANMBRS. 90

TABLE 2.1: BOUNDARY CONDITIONS FOR THE FEED AND PERMEATE DOMAINS. 121

TABLE 2.2: BOUNDARY CONDITIONS FOR THE MEMBRANE DOMAIN IN THE DCMD MODEL. . 131

TABLE 2.3: BOUNDARY CONDITIONS FOR THE MEMBRANE DOMAIN IN THE SGMD MODEL. . 131

TABLE 2.4: BOUNDARY CONDITIONS FOR ANMBR MODEL. 136

TABLE 3.1: PROPERTIES OF THE MEMBRANE USED IN THE EXPERIMENTS 138

TABLE 3.2: PROPERTIES OF THE MEMBRANE USED IN THE EXPERIMENTS 141

TABLE 3.3: PROPERTIES OF THE MEMBRANE AND REACTOR USED IN THE EXPERIMENTS. 142

TABLE 3.4: PROPERTIES OF THE INFLUENT AND OPERATION PARAMETERS. 142

TABLE 4.1: PARAMETERS FOR AM2B MODEL [7] 144

TABLE 5.1: RESULTS OF THE MESH STUDY FOR THE COMMERCIAL HOLLOW FIBRE DCMD MODULE. 146

TABLE 5.2: RESULTS OF THE MESH STUDY FOR THE FLAT SHEET SGMD MODULE. 156

TABLE 5.3: RESULTS OF THE MESH STUDY FOR ANMBR COUPLED WITH THE MMV SYSTEM. 164

APPENDIX

List of the published articles dedicated to modelling of DCMD and SGMD

1. V. Perfilov, V. Fila, J. Sanchez Marcano, A general predictive model for sweeping gas membrane distillation, Desalination. 443 (2018) 285–306. doi:10.1016/j.desal.2018.06.007.

Abstract

Among the configurations of membrane distillation processes, sweeping gas membrane distillation (SGMD) remains one of the less studied. In spite of an increasing number of publications, generally the modeling of SGMD has been carried out by fitting heat and mass transfer coefficients and with the use of empirical correlations. In this work, a general predictive model based on computational fluid dynamics (CFD) is presented. This model allows simulating hollow fiber and flat sheet configurations under wide range of process conditions; with a minimum number of input data and without requiring empirical parameters or laboratory experiments. For this purpose, the momentum, mass and heat balances of the process are described by partial differential equations, algebraic and ordinary differential equations. The model has been validated with experimental results available in the literature. Indeed, the influence of operating conditions and membrane geometric characteristics on the process performance was investigated. The conducted studies prove that the proposed model would be potentially applied for the optimization of process conditions, design of membrane modules as well as for the further cost estimation of the process.

2. V. Perfilov, A. Ali, V. Fila, A general predictive model for direct contact membrane distillation, Desalination. 445 (2018) 181–196. doi:10.1016/j.desal.2018.08.002.

Abstract

Direct contact membrane distillation (DCMD) is a nonisothermal technology applied for the separation of non-volatile components from aqueous solutions. Nowadays, a huge number of publications are dedicated to modeling of DCMD, however all of the presented models have at least one of the following disadvantages: oversimplification, the use of empirical heat and mass transfer coefficients and poor prediction for cases which are out of the experimental data range. To overcome these drawbacks, a multipurpose general predictive model of DCMD has been developed. The proposed model is suitable for hollow fiber and flat sheet configurations with or without spacers. For each compartment of the DCMD process, our model describes the momentum, mass and heat balances by systems of ordinary differential,

partial differential and algebraic equations. The performance of the model has been analyzed in terms of the operating parameters (concentration of a feed solution, feed flow rate and feed temperature) and membrane thickness and length. The simulated results were in very good agreement with experimental and literature data. The broad parametric study demonstrates the great potential of application of the proposed model not only in the process optimization but in design of DCMD modules.

Résumé

Dans cette thèse ont été développés des modèles mathématiques pour les procédés de distillation membranaire à contact direct (DCMD) et avec balayage gazeux (SGMD) ainsi qu'un modèle sur l'hydrodynamique des bioréacteurs membranaires anaérobiques (AnMBRs) équipés d'un système de vibration membranaire induite (MMV). Les modèles pour la DCMD et la SGMD permettent de simuler le comportement des modules plats ou à fibres creuses sous différentes conditions opératoires, sans avoir recours aux données expérimentales ou à des équations empiriques pour les transferts de masse et de chaleur. Les modèles ont été validés avec des résultats expérimentaux et de la littérature et ont permis de déterminer l'influence de différents paramètres opérationnels et de la géométrie des modules sur les performances des procédés. Le modèle développé pour les AnMBRs équipés du système MMV permet d'étudier l'effet de la vibration membranaire sur l'hydrodynamique du réservoir. L'analyse paramétrique a permis d'étudier l'effet de la fréquence et de l'amplitude des vibrations sur la vitesse du fluide et la fraction volumique des solides dans le réservoir. Dans ce travail il a été démontré que les modèles proposés pourront être potentiellement appliqués à des études expérimentales préliminaires, l'optimisation des conditions opératoires, la conception des modules membranaires ainsi que pour l'estimation des coûts des procédés.

Mots clefs: modélisation mathématique, distillation membranaire à contact direct, distillation membranaire avec balayage gazeux, bioréacteurs membranaires anaérobiques.

Abstract

In this work have been developed general predictive models for direct contact membrane distillation (DCMD) and sweeping gas membrane distillation (SGMD) as well as a hydrodynamic model for anaerobic membrane bioreactors (AnMBRs) equipped with the induced membrane vibration (MMV) system. DCMD and SGMD models allow simulating hollow fibre and flat sheet configurations under wide range of process conditions without empirical mass and heat transfer coefficients or laboratory experiments. The models have been validated with experimental and literature data. Indeed, the influence of operating conditions and membrane geometric characteristics on the process performance has been investigated. The model for AnMBRs with MMV studies the effect of the membrane vibration on the hydrodynamics of the AnMBR tank. The parametric study allows knowing, the effects of the vibration frequency and amplitude on the fluid velocity and volume fraction of solids. The conducted studies prove that all the proposed models would be potentially applied for the pre-experimental study, optimization of process conditions, design of membrane modules as well as for the further cost estimation of the processes.

Keywords: mathematical modelling, direct contact membrane distillation, sweeping gas membrane distillation, anaerobic membrane bioreactors.